MATERIALS AND MICROSTRUCTURES FOR HIGH TEMPERATURE ELECTROCHEMICAL DEVICES THROUGH CONTROL OF PEROVSKITE DEFECT CHEMISTRY

Dragos Neagu

A Thesis Submitted for the Degree of PhD
at the
University of St Andrews

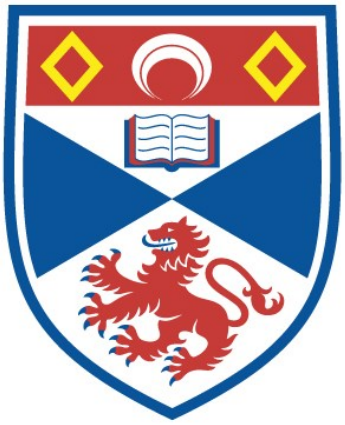

2013

Materials and Microstructures for High Temperature Electrochemical Devices through Control of Perovskite Defect Chemistry

Dragos Neagu

Supervised by Professor John T. S. Irvine

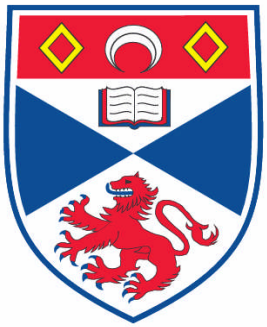

A Thesis Submitted for the Degree of PhD

at the

University of St Andrews

December 2012

DECLARATION

I, Dragos Neagu, hereby certify that this thesis, which is approximately 60,000 words in length, has been written by me, that it is the record of work carried out by me and that it has not been submitted in any previous application for a higher degree.

I was admitted as a research student in November, 2008 and as a candidate for the degree of PhD in September, 2009; the higher study for which this is a record was carried out in the University of St Andrews between 2008 and 2012.

Date …….. signature of candidate ……..……

I hereby certify that the candidate has fulfilled the conditions of the Resolution and Regulations appropriate for the degree of PhD in the University of St Andrews and that the candidate is qualified to submit this thesis in application for that degree.

Date ……. signature of supervisor ……

In submitting this thesis to the University of St Andrews I understand that I am giving permission for it to be made available for use in accordance with the regulations of the University Library for the time being in force, subject to any copyright vested in the work not being affected thereby. I also understand that the title and the abstract will be published, and that a copy of the work may be made and supplied to any bona fide library or research worker, that my thesis will be electronically accessible for personal or research use unless exempt by award of an embargo as requested below, and that the library has the right to migrate my thesis into new electronic forms as required to ensure continued access to the thesis. I have obtained any third-party copyright permissions that may be required in order to allow such access and migration, or have requested the appropriate embargo below.

The following is an agreed request by candidate and supervisor regarding the electronic publication of this thesis:

Access to printed copy but embargo of electronic publication of thesis for a period of one year on the following grounds:

Publication would preclude future publication.

Date …….. signature of candidate …… signature of supervisor ……

ACKNOWLEDGMENTS

I would like to express my sincere gratitude to my supervisor, Professor John T. S. Irvine, for offering me the opportunity to join his research group and thus make contact with people from a diverse area of expertise and culture. I am especially grateful to him for allowing me to explore different aspects of solid state chemistry independently while also providing key guidance at the right time.

I would also like to thank my friend and colleague Dr. George Tsekouras for a constructive, dynamic, inspiring and enjoyable collaboration which contributed significantly to this thesis.

I am also grateful to other past or present members in the JTSI group who helped me with various matters throughout my PhD. Dr. Paul Connor for generously sharing his time and extensive knowledge, for helping with electrochemistry, software, general advice, experimental setups and many other things. Dr. David Miller, for his assistance with conductivity measurements and TEM studies on my samples, but also for useful discussions on perovskites. Mr. Harald Schlegl, for valuable guidance on electron microscopy, infiltration and other discussions. Dr. Martin Smith, for insightful discussions about science or life in general and raising questions which led to answers that are now part of this thesis. Dr. Samir Boulfrad, for his help and expertise while at St Andrews, for doing TEM on my samples after he left to KAUST, and friendly recommendations throughout. Dr. Abul Kalam Azad, in particular for introduction to Rietveld refinement and assistance in experiments related to crystal structure determination. Dr. Cristian Savaniu, for introduction to equipment and techniques, and general advice. Mrs. Julie Nairn, for help with many experimental matters and dedication to improving the lab workspace.

I am also much obliged to various people in the School of Chemistry for their help with experimental matters and valuable recommendations, including Mrs. Silvia Williamson (TGA, dilatometry), Mr. Ross Blackley (SEM, XRD), Mr. George Anthony, Mr. Robert Cathcart and Mr. Brian Walker for fixing various pieces of equipment.

I am very grateful to Dr. Hervé Ménard (Sasol, St Andrews) for XPS measurements and for many other recommendations and discussions but also to Sasol Technology (UK) in St. Andrews for providing access to the XPS facility.

I would also like to give my heartfelt thanks to my high school chemistry teacher, Mrs. Diana Antonia Petcu, for helping me to discover myself; I will forever be in your debt.

I gratefully acknowledge the European Projects SOFC600 and METSAPP, and the EPSRC Supergen XIV Project Delivery of Sustainable Hydrogen for funding.

ABSTRACT

The development of technologies that enable efficient and reliable energy inter-conversion and storage is of key importance for tempering the intermittent availability of renewable energy sources, and thus for developing an energy economy based on sustainable, clean energy production. Solid oxide electrolysis cells (SOECs) may be used to store excess electrical energy as hydrogen, while solid oxide fuel cells (SOFCs) could convert back hydrogen into electricity, thus balancing energy availability and demand. However, the current state-of-the-art hydrogen electrode used in both SOECs and SOFCs, the Ni-yttria-stabilised zirconia cermet (Ni-YSZ), is unreliable in conjunction with intermittent energy sources, in particular due to its innate redox instability.

This thesis explores the fundamental properties of various inherently redox stable A-site deficient titanate perovskite systems ($A_{1-\alpha}BO_3$, B = Ti), seeking to uncover the principles that enhance their properties so that they may be used to replace Ni-YSZ.

In particular, this work demonstrates that the versatility of perovskites with respect to the introduction of lattice defects such as vacancies and cation substitutions enables considerable improvements in the extent of reduction, electronic conductivity and overall electrochemical activity. Most importantly, the defect chemistry context set by the presence of A-site vacancies was found to trigger the exsolution of electrocatalytically active nanoparticles from the parent perovskite, upon reduction. This is an entirely new phenomenon which was explored and exploited throughout this study to produce perovskite surfaces decorated with uniformly distributed catalytically active nanoparticles. As demonstrated in this study, the exsolution phenomenon excels in terms of producing nanoparticles with

uniform size, distribution, diverse composition and ‘unconventional’ surface anchorage.

The resulting enhanced properties, and especially the exsolution phenomenon, contributed coherently towards improving the suitability of the perovskites developed here towards their application as hydrogen electrode materials. Consequently, when integrated into SOEC button cells as hydrogen electrodes, they exhibited a step-change increase in performance compared to other perovskites considered to date.

Many of the principles and perovskite defect chemistry explored and exemplified in this study on perovskite titanates may be extended to other perovskites as well. In particular the advanced control and understanding achieved in this work over the exsolution phenomenon may inspire the formulation of new and sophisticated oxide materials with advanced functionality.

CONTENTS

1 INTRODUCTION

1.1 The energy context

Throughout history, the number and sophistication of energy sources but also the amount of energy used by the human race has gradually increased, closely reflecting the stage of its development. Currently, the global energy economy is dominated by fossil fuels (see Figure 1-1), but this is expected to shift in favour of renewable energies, in the 'not-so-distant' future.[1–3] Among several factors that drive the transition from fossil to renewable energy, two have proven to be particularly critical and will be highlighted next.

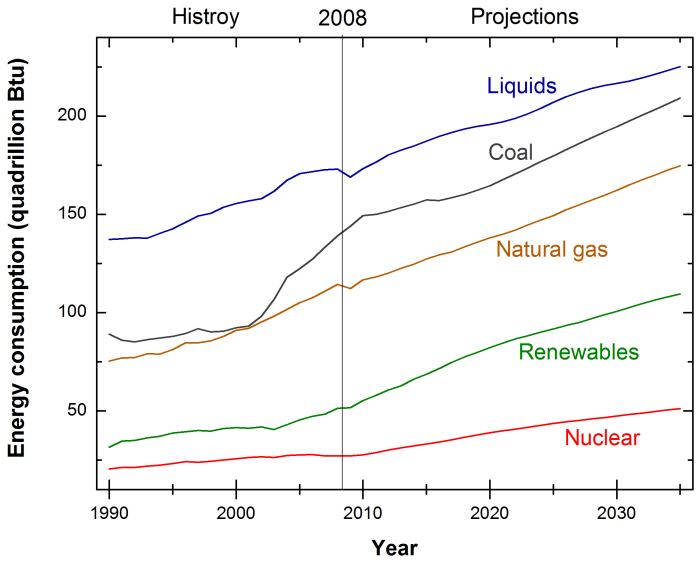

Figure 1-1 | World energy consumption by fuel, 1990–2035 (1 quadrillion = 10^{15}, 1 Btu ~ 1055 J)[2].

First, it is important to realise that as the supply of crude oil will peak soon, there will be not enough (cheap) oil to sustain world-wide economic growth.[1,2] Secondly, the burnout of fossil fuels is always accompanied by emission of greenhouse gases such as CO_2 which have been demonstrated to contribute towards the rise of Earth's average temperatures, a phenomenon also known as global warming. There are reasons to believe that if not controlled by a considerable decrease in greenhouse emissions over the coming years, global warming will eventually lead to significant changes in the global climate and landscape.[4,3]

In this context, there have been considerable world-wide efforts towards building an energy economy that is largely based on renewable energy generation from *e.g.* wind, tidal, wave, hydroelectric, biomass and photovoltaic systems, and that is less reliant on fossil fuels. The United Kingdom and Scotland in particular benefit from a considerable supply of renewable energy in the form of wind and tidal energy (Figure 1-2).

(a)

(b)

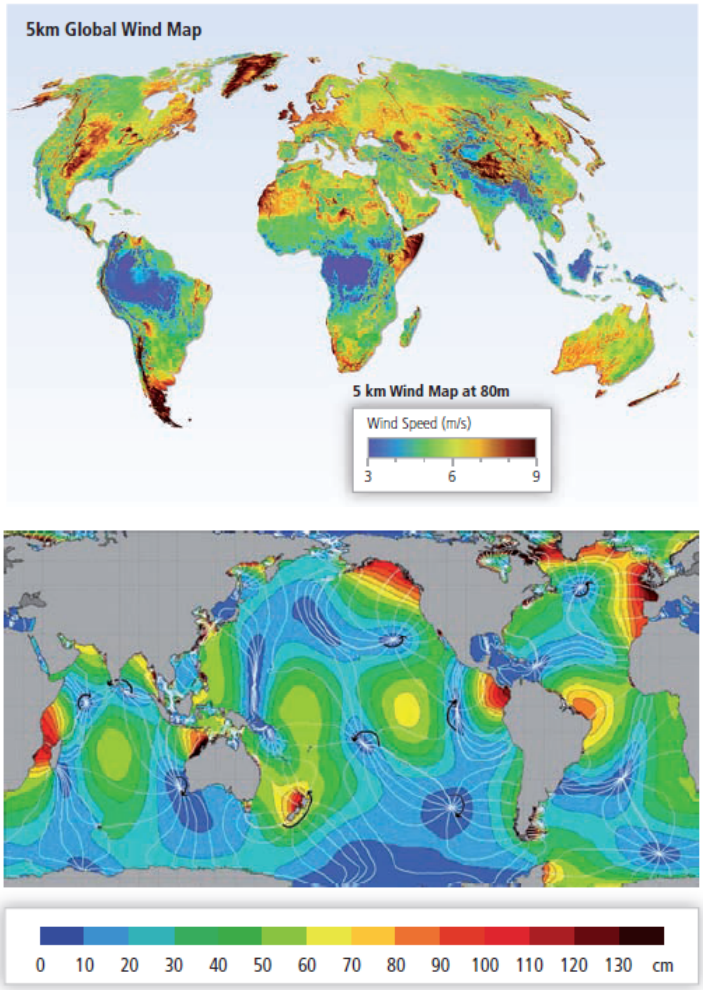

Figure 1-2 | Global distribution of energy resources: (a) wind power and (b) tidal power.[5]

1.2 The need for energy conversion and storage

A key characteristic of most of the renewable energy sources outlined above is they are not continuously available; they are *intermittent* by nature. Thus, while solar and tidal energy are *predictable* and *continuous* to a reasonable extent, wind or wave energy are at the opposite pole, exhibiting outputs that

vary considerably both over time and in intensity while also being highly unpredictable.

In this context, the ability to interconvert and store energy will be critical for running an economy reliant on renewables.[1,3,5] A very attractive technology that would enable this and bring other benefits is presented in Figure 1-3.

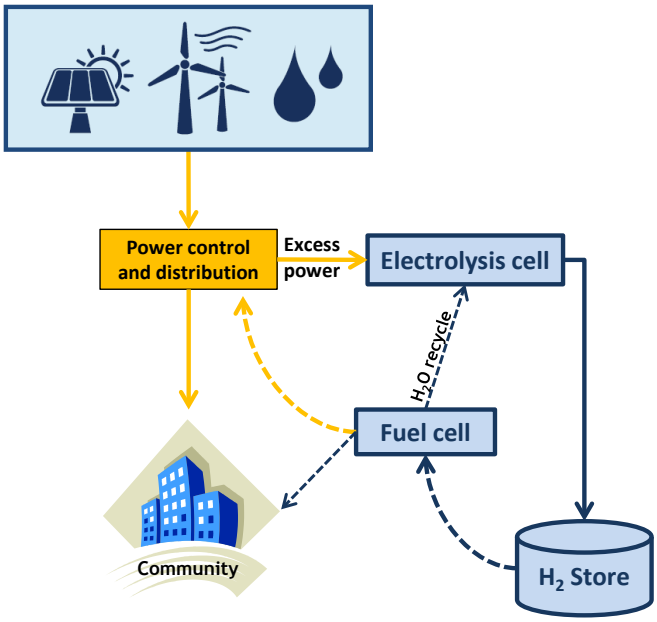

Figure 1-3 | Excess renewable energy could be stored as H_2 which in turn could be used when the need arises.

Thus, whenever possible, renewable energy would be used directly into the power grid (Figure 1-4), while power that is collected but cannot be accommodated at a certain time by the grid (*excess power*) could be directed towards an *electrolysis cell*. The role of the electrolysis cell is to use the excess power to convert water into H_2 and O_2. In this scenario, H_2 is the energy carrier and it will be stored for future use. Oxygen is also a valuable product, particularly useful in hospitals. When the direct renewable energy output cannot cope with the demand in the grid, part of the stored hydrogen may be used to balance the need, *via fuel cells*. Fuel cells fulfil the reverse role of electrolysis cells, converting H_2 (or other available stored fuels) and O_2 (from air) into electrical power and water, with reduced CO_2 emissions.

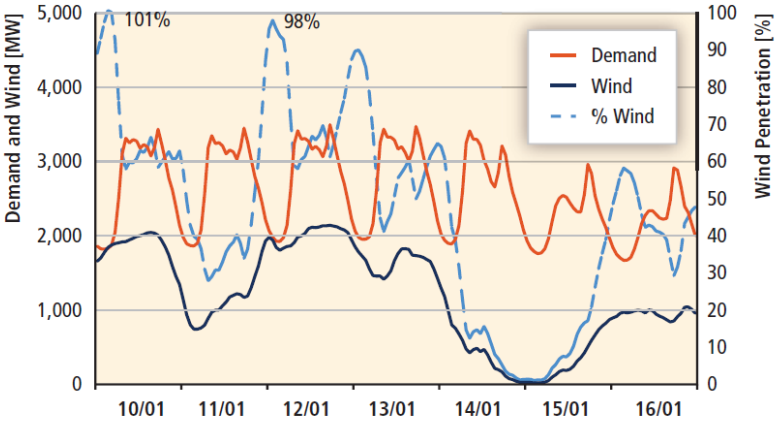

Figure 1-4 | Wind energy, electricity demand and instantaneous penetration levels in West Denmark for a week in January 2005.[5]

1.3 Solid oxide fuel cells – operating principle and components

As briefly explained above, fuel cells are devices that convert the chemical energy of a fuel into electrical energy through a series of electrochemical reactions between the fuel and oxygen.[6,7] The fuel and the oxidant never come into direct contact with each other in the process and thus combustion and the subsequent Carnot limitations are entirely avoided. Hence, fuel cells can potentially deliver higher fuel efficiency conversion compared to traditional energy conversion devices such as combustion engines.[6,8] Among other types of fuel cells *Solid Oxide Fuel Cell* (SOFCs) are particularly attractive because they operate at high temperatures which means they can potentially run on a wider variety of fuels and also produce exhaust heat which can be used in combined heat and power systems.[7]

A schematic representation of a SOFC is given in Figure 1-5. In a simplified view, a SOFC consists of two porous electrodes (*hydrogen electrode* and *cathode*) separated by a dense *electrolyte*. At the cathode side, molecular O_2 is reduced to oxygen anions O^{2-}, using electrons from the external circuit:

$$\frac{1}{2}O_2 + 2e^- \rightarrow O^{2-} \qquad \text{Eq. 1-1}$$

Thus, the cathode must possess high electrocatalytic activity towards O_2 dissociation but also sufficient electronic conductivity to accomplish this task.[9,10] Additionally, as for the other two main SOFC components, it is important that the material of choice is chemically and dimensionally stable in operating conditions while having similar thermal expansion coefficient to the other cell components.[6,11] The most commonly used cathode material is $La_{1-x}Sr_xMnO_3$ (also known as LSM), but many other *mixed ionic–electronic conductors* (MIECs) such as $La_{0.6}Sr_{0.4}Fe_{0.8}Co_{0.2}O_3$ (LSFC),[12] $Ba_{0.5}Sr_{0.5}Co_{0.8}Fe_{0.2}O_{3-\delta}$ (BSCF),[13] are known to perform extremely well as SOFC cathodes.[10,14]

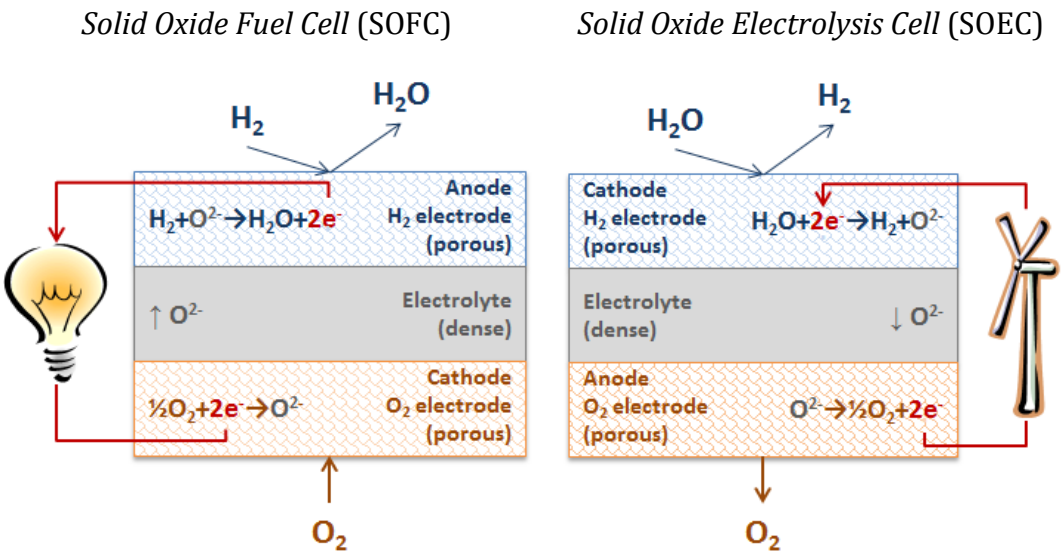

Figure 1-5 | Solid Oxide Fuel Cell (Left) and Solid Oxide Electrolysis Cell (Right) - schematic illustration of components and operating principle.

The electrolyte is made dense in order to avoid the direct reaction between the fuel and oxidant and chosen such that it displays very good oxide ion conductivity but no electronic conductivity, in order to force the electrons to travel exclusively through the outer circuit. Apart from the above mentioned requirements, the electrolyte must withstand the considerable p_{O_2} gradient between the cathode ($p_{O_2} \sim 1$ atm) and the hydrogen electrode ($p_{O_2} \sim 10^{-20}$ atm) which in fact constitutes the driving force for oxide ion migration across it. The most commonly used electrolyte material which fulfils these requirements and is also not high cost is yttria-stabilized zirconia

(YSZ). Some other oxides, such as doped ceria, $La_{0.9}Sr_{0.1}Ga_{0.8}Mg_{0.2}O_{2.85}$ (LSGM), are also under consideration because they have higher ionic conductivities.[11,15,16]

After travelling through the electrolyte, the oxide ions will reach the hydrogen electrode and react with the fuel to release the oxidation product (*e.g.* water) and electrons:

$$H_2 + O^{2-} \rightarrow H_2O + 2e^- \qquad \text{Eq. 1-2}$$

Therefore, it is important that the hydrogen electrode exhibits good catalytic properties towards fuel oxidation but also good electronic conductivity in order to enable fast electron transfer to the conducting contacts (*e.g. interconnects*). Usually electronic conductivity of at least $100\ S{\cdot}cm^{-1}$ is required but it has been shown that through appropriate cell design, materials with conductivity values as low as $1\ S{\cdot}cm^{-1}$ can be used succesfully.[17] The hydrogen electrode must also be stable in highly reducing conditions and be compatible with the adjacent cell components (the electrolyte and the interconnect) while still being sufficiently porous to allow the gas species access to the sites where the electrochemical oxidation occurs.[7] Ideally, the hydrogen electrode should also be electrochemically active and tolerant with respect to various fuels, especially if they contain a small measure of impurities (*e.g.* sulphur).

The most commonly used SOFC hydrogen electrode is a composite consisting of Ni metal and the oxide ion conducting ceramic YSZ (hence the name 'cermet').[18] A more detailed view of the performance and limitations of this hydrogen electrode will be provided in subchapter 1.5. Alternatives to Ni-YSZ have also been developed and section 1.6 offers a brief overview of the main research directions in this respect.

1.4 High temperature steam electrolysis

As mentioned in section 1.2 in passing, electrolysis cells are electrochemical devices that can split water into H_2 and O_2 by using electricity and are environmentally clean as long as the electricity comes from a renewable source. *High Temperature Steam Electrolysis* (HTSE) is a highly efficient electrolysis process that is carried out in *Solid Oxide Electrolysis Cells* (SOECs) and uses not only electrical energy but also thermal energy.[19,20] The advantage of performing steam electrolysis at high temperature comes from the fact that as the temperature increases, the electrical energy demand (ΔG) decreases, while the thermal energy demand ($T \cdot \Delta S$) increases and the total heat demand (ΔH) increases slightly. This means that less electrical energy may be required for the electrolysis of steam as the temperature increases. Additionally, as in the case of SOFCs, operation at high temperatures results in faster electrode kinetics.[21]

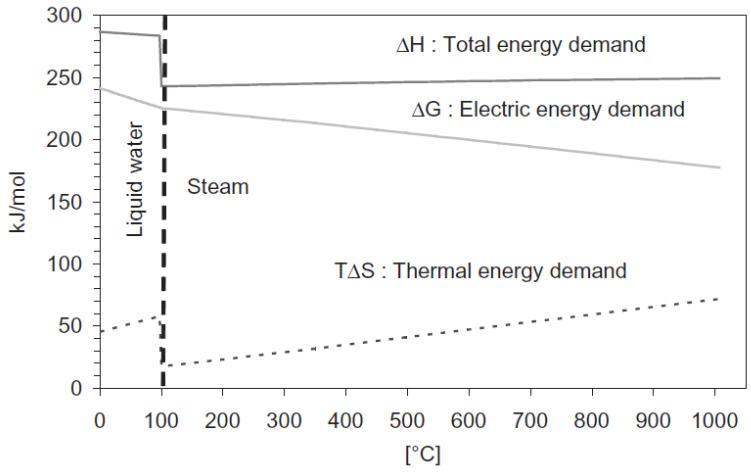

Figure 1-6 | Electrical, heat and total energy requirements for water electrolysis as a function of temperature.[19]

A related process is combined electrolysis of steam and carbon dioxide leading to synthesis gas from which several valuable compounds such as methanol or dimethyl ether may be produced.[1]

As suggested in Figure 1-5 the SOEC may be viewed as a SOFC operated in reverse, in which instead of using fuel to generate electricity, electricity is

consumed to generate fuel. Both the SOEC and the SOFC consist in principle of the same three components: an electrolyte, an hydrogen electrode and a cathode. The denomination of the latter two is, however, interchanged to reflect appropriately the redox processes that occur in each case. Thus, the hydrogen electrode of the fuel cell comes in contact with the same species as the cathode of the electrolysis cell, H_2, H_2O, e^-, hence this side of a SOFC or SOEC is often referred to as the *hydrogen electrode*. Moreover, since the same species are present at the hydrogen electrode in both SOFC and SOEC, it follows that the material requirements and hence the materials themselves could be similar if not identical for both technologies. The same applies to the 'air electrode'. Thus, it is no surprise that hydrogen electrode materials such as Ni-YSZ have been transferred to the relatively new field of high temperature electrolysis and performed equally well.[18]

1.5 The Ni-YSZ hydrogen electrode

Structurally, the Ni-YSZ cermet can be described as a porous assemblage of Ni and YSZ particles where each phase is in sufficient fraction to form percolating paths throughout the hydrogen electrode (Figure 1-7).[22,18] The electrochemical reactions occur *preferentially* across the *lines* where three phases (and main reactants) meet: the ceramic electrolyte (O^{2-}), the metallic electrode (e^-) and the gas phase containing the fuel (*e.g.* H_2).[18] Hence, these lines are known as the triple-phase boundary (TPB), and the electrochemical activity of the Ni-YSZ hydrogen electrode is directly related to the length of these boundaries. In consequence, a lot of attention has been direct towards maximising their length during preparation and minimising their degradation during operation.

The Ni-YSZ cermet excels in terms of catalytic properties for fuel oxidation (H_2 and CO), steam reforming of natural gas and exhibits good current collection, largely due to the high electrochemical activity and electronic conductivity of Ni metal.[18,15] Unfortunately, the wide applicability of this hydrogen electrode is restricted by several important drawbacks.

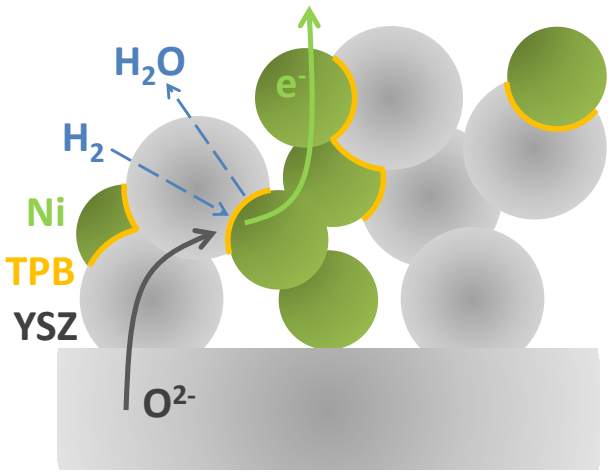

Figure 1-7 | Schematic representation of the Ni-YSZ hydrogen electrode microstructure and H_2 electro-oxidation occurring at the triple phase boundary (TPB).

Most importantly, it is not redox stable.[23,24,18] The oxidation of Ni to NiO may occur due to fuel starvation (*e.g.* lack of fuel or shut-down) or under high load (high steam conditions) and is typically accompanied by significant volume changes and Ni particle coarsening.[21] These in turn leads to severe structural degradation, considerable lowering of the TPB length and consequently sever decrease in performance. Thus, Ni-YSZ hydrogen electrodes would not be the optimal choice for use in conjunction with renewables which are inherently intermittent meaning that *e.g.* fast start-up/shutdown, high load/high steam are expected to be supported routinely over an adequate lifetime. Additionally, Ni-YSZ hydrogen electrodes may suffer from carbon deposition which blocks porosity[21] and sulphur poisoning.[25]

1.6 Alternative hydrogen electrodes

Thus, having in mind the limitations exhibited by the Ni-YSZ cermet, the challenge is to develop alternative hydrogen electrodes that apart from displaying good fuel oxidation properties, electronic conductivity and reasonable stability, they must also be *redox-stable*, ideally *single-phase*, while exhibiting some degree of *mixed ionic and electronic conduction*. The last two characteristics are desirable in order to avoid the electrochemistry being confined to certain boundaries (*e.g.* the TPB), and thus to a limited fraction of the hydrogen electrode volume, like in the Ni-YSZ. Instead, in the

case of a single phase MIEC all the surface of the hydrogen electrode that is in contact with the gas phase would theoretically be able to support electrochemical reactions since the MIEC phase could provide the flux of oxide ions and also carry away the generated electrons after the oxidation has occurred (Figure 1-8). The interface where electrochemical reactions occur would no longer be a sum of lines, but a sum of surfaces.

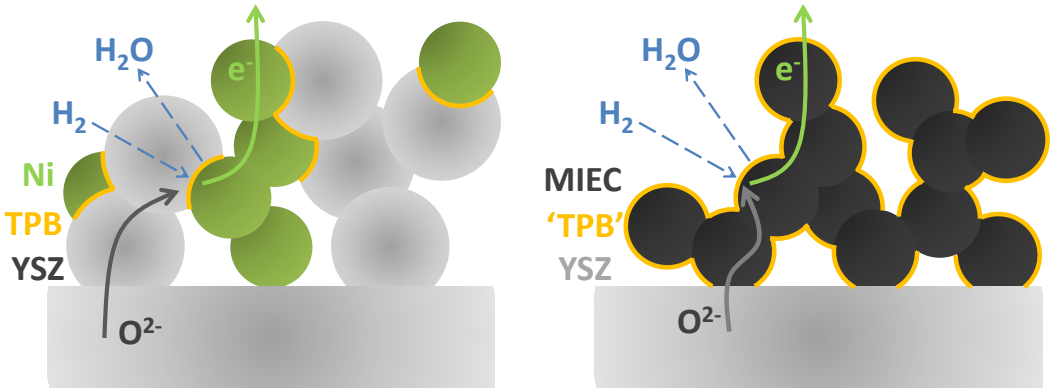

Figure 1-8 | Schematic comparison between: (Left) the Ni-YSZ cermet and (Right) an electro-catalytically active MIEC.

It is important to emphasize here that while high-performance, all-ceramic (single-phase), mixed ionic-electronic conductor materials have been identified for the air electrode (*e.g.* LSM, BSCF),[14,12,13] *an ideal all-ceramic hydrogen electrode material has not yet been found*.[17,26] This is perhaps not surprising, given the complexity of the functions and requirements that a hydrogen electrode material must fulfil. However, it remains an open challenge driving the field forward and also constitutes *one of the main motivations of this thesis*. Next, a brief, qualitative overview of the main alternative hydrogen electrodes development directions will be presented, based on some of the reviews published on this topic recently.[17,9,27,28,8,29,26,30]

Stemming from the Ni-YSZ concept, some of the approaches focused on replacing the metal and the ceramic in this composite, for example with Cu and CeO_2, respectively. *Cu-$CeO_{2-\delta}$* hydrogen electrodes exhibit significantly better performance than Ni-YSZ when operated on dry hydrocarbons, including liquid fuels, without reforming,[31,32] but suffers from inadequate

redox stability and Cu agglomeration during operation (Cu has high mobility at the SOFC operating temperatures).[33]

Rutile-type materials (*e.g.* TiO_2 doped with Nb, Cr etc) are redox stable, exhibit high electronic conductivity in reducing conditions but have very limited oxide ion conductivity and fuel oxidation activity.[34,35]

Tungsten bronze materials ($A_{0.6}BO_3$) were also found to exhibit high electronic conductivity when reduced, but their stability in reducing atmosphere, as well as catalytic activity is lacking, even when compared to other oxide hydrogen electrodes.[36,37]

Certain *pyrochlore* ($A_2B_2O_7$) systems were optimised for both ionic and electronic conductivity through doping, giving hope of MIEC behaviour. While electrochemical performance was reasonable with adequate B-site dopants, the stability of the phases even in reducing atmosphere still constitutes an issue.[38,39]

Some of the most exciting results have been obtained, however, for compositions belonging to the *perovskite* crystal structure (ABO_3). This is most likely a result of the unique properties and convenient engineering opportunities offered by the perovskite structure environment. This, along with in-depth look at the structure and properties of perovskites will be discussed in more detail in Chapter 2. Some key aspects are worth mentioning here in passing, however.

First, the perovskite structure can generally accommodate a wide variety of defects that may form in either reducing or oxidising environment. This means that the perovskite structure can natively and reversibly withstand redox cycling, provided that the composing cations redox characteristics do not interfere significantly with this. Indeed, most of the perovskites proposed as hydrogen electrodes were found to be redox stable, in spite of being incorporating a range of cations with diverse redox properties.[40–44]

Also, the vast majority of known catalytically active cations such as transition metal cations can substitute on the B-site the perovskite structure. This provides a lot of flexibility for tailoring catalytic activity and specific functionality in general. Moreover, some of these transition metal cations also support multiple oxidation states under different conditions which in turn may give rise to (high) electronic conductivity. Additionally, the presence of cations with variable oxidation states enables the creation (*i.e. doping*) of oxygen vacancies in reducing environment (*e.g.* operating conditions):

$$2B_B^x + O_O^x \rightleftharpoons 2B_B' + V_O^{\cdot\cdot} + \frac{1}{2}O_2 \qquad \text{Eq. 1-3}$$

This potentially gives rise to more adsorption sites[45] and hopping sites for oxide ion conduction, and thus to mixed electronic and ionic conductivity.[26]

Most of the perovskite hydrogen electrode materials developed so far stemmed from two perovskites: $LaCrO_3$ (*chromites*) and $SrTiO_3$ (*titanates*) mainly because these show exceptional stability in both oxidising and reducing conditions at high temperatures, providing a robust structure for further tailoring.[27]

On the basis of this stability and because $LaCrO_3$ and some of its derived compositions show exclusively electronic conduction, they have been successfully employed as interconnects.[8] Chromites however possess low inherent catalytic activity and lack oxide ion conduction possibly as a result of the strong preference Cr^{3+} has for 6-fold coordination, the full coordination of the B-site in perovskites.[27,46] This can be remedied to some extent by replacing some of the Cr with other transition metals that form cations which do support flexible coordination (*e.g.* Mn, Co, Fe).[47–50] Among chromites, the most impressive performance is demonstrated by the *double perovskite* ($A_2BB'O_3$) $La_{0.75}Sr_{0.25}Cr_{0.5}Mn_{0.5}O_{3-\gamma}$ (LSCM) which has been designed especially for improved B-site coordination flexibility.[46] As such, although oxygen ion mobility is low in the oxidized state, the diffusion coefficient for oxide ions in reduced LSCM is comparable to YSZ.[51] This

material is redox stable[52,46] and exhibits comparable electrochemical performance to Ni/YSZ cermets at 900 °C in 97%H_2/3% H_2O, but also displays good performance for methane oxidation without using excess steam.[46] Perhaps the major limitation of LSCM is the fact that it is a *p-type conductor*.[53] P-type conduction occurs through electron holes and most importantly increases with the increase of p_{O_2}:

$$V_O^{\cdot\cdot} + \frac{1}{2}O_2 \rightleftharpoons O_O^x + 2h^{\cdot} \qquad \text{Eq. 1-4}$$

This means that the conductivity of LSCM will be maximised in oxidising conditions, not in the reducing conditions found at the hydrogen side. For example, the conductivity of LSCM at 900 °C in air is ~ 30 S·cm^{-1}, and in 10%H_2/N_2 decreases to just below 1 S·cm^{-1}.[54] Thus, ideally, hydrogen electrode materials should exhibit *n-type conduction*. In this case the charge carriers are electrons and the conductivity increase with the decrease of p_{O_2}:

$$O_O^x \rightleftharpoons V_O^{\cdot\cdot} + \frac{1}{2}O_2 + 2e' \qquad \text{Eq. 1-5}$$

Thus, the stronger the reducing conditions become at the hydrogen electrode, the higher the number of charge carriers generated, resulting in increased electronic conductivity and current collection.

From this point of view, titanates appear to be a more natural choice for the hydrogen electrode compared to chromites, since titanates are primarily n-type conductors. Indeed, in reducing conditions a fraction of the Ti^{4+} ions reduce to Ti^{3+} according to the equilibrium described by Eq. 1-3. Additionally, Ti^{4+} is known to adopt 5-fold coordination to some degree which would allow for chemisorption, while the Ti^{4+}/Ti^{3+} redox couple is generally capable of accepting electrons from a hydrocarbon or from H_2, potentially carrying out the chemisorption dissociation reaction of these fuels.[29] Even so, $SrTiO_3$ is a poor n-type conductor with little catalytic activity of its own.[30,55]

As opposed to chromites, the behaviour of titanates as hydrogen electrode materials has been explored in-depth not only from the point of view of doping cations and oxygen vacancies, but of other point defects as well. As it

will be shown in Chapter 2, titanates (but other perovskites as well, *e.g.* chromites) can be doped in various ways to give rise to different defects and corresponding nonstoichiometry classes. The sum of characteristics (*e.g.* composition, structure, properties, behaviour) that a certain type or combination of defects bestows upon the perovskite that is part of is usually referred to as the *defect chemistry* of that perovskite nonstoichiometry class. When carefully tailored, defect chemistry can give rise to unique and potentially useful properties. Among the most important perovskite nonstoichiometry classes, A-site stoichiometric, *oxygen deficient* perovskites ($ABO_{3-\gamma}$) were exemplified for chromites (*e.g.* LSCM) while A-site stoichiometric, *oxygen excess* ($ABO_{3+\gamma}$) and *A-site deficient* perovskites ($A_{1-\alpha}BO_3$) will be discussed for titanates.

Excess is generally incorporated by alternating perovskite slabs with *intergrowth* regions where the excess species are located.[56–58] In the case where only oxygen excess is present, such as in $La_xSr_{1-x}TiO_{3+x/2}$, (equivalently, $La_4Sr_{n-4}Ti_nO_{3n+2}$), the intergrowth comprises of the region where perovskite slabs are offset in such a way to allow accommodation of extra oxygen ions (see Chapter 2). At high oxygen excess values the intergrowths are ordered in oxygen rich planes and constitute crystallographic features. As the amount of excess oxygen decreases, the ordering is gradually broken to the point corresponding to $\gamma = x/2 = 2/n < 0.167$ $(x \leq 1/3,$ or $n \geq 12)$, below which oxygen-rich defects are randomly distributed within the perovskite framework.[57,59] The presence of extra oxygen beyond the ABO_3 stoichiometry not only causes changes in the perovskite structure, but has implications on the electrochemical properties as well. As the ordering is broken below $\gamma < 0.167$, presence of such disordered defects appears to strongly the affect the titanate which becomes easier to reduce, achieves higher electronic conductivity and exhibits much better performance in high temperature steam electrolysis than its oxygen stoichiometric analogues.[59,20] In spite of these improvements, however, the electrochemical performance of these

materials does not improve considerably, perhaps due to the strong preference of Ti^{4+} for 6-fold coordination.[42,60] Once Mn and Ga are doped on the B-site, $La_4Sr_8Ti_{11}Ga_{0.5}Mn_{0.5}O_{38-\gamma}$, the performance of this material increase dramatically in a SOFC running on wet hydrogen and is active for methane oxidation as well.[59] The oxygen excess series $La_xSr_{1-x}TiO_{3+x/2}$ has received a lot of attention, with numerous other dopants tested to achieve further property improvements over $La_4Sr_8Ti_{11}Ga_{0.5}Mn_{0.5}O_{38-\gamma}$, without much success however.[61–63]

In A-site deficient titanates some of the A-sites are simply vacant. The most representative A-site deficient series are obtained by doping La^{3+} or Y^{3+} in $SrTiO_3$, leading to $La_xSr_{1-3x/2}TiO_3$ [64] and $Y_xSr_{1-3x/2}TiO_3$,[65] respectively (see Chapter 2). A-site deficiency offers a number of advantages over oxygen excess stoichiometry. A-site vacancies provide hopping sites for A-site cations which during phase formation or processing enhances grain growth and sintering allowing the production of mechanically robust microstructures at lower temperatures.[66,67] Also, La- or Y-containing perovskites may suffer degradation over time in high steam environment on account of the 'lanthanum oxide' in the perovskite reacting with the steam to form hydroxides $La(OH)_3$, a process accompanied by a significant change in volume. A slight number of A-site vacancies has been found to mitigate this.[66] Additionally, the electronic conductivity of A-site deficient titanates (*e.g.* $La_xSr_{1-3x/2}TiO_3$, $x < 0.4$) tends to be slightly higher compared to oxygen excess titanates (*e.g.* $La_xSr_{1-x}TiO_{3+x/2}$, $x < 1/3$).[20,63] This is probably due to the randomly distributed intergrowths that might disrupt the conduction network throughout the grain (at the intergrowths the corner sharing between octahedra is broken) leading to an overall decrease in electron mobility. In fact, recent studies on the Ruddlesden-Popper *A-site excess, oxygen excess* series $Sr_{n+1}Ti_nO_{3n+1}$ have pointed out that the electron density around the rock-salt intergrowths is very small and has a negative impact on the electronic conduction of the structure.[68]

On the other hand, the innate electrochemical activity of the oxygen excess perovskites (*e.g.* $La_xSr_{1-x}TiO_{3+x/2}$, $x = 0.3$) is generally higher than their A-site deficient analogues (*e.g.* $La_xSr_{1-3x/2}TiO_3$, $x = 0.2$), but still better than $SrTiO_3$, most likely due to the functionality brought by the mobile, randomly distributed oxygen rich defects, as explained above.[20] Efforts directed towards doping the B-site of A-site deficient titanates have not resulted, however, in the identification of a hydrogen electrode material with electrochemical performance on par with *e.g.* $La_4Sr_8Ti_{11}Ga_{0.5}Mn_{0.5}O_{38-\gamma}$. In the case of the Y-doped A-site deficient perovskites, the influence of many B-site dopants has been studied intensively, including first row transition metals, Nb, Zr etc.[65,69,70,67,71] In the case of the La-doped system, the B-site dopants studied have been limited so far to Nb.[64] Thus, additional understanding of A-site deficient titanate systems may be obtained by exploring B-site doping in the system $La_xSr_{1-3x/2}TiO_3$.

1.7 Aims of the thesis

In the light of the context presented so far, the aim of this thesis is to explore the A-site deficient titanate systems derived from the system $La_xSr_{1-3x/2}TiO_3$ in general and the optimised member[64] $x = 0.4$ in particular, in order to:

- Gain a wider understanding of A-site deficiency in titanates in the context of perovskite defect chemistry, especially in the presence of other defects such as cation substitutions, oxygen vacancies etc;
- Study the structure, structural characteristics and relationships in these A-site deficient perovskites;
- Identify the key parameters that control the reducibility of these perovskites and improve it;
- Enhance the electronic conductivity of these titanates (*e.g.* to at least $10\ S{\cdot}cm^{-1}$ for a sample with ~30% porosity, at 900 °C and $p_{O_2} \sim 10^{-20}$ atm);

- Explore ways of enhancing the electrochemical activity of these titanates;
- Demonstrate high temperature steam electrolysis using the developed materials as hydrogen electrodes.

1.8 Outline of the thesis

The chapters of this thesis are organised as follows:

Chapter 2 (*Background on perovskites*) presents an overview of perovskites focusing especially on the possible nonstoichiometry classes, the way defects are accommodated in perovskites and the resulting defects chemistry in general. This chapter also includes an introduction to reduction, electronic conduction and ionic conduction in perovskites. This chapter is not an exhaustive background on perovskites, but rather reunites essential aspects and concepts related to perovskites that were deemed relevant towards analysing the results of the work presented in this thesis.

Chapter 3 (*Experimental*) summarises the main methods and techniques employed in this study to prepare, analyse and test the developed materials.

Chapter 4 (*Crystal structure of the studied compositions*) describes the main structural characteristics of the materials developed in this study. It also reveals some of the reasoning based on which entirely new compositions were derived and prepared throughout this work. Several correlations between the structure, the defect chemistry and characteristics of constituting cations are presented and discussed as well.

Chapter 5 (*Reduction in perovskite titanates*) examines the reduction process primarily in A-site deficient titanates, and to some extent in oxygen excess titanates, seeking to uncover the main factors that control it but also various characteristics of this process. The chapter also demonstrates that in the light of these factors, the reduction characteristics of A-site deficient perovskites can be considerably enhanced to exceed their oxygen excess analogues.

Chapter 6 (*Enhancing electronic conductivity in strontium titanates*) proposes and exemplifies a new approach for enhancing the electronic conductivity of A-site deficient titanates building upon the knowledge gained in the work described in Chapter 5.

Chapter 7 (*Perovskites decorated with in-situ exsolved nanoparticles through control of defect chemistry*) explores a new phenomenon uncovered during this study which enables advanced control over the growth of catalytically active nanoparticles from perovskites and which is driven primarily by defect chemistry.

Chapter 8 (*High temperature steam electrolysis with transition metal doped, A-site deficient titanate cathodes*) presents an overview and brief analysis of the performance of titanate-based cathodes developed in this study for H_2 production in high temperature steam electrolysis cells.

Chapter 9 (*Conclusions*) summarises the main findings of this thesis.

1.9 List of publications

This thesis is based on several publications:

Published papers:

- D. Neagu & J. T. S. Irvine, *Structure and Properties of $La_{0.4}Sr_{0.4}TiO_3$ Ceramics for Use as Anode Materials in Solid Oxide Fuel Cells*. Chemistry of Materials 22, 5042–5053 (2010).
- D. Neagu & J. T. S. Irvine, *Enhancing Electronic Conductivity in Strontium Titanates through Correlated A and B-Site Doping.* Chemistry of Materials 23, 1607–1617 (2011).
- G. Tsekouras, D. Neagu & J. T. S. Irvine, *Step-change in high temperature steam electrolysis performance of perovskite oxide cathodes with exsolution of B-site dopants*. Energy and Environmental Science 6, 256-266 (2012).

Book chapter awaiting publication:

- Neagu, D. & Irvine, J. T. S., *Perovskite defect chemistry as exemplified by strontium titanate*, in Comprehensive Inorganic Chemistry II, Eds. K.R. Poeppelmeier and J. Reedijk, Elsevier Press, In Press, 2013.

Paper under review:

- D. Neagu, G. Tsekouras, D. M. Miller, H. Ménard & J. T. S. Irvine, *In-situ growth of Nanoparticles through Control of Defect Chemistry*.

Papers in preparation:

- G. Tsekouras, D. Neagu & J. T. S. Irvine, *Redox tolerance of ceramic perovskite titanate solid oxide electrolysis cell hydrogen electrodes*
- G. Tsekouras, D. Neagu & J. T. S. Irvine, *High temperature steam electrolysis with transition metal doped, A-site deficient titanate cathodes*
- D. Neagu & J. T. S. Irvine, *The structure, reduction and conductivity of transition metal doped, A-site deficient titanates.*

References

1. J. T. S. Irvine, *J. Power Sources*, 2004, **136**, 203–207.
2. *International Energy Outlook 2011*, U.S. Energy Information Administration, 2011.
3. A. Galich and L. Marz, *Energy, Sustainability and Society*, 2012, **2**, 2.
4. *Climate change 2007: Synthesis report.*, Intergovernmental Panel on Climate Change, 2007.
5. Potsdam-Institut für Klimafolgenforschung, *Renewable energy sources and climate change mitigation : special report of the Intergovernmental Panel on Climate Change*, Cambridge university press, New York, 2012.
6. N. Q. Minh and T. Takahashi, *Science and Technology of Ceramic Fuel Cells*, Elsevier Science, 1st edn., 1995.
7. S. C. Singhal, in *Solid Oxide Fuels Cells: Facts and Figures*, eds. J. T. S. Irvine and P. Connor, Springer London, 2013, pp. 1–23.
8. C. Sun and U. Stimming, *J. Power Sources*, 2007, **171**, 247–260.
9. L. J. Gauckler, D. Beckel, B. E. Buergler, E. Jud, U. P. Muecke, M. Prestat, J. L. M. Rupp, and J. Richter, *CHIMIA Int. J. Chem.*, 2004, **58**, 837–850.
10. J. Richter, P. Holtappels, T. Graule, T. Nakamura, and L. J. Gauckler, *Monatsh. Chem.*, 2009, **140**, 985–999.
11. D. S. C. Singhal and K. Kendall, Eds., *High-temperature Solid Oxide Fuel Cells: Fundamentals, Design and Applications*, Elsevier, 2003.
12. M. Juhl, S. Primdahl, C. Manon, and M. Mogensen, *J. Power Sources*, 1996, **61**, 173–181.
13. Z. Shao and S. M. Haile, *Nature*, 2004, **431**, 170–173.
14. C. Sun, R. Hui, and J. Roller, *J Solid State Electrochem*, 2010, **14**, 1125–1144.
15. T. Ishihara, Ed., *Perovskite oxide for solid oxide fuel cells*, Springer, New York ;London, 2008.
16. J. B. Goodenough, *Annu. Rev. Mater. Res.*, 2003, **33**, 91–128.
17. A. Atkinson, S. Barnett, R. J. Gorte, J. T. S. Irvine, A. J. McEvoy, M. Mogensen, S. C. Singhal, and J. Vohs, *Nat Mater*, 2004, **3**, 17–27.
18. M. Mogensen and P. Holtappels, in *Solid Oxide Fuels Cells: Facts and Figures*, eds. J. T. S. Irvine and P. Connor, Springer London, 2013, pp. 25–45.
19. A. Brisse, J. Schefold, C. Stoots, and J. O'Brien, in *Innovations in Fuel Cell Technologies*, eds. R. Steinberger-Wilckens and W. Lehnert, RSC, Cambridge, 2010.
20. G. Tsekouras and J. T. S. Irvine, *J. Mater. Chem.*, 2011.
21. J. T. S. Irvine and P. Connor, in *Solid Oxide Fuels Cells: Facts and Figures*, eds. J. T. S. Irvine and P. Connor, Springer London, 2013, pp. 163–180.
22. P. R. Shearing, J. Golbert, R. J. Chater, and N. P. Brandon, *Chem. Eng. Sci.*, 2009, **64**, 3928–3933.
23. J. Malzbender, E. Wessel, and R. W. Steinbrech, *Solid State Ionics*, 2005, **176**, 2201–2203.
24. T. Klemensø and M. Mogensen, *J. Am. Cer. Soc.*, 2007, **90**, 3582–3588.
25. Y. Matsuzaki and I. Yasuda, *Solid State Ionics*, 2000, **132**, 261–269.
26. J. Irvine, in *Perovskite Oxide for Solid Oxide Fuel Cells*, ed. T. Ishihara, Springer, 2009.

27. S. Tao and J. T. S. Irvine, *The Chemical Record*, 2004, **4**, 83–95.
28. J. W. Fergus, *Solid State Ionics*, 2006, **177**, 1529–1541.
29. J. B. Goodenough and Y.-H. Huang, *J. Power Sources*, 2007, **173**, 1–10.
30. X.-M. Ge, S.-H. Chan, Q.-L. Liu, and Q. Sun, *Adv. Energy Mater.*, 2012, n/a–n/a.
31. H. Kim, S. Park, J. M. Vohs, and R. J. Gorte, *J. Electrochem. Soc.*, 2001, **148**, A693–A695.
32. S. Park, J. M. Vohs, and R. J. Gorte, *Nature*, 2000, **404**, 265–267.
33. N. Kiratzis, P. Holtappels, C. E. Hatchwell, M. Mogensen, and J. T. S. Irvine, *Fuel Cells*, 2001, **1**, 211–218.
34. C. M. Reich, A. Kaiser, and J. T. S. Irvine, *Fuel Cells*, 2001, **1**, 249–255.
35. A. Lashtabeg, J. Canales-Vazquez, J. T. S. Irvine, and J. L. Bradley, *Chem. Mater.*, 2009, **21**, 3549–3561.
36. A. Kaiser, J. L. Bradley, P. R. Slater, and J. T. S. Irvine, *Solid State Ionics*, 2000, **135**, 519–524.
37. P. R. Slater and J. T. S. Irvine, *Solid State Ionics*, 1999, **124**, 61–72.
38. P. Holtappels, F. W. Poulsen, and M. Mogensen, *Solid State Ionics*, 2000, **135**, 675–679.
39. B. J. Wuensch, K. W. Eberman, C. Heremans, E. M. Ku, P. Onnerud, E. M. E. Yeo, S. M. Haile, J. K. Stalick, and J. D. Jorgensen, *Solid State Ionics*, 2000, **129**, 111–133.
40. T. Ikebe, H. Muroyama, T. Matsui, and K. Eguchi, *J. Electrochem. Soc.*, 2010, **157**, B970–B974.
41. P. Blennow, K. K. Hansen, L. R. Wallenberg, and M. Mogensen, *Solid State Ionics*, 2009, **180**, 63–70.
42. O. A. Marina, N. L. Canfield, and J. W. Stevenson, *Solid State Ionics*, 2002, **149**, 21–28.
43. D. M. Bastidas, S. Tao, and J. T. S. Irvine, *J. Mater. Chem.*, 2006, **16**, 1603–1605.
44. Q. Liu, X. Dong, G. Xiao, F. Zhao, and F. Chen, *Adv. Mater.*, 2010, **22**, 5478–5482.
45. H. Dai, H. He, P. Li, L. Gao, and C.-T. Au, *Catal. Today*, 2004, **90**, 231–244.
46. S. Tao and J. T. S. Irvine, *Nature Mater.*, 2003, **2**, 320–323.
47. S. Primdahl, J. R. Hansen, L. Grahl-Madsen, and P. H. Larsen, *J. Electrochem. Soc.*, 2001, **148**, A74–A81.
48. G. Pudmich, B. A. Boukamp, M. Gonzalez-Cuenca, W. Jungen, W. Zipprich, and F. Tietz, *Solid State Ionics*, 2000, **135**, 433–438.
49. V. Vashook, L. Vasylechko, J. Zosel, W. Gruner, H. Ullmann, and U. Guth, *J. Solid State Chem.*, 2004, **177**, 3784–3794.
50. V. Vashook, L. Vasylechko, J. Zosel, and U. Guth, *Solid State Ionics*, 2003, **159**, 279–292.
51. E. S. Raj, J. A. Kilner, and J. T. S. Irvine, *Solid State Ionics*, 2006, **177**, 1747–1752.
52. S. Zha, P. Tsang, Z. Cheng, and M. Liu, *J. Solid State Chem.*, 2005, **178**, 1844–1850.
53. S. M. Plint, P. A. Connor, S. Tao, and J. T. S. Irvine, *Solid State Ionics*, 2006, **177**, 2005–2008.
54. S. P. Jiang, L. Liu, K. P. Ong, P. Wu, J. Li, and J. Pu, *J. Power Sources*, 2008, **176**, 82–89.

55. P. Blennow, K. K. Hansen, L. Reine Wallenberg, and M. Mogensen, *Electrochim. Acta*, 2006, **52**, 1651–1661.
56. M. E. Bowden, D. A. Jefferson, and I. W. M. Brown, *J. Solid State Chem.*, 1995, **117**, 88–96.
57. J. Canales-Vázquez, M. J. Smith, J. T. S. Irvine, and W. Zhou, *Adv. Funct. Mater.*, 2005, **15**, 1000–1008.
58. S. N. Ruddlesden and P. Popper, *Acta Crystallogr.*, 1957, **10**, 538–539.
59. J. C. Ruiz-Morales, J. Canales-Vázquez, C. Savaniu, D. Marrero-López, W. Zhou, and J. T. S. Irvine, *Nature*, 2006, **439**, 568–571.
60. J. Canales-Vazquez, S. Tao, and J. T. S. Irvine, *Solid State Ionics*, 2003, **159**, 159–165.
61. J. Canales-Vázquez, J. C. Ruiz-Morales, J. T. S. Irvine, and W. Zhou, *J. Electrochem. Soc.*, 2005, **152**, A1458.
62. A. Ovalle, J. C. Ruiz-Morales, J. Canales-Vázquez, D. Marrero-López, and J. T. S. Irvine, *Solid State Ionics*, 2006, **177**, 1997–2003.
63. D. N. Miller and J. T. S. Irvine, *J. Power Sources*, 2011, **196**, 7323–7327.
64. P. R. Slater, D. P. Fagg, and J. T. S. Irvine, *J. Mater. Chem.*, 1997, **7**, 2495–2498.
65. S. Hui and A. Petric, *J. Eur. Ceram. Soc.*, 2002, **22**, 1673–1681.
66. J. W. Stevenson, T. R. Armstrong, L. R. Pederson, J. Li, C. A. Lewinsohn, and S. Baskaran, *Solid State Ionics*, 1998, **113-115**, 571–583.
67. Q. X. Fu, S. B. Mi, E. Wessel, and F. Tietz, *J. Eur. Ceram. Soc.*, 2008, **28**, 811–820.
68. N. Sirikanda, H. Matsumoto, and T. Ishihara, *Solid State Ionics*, 2010, **181**, 315–321.
69. S. Hui and A. Petric, *J. Electrochem. Soc.*, 2002, **149**, J1.
70. S. Hui and A. Petric, *Mater. Res. Bull.*, 2002, **37**, 1215–1231.
71. Q. Ma, F. Tietz, A. Leonide, and E. Ivers-Tiffée, *J. Power Sources*, 2011, **196**, 7308–7312.

2 BACKGROUND ON PEROVSKITES

2.1 Classes of nonstoichiometry

Perovskite oxide materials possess general stoichiometry ABO_3 in which conventionally the A-site is occupied by the larger cation and the B-site by the smaller cation. The perovskite lattice can display nonstoichiometry virtually with respect to all three sites (A, B and O), either individually (one site at a time) or in various combinations. B-site nonstoichiometry is, however, energetically unfavourable because of the important structural role of the B-site cations,[1,2] which form strong bonds with oxygen in a network consisting of BO_6 corner-sharing octahedra (see subsections 2.2.1 and 2.3)[i]. Consequently, the vast majority of perovskite systems exhibit a fully occupied B-site, with few examples of B-site nonstoichiometric perovskites being known.[3]

With respect to a fully occupied B-site, the A-site and O-site can be sub-stoichiometric (*e.g.* $A_{1-\alpha}BO_3$, $ABO_{3-\gamma}$; also known as *deficient*) or super-stoichiometric (*e.g.* $A_{1+\alpha}BO_3$, $ABO_{3+\gamma}$; usually called *excess*). The relationship between different perovskite nonstoichiometry domains can be better understood by representing the nonstoichiometry of the A and O sublattices on Cartesian axes having the defect-free ABO_3 as origin. Such a representation is depicted in Figure 2.1. Excess perovskites including the Ruddlesden-Popper phases $A_{n+1}B_nO_{3n+1}$ ($n \geq 1$),[4,5] or the $A_nB_nO_{3n+2}$ ($n \geq 4$) homologous series,[6,7] are located in quadrant **I**. Deficient perovskites such as the tungsten bronzes ($A_{0.6}BO_3$) or the $A_nB_nO_{3n-1}$ series ($n = 2$ being the *brownmillerite* structure) are located in quadrant **III**. Stoichiometries exhibiting A-site excess and O-deficient (quadrant **II**) or A-site deficient and O-excess (quadrant **IV**) are unlikely to exist.

The diagram emphasizes the diametrically opposed positions of the deficient and excess variants in the perovskite nonstoichiometry landscape. While this representation provides a straightforward way to visualise different perovskite nonstoichiometry in relation to each other, it also reveals the

[i] In contrast, fully A-site vacant perovskites such as WO_3 and ReO_3 are known.[2]

distinct defect chemistries one would anticipate from these two classes. Indeed, while deficiency can be easily accommodated by creating vacancies in the ABO_3 structure (see section 2.2.3), excess stoichiometry is achieved through the exceptional ability of the perovskite to inter-grow with other crystal structures (see section 2.2.4). This fundamental structural difference translates into contrasting properties for these two classes, some of which will be revealed across this study.

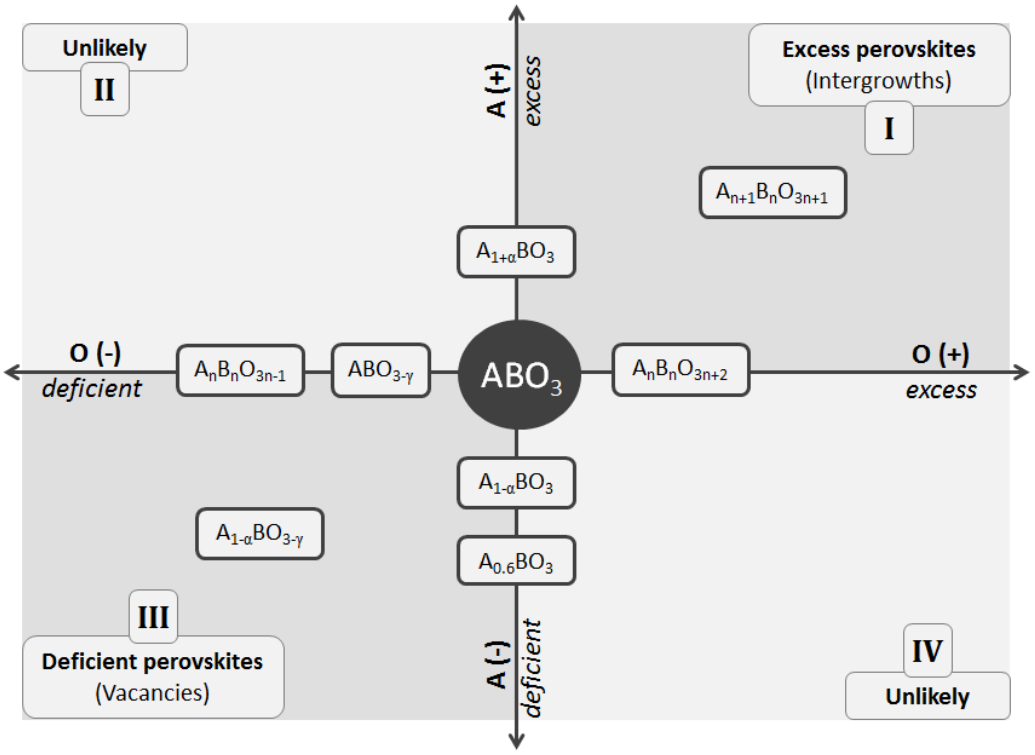

Figure 2.1 – Perovskite nonstoichiometry represented in a Cartesian plane. x and y axes are set to correspond to oxygen and A-site nonstoichiometry, respectively.

The nonstoichiometry class and hence the defect chemistry can be tailored through various approaches, including cation substitution, exposing the materials to different conditions (T, p_{O_2}), or, where possible, simply by formulating the stoichiometry in the desired way (*e.g.* preparing an A-site deficient perovskite $A_{1-\alpha}BO_3$ by using a mixture of raw materials having atomic ratio $A/B = (1-\alpha)/1$). Some of these approaches are exemplified below and summarised in Figure 2.2, focusing on compositions derived from the archetype perovskite, $Sr^{2+}Ti^{4+}O_3^{2-}$.

The perovskite structure allows for cations of similar size[ii] but different valence to be substituted on either the A-site or B-site. However, because of the different valence, various charge compensation mechanisms can be envisaged.[8] Doping the A-site with a cation of higher charge than Sr^{2+}, such as La^{3+}, can be compensated by introducing extra oxygen beyond the ABO_3 stoichiometry (thus creating an oxygen excess perovskite) as in $La_xSr_{1-x}TiO_{3+x/2}$; by creating A-site vacancies, as in $La_xSr_{1-3x/2}TiO_3$ (A-site deficient perovskite); or by reducing the oxidation state of some Ti^{4+} ions, $La_xSr_{1-x}Ti^{3+}_xTi^{4+}_{1-x}O_3$, when Ti^{3+} can be stabilized, for example by preparing the sample in highly reducing conditions.

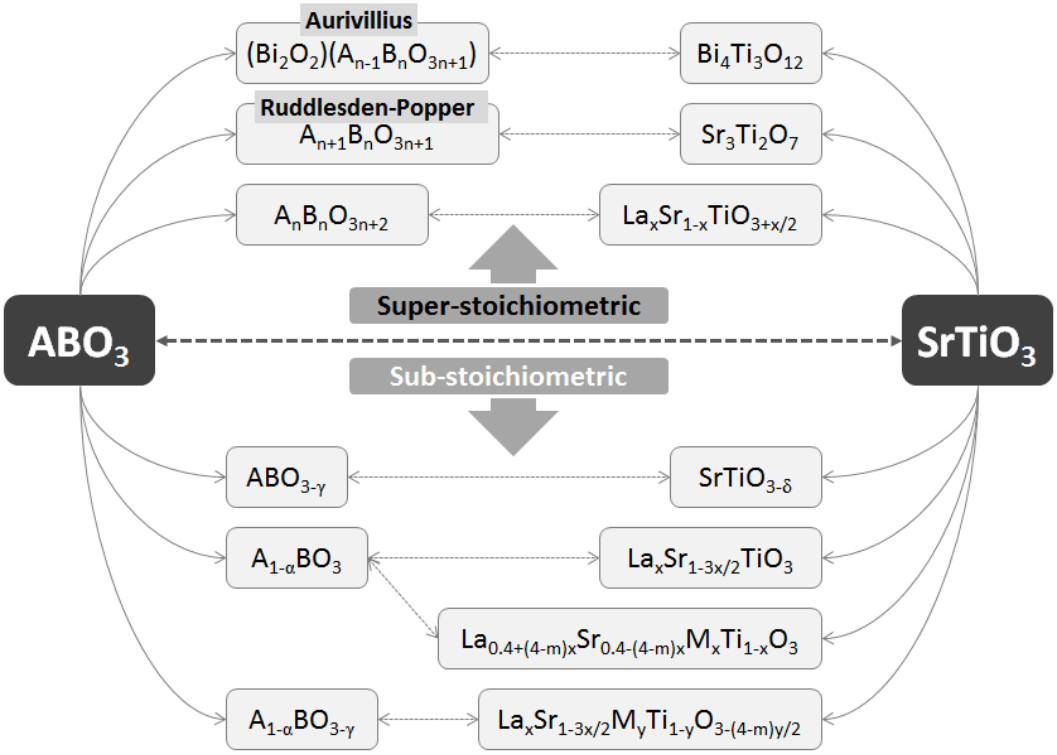

Figure 2.2 – Perovskite nonstoichiometry exemplified on $SrTiO_3$.

Oxygen ion vacancies or "interstitials" (intergrowths) can be generated by substitution of Ti^{4+} ions with cations M^{m+} of lower or higher charge respectively, producing compounds of stoichiometry $SrM_xTi_{1-x}O_{3-(4-m)\cdot x/2}$. Compounds exhibiting simultaneous A-site deficiency and oxygen deficiency,

[ii] Size requirements for cation substitution will be discussed in detail in section 2.2.2.

as in $La_xSr_{1-3x/2}M_yTi_{1-y}O_{3-(4-m)\cdot y/2}$, can be produced depending on the nature of M and if the overall deficiency is small enough.

When doping both A and B sites it is also possible to balance charge between sites, thus creating A-site deficient oxygen stoichiometric compounds such as the ones developed in this study, $La_{0.4+(4-m)\cdot x}Sr_{0.4-(4-m)\cdot x}M_xTi_xO_3$.

When exposed to atmospheres exhibiting low p_{O_2} values (*i.e. reduction conditions*, for example in H_2 containing atmospheres) at sufficiently high temperatures for the oxide ions to migrate (usually above 600 °C), oxide ions can be stripped from the lattice, essentially doping electrons and oxygen vacancies:

$$2Ti_{Ti}^{x} + O_O^x \rightleftharpoons 2Ti_{Ti}' + V_O^{\cdot\cdot} + \frac{1}{2}O_2$$

In general, if the B-site cation supports at least two oxidation states, the reduction process allows one to control the oxygen content of the perovskite, potentially sweeping across the x axis in the plot presented in Figure 2.1 (δ is the amount of oxygen lost during reduction – see section 2.5 for definition):

$$ABO_{3+\gamma} \xrightarrow{\text{Reduction}} \underbrace{ABO_{3+\gamma-\delta}}_{\substack{(\delta<\gamma)\\ excess}} \xrightarrow{\text{Reduction}} \underbrace{ABO_{3+\gamma-\delta}}_{\substack{(\delta=\gamma)\\ stoichiometric}} \xrightarrow{\text{Reduction}} \underbrace{ABO_{3+\gamma-\delta}}_{\substack{(\delta>\gamma)\\ deficient}}$$

2.2 Accommodation of defects in the perovskite structure

2.2.1 The ideal perovskite structure

The ideal perovskite lattice exhibited by $SrTiO_3$ (space group $Pm\bar{3}m$) can be visualised in various ways,[9] but only three of them will be frequently used throughout this study. Figure 2.3 a depicts the perovskite lattice as a cube in which the smaller B-site cations (Ti^{4+}) occupy the corners, in 6-fold coordination; the larger A-site cations (Sr^{2+}) are placed in the centre of the cube in 12-fold coordination, while the oxide ions are located half-way on the

edges. Alternatively, the structure can be viewed as having the A-site ions in the corners of the cube, while the B-site ions sit in the middle of the cube and of the octahedron described by the oxide ions which are now located in the centre of the faces. The third representation, shown in Figure 2.3 c, outlines the fact that the BO_6 octahedra presented in Figure 2.3 b are not isolated, but share oxide ions in all three orthogonal directions, giving rise to a network of corner-sharing octahedra. This is perhaps the most comprehensive representation of the perovskite structure because it emphasizes the important structural role the BO_6 entities alone but also their connectivity, in contrast to the A-site cations. As it will be shown in the following sections, in the light of this structural model, the accommodation of various defects in the perovskite lattice can be interpreted simply as distortions and/or discontinuities of this octahedra network which in turn reflect distinctively on properties.

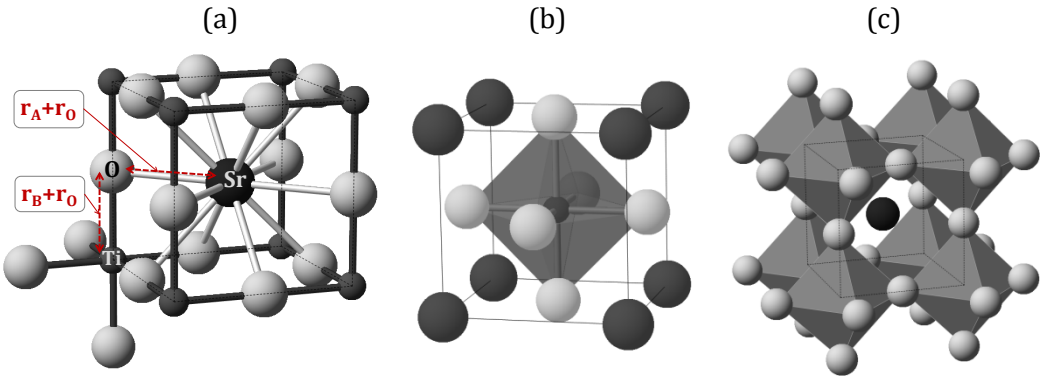

Figure 2.3 – Visualising the perovskite structure. (a) Emphasizes the coordination number and distances between atoms. (b) Representation in which the unit cell contains one inscribed TiO_6 octahedron. (c) Outlines the network of corner-sharing TiO_6 octahedra.

2.2.2 Accommodation of cation substitutions

The manner in which cation substitution type defects are incorporated into the perovskite lattice depends primarily on the size and charge[iii] of the dopant, relative to the cation being replaced. The aspects that are essentially related to the accommodation of "size" will be addressed throughout this section, whereas the incorporation of defects resulting from charge

[iii] The term *charge* used throughout this thesis is meant to be equivalent to *formal oxidation state.*

compensation will be addressed in sections 2.2.3 and 2.2.4 which cover the broader context concerning deficiency and excess in perovskites.

First and foremost, size dictates on which of the two primitive sites (A or B) the cation M^{m+} will fit. Cations that belong on the A-site are characterised by larger size and high coordination numbers, typically between 8 and 12, while the ones on the B-site are much smaller and are required to support coordination number 6, and in some cases coordination numbers as low as 5 or 4.

The distinct *size – coordination number* requirement for the two sites is outlined in Figure 2.4 which presents a plot of ionic radii against coordination number for some cations typically encountered in perovskites.[10] It is obvious from this plot that the A-site cations and the B-site cations cluster in distinct domains which do not intersect.

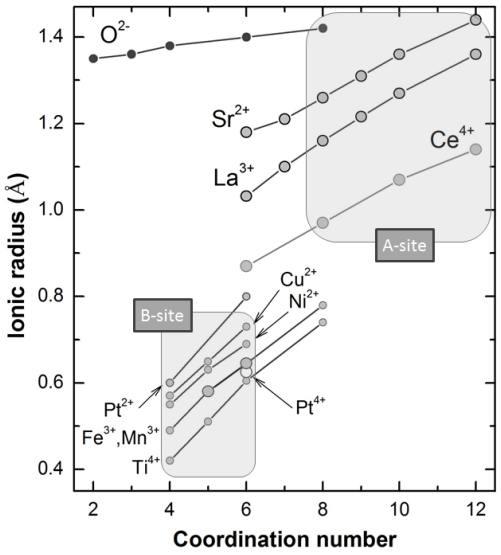

Figure 2.4 – Ionic radii vs. coordination number for some cations typically encountered in perovskites. The characteristic regions for A and B-site cations are emphasized and labelled. Ionic radii from Shannon.[11]

This suggests that based on size alone, generally, one can univocally predict which site a certain cation can occupy in a given perovskite system. This is unlike the spinel systems where inversion between sites easily occurs

because of the similar size of the constituting cations and this in turn causes difficulty in identifying which site is occupied by which cation.

Secondly, assuming the dopant is of the right size for the chosen site, it will, most likely, still have different volume compared to the cation being replaced. The means through which the perovskite lattice accommodates size mismatch is discussed below in relation to the so called *tolerance factor*, τ:

$$\tau = \frac{r_{AO}}{\sqrt{2} \cdot r_{BO}} = \frac{r_A + r_O}{\sqrt{2} \cdot (r_B + r_O)}$$

τ is defined as the mismatch between the A–O and B–O bond lengths which are calculated as the sums of empirical ionic radii (r_A, r_B, r_O) obtained from X-ray diffraction at room temperature and atmospheric pressure.[11] When multiple cations occupy the same site, the average of their ionic radii is used. The tolerance factor is derived from the geometry of the perovskite cell and it represents a measure of how far away in terms of size are the constituting cations in order to create a perfectly cubic cell (see Figure 2.3 a).

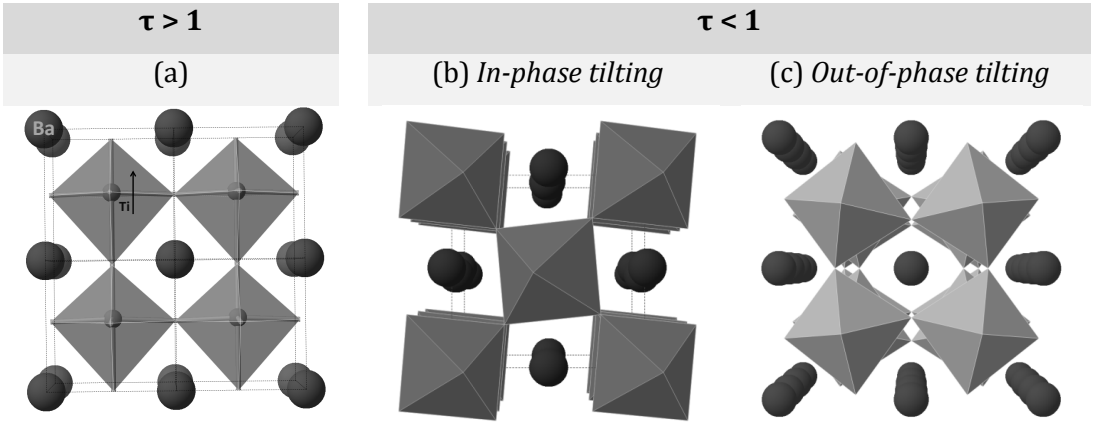

Figure 2.5 – Accommodation of cation substitution in perovskites. For τ > 1, the BO_6 octahedra are slightly stretched, allowing for displacement of the B-site ion from its symmetry position as shown in (a). For τ < 1, octahedra undergo a cooperative tilting that with respect to the adjacent layer can occur in the same direction which is known as in-phase tilting (b), or in opposite direction and is called out-of-phase tilting (c).

For $SrTiO_3$ the size of Sr^{2+} and Ti^{4+} are of just the right ratio to create a cubic lattice and in consequence **τ = 1**. For **τ > 1** the A-site cation is too large for the cuboctahedral cavity, therefore the TiO_6 octahedra need to stretch slightly in order to accommodate the A-site ion.[9,12] Because of this, Ti is not

pinned any more in the symmetry centre of the octahedra and can move, potentially giving rise to ferroelectricity as in the case of $BaTiO_3$ ($r_{Ba^{2+}} > r_{Sr^{2+}}$) depicted in Figure 2.5 a.[9,13] When size mismatch is even more significant, hexagonal polytypes are produced.[14]

Situations when $\boldsymbol{\tau < 1}$ are encountered, for example, when substituting some Sr^{2+} by smaller cations such as La^{3+} or $Ce^{4+/3+}$, and/or replacing some Ti^{4+} by larger cations such as Fe^{3+}, Zn^{2+} etc. In this case, the A-site cation is undersized for the cuboctahedral cavity and thus it cannot make contact with all 12 oxide ions. The structure adjusts by undergoing cooperative rotations of the octahedra while maintaining both the regularity and the corner-sharing, a process that brings some of the oxide ions in touch with the small A-site cation. This is known as *octahedral tilting* and it has been the subject of many studies over the years.[9,15–21] Octahedra in adjacent layers can tilt in the same direction (*in-phase tilting* – see Figure 2.5 b) or in opposite direction (*out-of-phase tilting* – see Figure 2.5 c), and with respect to all three crystallographic directions (although some combinations are restricted, see ref [20]).

There are two main consequences arising from octahedral tilting, aside from the overall decrease in symmetry that accompanies the process. Most importantly, the angle between Ti–O–Ti bonds drops from 180° as it is in the ideal structure to (180° – ϕ). ϕ usually increases with τ, but is typically not larger than 15° in titanates. This change in the Ti–O interactions (orbital overlap, inter-atomic distances etc) is expected to have a direct impact on many properties including the width of the conduction band, the band gap, or the strength of the Ti–O bond itself.[14,22,23] Secondly, tilting leads to a reduction in the coordination number of the A-site cation from 12 to 8-10, creating an asymmetric environment. This in turn may alter the diffusion pathways of the oxide ions and cause further splitting of the degeneracy.[10] It is worth noting that for most perovskites tilting gradually decreases with increasing temperature,[19,24–29] such that at sufficiently high temperatures (500-1500 °C) some even become cubic. This is possibly due to the fact that

the A–O bonds expand more than the B–O bonds with temperature,[14,30] thus if the perovskite starts with $\tau < 1$, upon heating the numerator in Eq.2 will increase faster that the denominator, meaning that the tolerance factor can approach unity.

Although this description of tilting as an effect originating essentially from steric causes explains many observed phenomena,[31] there have been indications that increased covalent interactions between cations and anions would actually be the driving force behind tilting.[9,32] Either way, the tilting phenomenon is what makes the perovskite structure so easy to adapt and thus to be able to incorporate a wide variety of substitutions. Generally, the perovskite can accommodate cations by tilting such that $0.78 < \tau < 1$. Below this value, the ilmenite structure becomes more stable.[9]

The substitution level can also play an important role. When in small enough number, the dopants are randomly distributed on the host sites. However, if the doping level can lead to the formation of ordered structures then these structures will be preferred over the random ones. As a result, a large number of perovskites exhibiting A or B-site ordering are known.[18,21,33]

2.2.3 Accommodation of deficiency

Sub-stoichiometry (deficiency) is accommodated through the creation of vacancies in the perovskite lattice. Thus, the characteristic corner sharing connectivity of the BO_6 octahedra is retained throughout the structure, but A and/or O-sites vacancies are present. The incorporation of vacancies is often accompanied by tilting of the octahedra, most likely because vacancies behave as dopants of different size compared to the host.

The accomodation of A-site vacancies is illustrated in Figure 2.6 for the series $La_xSr_{1-3x/2}TiO_3$. Until $x \sim 0.4$, which corresponds to an A-site deficiency of $\alpha = 0.2$, the vacancies are randomly distributed in the perovskite, occasionaly associating into pairs (see Figure 2.6 b).[25,34,35] Although the substitution fraction is considerable ($x = 0.4$), the perovskite is only slightly distorted

from ideal (b), probably due to the similar size of the dopant and the host cation (Figure 2.4). As soon as more A-site vacancies are inserted into the structure by increasing La doping, x, they start to associate on a larger scale, eventually reaching a clear repetitive arrangement for $x = 0.6$ (Figure 2.6 c). The A-site species order in such a way that fully occupied planes alternate with planes that are only ~1/3 occupied. The octahedra are strongly tilted only around the x axis which is perpendicular to the direction of cation-vacancy ordering. As it will be shown in Chapters 4 and 5, ordering plays a key role in the variation of properties.

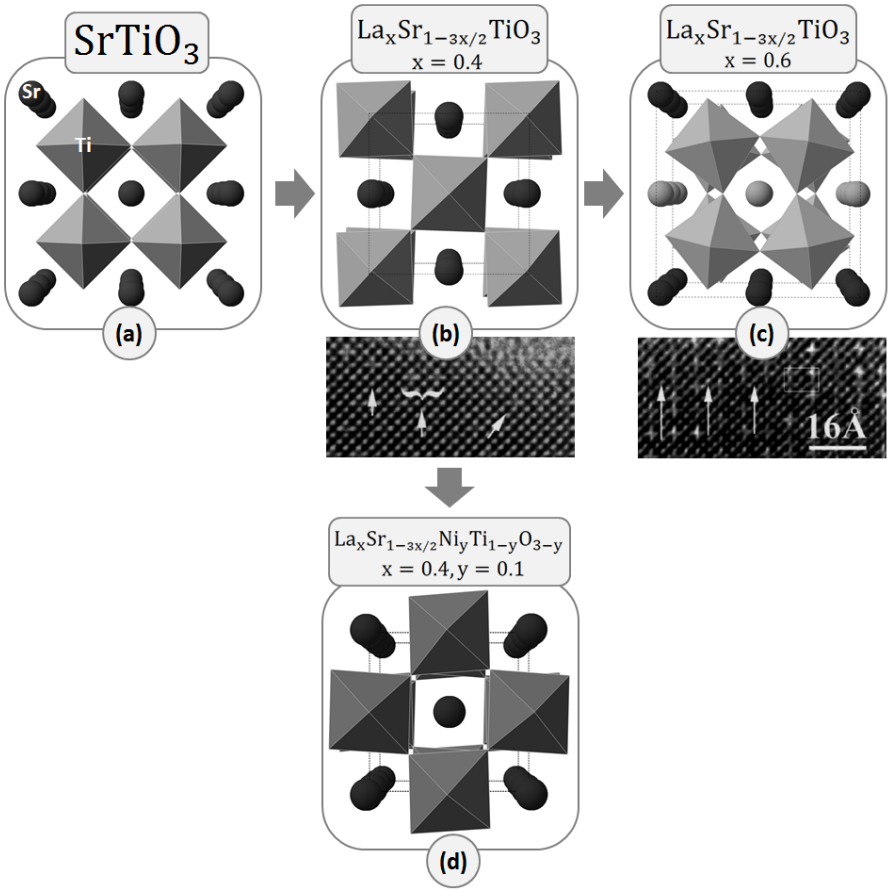

Figure 2.6 – Accommodation of A-site deficiency and small oxygen deficiency in $SrTiO_3$. (a) The defect-free $SrTiO_3$. (b) Randomly distributed A-site vacancies.[25,35] (c) Cation-vacancy ordering on the A-site.[35,36] (d) Randomly distributed A, O-site vacancies (data from this study, see Chapter 4).

Substituting Ni on the B-site of the $x = 0.4$ member of $La_xSr_{1-3x/2}TiO_3$, which is accompanied by generation of vacancies, $La_xSr_{1-3x/2}Ni_yTi_{1-y}O_{3-y}$, does not lead to major changes in the perovskite lattice, nor is any ordering

observed. However, tilting increases noticeably with respect to all three axes (Figure 2.6 d).

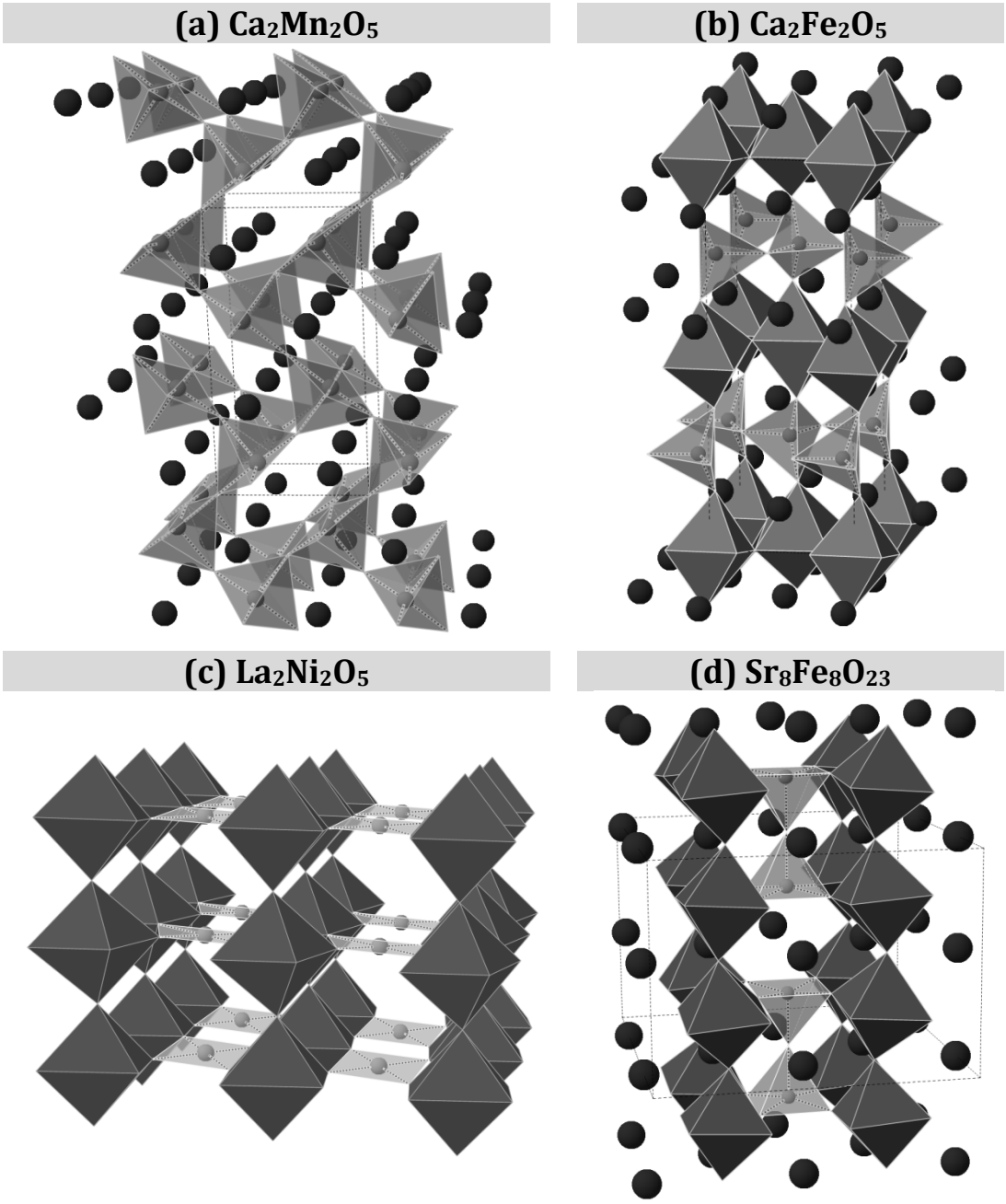

Figure 2.7 – Accommodation of oxygen deficiency in the $A_nB_nO_{3n-1}$ series. (a) $Ca_2Mn_2O_5$, atomic structure from refs [39,40]; (b) $Ca_2Fe_2O_5$, atomic structure from refs [41–43]; (c) $La_2Ni_2O_5$, atomic structure from refs [44,45] (La ions are omitted for clarity); (d) $Sr_8Fe_8O_{23}$, atomic structure from refs [46,47].

The way in which oxygen vacancies alone alter the perovskite structure can be better understood by examining the $A_nB_nO_{3n-1}$ ($n \geq 2$) series.[7,37,38] The creation of oxygen vacancies implies that some of the oxygen ions are

removed, and thus, some of the BO_6 octahedra become incomplete. Because different B-cations favour different coordination geometries with respect to oxygen, the same concentration of oxygen vacancies can be accommodated by various BO_ζ ($4 \leq \zeta < 6$) geometries, depending on the nature of the B-cation. Figure 2.7 exemplifies this aspect for the $n = 2$ member of the $A_nB_nO_{3n-1}$series, $ABO_{2.5}$. For B = Mn, the perovskites accommodates 0.5 oxygen deficiency by losing one oxygen from all its MnO_6 octahedra, forming a network of corner-sharing square pyramids.[39,40] For B = Fe however, the same amount of oxygen deficiency is achieved by a combination of FeO_6 octahedra and FeO_4 tetrahedral units which is known as the *brownmillerite* structure.[41,42,48] When B = Ni, the perovskite lattice consists of NiO_6 octahedra alternating with NiO_4 square planar units.[44,45] Certain geometries are also favoured by a large number of vacancies, as it is the case for the $ABO_{2.5}$ stoichiometry. When the number of vacancies is smaller, and there is no need to form 4-fold coordinated B-sites, 5-fold coordination (square pyramid) predominates, as found for $Sr_8Fe_8O_{23}$ ($\equiv SrFeO_{2.875}$).[46,47]

2.2.4 Accommodation of excess

The means through which additional oxygen beyond the normal ABO_3 stoichiometry can be accomodated by the perovskite structure has been subject to many debates. While it is difficult to imagine that oxygens could be accomodated in interstitials of a cubic close-packed arrangement, compensation through cation vacancies has also been ruled out recently for the strontium titanate system.[49]

The accomodation of excess oxygen is based on a distinct mechanism which allows the perovskite structure to alternate with intergrowths belonging to other crystal structures as exemplified in Figure 2.8. The most characteristic structural change induced by intergrowths is the breaking of the corner sharing between octahedra in adjacent slabs.

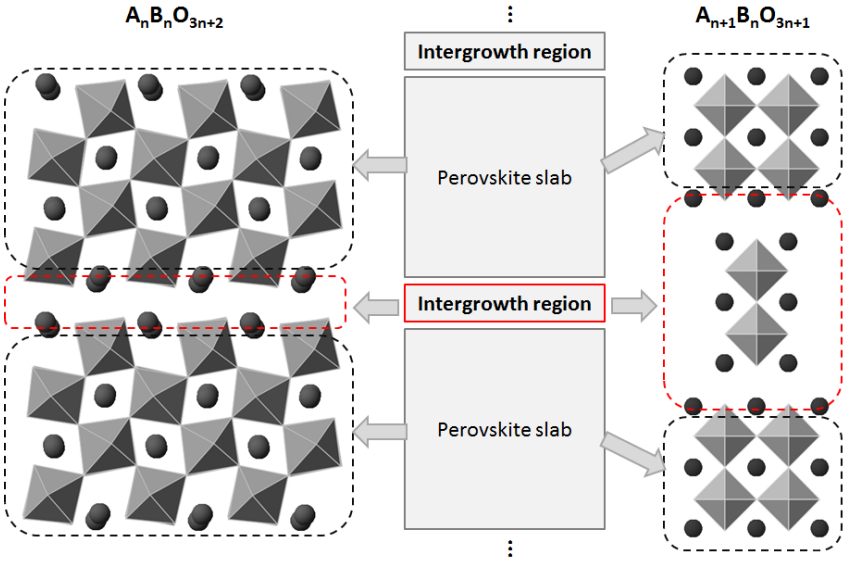

Figure 2.8 – The incorporation of excess (super-stoichiometry) in perovskite.

Ruddlesden-Popper phases,[4,5] $A_{n+1}B_nO_{3n+1}$, consist of rock-salt intergrowths between n-layer thick perovskite blocks and are of interest particulary in the area of high temperature superconductors.[50] The Aurivillius phases[51] are made of $[Bi_2O_2]^{2+}$ layers alternating with $(A_{n-1}B_nO_{3n+1})^{2-}$ perovskite blocks.[52,53] In Dion-Jacobson perovskite block intergrow with halides.[54,55]

The $A_nB_nO_{3n+2}$ $(n \geq 4)$ series has been subject to many studies[49,56,6] which indicate that the structure of these compounds consists of {110} perovskite slabs joined by crystallographic shearing along the cubic [001] direction. This structure can be better visualized by examining the member $n = 4$, $La_4Ti_4O_{14}$ $(\equiv La_2Ti_2O_7)$, shown in Figure 2.9 (a). $La_4Ti_4O_{14}$ has a layered structure consisting of 4-layers thick perovskite blocks that are offset from one another at the crystallographic shear. Thus, the connectivity between the corners of the octahedra is broken along the shears where the excess oxygen is actually located. The octahedra are tilted within the perovskite blocks and additionally become increasingly distorted as they approach the crystallographic shear. Moreover, the A-site cations in the perovskite layers adjacent to the crystallographic shear are significantly displaced from their ideal lattice position towards the shear.

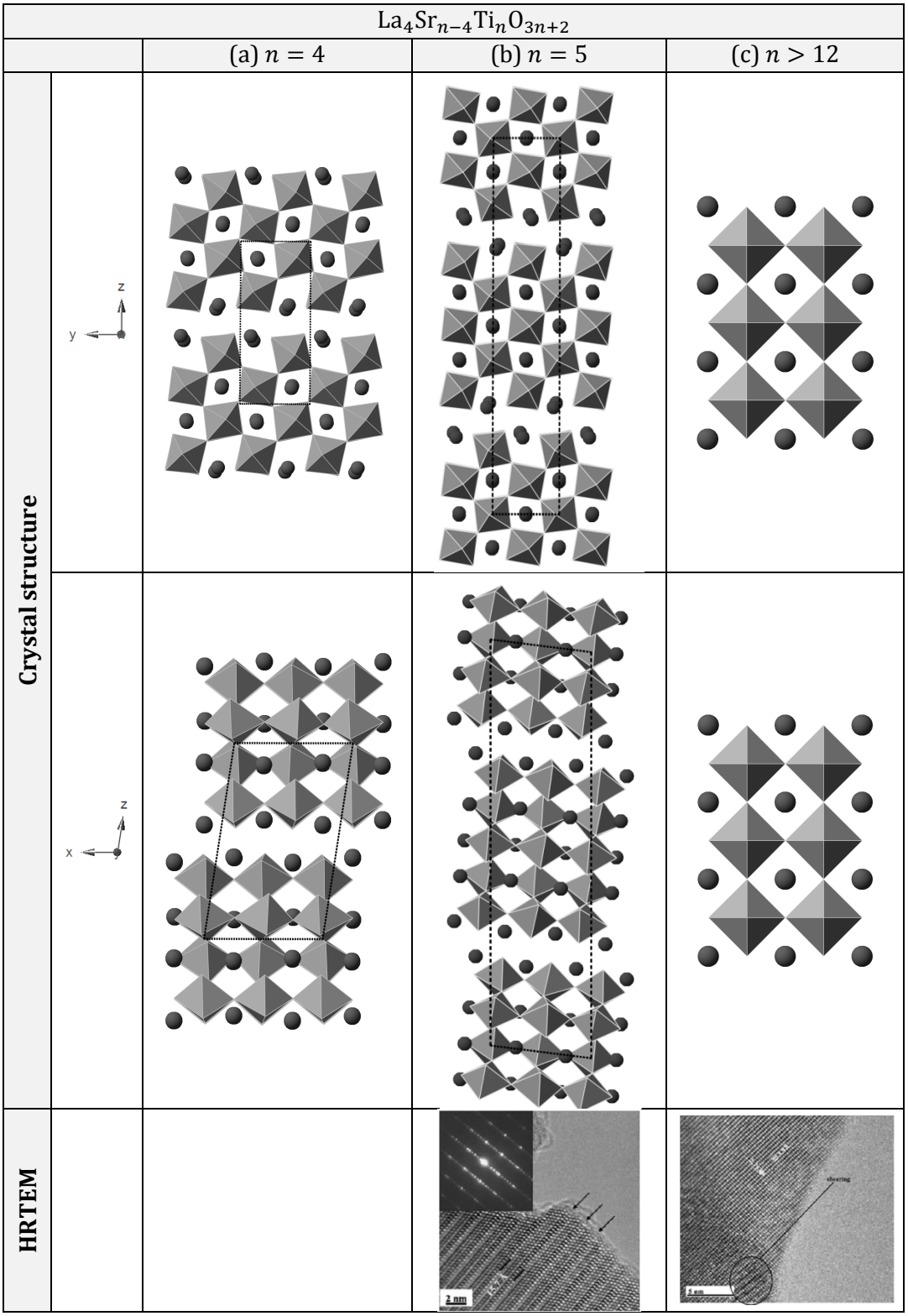

Figure 2.9 – Accommodation of oxygen excess in the solid solution $La_4Sr_{n-4}Ti_nO_{3n+2}$. (a) the end-member of the solid solution $La_4Sr_{n-4}Ti_nO_{3n+2}$, $La_2Ti_2O_7$;[56,57] (b) ordered oxygen excess intergrowths form distinct crystallographic shears,[49,56] (c) randomly distributed oxygen excess intergrowths for low La doping levels.[49,58]

By considering a solid solution between the cubic $SrTiO_3$ and the layered $La_4Ti_4O_{14}$, ($La_4Sr_{n-4}Ti_nO_{3n+2}$, $n \geq 4$), it has been shown possible to decrease the frequency of crystallographic shears by increasing n.[49] Increasing n from 4 to 5 leads to an increase in the number of perovskite layers composing the perovskite blocks (compare Figure 2.9 (a) to Figure 2.9 (b)), but the structure still retains its layered appearance. As n is further increased, the shearing is broken, the extended defects becoming more and more sporadic until $n \sim 12$ where even though oxygen excess is still present, these intergrowths are randomly distributed throughout the structure in such a way that the overall symmetry resembles the cubic $SrTiO_3$ end-member (see Figure 2.9 (c)).[49] The possibility to control the extent of ordering in this system allows one to control the functionality of these materials, an aspect that will be further addressed in Chapter 5. It is also worth noting that the series $La_xSr_{1-x}TiO_{3+x/2}$has been shown to be equivalent to $La_4Sr_{n-4}Ti_nO_{3n+2}$.[56]

2.3 Electronic structure

So far, the ions constituting the perovskite have been regarded as charged spheres in describing the ideal perovskite and its adaptation to nonstoichiometry. While this simplification offers a "bird's eye" view of the *crystal structure*, it neglects the electronic states of the ions constituting the perovskite, the resultant interactions between them, and thus, alone cannot account for the properties originating in the *electronic structure* of the perovskite. Therefore, the aim of this chapter is to complement the previously presented features of the perovskite with elements regarding their electronic states.

In a first approximation, the change in the electronic structure of an ion occupying a particular site in the perovskite can be described as the combined effect of the electrostatic field exerted by the neighbouring ions, and the way these ions are disposed around the site of interest (symmetry of the site). Cations located at the B-site have their five-fold degenerated *d* states split into two subgroups, as shown in Figure 2.10.[59,60]

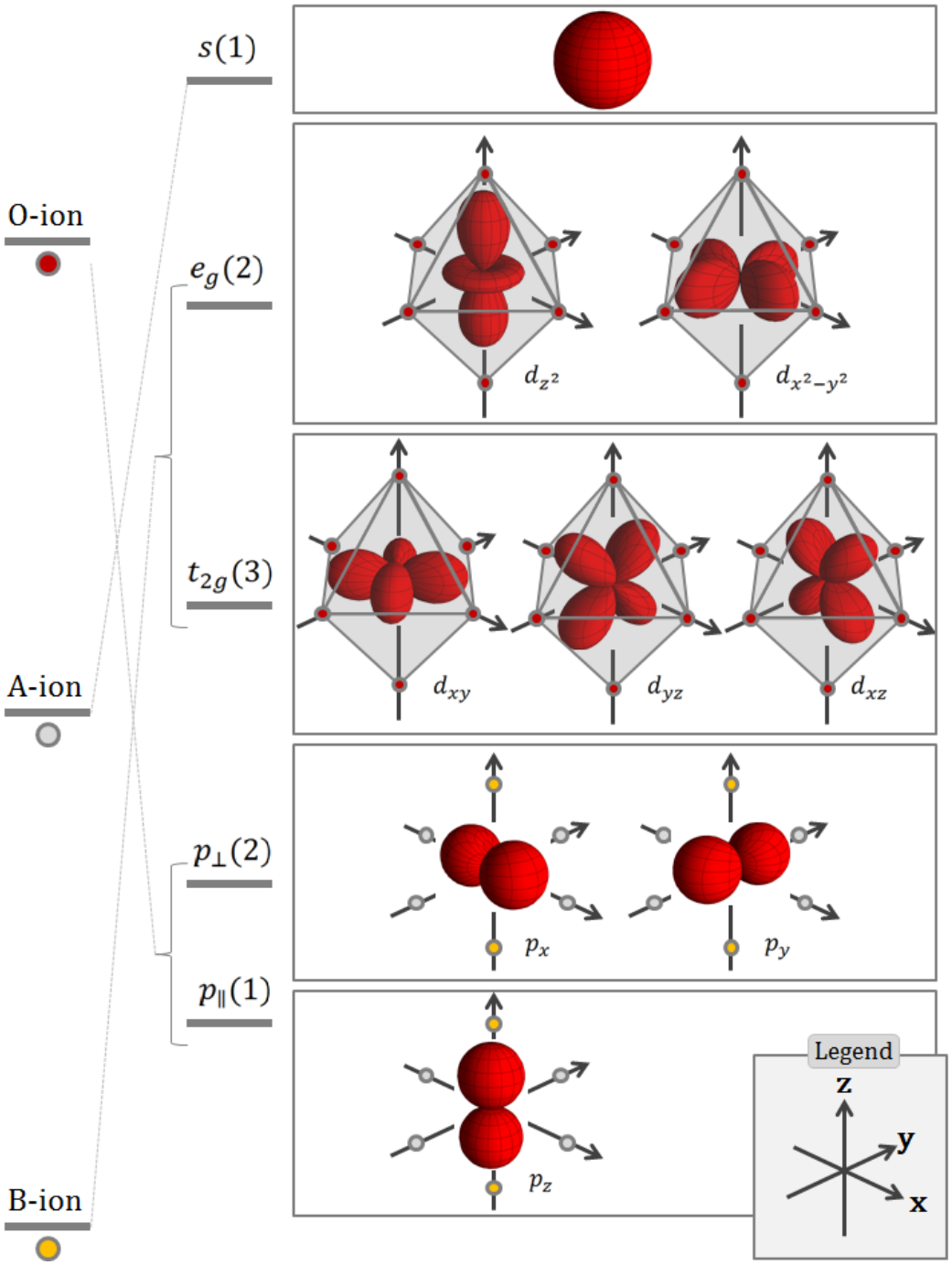

Figure 2.10 – The effect of electrostatic potentials on ion states. Number in brackets indicate degeneracy.[10,59]

The doubly degenerate e_g group corresponds to the orbitals having symmetry $d_{x^2-y^2}$ and d_{z^2}, while the three-fold degenerate group t_{2g} corresponds to the ones with d_{xy}, d_{yz} and d_{xz} symmetry. The oxygen $2p$ states are split into a doubly degenerate level labelled here $p_\perp$ ($2p$ orbitals oriented perpendicular to a B-O axis) and a non-degenerate state $p_\parallel$ ($2p$

orbitals oriented parallel to a B-O axis). The lowest unoccupied state of the A ions which is an s state, suffers no splitting because of its non-degenerate spherical charge distribution at a site of cubic symmetry.[10,61]

The energy level of the states after splitting depends on the orientation of the orbitals with respect to the neighbouring ions. In particular, orbitals that experience greater repulsion from anions lying in their proximity have their energy levels increased.[10] For example, the lobes of the e_g orbitals point directly towards the negative charge clouds of the anions, while the lobes of the t_{2g} orbitals point in between them, thus the e_g states are located at higher energy compared to the t_{2g} states. On the contrary, the $p_{\parallel}$ orbital points towards the positively charged B-site ion and thus its energy lies below the $p_{\perp}$ states. By analogy to the Crystal Field Theory (CFT)[iv], the energy difference between the t_{2g} and e_g is the octahedral crystal field splitting and is denoted by Δ_O. This parameter plays a crucial role in explaining the optical and magnetic properties of transitional metal complex compounds, and has been shown to influence cation site preference (tetrahedral vs. octahedral) in spinel systems, which in turn reflects on most spinel properties.[59] Section 5.8 will discuss the importance of d orbital splitting for the reduction of perovskite titanates.

Usually, the p states are completely filled (with electrons coming from the oxygens – the "ligands"), the d states are occupied to a various degree, depending on the electronic configuration of the B-site ion, while the s states are empty in the vast majority of perovskites. The latter is due to the much higher energy of these states compared to the other energy levels. As a result, the s states do not usually play a significant role in describing the electronic properties of perovskites and thus can be omitted from calculations and interpretations of properties.[61,62] In turn, this observation allows one to regard the electronic properties of perovskites as originating exclusively from the BO_3 part of the ABO_3, particularly from the BO_6 octahedra. However,

[iv] CFT describes the splitting of the *d* orbitals in the crystal field of the ligand for transitional metal complexes.

this does not mean that the A-site cation has no effect, whatsoever, on the electronic properties. The influence of this cation manifests mainly through its electrostatic potential which influences the position of the other energy states and also through the structural distortions it can induce via the tilting phenomena.[10,1,23,17,18]

In addition to electrostatic interactions, the ions can experience overlap of the orbitals leading to $p-d$ hybridisation and thus to covalent bonds between the transitional metal ions and the oxygen ions. Although the covalent component is assumed to be negligible in perovskites such as $SrTiO_3$, it has been shown this is not true, and that many properties are notably affected by covalency effects.[61,63,64]

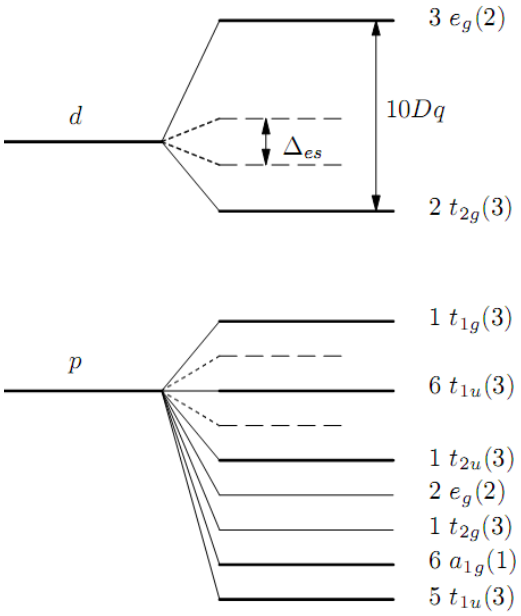

Figure 2.11 – Energy levels resulting from covalent interactions in a BO_6 octahedra. Dashed lines correspond to the energy levels resulted from the electrostatic splitting model.[10,63,61]

The covalent mixing in the BO_6 octahedra is presented in Figure 2.11 and described as follows, according to refs.[63,61,64] "Sigma" overlap (σ *bonding*) occurs between the e_g and $p_{\parallel}$ orbitals, while "pi" overlap (π *bonding*) between t_{2g} and $p_{\perp}$. It is apparent from Figure 2.11 that the d orbitals are still split into the e_g and t_{2g} groups, now denoted by $3e_g$ and $2t_{2g}$, respectively. However, there are two main differences compared to the situation described

in the exclusively electrostatic model. First, the $3e_g$ and $2t_{2g}$ are now mixtures of p and d orbitals and second, the energy separation between them is much more significant compared to the electrostatic model. Because the $3e_g$ and $2t_{2g}$ consist of wave-functions in which the d orbitals combine out-of-phase with the p orbitals, they represent *antibonding* states. The *bonding states* are denoted by the $2e_g$ and $1t_{2g}$ and have typically 30% d character and 70% p character.[64] The remaining energy levels are combinations of p orbitals located on the oxygen ion, do not contribute to the B-O bonding, and therefore are called *non-bonding*.

2.4 Conduction in the perovskite lattice

2.4.1 Electronic conduction

Section 2.3 showed that the electronic structure of perovskites is mainly governed by the electronic states of the BO_6 entities and that covalent mixing does occur between the B-site cation and surrounding oxygen ions. In turn, partial covalency allows electrons to be transferred back and forth between ions, and more importantly between the B-site cations in adjacent BO_6 octahedra, via the shared oxygen ion that links them[v].[10,61,66] Electron delocalisation of this sort leads to the formation of energy bands.

Insulating perovskites such as $SrTiO_3$ have filled p states and empty d states. Metallic or semiconducting perovskites have d states partly filled. Metallic perovskites tend to have one electron in the t_{2g} states, while more than this can lead to a preference for localised electrons.[10,66]

The usual way of transforming $SrTiO_3$ from an insulator to an electronic conductor is by reduction (see section 2.5 for details). In this process, oxygen ions are removed from the lattice and leave behind electrons which can be formally regarded to create Ti^{3+} ions, and oxygen vacancies:

[v] The B-B distance is too long in perovskites (~4 Å) to allow direct overlap of the metal orbitals.[65]

$$2Ti_{Ti}^{x} + O_{O}^{x} \rightleftharpoons 2Ti_{Ti}' + V_{O}^{\cdot\cdot} + \frac{1}{2}O_2 \qquad \text{Eq. 2-1}$$

Because of the strong tendency of the Ti^{3+} "electrons" to delocalise to their Ti^{4+} neighbours, electronic conduction can also be visualised as electron hopping (Figure 2.12) from Ti^{3+} to Ti^{4+} leading to delocalisation of charge across the crystal.[67] Electron doped $SrTiO_3$ has been shown to be superconductor at temperatures below 0.3 K.[68]

At the macroscopic scale, conductivity is proportional to the concentration of (free) charge carriers [e′], their charge Z, and their mobility μ_e:

$$\sigma_e = [e'] \cdot Z \cdot e \cdot \mu_e \qquad \text{Eq. 2-2}$$

As shown above, in titanates the concentration of charge carriers depends on the concentration of Ti^{3+} ions in the sample. If the electrons are not localized (trapped), and thus are free to take part in conduction, then $[e'] = [Ti^{3+}]$.

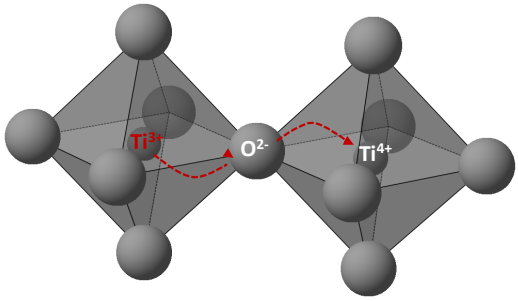

Figure 2.12 – Schematic view of electron conduction in the perovskite.

This is usually the case in systems in which only Ti^{3+}/Ti^{4+} occupy the B-site, as it will be shown in Chapter 6. The mobility of the electrons depends mainly on the crystal composition, the structure of Ti-O-Ti bonds (*i.e.* orbital overlap), and the microstructure of the sample (for polycrystalline samples). Factor including tilting, size of the cell and nature of the A-site cation can change the degree of overlap between the Ti orbitals and oxygen orbitals.

2.4.2 Ionic conduction

Generally, ionic conduction can occur in the perovskite structure when some of the oxygen sites are vacant (*i.e.* when oxygen vacancies are present). As shown previously, the perovskite structure allows for oxygen deficient

stoichiometry. Some of the perovskite or perovskite related systems that display high ionic conductivity are included in Table 2.1, together with their perovskite class, acronym and bulk ionic conductivity of the optimised composition.

Table 2.1 – Oxide ion conducting perovskite systems.

Perovskite class	**Composition**	**Acronym** [vi]	**Representative σ_i (S·cm^{-1})** [vii]	**Refs.**
$ABO_{3-\gamma}$	$La_{1-x}Sr_xGa_{1-y}Mg_yO_{3-\frac{x+y}{2}}$	LSGM	$0.14\ at\ 800$ °C [viii]	69,70
$ABO_{2.5}$ [ix]	$Ba_2In_2O_5$	BI	$0.11\ above\ 930$°C [x]	71,72
Aurivillius [xi]	$Bi_2Me_xV_{1-x}O_{5-\gamma}$	BIMEVOX	$4 \cdot 10^{-4}\ at\ 230$ °C [xii]	73,74

The diffusion of oxide ions in the perovskite lattice occurs by hopping of oxide ions from an available adjacent oxide ion vacancy to another. Most of the literature concerning the oxide ion conduction in the perovskites comes from in depth studies performed on LSGM.[69,75–79,29,80,81] The diffusion pathway in an undistorted perovskite is illustrated in Figure 2.13 and synthetically expressed in the equation below:

$$D_{O_2} \propto [V_O^{\cdot\cdot}] \cdot a^2 \cdot e^{-\frac{\Delta H_f + \Delta H_m + \Delta H_a}{R \cdot T}} \qquad \text{Eq. 2-3}$$

The above equation shows that diffusion is a *thermally activated process*, is proportional to the concentration of *mobile* vacancies $[V_O^{\cdot\cdot}]$, and the square of the cell parameter a. Diffusion also depends on three main processes and their associated thermal effects: formation ΔH_f, migration ΔH_m, and

[vi] The abbreviations LSGM and BIMEVOX are widely used in the literature, while BI is only used in this study.
[vii] For comparison, the conductivity of the classical oxide ion conductor, yttria stabilised zirconia $Zr_{0.91}Y_{0.09}O_{1.955}$, is $\sim 4 \cdot 10^{-2} S \cdot cm^{-1}$ at 800 °C.
[viii] For the optimised composition with x = 0.2 and y = 0.17.
[ix] Brownmillerite type structure.
[x] BI suffers a breakdown of the vacancy ordering at t > 930 °C, which is accompanied by a massive increase in conductivity; at 800 °C, the conductivity is only $10^{-3} S \cdot cm^{-1}$.
[xi] See section 2.2.4 for structural details of this class.
[xii] For the optimised composition $Bi_2V_{0.85}Ti_{0.15}O_{5.425}$.

association ΔH_a of vacancies. The way these factors come into play can be better understood by examining Figure 2.13.

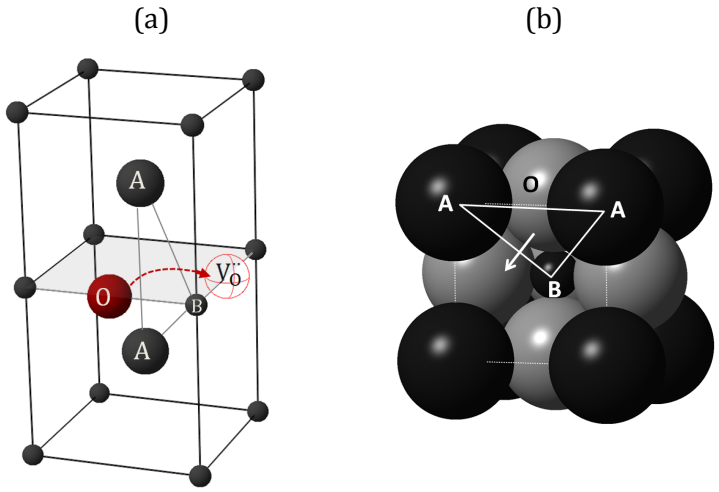

Figure 2.13 – Diffusion of oxide ions (or oxygen vacancies) in undistorted perovskites. (a) Model emphasizing the curved diffusion pathway between the triangle described by the two A-ions and the B-ion.[82] (b) Space filling model showing the real size of the ions (after [29]).

When the oxide ion starts moving from its position, it will need to break the bond shared with one of the adjacent B-site cations. The A-O bonds are significantly longer and thus weaker compared to the B-O bonds and are not expected to play an important role at this stage. When the B-O bond breaks, the corresponding B-site cation will have its coordination number lowered from 6 to 5. Most of the B-site ions tend to form very strong bond with oxygen and strongly prefer 6-fold coordination. As a result, the energy required for the formation of vacancy ΔH_f is high. Titanium is a typical example of such a cation, because although the stability of the Ti-O bond detrimental for promoting oxide ion mobility, it also confers the remarkable stability of the $SrTiO_3$ structure. On the contrary, other cations such as $Mn^{2+/3+}$, $Co^{2+/3+}$, $Fe^{2+/3+}$, Ga^{3+} etc are known to be stable in coordination numbers lower than 6 as well[8] and have been successfully employed in the design of materials with higher oxide ion mobility.[83,84] Once the B-O bond has been broken, the oxide ion will have to migrate through the triangle described by the two A-site cations and the B-site cation, while maintaining constant distance with respect to the B-site cation it is still bonded to. As a

consequence, the trajectory will be curved, as depicted in Figure 2.13 (a). Previous studies indicate that this is probably the most energy intensive step in the migration of the oxide ion.[75,78,29,80] Among the factors that come into play at this stage, the most important are the nature (electronic structure, size) of the A-site cations and the distortions of the lattice which can prevent the oxide ion from taking the simple path indicated in Figure 2.13. Several studies point out that the highest mobility for vacancy hopping should be expected for lattices exhibiting the highest symmetry where repulsion effects are minimised.[75,79,80] Usually, the migration energy is smaller than the vacancy formation energy.[78]

At low concentrations, the interaction between defects is negligible. However, when in sufficiently large numbers, defect-defect interactions can become a dominant factor in the energy requirements for ionic movement. These interactions usually manifest themselves as associations between defects of the same type or and/or defects of different nature. Associations can be local or extended over significant distances, in either case potentially leading to an increase of the term ΔH_a and also greatly diminishing the number of mobile vacancies. This is the case in the Bi-based brownmillerite system where below 930 °C the oxide ion vacancies are pinned in ordered layers. Upon heating the material above this point, the ordering is broken and an increase of two orders of magnitude in ionic conductivity is recorded.[72] Therefore, a random distribution of oxide ion vacancies is to be desired in order to maximise ionic conduction. Vacancies can also be trapped around dopants due to size mismatch compared to the host ion. Where the size of the host and the dopant are similar, for example when substituting Sr^{2+} (1.44 Å) for La^{3+} (1.36 Å) in lanthanum gallates, ΔH_a has been calculated to be zero.[85]

2.5 Reduction in perovskite titanates

The reduction of perovskites is generally carried out by heating the material in environments having low oxygen partial pressures (p_{O_2}). The temperatures employed are usually between 800-1000 °C, but can be as low

as 500-600 °C or as high as 1400 °C. Various p_{O_2} values can be achieved by using inert gases (Ar, N_2), purely reducing gases (H_2), mixtures of the latter two or other methods. During the reduction process some oxide ions are stripped from the perovskite lattice, leaving behind vacancies, and a corresponding number of electrons (B-site cations are reduced):

$$2B_B^x + O_O^x \rightleftharpoons 2B_B' + V_O^{\cdot\cdot} + \frac{1}{2}O_2 \qquad \text{Eq. 2-4}$$

The decrease in oxygen stoichiometry that occurs upon reduction, from $ABO_{3\pm\gamma}$ to $ABO_{3\pm\gamma-\delta}$, denoted by δ, represents the oxygen ions lost or equivalently the number of oxide ion vacancies created in the process, per formula unit of perovskite. It is often referred to as the *extent of the reduction*, oxygen deficiency on reduction, or even simply oxygen content. It is worth noting that from the definition of δ and above written equilibrium, it follows that $[V_O^{\cdot\cdot}] \propto \delta$ and $[B_B'] \propto 2 \cdot \delta$. Because the reduction process occurs with weight loss, δ values can be easily obtained by thermogravimetry.

δ plays an important role in understanding the structure-property relationship in perovskites as it correlates with many of their properties, including electronic conductivity,[85–89] catalytic activity,[86] transition temperature of oxide superconductors[87,88] or magnetic ordering.[89,90]

Information on the reduction of perovskite titanates is, however, scarce and often intermixed with conductivity studies. Systems that have been investigated include $SrTiO_3$,[91–95,66] $(La,Sr)(Ti,M)O_{3+\gamma}$,[96] $(La, Sr)_{1-\alpha}(Ti,M)O_3$, [97,98] $(Sr,Y)_{1-\alpha}(Ti,M)O_3$,[22,99,100] $(La,Ca)(Ti,Cr)O_3$.[101,102]

There seems to be a general consensus that the reduction in polycrystalline titanates is a slow, thermally activated process.[97,98,103,102] The kinetics and the extent of the reduction are enhanced by the presence of A-site vacancies[97,8] and B-site cations that allow good oxide ion mobility[8,83,84] and are hindered by ordering of defects.[58]

2.6 Conclusions

Perovskite oxides ABO_3 consist of a 3D network of BO_6 corner-sharing octahedra, with the A-ions located in the resulting cuboctahedral cavities. The BO_6 entities are not only the building blocks of the structure but are also vastly responsible for the electronic structure of the perovskite.

Perovskite oxides can accommodate defects from three fundamental points of view: *size* of constituents through tilting or stretching of the octahedra; *deficiency* (A and/or O-site) by creation of vacancies, while preserving corner-sharing of the octahedra; and *excess* (A and/or O-site) through intergrowths, locally interrupting the corner-sharing octahedra chains.

If the B-site cation can support at least two oxidation states, electronic conduction can occur between adjacent octahedra containing different B oxidation states, through charge delocalisation *via* the oxygen bridge.

The perovskite structure can also display oxide ion conductivity if oxide ion vacancies are present. The likelihood and magnitude of oxide ion conductivity is dictated by several factors, including the number of mobile oxide ion vacancies, the free space in the unit cell and the energy of formation, migration and association of vacancies.

Through a reduction process, electrons and vacancies can be doped into perovskites. In particular, in doped $SrTiO_3$ systems reduction has been found to be a slow, thermally activated process, primarily depending on the defect chemistry of the titanate and the constituting ions.

References

1. E. Kaxiras, *Atomic and Electronic Structure of Solids*, Cambridge University Press, 2003.
2. J. B. Goodenough, *Rep. Prog. Phys.*, 2004, **67**, 1915–1993.
3. G. Trolliard, N. Ténèze, P. Boullay, and D. Mercurio, *J. Solid State Chem.*, 2004, **177**, 1188–1196.
4. S. N. Ruddlesden and P. Popper, *Acta Crystallogr.*, 1957, **10**, 538–539.
5. S. N. Ruddlesden and P. Popper, *Acta Crystallogr.*, 1958, **11**, 54–55.
6. T. Williams, H. Schmalle, A. Reller, F. Lichtenberg, D. Widmer, and G. Bednorz, *J. Solid State Chem.*, 1991, **93**, 534–548.
7. M. T. Anderson, J. T. Vaughey, and K. R. Poeppelmeier, *Chem. Mater.*, 1993, **5**, 151–165.
8. J. Irvine, in *Perovskite Oxide for Solid Oxide Fuel Cells*, ed. T. Ishihara, Springer, 2009.
9. H. D. Megaw, *Ferroelectricity in Crystals*, Methuen & Co, Ltd, 1957.
10. T. Wolfram and Ş. Ellialtıoğlu, *Electronic and optical properties of D-band perovskites*, Cambridge University Press, 2006.
11. R. D. Shannon, *Acta Crystall. A-Crys.*, 1976, **32**, 751–767.
12. N. L. Allan, M. J. Dayer, D. T. Kulp, and W. C. Mackrodt, *J. Mater. Chem.*, 1991, **1**, 1035–1039.
13. A. R. West, *Basic Solid State Chemistry*, Wiley, 2nd edn., 1999.
14. J. Goodenough, Ed., *Localized to itinerant electronic transition in perovskite oxides*, Springer, Berlin, 2001.
15. A. M. Glazer, *Acta Crystall. B-Stru.*, 1972, **28**, 3384–3392.
16. A. M. Glazer, *Acta Crystallogr. A*, 1975, **31**, 756–762.
17. P. M. Woodward, *Acta Crystall. B-Stru.*, 1997, **53**, 32–43.
18. P. M. Woodward, *Acta Crystall. B-Stru.*, 1997, **53**, 44–66.
19. C. J. Howard and H. T. Stokes, *Acta Crystallogr. A*, 2004, **61**, 93–111.
20. C. J. Howard and H. T. Stokes, *Acta Crystall. B-Stru.*, 1998, **54**, 782–789.
21. M. Lufaso and P. Woodward, *Chemistry Faculty Publications*, 2001.
22. S. Hui and A. Petric, *J. Electrochem. Soc.*, 2002, **149**, J1.
23. H. W. Eng, P. W. Barnes, B. M. Auer, and P. M. Woodward, *J. Solid State Chem.*, 2003, **175**, 94–109.
24. M. A. Carpenter, C. J. Howard, K. S. Knight, and Z. Zhang, *J. Phys.: Condens. Mat.*, 2006, **18**, 10725–10749.
25. C. Howard, G. Lumpkin, R. Smith, and Z. Zhang, *J. Solid State Chem.*, 2004, **177**, 2726–2732.
26. C. J. Howard and B. J. Kennedy, *J. Phys.: Condens. Mat.*, 1999, **11**, 3229–3236.
27. B. J. Kennedy, C. J. Howard, G. J. Thorogood, M. A. T. Mestre, and J. R. Hester, *J. Solid State Chem.*, 2000, **155**, 455–457.
28. B. J. Kennedy, C. J. Howard, and B. C. Chakoumakos, *J. Phys.: Condens. Mat.*, 1999, **11**, 1479–1488.
29. P. R. Slater, J. T. S. Irvine, T. Ishihara, and Y. Takita, *J. Solid State Chem.*, 1998, **139**, 135–143.
30. B. Dabrowski, O. Chmaissem, J. Mais, S. Kolesnik, J. D. Jorgensen, and S. Short, *J. Solid State Chem.*, 2003, **170**, 154–164.

31. J. P. Attfield, *Cryst. Eng.*, 2002, **5**, 427–438.
32. P. Garcia-Fernandez, J. A. Aramburu, M. T. Barriuso, and M. Moreno, *J. Phys. Chem. Lett.*, 2010, **1**, 647–651.
33. C. J. Howard, B. J. Kennedy, and P. M. Woodward, *Acta Crystall. B-Stru.*, 2003, **59**, 463–471.
34. K. L. Smith, G. R. Lumpkin, M. G. Blackford, M. Colella, and N. J. Zaluzec, *J. Appl. Phys.*, 2008, **103**, 083531.
35. P. Battle, J. E. Bennett, J. Sloan, R. J. D. Tilley, and J. F. Vente, *J. Solid State Chem.*, 2000, **149**, 360–369.
36. Z. Zhang, C. J. Howard, K. S. Knight, and G. R. Lumpkin, *Acta Crystall. B-Stru.*, 2006, **62**, 60–67.
37. L. G. Tejuca, J. L. G. Fierro, and J. M. D. Tascón, in *Advances in Catalysis*, eds. B. C. Gates and F. C. Jentoft, Academic Press, 1989, vol. 36, pp. 237–328.
38. S. Stølen, E. Bakken, and C. E. Mohn, *Phys. Chem. Chem. Phys.*, 2005, **8**, 429–447.
39. K. R. Poeppelmeier, M. E. Leonowicz, and J. M. Longo, *J. Solid State Chem.*, 1982, **44**, 89–98.
40. A. Reller, J. M. Thomas, D. A. Jefferson, and M. K. Uppal, *Proc. R. Soc. Lond. A*, 1984, **394**, 223–241.
41. E. Asenath-Smith, S. T. Misture, and D. D. Edwards, *J. Solid State Chem.*, 2011, **184**, 2167–2177.
42. A. L. Shaula, Y. V. Pivak, J. C. Waerenborgh, P. Gaczyñski, A. A. Yaremchenko, and V. V. Kharton, *Solid State Ionics*, 2006, **177**, 2923–2930.
43. A. M. Abakumov, J. Hadermann, M. Batuk, H. D'Hondt, O. A. Tyablikov, M. G. Rozova, K. V. Pokholok, D. S. Filimonov, D. V. Sheptyakov, A. A. Tsirlin, D. Niermann, J. Hemberger, G. Van Tendeloo, and E. V. Antipov, *Inorg. Chem.*, 2010, **49**, 9508–9516.
44. J. A. Alonso, M. J. Mart, and J. L. Garc, *J. Phys.: Condens. Mat.*, 1997, **9**, 6417–6426.
45. J. A. Alonso and M. J. Martínez-Lope, *Mater. Sci. Forum*, 1996, **228-231**, 747–752.
46. J. P. Hodges, S. Short, J. D. Jorgensen, X. Xiong, B. Dabrowski, S. M. Mini, and C. W. Kimball, *J. Solid State Chem.*, 2000, **151**, 190–209.
47. P. Villars and K. Cenzual, Eds., *Space Groups (140) I4/mcm - (136) P42/mnm: Structure Types*, Springer, 2011, vol. 43.
48. H. D'Hondt, A. M. Abakumov, J. Hadermann, A. S. Kalyuzhnaya, M. G. Rozova, E. V. Antipov, and G. Van Tendeloo, *Chem. Mater.*, 2008, **20**, 7188–7194.
49. J. Canales-Vázquez, M. J. Smith, J. T. S. Irvine, and W. Zhou, *Adv. Funct. Mater.*, 2005, **15**, 1000–1008.
50. J. G. Bednorz and K. A. Muller, *Z. Phys. B Con. Mat.*, 1986, **64**, 189–193.
51. Aurivillius, *Ark. Kemi*, 1949, **1**, 499.
52. A. M. Kusainova, S. Y. Stefanovich, J. T. S. Irvine, and P. Lightfoot, *J. Mater. Chem.*, 2002, **12**, 3413–3418.
53. A. M. Kusainova, W. Zhou, J. T. S. Irvine, and P. Lightfoot, *J. Solid State Chem.*, 2002, **166**, 148–157.
54. M. Dion, M. Ganne, and M. Tournoux, *Mater. Res. Bull.*, 1981, **16**, 1429–1435.

55. A. J. Jacobson, J. W. Johnson, and J. T. Lewandowski, *Inorg. Chem.*, 1985, **24**, 3727–3729.
56. M. E. Bowden, D. A. Jefferson, and I. W. M. Brown, *J. Solid State Chem.*, 1995, **117**, 88–96.
57. E. J. Harvey, S. E. Ashbrook, G. R. Lumpkin, and S. A. T. Redfern, *J. Mater. Chem.*, 2006, **16**, 4665–4674.
58. J. C. Ruiz-Morales, J. Canales-Vázquez, C. Savaniu, D. Marrero-López, W. Zhou, and J. T. S. Irvine, *Nature*, 2006, **439**, 568–571.
59. C. Housecroft and A. G. Sharpe, *Inorganic Chemistry*, Prentice Hall, 3rd edn., 2007.
60. K. F. Purcell and J. C. Kotz, *Inorganic Chemistry*, W B Saunders Co, 1977.
61. T. Wolfram, E. A. Kraut, and F. J. Morin, *Phys. Rev. B*, 1973, **7**, 1677–1694.
62. R. Zimmermann, P. Steiner, R. Claessen, F. Reinert, and S. Hüfner, *J. Electron Spectrosc.*, 1998, **96**, 179–186.
63. Ş. Ellialtioğlu and T. Wolfram, *Phys. Rev. B*, 1977, **15**, 5909–5911.
64. W. Luo, W. Duan, S. G. Louie, and M. L. Cohen, *Phys. Rev. B*, 2004, **70**, 214109.
65. J. B. Goodenough, *J. Appl. Phys.*, 1960, **31**, S359.
66. A. Spinelli, M. A. Torija, C. Liu, C. Jan, and C. Leighton, *Phys. Rev. B*, 2010, **81**, 155110.
67. S. Lenjer, O. F. Schirmer, H. Hesse, and T. W. Kool, *Phys. Rev. B*, 2002, **66**, 165106.
68. M. Jourdan, N. Blümer, and H. Adrian, *Eur. Phys J. B*, 2003, **33**, 25–30.
69. T. Ishihara, H. Matsuda, M. Azmi bin Bustam, and Y. Takita, *Solid State Ionics*, 1996, **86-88**, 197–201.
70. K. Huang, R. S. Tichy, and J. B. Goodenough, *J. Am. Cer. Soc.*, 1998, **81**, 2565–2575.
71. J. B. Goodenough, *Annu. Rev. Mater. Res.*, 2003, **33**, 91–128.
72. J. B. Goodenough, J. E. Ruiz-Diaz, and Y. S. Zhen, *Solid State Ionics*, 1990, **44**, 21–31.
73. J. Yan and M. Greenblatt, *Solid State Ionics*, 1995, **81**, 225–233.
74. N. Kim and C. P. Grey, *Science*, 2002, **297**, 1317–1320.
75. T. Ishihara, in *Perovskite Oxide for Solid Oxide Fuel Cells*, ed. T. Ishihara, Springer, 2009.
76. H. Iwahara, in *Perovskite Oxide for Solid Oxide Fuel Cells*, ed. T. Ishihara, Springer, 2009.
77. V. V. Kharton, F. M. B. Marques, and A. Atkinson, *Solid State Ionics*, 2004, **174**, 135–149.
78. J. A. Kilner, A. Berenov, and J. Rossiny, in *Perovskite Oxide for Solid Oxide Fuel Cells*, ed. T. Ishihara, Springer, 2009.
79. M. Mogensen, D. Lybye, N. Bonanos, P. V. Hendriksen, and F. W. Poulsen, *Solid State Ionics*, 2004, **174**, 279–286.
80. M. Yashima, in *Perovskite Oxide for Solid Oxide Fuel Cells*, ed. T. Ishihara, Springer, 2009.
81. M. Yashima, *Solid State Ionics*, 2008, **179**, 797–803.
82. D. Neagu and J. T. S. Irvine, *Chem. Mater.*, 2011, **23**, 1607–1617.
83. S. Tao and J. T. S. Irvine, *Nature Mater.*, 2003, **2**, 320–323.
84. M. J. Escudero, J. T. S. Irvine, and L. Daza, *J. Power Sources*, 2009, **192**, 43–50.

85. M. S. Islam and R. A. Davies, *J. Mater. Chem.*, 2004, **14**, 86.
86. H. Dai, H. He, P. Li, L. Gao, and C.-T. Au, *Catal. Today*, 2004, **90**, 231–244.
87. R. Liang, T. Nakamura, H. Kawaji, M. Itoh, and T. Nakamura, *Physica C*, 1990, **170**, 307–314.
88. K. Kishio, J. Shimoyama, T. Hasegawa, K. Kitazawa, and K. Fueki, *Jpn. J. Appl. Phys.*, 1987, **26**, L1228–L1230.
89. J. M. D. Coey, M. Viret, and S. von Molnár, *Adv. Phys.*, 1999, **48**, 167–293.
90. B. Dabrowski, R. Dybzinski, Z. Bukowski, O. Chmaissem, and J. D. Jorgensen, *J. Solid State Chem.*, 1999, **146**, 448–457.
91. R. Moos and K. H. Hardtl, *J. Am. Cer. Soc.*, 1997, **80**, 2549–2562.
92. R. Moos, S. Schöllhammer, and K. H. Härdtl, *Appl. Phys. A-Mater.*, 1997, **65**, 291–294.
93. K. Szot and W. Speier, *Phys. Rev. B*, 1999, **60**, 5909–5926.
94. K. Szot, M. Pawelczyk, J. Herion, C. Freiburg, J. Albers, R. Waser, J. Hulliger, J. Kwapulinski, and J. Dec, *Appl. Phys. A-Mater.*, 1996, **62**, 335–343.
95. K. Szot, W. Speier, G. Bihlmayer, and R. Waser, *Nat Mater*, 2006, **5**, 312–320.
96. D. N. Miller and J. T. S. Irvine, *J. Power Sources*, 2011, **196**, 7323–7327.
97. P. R. Slater, D. P. Fagg, and J. T. S. Irvine, *J. Mater. Chem.*, 1997, **7**, 2495–2498.
98. T. D. McColm and J. T. S. Irvine, *Solid State Ionics*, 2002, **152-153**, 615–623.
99. S. Hui and A. Petric, *Mater. Res. Bull.*, 2002, **37**, 1215–1231.
100. Q. X. Fu, S. B. Mi, E. Wessel, and F. Tietz, *J. Eur. Ceram. Soc.*, 2008, **28**, 811–820.
101. V. Vashook, L. Vasylechko, N. Trofimenko, M. Kuznecov, P. Otchik, J. Zosel, and U. Guth, *Journal of Alloys and Compounds*, 2006, **419**, 271–280.
102. V. Vashook, L. Vasylechko, H. Ullmann, and U. Guth, *Solid State Ionics*, 2003, **158**, 317–325.
103. P. Blennow, A. Hagen, K. Hansen, L. Wallenberg, and M. Mogensen, *Solid State Ionics*, 2008, **179**, 2047–2058.

3 EXPERIMENTAL

3.1 Sample preparation and processing

3.1.1 Solid state synthesis

The samples have been prepared by a modified solid state route developed in this study. The main steps of this process are given in Figure 3-1 and illustrated for the synthesis of the perovskite composition $La_{0.8}Ce_{0.1}Ni_{0.4}Ti_{0.6}O_3$. High purity precursors including oxides (La_2O_3, TiO_2, Ga_2O_3, Fe_2O_3 etc), carbonates ($SrCO_3$), or nitrates (*e.g.* $Ni(NO_3)_2*6H_2O$) were used in the appropriate stoichiometric ratios. The oxides and carbonates were dried at different temperatures depending on the nature of the precursor and weighed while hot (300-800 °C). All the precursors were quantitatively transferred to a beaker and mixed with acetone and a small amount (~0.05 wt.%) of non-aqueous Hypermer KD-1 (polyester/polyamide copolymer) dispersant (Figure 3-1 (a)). The mixture then undergoes ultrasonic probe mixing in order to break down agglomerates. This is carried out in a Hielscher UP200S ultrasonic probe operated at ~75% of maximum wave frequency and amplitude. The correlated action of the dispersant and ultrasonic waves led to the formation of a fine, stable dispersion (Figure 3-1 (b)) with better homogeneity compared to typical powder mixing in mortar and pestle used in solid state synthesis. The acetone is then evaporated under continuous stirring to ensure further homogenisation (Figure 3-1 (c)). After the acetone was completely evaporated (Figure 3-1 (d)), the content of the beaker was quantitatively transferred into a crucible (Figure 3-1 (e)) and calcined at 1000 °C for 12 h in order to decompose the carbonates, remove adsorbed water and start the nucleation of the perovskite phase. The aspect of the calcined powder in the case of the composition $La_{0.8}Ce_{0.1}Ni_{0.4}Ti_{0.6}O_3$ is shown in Figure 3-1 (f). After the calcination stage, while still warm, the powder consists exclusively of oxides, hence the weight of the powder at this stage should equal the mass of perovskite planned to be prepared. The deviation from the target value may provide a measure of how much powder was lost in various stages and estimate the implications on the overall stoichiometry accuracy of the final perovskite. Usually the target weight is

10 g of perovskite per batch. Out of this target weight, after the calcination step, weights in between 9.95-9.99 g were routinely obtained (see Figure 3-1 (g)).

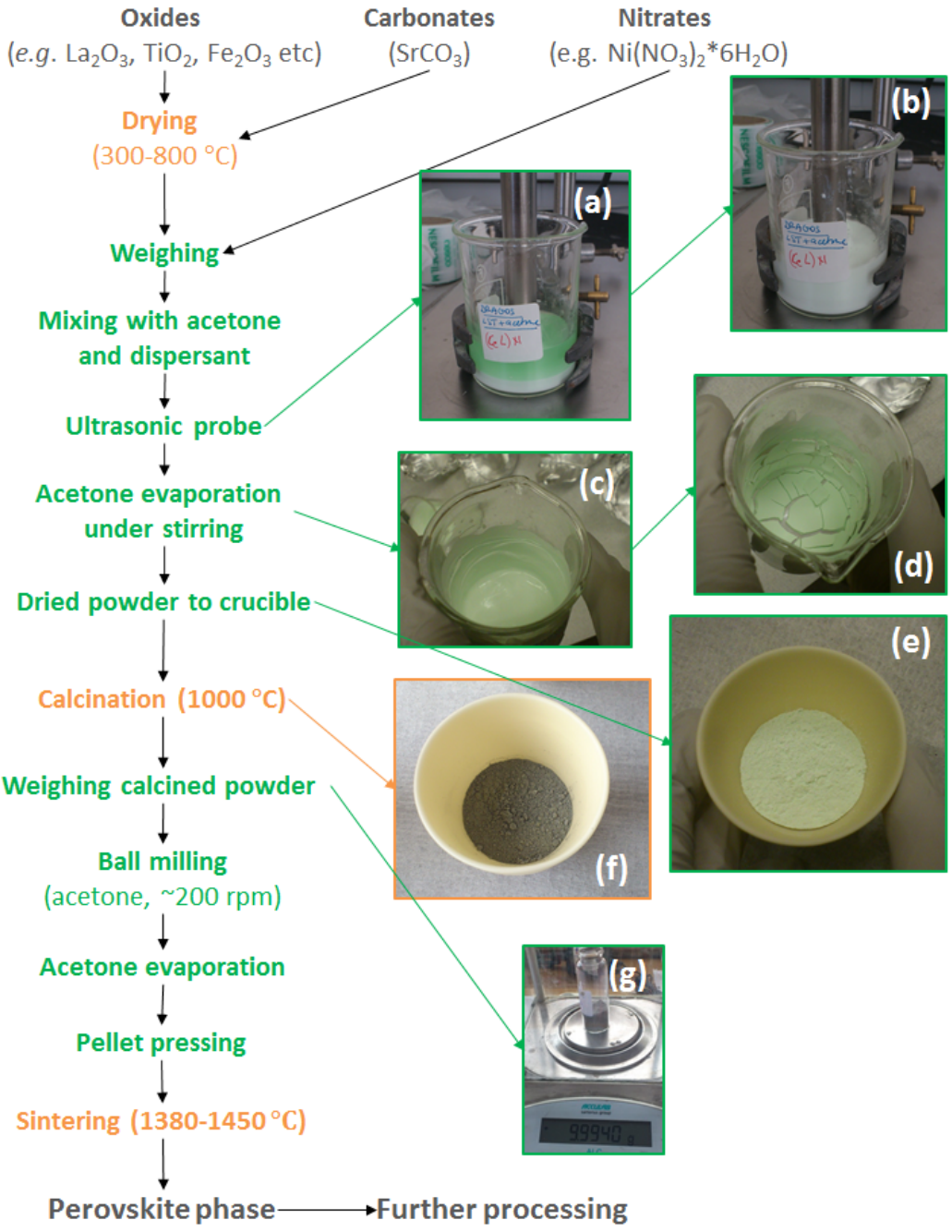

Figure 3-1 | Flow chart of the modified solid state synthesis used for the preparation of perovskites in this study (see text for details). Selected pictures at different stages, exemplified for the synthesis of $La_{0.8}Ce_{0.1}Ni_{0.4}Ti_{0.6}O_3$ are included as follows: (a) precursors mixture before ultrasonic probe mixing, (b) homogenous dispersion after ultrasonic probe mixing, (c) intermediate stage in the process of drying acetone, (d) final drying stage of acetone, (e) dried powder before calcination, (f) calcined powder, (g) weighing to confirm that target value of 10g of oxide was met.

After calcination the powder was milled for 1.5 h in a planetary ball mill at ~200 rpm. The resulting powder was pressed into dense pellets and fired for 12-14 h at 1380-1450 °C depending on the nature of the perovskite. The sintered pellets were crushed and ball-milled for 1 h, at ~200 rpm (for porous pellets) and subsequently at 1100 rpm (for inks), depending on the desired grain size.

3.1.2 Porous pellet preparation

Porous perovskite pellets were prepared by mixing the ball-milled powder with a pore-former (glassy carbon), followed by uniaxial pressing and firing at high temperature. Spherical glassy carbon was used as pore former since its particle size was similar to the particle size of the ball-milled perovskite, which is important for achieving uniform pore distribution and size (see Figure 3-2).

(a) (b)

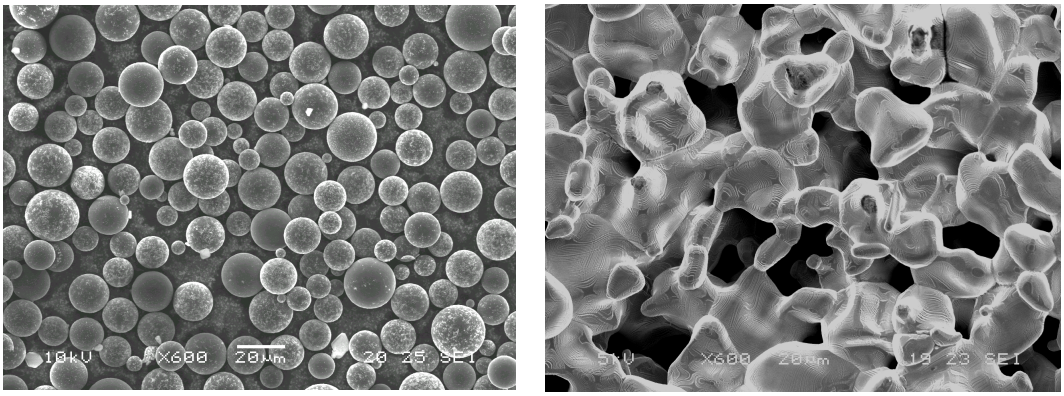

Figure 3-2 | (a) The morphology of spherical glassy carbon. (b) Example of perovskite microstructure obtained by using ~10% glassy carbon as poreformer. Sintering was done in air at 1380 °C, for 5 h. The sample was slowly heated to 900 °C at the rate of at 2 °C/min and then with at 5 °C/min up to the sintering temperature.

The initial perovskite-glassy carbon mixture (usually 15 wt.% of the latter) was prepared by homogenizing the two solid components in acetone with the help of a small amount (~0.1 mL) of *Zschimmer-Schwarz DECOFLUX WB 41* acting as surfactant. The "green" pellets were afterwards fired slowly to 1390 °C, in air. The initial ramp rate of the program was set at 2 °C/min until 900 °C, in order to allow a slow burn-out of the carbon, and thus create pores in the ceramic bodies. The samples were then heated with 5 °C/min to the

sintering temperature, 1380-1400 °C, and kept there for 4-6 h. This relative density of the perovskite pellets prepared in such a way was in between 50-70% depending on the cation composition and defect chemistry.

3.1.3 Button cell manufacture for SOEC testing

As-prepared perovskite powders were milled in a planetary ball-mill at 1000 rpm for 30 min using 1 mm diameter zirconia balls and isopropanol as milling medium. Fine powders with < 1 µm particle size and thus increased specific surface area (SSA) were obtained.

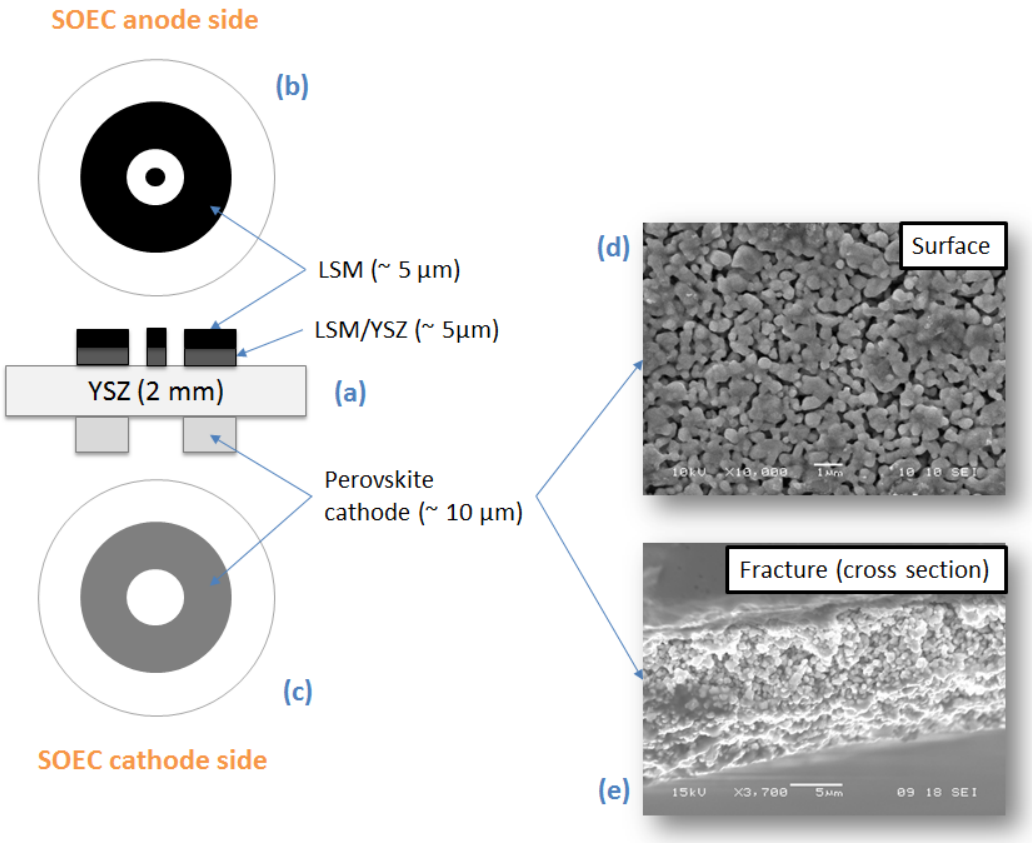

Figure 3-3 | Button cell used for SOEC testing: (a) cross-section view of the button cell showing the composition and thickness of each component, (b) top view of the anode geometry, (c) top view of the cathode geometry, (d) typical SEM micrograph of the cathode surface and (e) typical SEM micrograph of cathode cross-section.

The perovskite fine powders were then used to prepare inks to be used for screen printing. For this, the perovskite powder were dispersed in acetone using 2 wt.% Hypermer KD1 dispersant and an ultrasonic probe for 5-15 min. A vehicle was added to this dispersion in a ceramic: vehicle mass

ratio of 70:30 and the mixture was magnetically stirred at room temperature overnight to evaporate the acetone and yield the final ink. The vehicle consists of 5 wt.% poly (vinyl butyrate) in terpineol. Through a similar procedure inks for the screen-printing anodes were prepared using commercial YSZ and $(La_{0.8}Sr_{0.2})_{0.95}MnO_3$ (LSM) powders.

Titanate cathodes and LSM-based anodes were applied on either side of YSZ and co-sintered at 1000-1100 °C for 2 h. Gold paste was applied for current collection in a radial pattern and fired at 900 °C for 1 h to sinter it to the electrodes. The geometry of the screen printed electrodes and the microstructure of the perovskite cathode are shown in Figure 3-3.

3.1.4 Reduction

Reduction was carried out at various temperatures in a controlled atmosphere tubular furnace supplied with dry 5% H_2/Ar ($p_{O_2} \sim 10^{-20}$ atm) or humidified reducing gas ($\sim$3%H_2O in 5% H_2/Ar, $p_{O_2} \sim 10^{-16}$ atm). Oxidations were done in static air.

3.2 Characterisation methods and techniques

3.2.1 Powder X-ray diffraction

X-ray diffraction is a non-destructive technique that provides valuable information regarding the crystal structure and chemical composition of a given sample by recording the scattered intensity of an X-ray beam diffracting from the sample as a function of angle. A summary of the information contained within a powder X-ray diffraction pattern is given in Figure 3-4.

In this study, room temperature powder X-ray diffraction (XRD) was performed on a PANalytical Empyrean diffractometer operated in reflection mode using Cu-Kα1 radiation. The obtained XRD patterns were analysed with STOE Win XPOW software in order to determine the crystal structure and the cell parameter.

Rietveld refinement was also carried out for most samples, using FullProf software. Rietveld refinement associates variables to several structural parameters and attempts to solve them by minimising the difference between the calculated XRD pattern corresponding to a proposed model of the crystal structure and the XRD pattern obtained experimentally. Diffraction peaks were fitted using a pseudo-Voigt profile. Refined parameters included scale factor, background polynomial parameters or linear interpolation between a set of background points of refinable heights, unit cell parameters, peak profile parameters u, v, w and η (Lorentzian–Gaussian distribution), zero shift atomic positions and site occupancies. A general thermal factor was initially set for the whole pattern and in later stages refined and eventually converted to atomic isotropic displacement factors for individual atomic sites.

Visualisation of crystal structures was achieved using atomic positions obtained from Rietveld refinement in Crystal Maker® 2.6.4 for Windows.

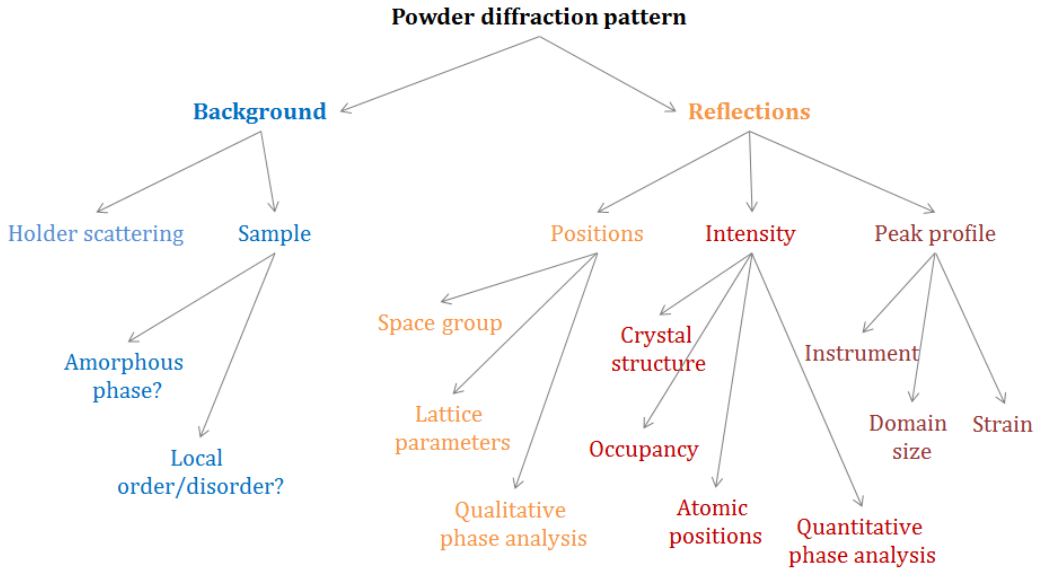

Figure 3-4 | Information that may be obtained from Rietveld refinement of powder XRD patterns. Adapted from reference [1].

3.2.2 Scanning electron microscopy

The microstructure of the samples was analysed using either a JEOL JSM-5600 Scanning Electron Microscope (SEM) or a JEOL JSM-6700 field emission

scanning electron microscope (FEG-SEM). Energy Dispersive X-Ray (EDX) analysis was also employed in some of the cases in order to confirm the stoichiometry of the samples.

3.2.3 Dilatometry

The thermal expansion of the selected pellets was investigated in various atmospheres using a Netzsch DIL 402 C instrument equipped with Proteus analysis software.

3.2.4 Thermogravimetry

Thermo-gravimetric analysis (TGA) is used to continuously record the weight change of a small quantity of sample throughout different thermal profiles carried out in various atmospheres. Here, TGA was performed using a Netzsch STA 449C instrument equipped with Proteus thermal analysis software.

Alternatively, thermogravimetry was studied on porous pellets of sufficiently high weight (~1 g) as to provide good weight measurement accuracy. Pellet thermogravimetry is done by measuring the mass of the pellets before and after certain high temperature processing steps, *i.e.* where only initial and final mass values are of interest. If intermediary weight changes are important the TGA is more suitable. However, if this is not the case, then pellet thermogravimetry may be an effective technique for investigating weight changes due to several advantages. First, it may be carried out in controlled atmosphere furnaces; hence several samples can be investigated simultaneously. This results in considerable time savings and provides direct comparison between samples that have experienced identical conditions. This also means that one of the samples can act as reference to provide consistency across measurements performed at different times. Also, samples of various sizes and geometry can be studied, which otherwise might not be accommodated by the small holders in TGAs.

3.2.5 DC Conductivity

The total conductivity of the samples was measured using a direct current (DC), van der Pauw setup.[2] In order to perform a measurement, 4 small strips of gold mesh were attached to the periphery of the sample using gold paste and fired at 850 °C for 1 h, to ensure the consolidation of the contacts. The sample was then mounted on the testing jig which is equipped with a thermocouple and a zirconia sensor in the vicinity of the sample so that the temperature of the sample and the oxygen partial pressure can be recorded. The jig was then inserted in a vertical, controlled atmosphere furnace. Low oxygen partial pressure was achieved by using a continuous flow of 5%H_2/Ar. In the van der Pauw method, the conductivity is given by the thickness of the sample *d*, the potential between two of the contacts U and the current passed between the other two, I:

$$\sigma = \frac{\ln 2}{\pi \cdot d} \cdot \frac{I}{U} \qquad \text{Eq. 3-1}$$

3.2.6 X-ray photoelectron spectroscopy

X-ray photoelectron spectroscopy (XPS) is a quantitative spectroscopic technique that measures the elemental composition and the chemical and electronic state of the elements on the surface of materials.[3] XPS spectra are collected by irradiating a material with a beam of X-rays in ultra-high vacuum (UHV) while simultaneously measuring the kinetic energy and number of electrons that escape from the surface of the material. XPS provides information only from the first 1 to 10 nm from the surface.

Here, XPS experiments were carried out using a Kratos Axis Ultra-DLD photoelectron spectrometer. Sasol Technology (UK) in St. Andrews is gratefully acknowledged for providing access to this facility. The data were analysed using CasaXPS software.

3.3 SOEC testing setup

For testing, a button cell prepared as described in section 3.1.3 was sealed to the alumina tube of the testing jig as shown in Figure 3-5, by using a high temperature ceramic adhesive paste. The jig was then placed within a vertical furnace.

The delivery of steam to the electrolysis cell cathode was based around a controlled evaporator mixer (CEM). The steam carrier gas consisted of a mixture of H_2 and N_2. The total flow rate and the ratio between the two gas components were controlled using gas mass flow controllers. H_2O flow was controlled by a valve integrated within the CEM that was linked *via* a feedback loop to a liquid flow meter. The controlled carrier gas and H_2O flows were mixed within the CEM and simultaneously heated to a temperature above the dew point to produce the $H_2O/H_2/N_2$ stream. The gas mixture was then directed to the electrolysis cell cathode through tubing heated to above the dew point in order to avoid condensation. The dew point of the vapour flow was monitored upstream and downstream of the electrolysis cell using dew point probes. At the anode side air was continuously passed over the LSM-based anode during electrolysis experiments.

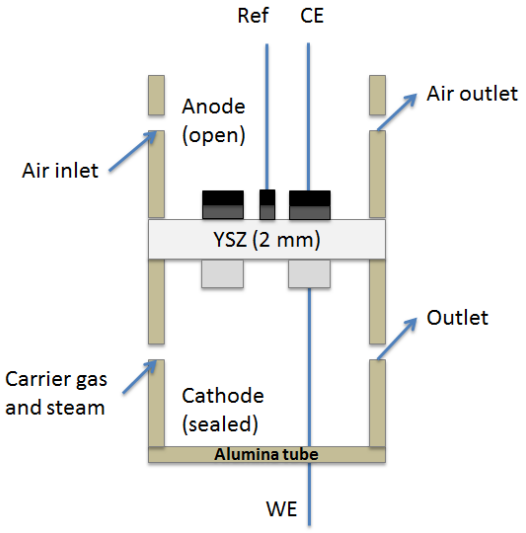

Figure 3-5 | Schematic view of the testing jig and (three) electrode configuration.

References

1. R. Dinnebier, *International union of crystallography newsletter*, 2001.
2. C. Kasl and M. J. R. Hoch, *Rev. Sci. Instrum.*, 2005, **76**, 033907.
3. A. R. West, *Basic Solid State Chemistry*, Wiley, 2nd edn., 1999.

4 CRYSTAL STRUCTURE OF THE STUDIED COMPOSITIONS

4.1 Studied systems in the context of defect chemistry

The most important compositions for this thesis are summarised in Figure 4-1, emphasizing the nonstoichiometry class to which they belong. Throughout this chapter the crystal structure of most of these compositions will be discussed in detail seeking to highlight the structural features that make deficient and excess perovskites so distinct, which will serve later on in the thesis to explain their properties and behaviour.

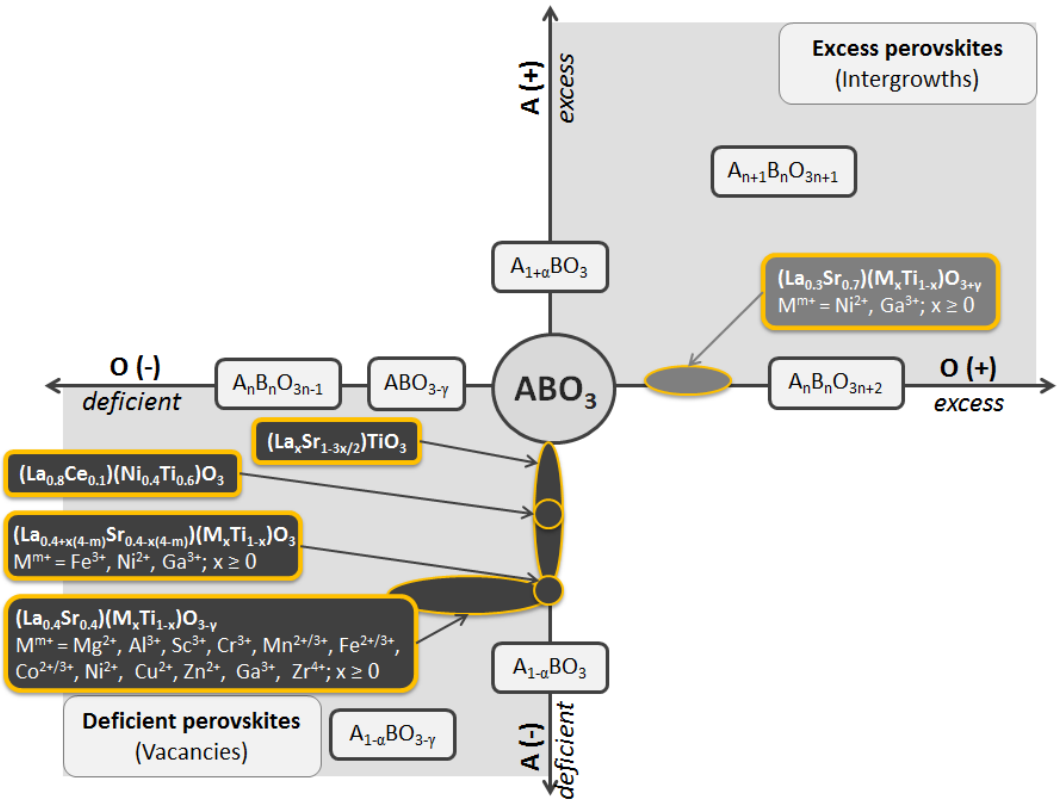

Figure 4-1 | Studied compositions in the perovskite nonstoichiometry landscape synthetically represented through a Cartesian plot.

It is worth noting from Figure 4-1 that two main 'parent' compositions served as starting point for the creation of new materials via doping, namely the A-site deficient $La_{0.4}Sr_{0.4}TiO_3$ and the oxygen excess $La_{0.3}Sr_{0.7}TiO_{3.15}$. As explained in Chapter 2, these were chosen to avoid the compositional domain where A-site vacancies or oxygen defects, respectively, start ordering[1–3] which would otherwise be expected to have a negative impact on properties (see Chapter 5).

Two entirely new compositional series were developed during this study, $La_{1.6-2x}Ce_{2x-0.7}Ni_xTi_{1-x}O_3$ and $La_{0.4+(4-m)\cdot x}Sr_{0.4-(4-m)\cdot x}M_x^{m+}O_3$ (M^{m+} = Ga^{3+}, Fe^{3+}, Ni^{2+}). The reasoning behind the chosen stoichiometry will also be explained during this chapter.

4.2 Methodology for solving the crystal structure from XRD

The method employed here for the identification of the crystal structure from XRD spectra is an algorithm-like approach based on various rules initially described by Glazer[4,5] and later improved by different groups.[6–15] However, before proceeding to the description of the above mentioned algorithm, some supporting concepts and conventions used in this algorithm need to be summarised.

As suggested in Chapter 2, the lowering of the symmetry compared to the ideal perovskite structure typically occurs due to octahedral tilting and/or cation displacement, which in turn are caused by size mismatch and electronic effects. When intergrowths are present, of course, additional lowering of the symmetry is to be expected, but within the perovskite blocks distortion can still be primarily described by octahedral tilting and cation displacement. As such, it is useful to refer to the way tilting occurs by the conventional *Glazer tilt nomenclature*. In this notation, the magnitude of the octahedral tilting with respect to the (pseudo)cubic x, y, z axes is designated by the letters a, b, c, while in-phase tilting, out-of-phase tilting and no tilting are denoted by $+, -$ and 0 superscripts, respectively. If tilting along two axes is equal in magnitude, then the corresponding letter is repeated to reflect this, *e.g.* equal titling along only the x and y axes is denoted aac. Thus, for example, the ideal cubic perovskite structure (*i.e.* no tilting) is designated by $a^0a^0a^0$; equal, out-of-phase tilting along the x and z axes with in-phase tilting along the y axis is denoted by $a^-b^+a^-$.

The lowering of the symmetry also means that the unit cell is no longer composed of a single ABO_3 unit, as in the case of the ideal perovskite cell (see,

for example, Fig 2-3 (Chapter 2), where each unit cell of the ideal ABO_3 structure contains 1 A ion, 8 'eighths' of B ions, *i.e.* one B ion, and 12 'quarters' of O^{2-} ions, *i.e.* 3 O^{2-} ions.). This is exemplified in Figure 4-2 for the simple cases of tetragonal and orthorhombic cell distortions caused by tilting. By making use of basic geometry, the tetragonal and the orthorhombic cells can be shown to be related to the primitive perovskite cell with cell parameter = a_p by $\sim \sqrt{2}a_p \times \sqrt{2}a_p \times 2a_p$ and $\sim 2a_p \times 2a_p \times 2a_p$, respectively. It follows that the tetragonal unit cell contains $\sqrt{2} \cdot \sqrt{2} \cdot 2 = 4$ ABO_3 units, and the orthorhombic cell $2 \cdot 2 \cdot 2 = 8$ ABO_3 units.

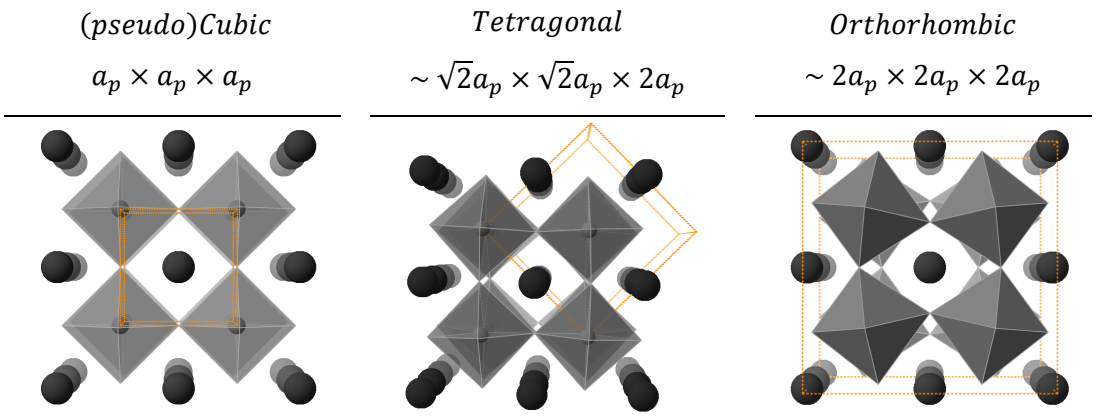

Figure 4-2 | Ideal and distorted perovskites and their pseudocubic (reduced) unit cell.

To allow for an easier comparison between unit cells of different symmetry, a *pseudocubic cell parameter*[xiii] is defined for these, as the lattice parameter of a hypothetical cubic cell that would contain only a single ABO_3 unit, similar to the archetype $SrTiO_3$ structure:

$$a_p = \sqrt[3]{\frac{V_{uc}}{n_{uc}}} \qquad \text{Eq. 4-1}$$

Where V_{uc} is the volume of the real (distorted cell) and n_{uc} is the number of ABO_3 units contained within it. Of course, for $SrTiO_3$ $a_p = a_{SrTiO_3} = 3.905$ Å,

[xiii] The pseudocubic cell parameter is sometimes referred to as the *reduced* cell parameter. This is because most perovskites have unit cells consisting of multiple ABO_3 units due to lower symmetry, and thus, by 'reducing/normalizing' the real cell to one a cell containing an ABO_3 unit, the size of perovskite cells with different symmetry can be compared.

but the vast majority of perovskites display, in fact, similar pseudocubic cell sizes, within the range 3.8 Å $< a_p <$ 4 Å.[16]

Finally, the procedure used for the identification of possible space groups and thus structure from diffraction patterns is summarised in Figure 4-3 and detailed below.

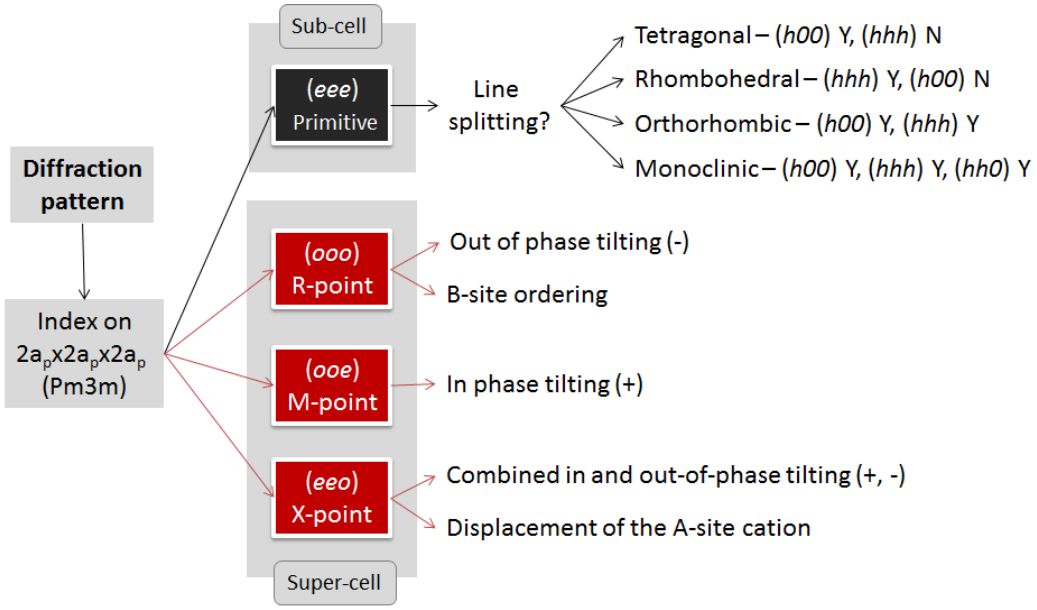

Figure 4-3 | Diagram summarising the main steps and information that can be gathered about a perovskite from its (neutron or X-ray) diffraction pattern.

The first step of this algorithm consists of indexing[xiv] the diffraction pattern on a cubic $Pm\bar{3}m$ perovskite cell having double *pseudocubic* cell parameters, $2a_p \times 2a_p \times 2a_p$ (henceforth Miller indices will be referred to based on a double cell, unless otherwise stated). Once Miller indexes have been assigned a_p can be estimated from an appropriate reflection by using the equation which relates the d-spacing of the chosen reflection to its corresponding Miller indices and to the cell parameter (for cubic systems):

$$d^2_{(hkl)} = \frac{a^2}{h^2 + k^2 + l^2} \qquad \text{Eq. 4-2}$$

[xiv] Indexing is done by assigning Miller indices to the peaks in the diffraction pattern according to the chosen symmetry.

The peak usually chosen for this is the one corresponding to the (220) reflection which is typically the strongest reflection arising from perovskites and occurs in the range $30° < 2\theta < 32°$. Thus, a_p can be calculated to be:

$$d_{(220)}^2 = \frac{\left(2a_p\right)^2}{2^2 + 2^2 + 0^2} = \frac{a_p^2}{2} \Longrightarrow a_p \approx \sqrt{2} \cdot d_{(220)} \qquad \text{Eq. 4-3}$$

The next step in the algorithm consists of classification and examination of the Miller indices which correspond to the observed reflections in the diffraction pattern. Miller indices having all even numbers, denoted here (*eee*) correspond to the fundamental perovskite peaks (also termed *sub-cell* peaks) and will always be present in the diffraction pattern of a perovskite.[15,17] The splitting or broadening of these reflections provides useful information for identifying the overall symmetry of the perovskite. Thus, if only the (h00) peaks are split but not the (hhh), *e.g.* (400) and (444) respectively, then this is should be interpreted as a tetragonal distortion.[15,13] On the contrary, if the (hhh) peaks are split, but (h00) are not, then the symmetry is most likely rhombohedral.[15,12] Splitting of both (h00) and (hhh) is typically cause by an orthorhombic distortion.[13] If (h00), (hhh) and (hh0) peaks are split, the distortion is monoclinic.[15,12] Reflections with all odd Miller indices (*ooo*) are an indication of out-of-phase tilting and/or B-site cation ordering. These are generally weak, especially in XRD spectra[xv].[9,8] Reflections with two odd and one even Miller indices (*ooe*) – in any permutations, *i.e.* (*eoo*), (*oeo*) – are only present when in-phase tilting occurs in the perovskite.[15,10] Reflections with two even and one odd Miller indices (*eeo*) – again, in various permutations – indicate combined in and out-of-phase tilting and displacement of A-site cations from their symmetry positions.[12]

With the type of tilting present and the expected symmetry determined, one can then choose the appropriate space group from a list initially proposed by

[xv] When looking for weak reflections it is best to represent the diffraction pattern as the square root of the intensity as a function of 2θ, $\sqrt{I} = f(2\theta)$, rather than the traditional linear $I = f(2\theta)$.

Glazer[5] and recently adjusted by Howard and Stokes,[10,9] the latter also being shown in Figure 4-4. The validity of the chosen space group is then verified through Rietveld refinement. This procedure was successfully applied for solving the crystal structure of various perovskite systems, as will be exemplified in the following subchapters. In order to visualise the crystal structures of the analysed compositions, the structural parameters available from refinements were used to generate associated crystal structures by using Crystal Maker® 2.6.4 for Windows.

Glazer tilt system	**Space group**	**Degrees of freedom**
Group A: *High-symmetry*		
$a^0a^0a^0$	$Pm\bar{3}m$	1
$a^-a^-a^-$	$R\bar{3}c$	3
$a^0a^0c^-$	$I4/mcm$	3
$a^0a^0c^+$	$P4/mbm$	3
$a^0b^-b^-$	$Imma$	6
$a^-b^+a^-$	$Pnma$	10
Group B: *Multiple A-site tilt systems*		
$a^+a^+a^+$	$Im\bar{3}$	3
$a^0b^-c^+$	$Cmcm$	10
$a^0b^+b^+$	$I4/mmm$	5
$a^+a^+a^-$	$P4_2/nmc$	8
Group C: L*ow symmetry tilt systems*		
$a^-a^-c^-$	$C2/c$	9
$a^0b^-c^-$	$C2/m$	10
$a^-b^-c^-$	$P\bar{1}$	18
$a^+b^-c^-$	$P2_1/m$	18
$a^+b^+c^+$	$Immm$	9

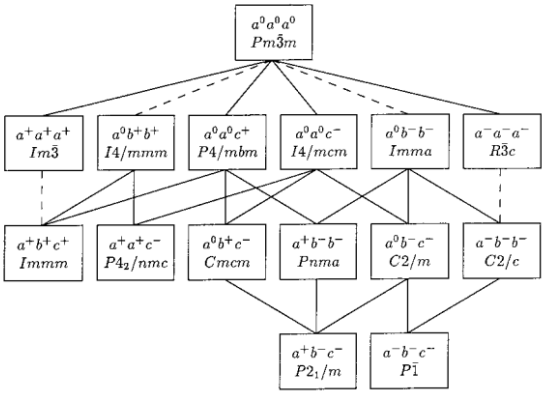

Figure 4-4 | Possible Glazer tilt systems and associated symmetries.[10,9]

4.3 Crystal structure of the $La_{0.4}Sr_{0.4}M_xTi_{1-x}O_{3-\gamma}$ compositions

Throughout this study different members belonging to the series $La_{0.4}Sr_{0.4}M_xTi_{1-x}O_{3-\gamma}$ were prepared by varying x and M. The plot in Figure 4-5 displays the XRD patterns of the members with a fixed doping level of $x = 0.06$, but having different B-site dopant, M = Mg, Al, Sc, Ti, Cr, Mn, Fe, Co, Ni, Cu, Zn, Ga and Zr.

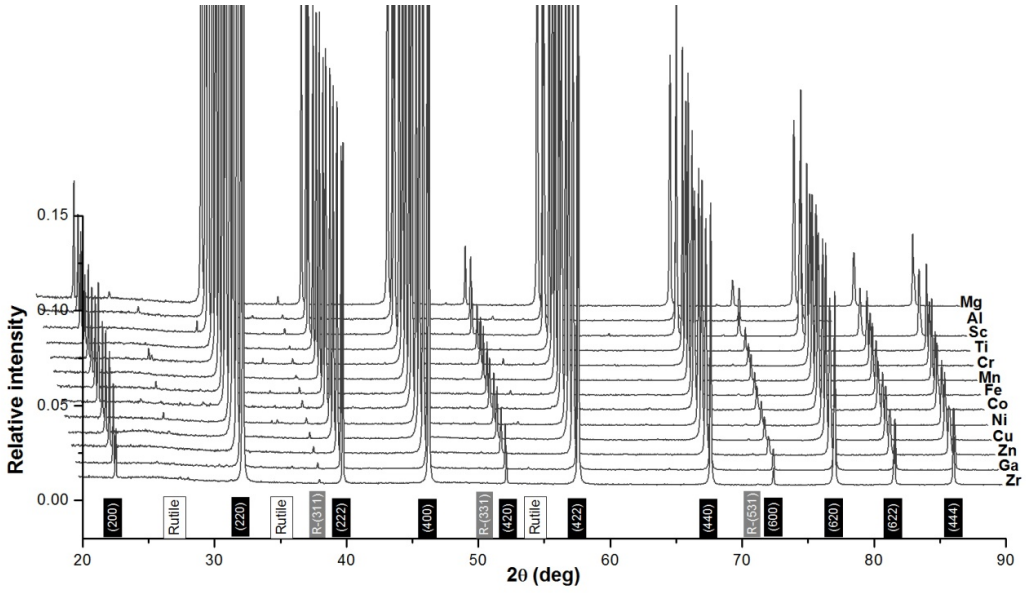

Figure 4-5 | Room temperature powder XRD patterns collected for the system $La_{0.4}Sr_{0.4}M_xTi_{1-x}O_{3-\gamma}$ with various M dopants. Miller indices of a double perovskite cell are also shown.

A first observation that emerges by examining Figure 4-5 is that not all of the formulated compositions resulted in a single-phase. Traces ($I_{relative}$ < 1%) of rutile (TiO_2) are clearly visible when M = Al, Cr, Fe and Ni. The reason for this behaviour is most likely related to the defects created upon doping as explained next.

Since all of the selected transition metals are typically stable in oxidation states less than 4+ (*i.e.* the charge of the host cation, Ti^{4+}), upon substitution the decrease in the average charge of the B-site is compensated by a decrease in the oxygen stoichiometry, denoted here γ and equal to $\frac{4-m}{2} \cdot x$ (m being the charge of the dopant, M^{m+}). Because the A-site deficient composition starts

formally as oxygen stoichiometric $La_{0.4}Sr_{0.4}TiO_3$, it ends up as oxygen deficient after substitution, $La_{0.4}Sr_{0.4}M_{0.06}Ti_{0.94}O_{3-\gamma}$.

Although the perovskite structure can accommodate a large number of vacancies on the A and O sublattices simultaneously, its natural tendency will always be to limit their number, since the fully stoichiometric structure is the most stable. In the scenario in which some of the TiO_2 from the initial formulation is not included in the final phase, a perovskite with slightly higher A and O-site occupancy and thus greater stability may form. Following the principle of minimising the number of starting defects in the perovskite lattice, new compositions were formulated by compensating B-site doping by balancing the charge among cations on the A-site rather than by oxide ion vacancies, but retaining the same 0.2 A-site deficiency. As expected, this resulted in rutile-free samples as will be shown in the next sub-chapter.

Turning now to the crystal structure of these compositions, indexing on a double cubic cell reveals two key aspects: (*1*) the (444) peak is a single peak for compositions with M = Ti, Mn, Zr suggesting these compositions share tetragonal symmetry, but split/broadened for the rest of the dopants pointing towards rhombohedral symmetry (see Figure 4-6), a conclusion supported also by the fact that peak (400) does not appear to be split in the latter cases (see Figure 4-6 and Figure 4-7); (*2*) only weak reflections indicative of out-of-phase tilting are present *i.e.* (311), (331) and (531) – see Figure 4-5. Thus, the most likely space groups chosen based on the above mentioned observations from the list in Figure 4-4 are tetragonal $I4/mcm$ for the samples containing M = Ti, Mn, Zr, and rhombohedral $R\bar{3}c$ for the samples containing the rest of the doped elements, M = Mg, Al, Sc, Cr, Fe, Co, Ni, Cu, Zn, Ga.

Rietveld refinement showed that the proposed tetragonal model fitted very well for the corresponding compositions (M = Ti, Mn, Zr). This is exemplified for the $La_{0.4}Sr_{0.4}TiO_3$ composition in Figure 4-8 while highlighting in particular the good fitting of the (444) peak by the tetragonal model. As

anticipated from the weak intensity of the R-type (311) reflection, this perovskite only shows slight tilting. Moreover, as the space group implies, tilting only occurs along the *z* axis.

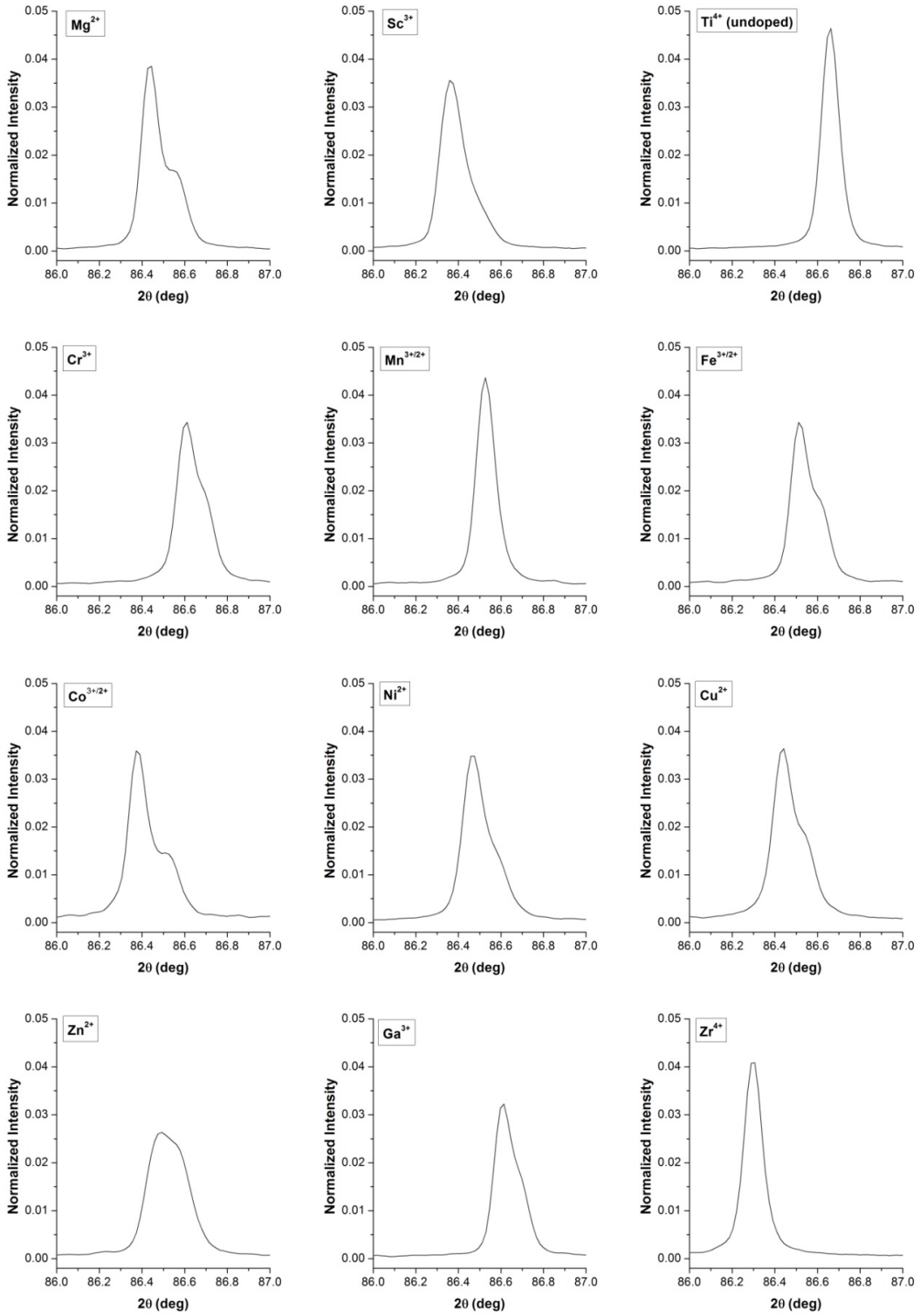

Figure 4-6 | Peak (444) from the patterns shown in Figure 4-5.

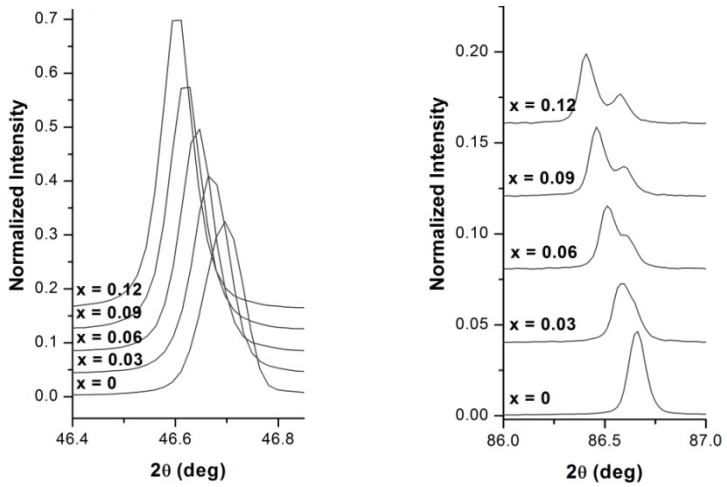

Figure 4-7 | Details of peaks (400) and (444) from powder XRD patterns collected for the series $La_{0.4}Sr_{0.4}Fe_xTi_{1-x}O_{3-\gamma}$.

Rietveld refinement of $La_{0.4}Sr_{0.4}TiO_3$

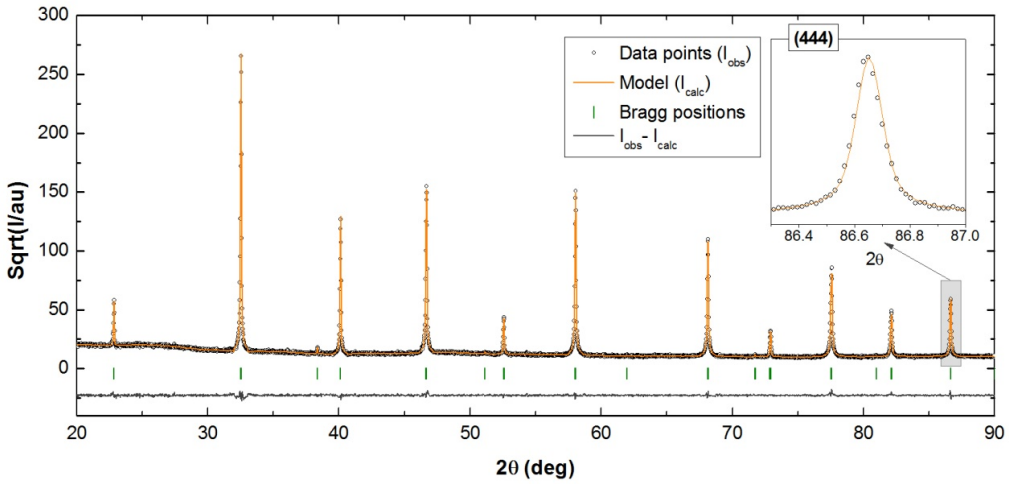

Crystal structure – $I4/mcm$ $(a^0a^0c^-)$

Perspective view | Projection along z | Projection along y

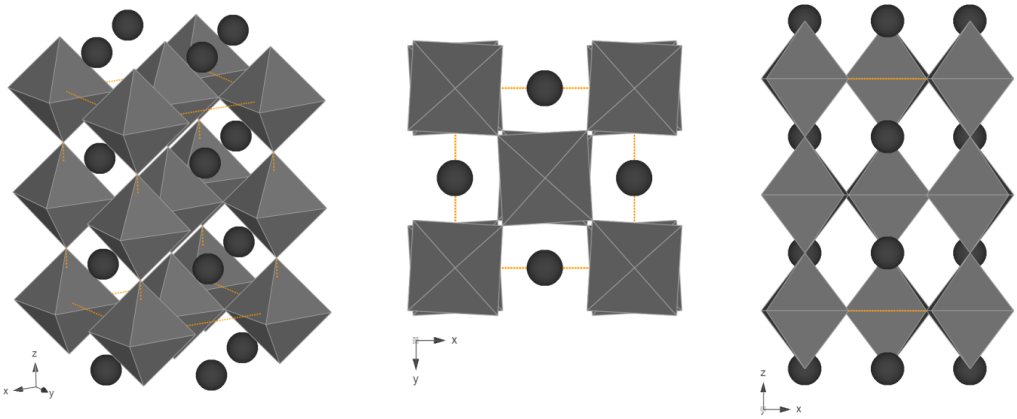

Figure 4-8 | Rietveld refinement and visualisation of associated crystal structure for $La_{0.4}Sr_{0.4}TiO_3$. The fitting of the (444) peak and projections showing out-of-phase tilting are highlited.

When applied to the rest of the compositions, the rhombohedral model yielded satisfactory fits, which, however, became rather unstable for samples with greater distortion. Moreover, the rhombohedral $R\bar{3}c$ space group seemed incapable to model accurately certain peaks, a characteristic which is most visible for the (440) peak shown in Figure 4-9.

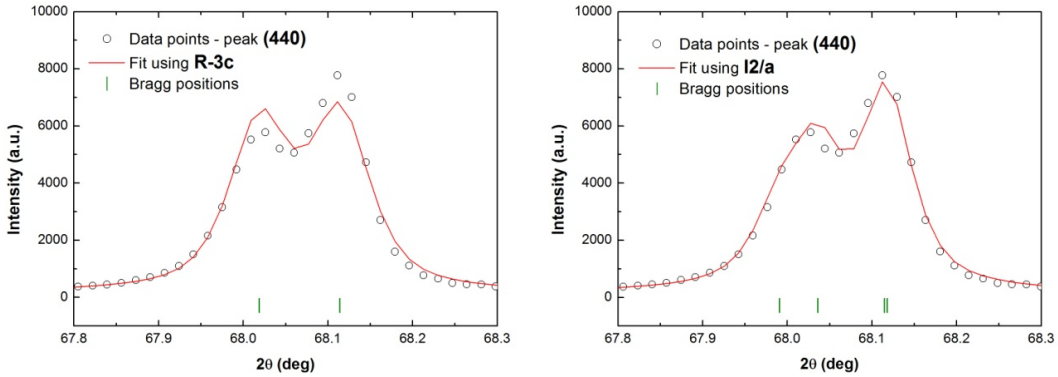

Figure 4-9 | Comparison between Rietveld refinements conducted on $La_{0.52}Sr_{0.28}Ni_{0.06}Ti_{0.94}O_3$ using two different space groups: the rhombohedral $R\bar{3}c$ and the monoclinic $I2/a$.

The obvious alternative to this space group would be the lower symmetry orthorhombic $Imma$ (see Figure 4-4). However, all attempts to refine the data using this space group resulted in the model either crashing or yielding unsatisfactory fits. This leads to the observation that the entire approach of trying to fit a space group with $a^0b^-b^-$ type tilting might be flawed since the $R\bar{3}c$ group which assumes tilting with respect to all axes, $a^-a^-a^-$, fitted the data much better. Thus, the space group $I2/a$ ($\equiv C2/c$) with out of phase tilting along all axes, $a^-a^-c^-$ was used. The refinements were all stable and yielded very good fits and solved the problem of the fitting of the (440) peak seen when the $R\bar{3}c$ space group was used (see Figure 4-9). A refinement performed with the $I2/a$ space group model is exemplified in Figure 4-10 for $La_{0.4}Sr_{0.4}Co_{0.06}Ti_{0.94}O_{3-\gamma}$ which shows higher distortion.

For this sample the slightly higher residuals found for the (400) peak compared to the other peaks might be due to preferred orientation; this will be investigated in a future study. The higher distortion is seen from the splitting of the (444) peak but also from the higher intensity of the R-type

(311) peak. This reflects into considerable more tilting along the x axis, but also along other axis, as shown in the crystal structure of this composition depicted in Figure 4-10.

The results of the Rietveld refinement (cell parameters, pseudocubic cell parameters, Rietveld fit parameters) for most of the compositions belonging to the series $La_{0.4}Sr_{0.4}M_xTi_{1-x}O_{3-\gamma}$ are listed in Table 4-2 while their appearance in powder form can be seen in Table 4-1.

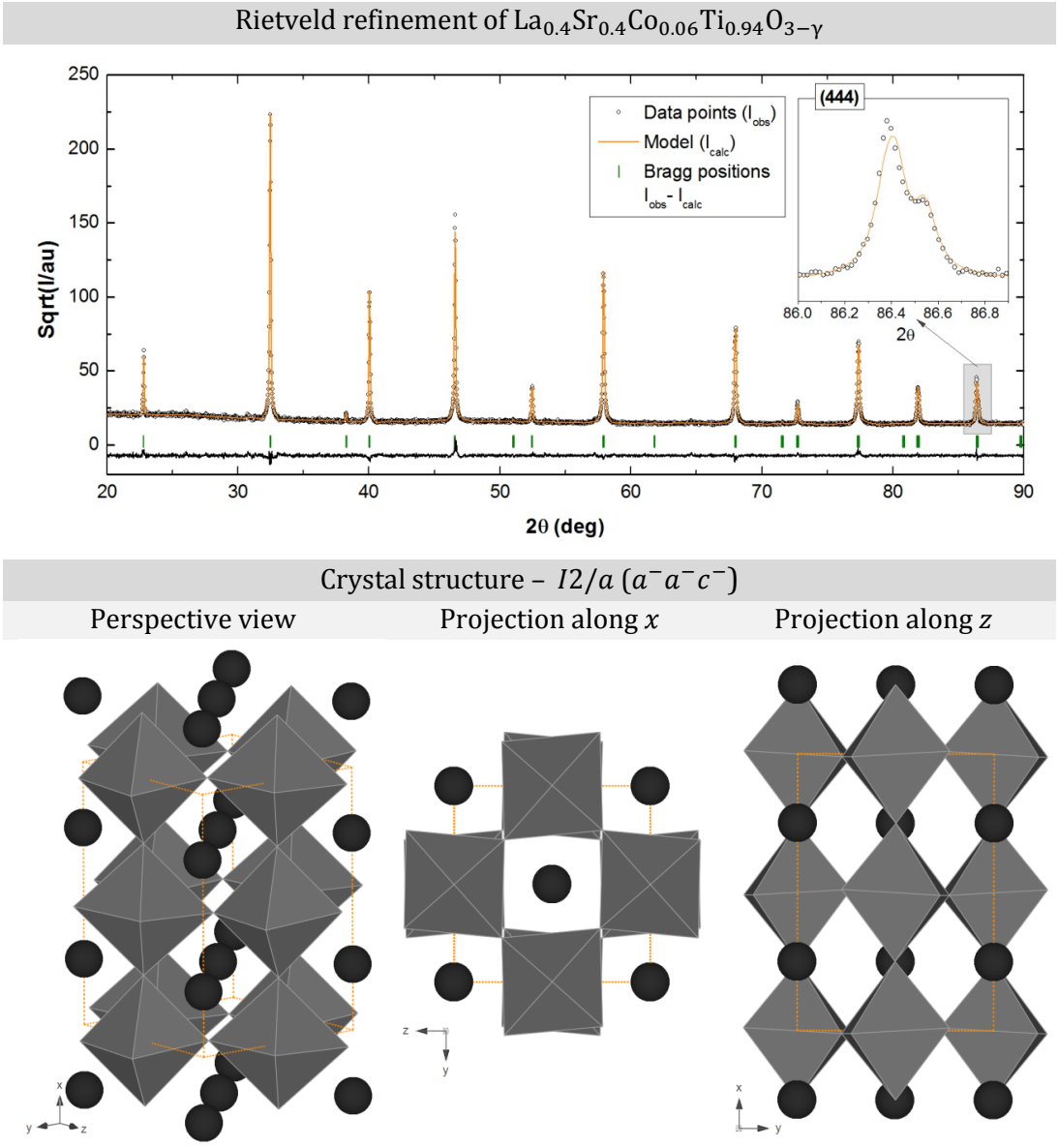

Figure 4-10 | Rietveld refinement and visualisation of associated crystal structure for $La_{0.4}Sr_{0.4}Co_{0.06}Ti_{0.94}O_{3-\gamma}$. The fitting of the (444) peak and projections showing out-of-phase tilting are highlited.

Table 4-1 | Phase purity, crystal structure and powder colour of the series $La_{0.4}Sr_{0.4}M_xTi_{1-x}O_{3-\gamma}$, for various M dopants.

Dopant	Space group	Sec. Phase (<1%)	Colour (powder)	Dopant	Space group	Sec. Phase (<1%)	Colour (powder)
Mg	$I2/a$	-		**Fe**	$I2/a$	TiO_2	
Al	$I2/a$	TiO_2		**Co**	$I2/a$	-	
Sc	$I2/a$	Sc_2O_3		**Ni**	$I2/a$	TiO_2	
Ti	$I4/mcm$	-		**Cu**	$I2/a$	-	
Cr	$I2/a$	TiO_2		**Zn**	$I2/a$	-	
Mn	$I4/mcm$	-		**Ga**	$I2/a$	-	

Table 4-2 | Results of the Rietveld refinements performed on various members of the series $La_{0.4}Sr_{0.4}M_xTi_{1-x}O_{3-\gamma}$.

Dopant	Space group	Cell parameters (Å)	β (°)	a_p (Å) (±0.0002)	Rietveld fit parameters
Mg (x = 0.06)	$I2/a$	a = 7.7879(1) b = 5.5143(1) c = 5.5076(1)	90.055(1)	3.8959	R_p= 5.2, R_{wp} = 7.2, R_e = 5.2, χ^2 = 1.91
Al (x = 0.06)	$I2/a$	a = 7.7759(1) b = 5.4938(5) c = 5.4943(6)	90.037(4)	3.8856	R_p = 5.8, R_{wp}= 7.6, R_e = 5.0, χ^2 = 2.26
Sc (x = 0.06)	$I2/a$	a = 7.8038(2) b = 5.5151(1) c = 5.5100(1)	90.043(3)	3.8993	R_p= 6.7, R_{wp} = 9.2, R_e = 5.0, χ^2 = 3.40
Ti	$I4/mcm$	a = b = 5.49833(6) c = 7.7819(1)	90.000	3.8889	R_p=4.7, R_{wp}=6.4, R_e=5.1, χ^2=1.60
Cr (x = 0.06)	$I2/a$	a = 7.7825(2) b = 5.5000(1) c = 5.4985(1)	90.061(2)	3.8895	R_p =5.7, R_{wp}= 7.8, R_e = 5.5, χ^2 = 2.12
Mn	$I4/mcm$	a = b = 5.50761(7)	90.000	3.8935	R_p = 6.3, R_{wp}=8.3,

(x = 0.06)		c = 7.7832(1)			R_e = 5.5, χ^2 = 2.28
Fe (x = 0.03)	$I2/a$	a = 7.7855(1) b = 5.5014(1) c = 5.5008(1)	90.044(2)	3.8908	R_p = 6.4, R_{wp}=8.2, R_e = 5.3, χ^2 = 2.43
Fe (x = 0.06)	$I2/a$	a = 7.7889(2) b = 5.5050(1) c = 5.5032(1)	90.068(1)	3.8928	R_p = 5.8, R_{wp}= 7.6, R_e = 5.0, χ^2 = 2.26
Fe (x = 0.09)	$I2/a$	a = 7.7918(2) b = 5.5080(1) c = 5.5049(1)	90.087(1)	3.8944	R_p = 5.7, R_{wp}= 7.7, R_e = 4.8, χ^2 = 2.63
Fe (x = 0.12)	$I2/a$	a = 7.7955(2) b = 5.5111(1) c = 5.5072(1)	90.105(1)	3.8963	R_p = 7.1, R_{wp}= 9.5, R_e = 4.7, χ^2 = 4.02
Co (x = 0.06)	$I2/a$	a = 7.7965(2) b = 5.5114(1) c = 5.5080(1)	90.092(1)	3.8967	R_p = 5.4, R_{wp}= 7.1, R_e = 4.8, χ^2 = 2.21
Ni (x = 0.06)	$I2/a$	a = 7.7926(2) b = 5.5085(2) c = 5.5058(2)	90.067(2)	3.8949	R_p = 6.3, R_{wp}= 8.6, R_e = 5.2, χ^2 = 2.68
Cu (x = 0.06)	$I2/a$	a = 7.7940(2) b = 5.5093(1) c = 5.5071(1)	90.071(1)	3.8956	R_p = 5.5, R_{wp}= 7.1, R_e = 4.7, χ^2 = 2.30
Zn (x = 0.03)	$I4/mcm$	a = b = 5.5018(1) c = 7.7846(1)	90.000	3.8910	R_p = 5.9, R_{wp}= 7.7, R_e = 6.1, χ^2 = 1.62
Zn (x = 0.06)	$I2/a$	a = 7.7905(3) b = 5.5069(3) c = 5.5045(3)	90.059(4)	3.8939	R_p = 5.2, R_{wp}= 7.1, R_e = 5.5, χ^2 = 1.63
Zn (x = 0.09)	$I2/a$	a = 7.7979(3) b = 5.5130(2) c = 5.5095(2)	90.100(2)	3.8977	R_p = 6.2, R_{wp}= 8.2, R_e = 5.7, χ^2 = 2.00
Zn (x = 0.12)	$I2/a$	a = 7.8044(3) b = 5.5170(2) c = 5.5128(2)	90.128(2)	3.9005	R_p = 7.8, R_{wp}= 10.6, R_e = 5.8, χ^2 = 3.44
Ga (x = 0.03)	$I2/a$	a = b = 5.49971(8) c = 7.7817(1)	90.000	3.8895	R_p = 5.7, R_{wp}= 7.6, R_e = 5.3, χ^2 = 2.08
Ga (x = 0.06)	$I2/a$	a = 7.7768(1) b = 5.50519(8) c = 5.49999(7)	90.035(1)	3.8899	R_p = 5.2, R_{wp}= 6.8, R_e = 5.1, χ^2 = 1.85
Ga (x = 0.09)	$I2/a$	a = 7.7769(1) b = 5.50583(9) c = 5.49966(9)	90.047(1)	3.8902	R_p = 6.5, R_{wp}= 8.7, R_e = 5.3, χ^2 = 2.78
Zr (x = 0.06)	$I4/mcm$	a = b = 5.51636(7) c = 7.8104(1)	90.000	3.9022	R_p = 4.9, R_{wp}= 6.7, R_e = 4.9, χ^2 = 1.83

4.4 Crystal structure of $La_{0.4+x(4-m)}Sr_{0.4-x(4-m)}M_x^{m+}Ti_{1-x}O_3$ compositions

As briefly explained in the previous subchapter, the series in which B-site doping was compensated by balancing the cation charge on the A-site rather than by oxygen vacancies, $La_{0.4+x\cdot(4-m)}Sr_{0.4-x\cdot(4-m)}M_x^{m+}Ti_{1-x}O_3$, was devised to avoid coexistence of a significant number of oxide ion vacancies and that of the already numerous A-site vacancies, which in turn would be expected to greatly influence the stability of the B-site dopant in the perovskite lattice.

This stoichiometry was derived by considering a perovskite with generic stoichiometry $La_xSr_yM_z^{m+}Ti_{1-z}O_t$ on which constraints are applied to reflect the desired compositional characteristics through the variables x, y, and t. Thus, the new perovskite should retain the 0.8 A-site composition but still be oxygen stoichiometric, meaning that $x + y = 0.8$ and $t = 3$. Including the charge balance equation, it comes to the following system of equations to be solved:

$$\begin{cases} 3 \cdot x + 2 \cdot y + m \cdot z + 4 \cdot (1 - z) = 2 \cdot t & \text{Eq. 4-4} \\ x + y = 0.8 & \text{Eq. 4-5} \\ t = 3 & \text{Eq. 4-6} \end{cases}$$

This is an equation system with three equations and four unknown variables which can be solved with respect to one variable, *e.g.* the B-site doping level, z. This leads to the following expressions:

$$\begin{cases} x = 0.4 + (4 - m) \cdot z & \text{Eq. 4-7} \\ y = 0.4 - (4 - m) \cdot z & \text{Eq. 4-8} \end{cases}$$

Thus, by inserting equations Eq. 4-7 and Eq. 4-8 into the generic starting formula, $La_xSr_yM_z^{m+}Ti_{1-z}O_t$, the new stoichiometry can be written as:

$$La_{0.4+(4-m)\cdot x}Sr_{0.4-(4-m)\cdot x}M_x^{m+}Ti_{1-x}O_3$$

Which can be further generalized to include parameters for A-site deficiency as well as B-site doping:

$$La_{x+(4-m)\cdot y}Sr_{1-3x/2-(4-m)\cdot y}M_y^{m+}Ti_{1-y}O_3$$

Figure 4-11 compares XRD patterns of previous stoichiometries ($La_{0.4}Sr_{0.4}Fe_xTi_{1-x}O_{3-\gamma}$ and $La_{0.4}Sr_{0.4}Ni_xTi_{1-x}O_{3-\gamma}$) to the newly developed ones ($La_{0.4+x}Sr_{0.4-x}Fe_xTi_{1-x}O_3$ and $La_{0.4+2x}Sr_{0.4-2x}Ni_xTi_{1-x}O_3$). From this figure it is obvious that none of the newly formulated compositions contain rutile (at least to the resolution of the XRD employed) demonstrating the effectiveness of the approach of rethinking stoichiometry on the basis of type and number of defects in the perovskite lattice to achieve full incorporation of dopants.

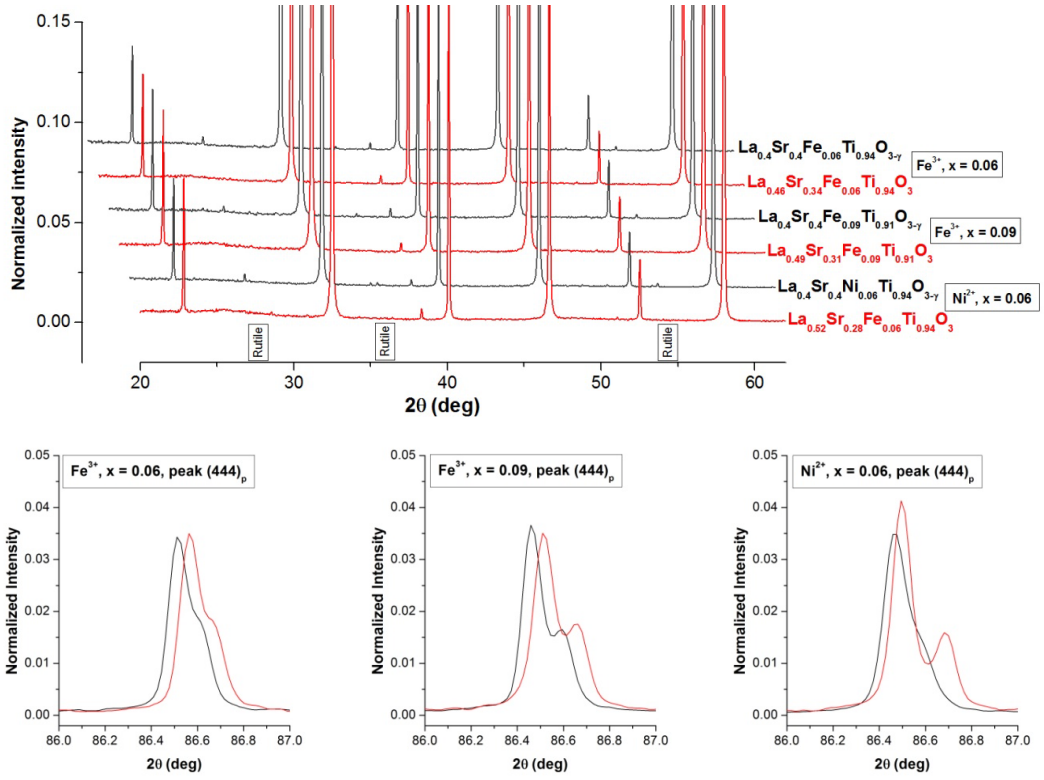

Figure 4-11 | Comparison between XRD patterns of new compositions belonging to the series $La_{0.4+x}Sr_{0.4-x}Fe_xTi_{1-x}O_3$ and $La_{0.4+2x}Sr_{0.4-2x}Ni_xTi_{1-x}O_3$ as opposed to the 'older' ones containing traces of rutile, $La_{0.4}Sr_{0.4}Fe_xTi_{1-x}O_{3-\gamma}$ and $La_{0.4}Sr_{0.4}Ni_xTi_{1-x}O_{3-\gamma}$.

Structurally, however, the new compositions are similar to the previous ones, displaying the same type of distortion (see *e.g.* the (444) peak in Figure 4-11) and thus sharing the same $I2/a$ space group (see Table 4-3 and Figure 4-12). The results of the Rietveld refinement (cell parameters, pseudocubic cell parameters, Rietveld fit parameters) for most of the compositions belonging

to the series $La_{0.4+(4-m)\cdot x}Sr_{0.4-(4-m)\cdot x}M_x^{m+}Ti_{1-x}O_3$ are summarised in Table 4-3, while one Rietveld refinement is exemplified in Figure 4-12 for $La_{0.52}Sr_{0.28}Ni_{0.06}Ti_{0.94}O_3$.

Table 4-3 | Results of the Rietveld refinements performed on various members of the series $La_{0.4+(4-m)\cdot x}Sr_{0.4-(4-m)\cdot x}M_x^{m+}Ti_{1-x}O_3$, where M^{m+} = Fe^{3+}, Ni^{2+} and Ga^{3+}.

Dopant	Space group	Cell parameters (Å)	β (°)	a_p (Å) (±0.0001)	Rietveld fit parameters
Fe (x = 0.06) $La_{0.46}Sr_{0.34}Fe_{0.06}Ti_{0.94}O_3$	$I2/a$	a = 7.7787(1) b = 5.5074(1) c = 5.5010(1)	90.044(1)	3.8911	R_p = 4.9, R_{wp}= 6.4, R_e = 4.9, χ^2 = 1.72
Fe (x = 0.09) $La_{0.49}Sr_{0.31}Fe_{0.09}Ti_{0.91}O_3$	$I2/a$	a = 7.7808(1) b = 5.51058(9) c = 5.5023(1)	90.057(1)	3.8925	R_p = 5.7, R_{wp}= 7.7, R_e = 4.8, χ^2 = 2.63
Ni (x = 0.06) $La_{0.52}Sr_{0.28}Ni_{0.06}Ti_{0.94}O_3$	$I2/a$	a = 7.7820(1) b = 5.5106(1) c = 5.5017(1)	90.086(1)	3.8926	R_p = 4.8, R_{wp}= 6.3, R_e = 4.7, χ^2 = 1.82
Ga (x = 0.03) $La_{0.43}Sr_{0.37}Ga_{0.03}Ti_{0.97}O_3$	$I2/a$	a = 7.7729(2) b = 5.5019(1) c = 5.4983(1)	90.013(1)	3.8883	R_p = 6.4, R_{wp}= 8.3, R_e = 5.5, χ^2 = 2.34
Ga (x = 0.06) $La_{0.46}Sr_{0.34}Ga_{0.06}Ti_{0.94}O_3$	$I2/a$	a = 7.7725(1) b = 5.5025(1) c = 5.4971(1)	90.036(1)	3.8881	R_p = 6.5, R_{wp}= 8.4, R_e = 5.3, χ^2 = 2.76
Ga (x = 0.09) $La_{0.49}Sr_{0.31}Ga_{0.09}Ti_{0.91}O_3$	$I2/a$	a = 7.7722(1) b = 5.5029(1) c = 5.4959(1)	90.053(1)	3.8878	R_p = 6.5, R_{wp}= 8.7, R_e = 5.3, χ^2 = 2.78
Ga (x = 0.12) $La_{0.52}Sr_{0.28}Ga_{0.12}Ti_{0.88}O_3$	$I2/a$	a = 7.7718(2) b = 5.5028(1) c = 5.4950(1)	90.073(1)	3.8875	R_p = 5.5, R_{wp}= 7.5, R_e = 5.3, χ^2 = 1.97
Ga (x = 0.15) $La_{0.55}Sr_{0.25}Ga_{0.15}Ti_{0.85}O_3$	$I2/a$	a = 7.7713(2) b = 5.5028(1) c = 5.4938(1)	90.089(1)	3.8871	R_p = 5.7, R_{wp}= 7.6, R_e = 5.6, χ^2 = 1.84
Ga (x = 0.18) $La_{0.58}Sr_{0.22}Ga_{0.18}Ti_{0.82}O_3$	$I2/a$	a = 7.7706(2) b = 5.5028(1) c = 5.4926(1)	90.104(1)	3.8868	R_p = 7.0, R_{wp}= 7.6, R_e = 5.8, χ^2 = 2.52

Since the new stoichiometry implies that some of the larger Sr^{2+} ions are replaced by the slightly smaller La^{3+} ions and at the same time the larger M^{m+} ions (Fe^{3+}, Ni^{2+} and Ga^{3+}) replace some of the smaller Ti^{4+}, it follows that the average A-site cation should become undersized for the cuboctahedral cavity and thus more pronounced distortion and tilting should be observed. This is clearly demonstrated by the insets of Figure 4-11 which compare peak (444)

for samples having the same dopant, M^{m+}, but belonging to the two different series, $La_{0.4+(4-m)\cdot x}Sr_{0.4-(4-m)\cdot x}M_x^{m+}Ti_{1-x}O_3$ and $La_{0.4}Sr_{0.4}M_x^{m+}Ti_{1-x}O_{3-\gamma}$. As expected from cation size considerations, among the Fe and Ni-doped samples, $La_{0.52}Sr_{0.28}Ni_{0.06}Ti_{0.94}O_3$ shows the most significant distortion and tilting as can be seen from the Rietveld refinement and corresponding structure presented in Figure 4-12. The figure also emphasizes the considerable tilting along both the x and z axis.

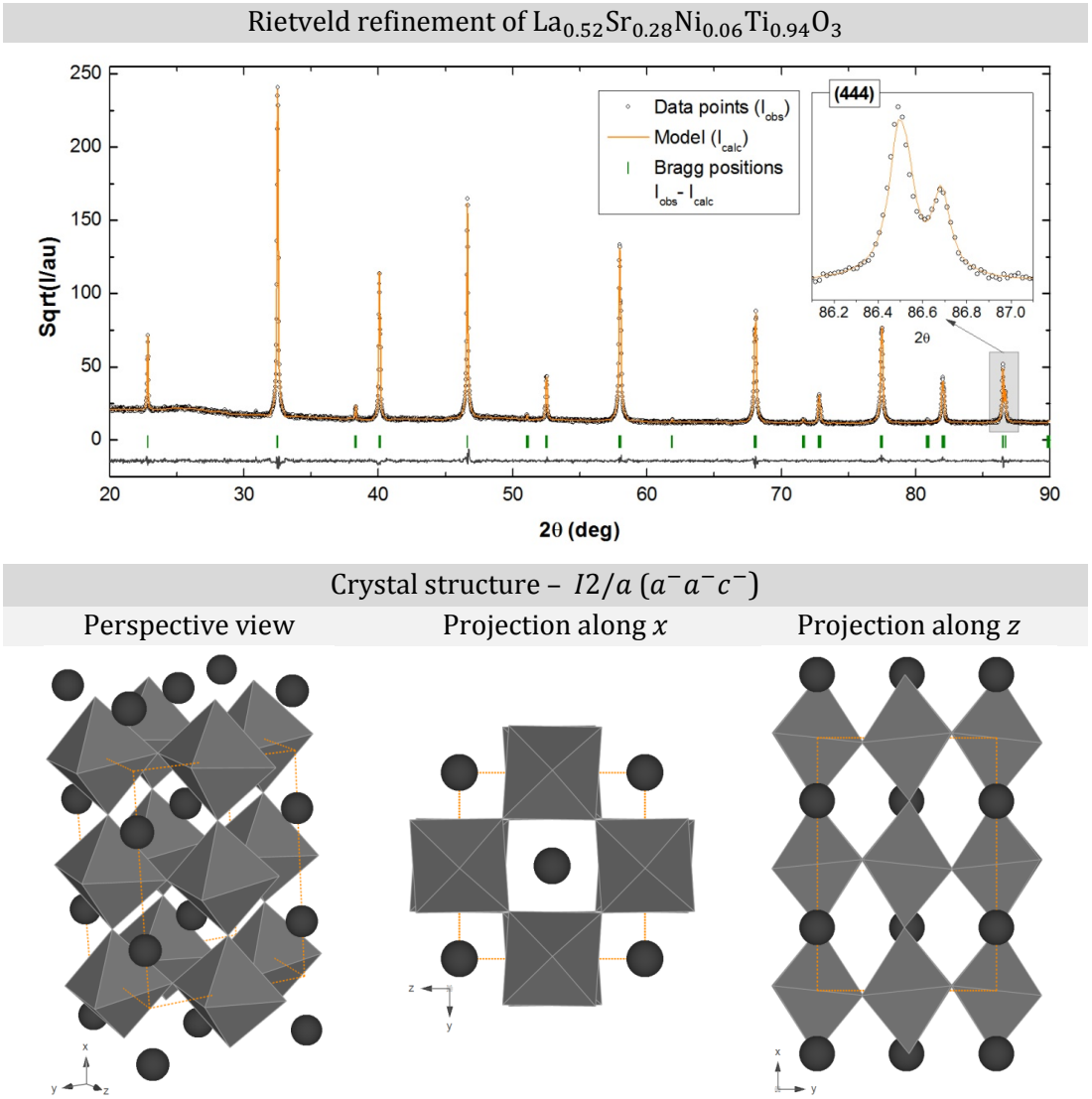

Figure 4-12 | Rietveld refinement and visualisation of associated crystal structure for $La_{0.52}Sr_{0.28}Ni_{0.06}Ti_{0.94}O_3$. The fitting of the (444) peak and projections showing out-of-phase tilting are highlited.

The evolution of distortion as doping level increases is better exemplified by the $La_{0.4+x}Sr_{0.4-x}Ga_x^{3+}Ti_{1-x}O_3$ series for which members up to $x = 0.18$ were prepared. Figure 4-13 shows that as Ga doping increases, the β angle increases linearly, matching with the gradual split of what was the (444) peak as indexed on a double primitive cubic cell. In terms of structure this means significantly increased tilting angles for the $x = 0.18$ member compared to the $x = 0.03$ member as illustrated in Figure 4-14.

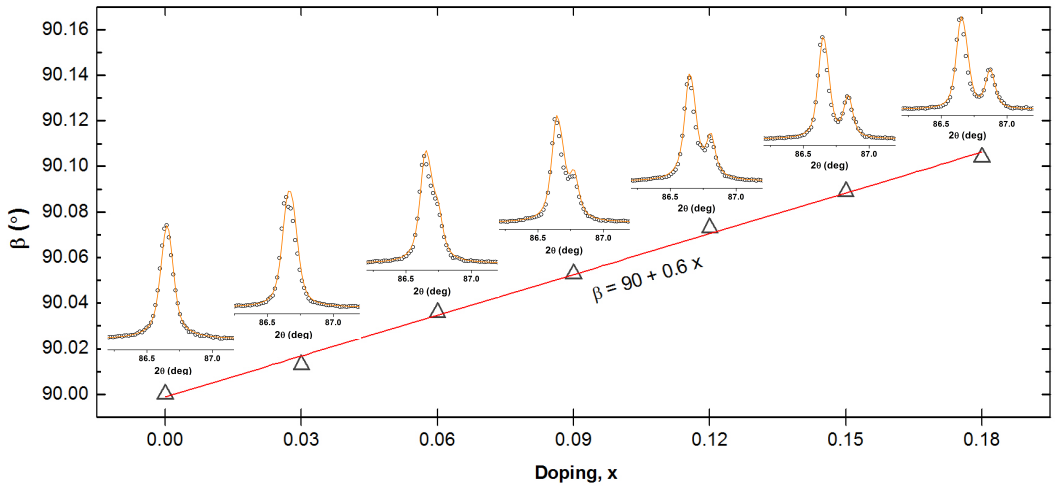

Figure 4-13 | The increase of distortion as Ga doping increases in the system $La_{0.4+x}Sr_{0.4-x}Ga_x^{3+}Ti_{1-x}O_3$ illustrated by plotting $\beta(x)$ and superimposing corresponding Rietveld fits of the '(444)' peaks (*I2/a* model).

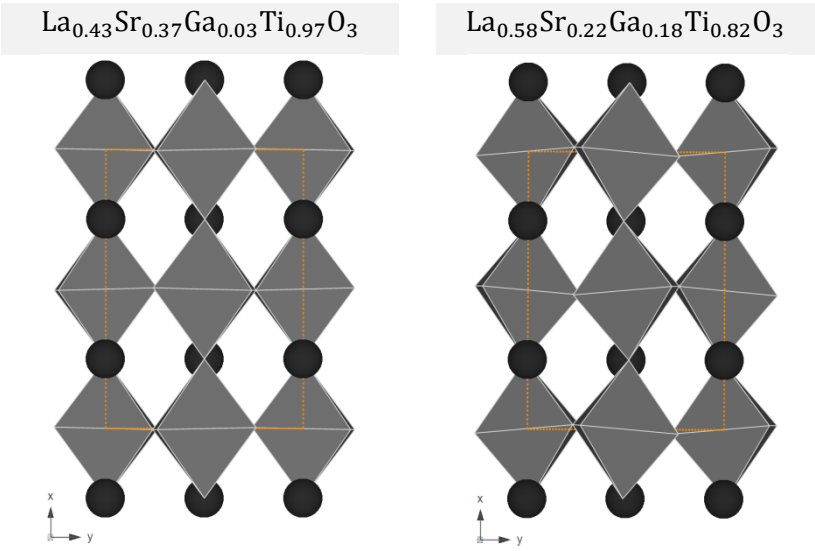

Figure 4-14 | Projections of the crystal structure of $La_{0.43}Sr_{0.37}Ga_{0.03}Ti_{0.97}O_3$ and $La_{0.58}Sr_{0.22}Ga_{0.18}Ti_{0.82}O_3$.

4.5 Crystal structure of the $La_{0.3}Sr_{0.7}M_xTi_{1-x}O_{3+\gamma}$ compositions

From the A-site stoichiometric, oxygen excess series $La_{0.3}Sr_{0.7}M_xTi_{1-x}O_{3+\gamma}$ two compositions were prepared: $La_{0.3}Sr_{0.7}TiO_{3.15}$ and $La_{0.3}Sr_{0.7}Ni_{0.06}Ti_{0.94}O_{3.09}$, and also the related $La_{0.33}Sr_{0.67}Ga_{0.33}Ti_{0.67}O_3$ and $La_{0.33}Sr_{0.67}Ga_{0.167}Ti_{0.833}O_{3+\gamma}$. Based on the discussion on oxygen excess perovskites carried out in Chapter 2, these compositions were expected to have a nearly-cubic perovskite structure with randomly distributed, small, oxygen-rich intergrowth regions.

From Figure 4-15, it is apparent that the $La_{0.3}Sr_{0.7}Ni_{0.06}Ti_{0.94}O_{3.09}$ composition only shows typical perovskite reflections (*i.e.* sub-cell reflections and a single R-type reflection), while the $La_{0.3}Sr_{0.7}TiO_{3.15}$ composition shows additional weak, broad peaks, especially visible in the 2θ range 20-35°.

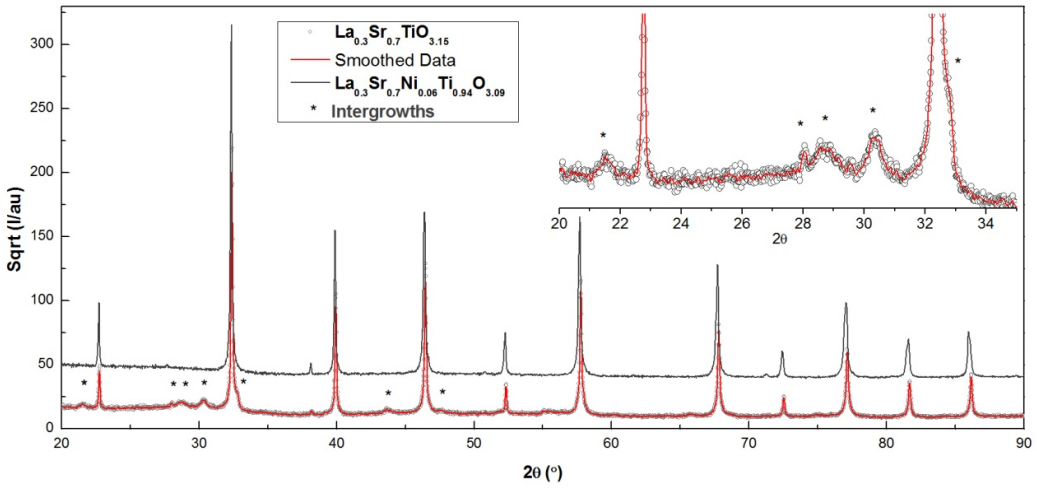

Figure 4-15 | Room temperature powder XRD patterns of $La_{0.3}Sr_{0.7}TiO_{3.15}$and $La_{0.3}Sr_{0.7}Ni_{0.06}Ti_{0.94}O_{3.09}$. The inset highlights the 2θ range where peaks originating from intergrowths usually appear.

The presence of such reflections is most likely a sign that some of the oxygen rich intergrowths are in fact not randomly distributed within the perovskite matrix, but are ordering over sufficiently large distances such that they become visible by X-rays. The Ni-containing composition does not show such features since its oxygen excess is considerably smaller than in the undoped composition. Thus, in the former composition, oxygen intergrowths must be

present as indicated by stoichiometry but they are finely dispersed within the perovskite and thus not visible by X-rays.

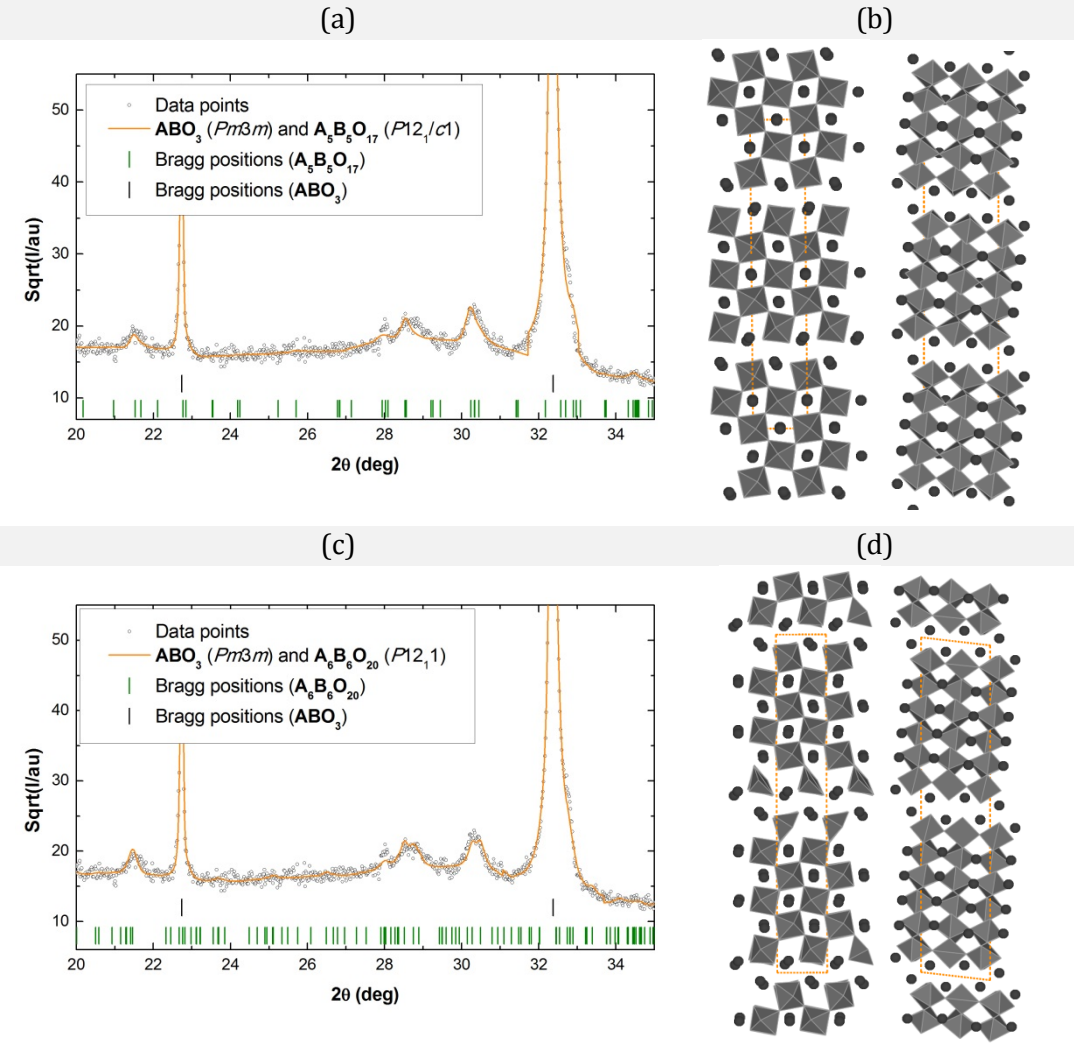

Figure 4-16 | Rietveld refinement of the XRD pattern collected from on the system '$La_{0.3}Sr_{0.7}TiO_{3.15}$' focusing on the 20-35° range when an $A_5B_5O_{17}$ model (a) or and $A_6B_6O_{20}$ model (c) is used to fit the peaks originating from intergrowths. Corresponding crystal structures are given as projections in (b) and (d), respectively.

An attempt to refine the cubic perovskite structure contribution to the XRD pattern of the $La_{0.3}Sr_{0.7}TiO_{3.15}$ composition revealed that for the best fit the cubic phase should contain considerably less La than the formal stoichiometry implies. This observation, coupled with the observations mentioned in the previous paragraph imply that the structure of the system '$La_{0.3}Sr_{0.7}TiO_{3.15}$' can be visualised as consisting of: 1) a Sr rich cubic perovskite, 2) randomly distributed and thus unseen by X-rays $A_nB_nO_{3n+2}$–

type intergrowth regions and 3) slightly extended La rich, $A_nB_nO_{3n+2}$–type intergrowth regions as detected by the X-rays.

La enrichment at the intergrowth regions has been observed previously *via* TEM in related compositions.[2] In order to confirm that the peaks small peaks observed in the pattern originate in a $A_nB_nO_{3n+2}$–type oxygen excess structure, an attempt was made to fit the weak and broad reflections with one of members of the $A_nB_nO_{3n+2}$ series. It was found that the fit became progressively better as n increased, with the most considerable improvements when going from an $n = 5$ to $n = 6$ type structure, as shown in Figure 4-16. Thus, a very good fit (R_p = 5.35, R_{wp} = 6.98, R_e = 5.34, χ^2 = 1.71) especially in terms of modelling the peak splitting and the shoulder appearing on the left of the (220) perovskite peak was achieved when using $n = 6$ as shown in Figure 4-16 and Figure 4-17.

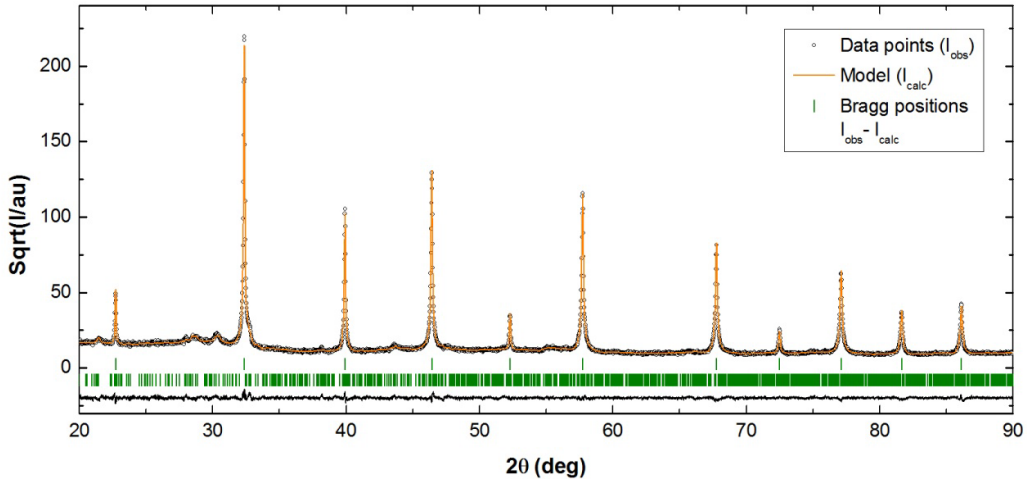

Figure 4-17 | Rietveld refinement on the XRD pattern collected from on the system '$La_{0.3}Sr_{0.7}TiO_{3.15}$' where a cubic $Pm\bar{3}m$ model was used for the main perovskite peaks in conjunction with an $A_6B_6O_{20}$ model for the intergrowths.

Another interesting aspect to point out is the apparent coherence in terms of cell size between the cubic perovskite (a_{cp} = 3.9080 Å) and the $A_6B_6O_{20}$ oxygen excess perovskite (a_{oep} = 7.839 Å, b_{oep} = 5.513 Å, c_{oep} = 37.791 Å – cell parameters given with only 3 decimals to reflect the uncertainty associated with fitting peaks of such small intensity). Thus, $a_{oep} \sim a_{cp} \cdot 2 = 7.821$ Å and

$b_{oep} \sim a_{cp} \cdot \sqrt{2} = 5.526$ Å. This confirms that the intergrowths, even when extended, are continuously 'woven' with the perovskite.

4.6 Crystal structure of the $La_{0.8}Ce_{0.1}Ni_{0.4}Ti_{0.6}O_3$ composition

The composition $La_{0.8}Ce_{0.1}Ni_{0.4}Ti_{0.6}O_3$ is the member $x = 0.4$ belonging to the series $La_{1.6-2x}Ce_{2x-0.7}Ni_xTi_{1-x}O_3$ ($0.35 \leq x \leq 0.8$). This series was derived in the same way as described in subchapter 4.4 (Eq. 4-5-Eq. 4-7), with the criteria that the perovskite should have 0.1 A-site deficiency, Ce instead of Sr on the A-site and be oxygen stoichiometric (these choices will be motivated in section 7.6.1).

The XRD pattern of the as-prepared sample (shown in Figure 4-18) displays additional reflections compared to the patterns examined so far suggesting the presence of secondary phases and/or lower symmetry. However, by applying the procedure described in section 4.2 all but one very small peak (probably rutile) can be attributed to sub-cell reflections, thus implying that this entirely new compound is a highly distorted perovskite.

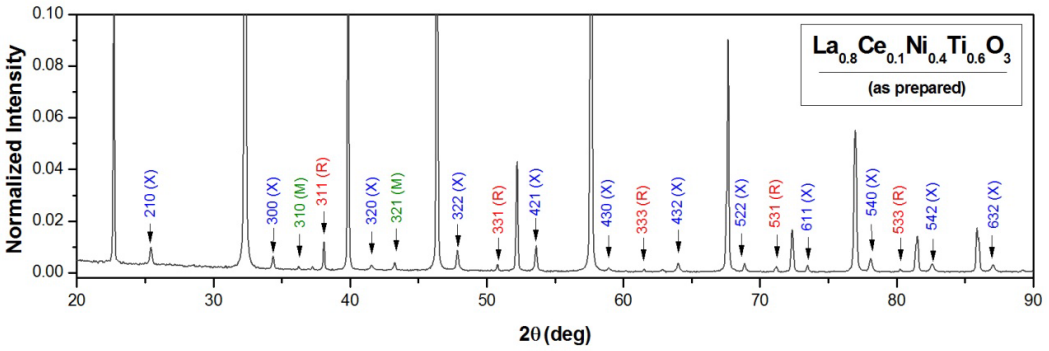

Figure 4-18 | Room temperature powder XRD pattern of as prepared $La_{0.8}Ce_{0.1}Ni_{0.4}Ti_{0.6}O_3$. R, X and M-type super reflections present in this composition are also shown.

As shown in Figure 4-18, all three types of sub-cell reflections are present: X, M and R, and thus the most likely space group will be *Pnma*. This space group (used here in its other setting, *Pbnm*) is easily confirmed through Rietveld refinement with very good fit (Figure 4-19). The corresponding structure is, as anticipated, very distorted, with significant in-phase tilting along the *z* axis

and even more pronounced out-of-phase tilting along the x and y axes (Figure 4-19).

Rietveld refinement of $La_{0.8}Ce_{0.1}Ni_{0.4}Ti_{0.6}O_3$

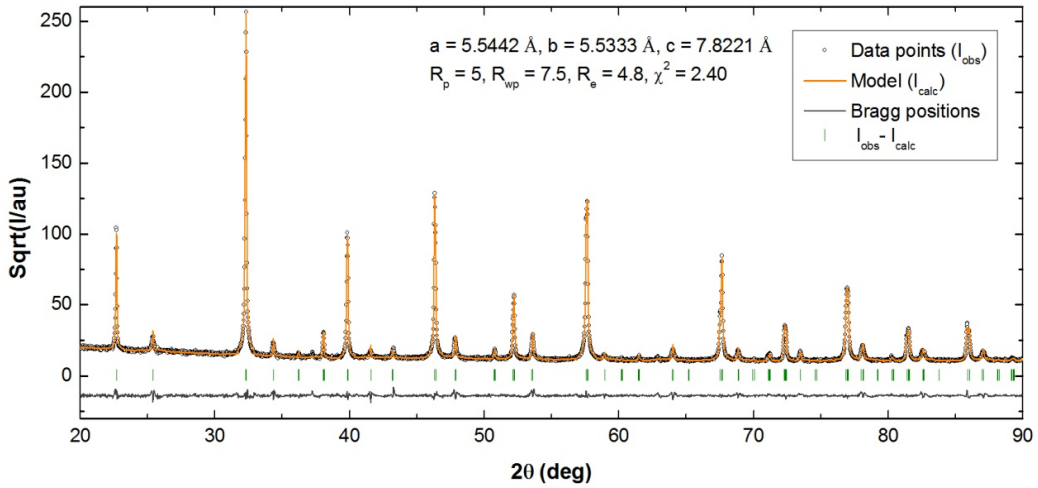

Crystal structure – $Pbnm$ $(a^-a^-c^+)$

Perspective view | Projection along z | Projection along y

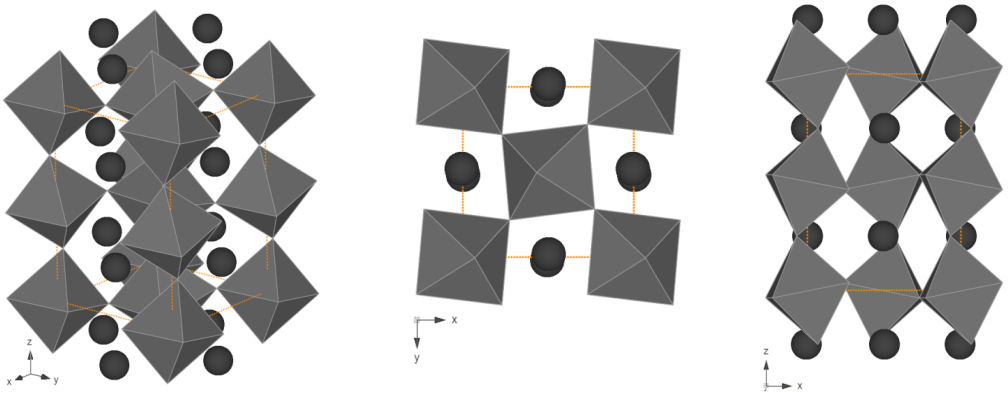

Figure 4-19 | Rietveld refinement and crystal structure of as-prepared $La_{0.8}Ce_{0.1}Ni_{0.4}Ti_{0.6}O_3$.

4.7 The variation of the unit cell size with the size and concentration of doping cations

The most frequent method for introducing defects in a structure is through cation doping. When a cation is doped into a certain structure the changes it inflicts upon the host lattice depend mainly on size, charge and 'shape'[xvi] of the dopant with respect to the cation being substituted, as summarised in Figure 4-20. The difference in size between the dopant and the host can lead to tilting and/or distortion of the octahedra which in turn leads to a change in

[xvi] Given by the shape of the outer electron orbitals.

symmetry and unit cell volume. If the dopant and the host cation have different oxidation states, then charge compensation can lead to a change in the perovskite nonstoichiometry class and consequently in its defect chemistry. In turn, this may cause changes to the overall structure and symmetry of the cell and also to the cell volume which will reflect contributions from both the dopant-host cation size difference and the size of the created defects.

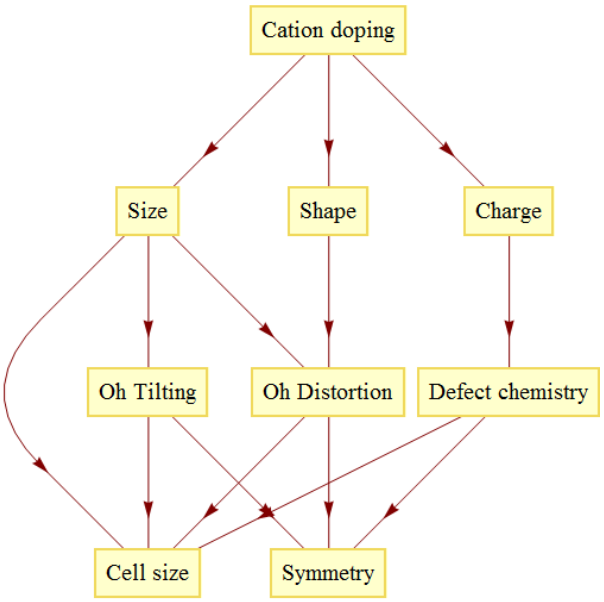

Figure 4-20 | Overview of the changes to perovskite crystal structure brought about by cation doping.

So far, only the overall structure and symmetry changes upon cation doping were addressed. Next, the variation of unit cell parameters will be discussed as a function of dopant size and concentration (*i.e.* doping level), while changes brought about by a shift in defect chemistry will be addressed in section 4.8.

An initial, qualitative, idea about the correlation between unit cell size and dopant size can be obtained by examining the plots presented in Figure 4-21. This figure compares in parallel two plots: 1) the pseudocubic cell parameters of the series $La_{0.4}Sr_{0.4}M_{0.06}Ti_{0.94}O_{3-\gamma}$ (same doping level, $x = 0.06$, taken from Table 4-2) as a function of the doping cation M (in the

order of their atomic number); 2) the Shannon ionic radii[18] of the corresponding dopants (all in CN = 6, high spin), as a function of cation M.

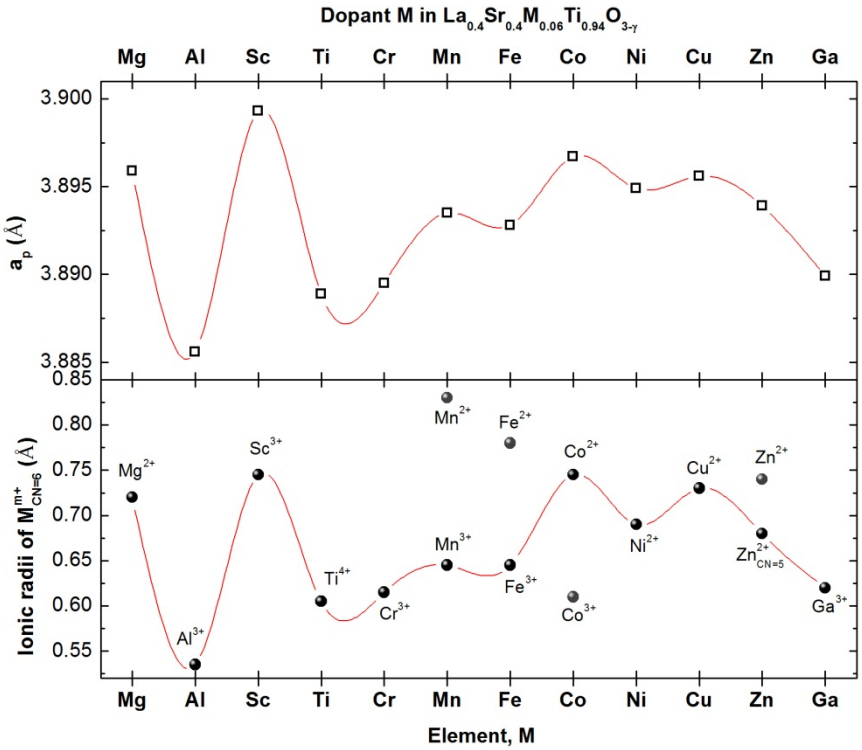

Figure 4-21 | Comparative plots of the pseudocubic cell parameter a_p of the series $La_{0.4}Sr_{0.4}M_{0.06}Ti_{0.94}O_{3-\gamma}$ as a function of M, and the size of 6-fold coordinated, high spin analogue cations (according to Shannon[18]).

As can be seen from this figure, the trend-line of the variation $a_p(M)$ follows closely the trend-line for variation $r_{M^{m+}_{CN=6}}(M^{m+})$ implying that unit cell size is very sensitive to changes in cation size, while the effect of charge compensation (*i.e.* oxygen vacancy creation) is largely negligible. Two major observations can be made, however: 1) while the jump in ionic size from Cr^{3+} to Mn^{3+} or Fe^{3+} is rather small, the jump in cell size when going from $La_{0.4}Sr_{0.4}Cr_{0.06}Ti_{0.94}O_{3-\gamma}$ to $La_{0.4}Sr_{0.4}Mn_{0.06}Ti_{0.94}O_{3-\gamma}$ or $La_{0.4}Sr_{0.4}Fe_{0.06}Ti_{0.94}O_{3-\gamma}$ is rather significant, suggesting larger cations than Mn^{3+} and Fe^{3+} are also present (*e.g.* Mn^{2+} and Fe^{2+}, respectively); 2) according to the $r_{M^{m+}_{CN=6}}(M^{m+})$ trend-line which shows a slight increase in radius going from Cu^{2+} to Zn^{2+}, the cell parameter of the corresponding compositions should follow the same trend, but does not. By considering the radius of 5-fold coordinated Zn^{2+}, $Zn^{2+}_{CN=5}$ = 0.68 Å, the ionic radii plot would follow

precisely the trend observed experimentally through a_p(M). Bearing in mind that the charge compensation in this compound would result in one oxygen vacancy produced per Zn dopant, $La_{0.4}Sr_{0.4}Zn_xTi_{1-x}O_{3-x}$, it would seem as if the oxygen vacancies are preferentially associated with the dopant, Zn''_{Ti}, effectively lowering its coordination number from an average value of 6 to an average value of 5.

To investigate the correlation between the unit cell size and concentration of dopants, pseudocubic cell parameters (a_p) were plotted against doping level x of cation M for selected systems belonging to the family $La_{0.4}Sr_{0.4}M_xTi_{1-x}O_{3-\gamma}$, as shown in Figure 4-22. As can be seen from this figure, all $a_p(x)$ variations are linear, with slopes that have higher values as the size of the dopant cation increases ($r_{Ga^{3+}} < r_{Ti^{3+}} < r_{Zn^{2+}}$).

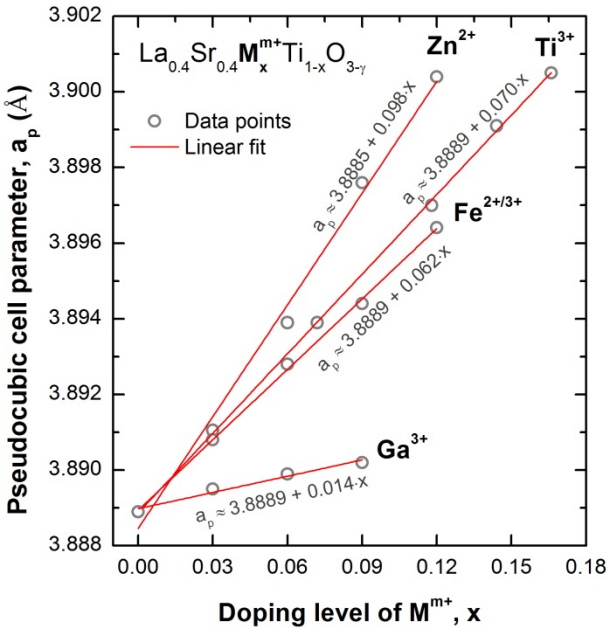

Figure 4-22 | Pseudocubic cell parameter as a function of doping level and the corresponding linear fits for selected systems belonging to the series $La_{0.4}Sr_{0.4}M_xTi_{1-x}O_{3-\gamma}$. The Ti^{3+} dependency was obtained by reducing $La_{0.4}Sr_{0.4}M_xTi_{1-x}O_{3-\gamma}$ and measuring the exte of reduction by thermogravimetry as shown in Chapter 5.

Previously, an empirical equation for the prediction of the cell parameters based on the Shannon radii[18] has been proposed for fluorite materials.[19] This equation relates the change in cell size upon doping with the difference in size and charge between the doping cation and the host cation:

$$a = a_0 + \sum_M (b_0 \cdot \Delta r_M + b_1 \cdot \Delta z_M) \cdot x_M \quad \text{Eq. 4-9}$$

Where: a is the cell parameter, a_0, b_0 and b_1 are constants, x_M is the mole fraction of the cation M substituting the host cation, Δr_M is the difference in the ionic radius between the substituting cation M and the host, and Δz_M is the difference in charge between the substituting cation M and the host cation. While this equation can take complicated forms for fluorite systems, by using the results in this study (*e.g.* Figure 4-22) it can be shown in a first approximation, for perovskites $b_0 = 1$ and $b_1 = 0$, so for one dopant, the equation becomes:

$$a \approx a_0 + (r_{M^{m+}} - r_{Ti^{4+}}) \cdot x_M \quad \text{Eq. 4-10}$$

Thus, the slopes shown in Figure 4-22 should be close to the difference in ionic radius between corresponding dopant and host cation (Ti^{4+}). This is clearly valid for Ti^{3+} doping: slope = 0.070 and $r_{Ti^{3+}} - r_{Ti^{4+}} = 0.67 - 0.605 = 0.065$, or Ga^{3+} doping: slope = 0.014 and $r_{Ga^{3+}} - r_{Ti^{4+}} = 0.67 - 0.605 = 0.015$.

To further confirm the validity of Eq. 4-10 for a greater range of dopants a new plot was constructed: a_p as a function of $(r_{M^{m+}_{CN=6}} - r_{Ti^{4+}_{CN=6}})$ for a fixed doping ratio of $x = 0.06$. So, in this case, the slope of the plot points should be 0.06, and thus compositions that follow this law should align to a line having this slope. Such a plot is presented in Figure 4-23. It is obvious from this figure that cations with fixed oxidation states lie on the line or very close to it (*e.g.* Al^{3+}, Cr^{3+}, Ga^{3+}, Ti^{3+}, Mg^{2+}, Cu^{2+}) with the exception of Zn^{2+} (as seen from the discussion of Figure 4-21 as well) and Sc^{3+} both located quite far from the trend. As anticipated from Figure 4-21, cations with multiple oxidation states such as $Fe^{2+/3+}$ or $Mn^{2+/3+}$ are also far away compared to their expected position when it is assumed they are only present in the higher oxidation state (assumption used in the trend highlighted in Figure 4-21). For Mn and Fe compositions to be located on the trendline, they would have to consist of a mixture of oxidation sates, roughly {20% Fe^{2+}, 80% Fe^{3+}} for the

Fe-based composition and {65% Mn^{2+}, 35% Mn^{3+}} for the Mn-based composition.

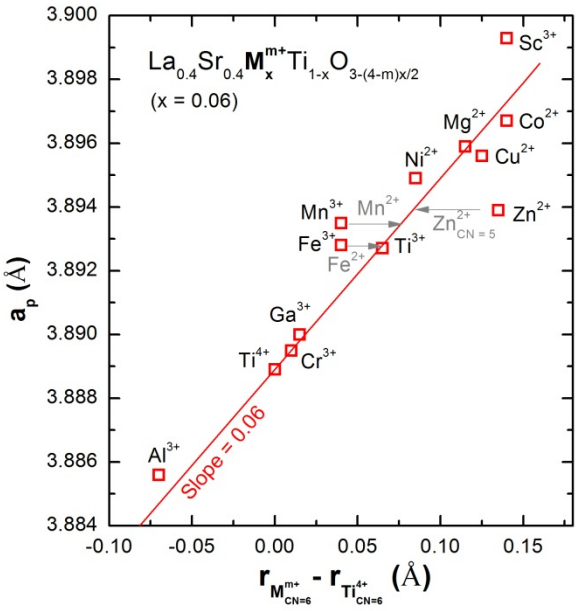

Figure 4-23 | Pseudocubic cell parameter as a function of the difference between the ionic radius of the dopant and host cation (CN = 6, high spin) for various dopants in the series $La_{0.4}Sr_{0.4}M_xTi_{1-x}O_{3-\gamma}$.

Thus, it appears that Eq. 4-10 describes quite well the dependency between the unit cell size and the size of the B-site of perovskites. This equation was further put to the test against data in the literature. Table 4-4 summarises other perovskite systems which were found to obey Eq. 4-10. These were chosen such that they contained cations with variable oxidation state, where the references also offered quantitative information about the oxidation state composition so that Eq. 4-10 could be applied properly.

Table 4-4 | Selected perovskites from the literature that obey Eq. 4-10. (*) denotes average ionic radius calculated as an weighted average based on the oxidation states data provided in the indicated references.

Composition	**Ref**	**$a_p(x)$ slope**	**r_{dopant} (Å)**	**r_{host} (Å)**	**Δr (Å)**
$La_2Sr_4Ti_{6-x}Sc_xO_{19+\delta}$	[20]	0.121	0.745	0.605	0.14
$LaMn_xFe_{1-x}O_{3-\delta}$	[21]	-0.10	0.595*	0.71*	-0.115
$La_{0.7}Sr_{0.3}Mn_{1-x}Sc_xO_{3-\delta}$	[22]	0.164	0.745	0.595*	0.15
$La_{0.9}Sr_{0.1}(Ga_{1-x}Fe_x)_{0.8}Mg_{0.2}O_{3-\delta}$	[23]	-0.032	0.593*	0.62	-0.027
$La_{0.9}Sr_{0.1}(Ga_{1-x}Cr_x)_{0.8}Mg_{0.2}O_{3-\delta}$	[23]	-0.018	0.608*	0.62	-0.012

In all selected cases Eq. 4-10 predicts the $a_p(x)$ dependency rather well proving this equation which relates the size of the unit cell to the size of the B-site might be valid for perovskites in general and is definitely not limited the A-site deficient perovskites investigated in this study.

Thus, according to Eq. 4-10 and Figure 4-22, the following equation can be written in general for the series $La_{0.4}Sr_{0.4}M_xTi_{1-x}O_{3-\gamma}$:

$$a_{La_{0.4}Sr_{0.4}M_xTi_{1-x}O_{3-\gamma}} \approx a_{La_{0.4}Sr_{0.4}TiO_3} + (r_{M^{m+}} - r_{Ti^{4+}}) \cdot x \qquad \text{Eq. 4-11}$$

Having confirmed that equations of the form of Eq. 4-11 are generally valid for perovskites, one might wonder if a similar, more general equation can be envisaged to reflect unit cell changes when both A and B-sites are doped. Assuming A-site doping would also increase the unit cell size linearly with doping level, a composite equation such as the one below can be imagined for an ABO_3 perovskite with both sites being doped, $A_{1-x}A'_xB_{1-y}B'_yO_{3\pm\gamma}$:

$$a_{A_{1-x}A'_xB_{1-y}B'_yO_{3\pm\gamma}} \approx a_{ABO_3} + \zeta \cdot (r_{A'} - r_A) \cdot x + \beta \cdot (r_{B'} - r_B) \cdot y \qquad \text{Eq. 4-12}$$

Where ζ and β are coefficients showing the contribution to the unit cell change when both A or B site are doped, respectively. So far it has been shown that β = 1. To find the A-site contribution ζ the pseudocubic unit cell parameters were plotted against doping level for the series in which both A and B site doping was performed simultaneously, $La_{0.4+x}Sr_{0.4-x}M_xTi_{1-x}O_3$, where M = Ga, Fe (plots shown in Figure 4-24).

First, it is important to note that the assumption that the $a_p(x)$ dependency would be linear in the case of A-site doping was correct, since the points in Figure 4-24 clearly follow linear trends for both Ga and Fe doping data sets. However, one has a negative slope (Ga), while the other has a positive slope (Fe) which in fact tells about the contribution of ζ since both unit cells should have expanded if no contribution from the A-site was felt since both Ga^{3+} and Fe^{3+} are larger in size compared to the host cation, Ti^{4+}.

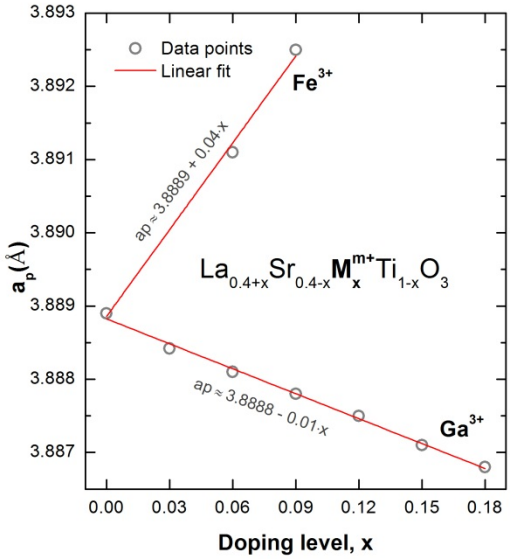

Figure 4-24 | Pseudocubic cell parameter as a function of doping level and the corresponding linear fits for selected systems belonging to the series $La_{0.4+x}Sr_{0.4-x}M_xTi_{1-x}O_3$ (M = Ga, Fe).

In general, Eq. 4-12 can be written for the systems $La_{0.4+x}Sr_{0.4-x}M_xTi_{1-x}O_3$:

$$a_{La_{0.4+x}Sr_{0.4-x}M_xTi_{1-x}O_3} \approx a_{La_{0.4}Sr_{0.4}TiO_3} + \zeta \cdot (r_{La^{3+}} - r_{Sr^{2+}}) \cdot x + \beta \cdot (r_{M^{m+}} - r_{Ti^{4+}}) \cdot x \quad \text{Eq. 4-13}$$

Or, simplified,

$$a_{La_{0.4+x}Sr_{0.4-x}M_xTi_{1-x}O_3} \approx 3.8889 + \zeta \cdot (-0.08) \cdot x + (r_{M^{m+}} - r_{Ti^{4+}}) \cdot x \quad \text{Eq. 4-14}$$

Thus, for *Fe doping*, by using the 'B-site slope' corresponding to a real Fe ion in a perovskite {20% Fe^{2+}, 80% Fe^{3+}} (Figure 4-22), Eq. 4-14 becomes:

$$a_{La_{0.4+x}Sr_{0.4-x}Fe_xTi_{1-x}O_3} \approx 3.8889 + \zeta \cdot (-0.08) \cdot x + (0.062) \cdot x \quad \text{Eq. 4-15}$$

Or, simplified,

$$a_{La_{0.4+x}Sr_{0.4-x}Fe_xTi_{1-x}O_3} \approx 3.8889 + (-0.08 \cdot \zeta + 0.062) \cdot x \quad \text{Eq. 4-16}$$

Thus, the slope is $-0.08 \cdot \zeta + 0.062$ and should equal +0.04 (from Figure 4-24), resulting in $\zeta = 0.275$ or $\zeta \sim 0.3$.

Similarly, for *Ga doping*, Eq. 4-14becomes:

$$a_{La_{0.4+x}Sr_{0.4-x}Ga_xTi_{1-x}O_3} \approx 3.8889 + \zeta \cdot (-0.08) \cdot x + (0.014) \cdot x \quad \text{Eq. 4-17}$$

Thus, the slope is $-0.08 \cdot \zeta + 0.014$ and should equal -0.01, resulting in $\zeta = 0.3$, almost the same value as in the case of Fe doping.

Thus ζ = 0.3 and β = 1 in Eq. 4-12, which means that B-site doping has much more impact on the size of the resulting unit cell compared to A-site doping. This is not surprising, since, as explained in Chapter 2, the B-site cation and the BO_6 octahedra are the core structural units of the perovskite structure and thus any change in size of the B-site will be immediately reflected on the overall structure.

While β = 1 has been shown to be general to perovskites, in absence of further proof it is speculative to say Eq. 4-12 with $\zeta = 0.3$ is general to perovskites (perhaps that particular ζ value is only valid for 0.2 A-site deficient perovskites). However, if Eq. 4-12 is at all valid for perovskites in general, then most likely, ζ will always be smaller than β as a direct consequence of the stronger bonds/role of the B-site compared to the A-site.

4.8 The influence of defect chemistry on the size of perovskite cells

Depending on how the defects are actually incorporated in the perovskite, the lattice will react accordingly. In Figure 4-25, the pseudo-cubic cell parameters for the primitive perovskite cell were plotted against dopant content (La) in two representative series: the oxygen excess $La_xSr_{1-x}TiO_{3+x/2}$ and the A-site deficient series $La_xSr_{1-3x/2}TiO_3$.

The plot shows linear fits to the experimental data taken from refs [24] and [25] respectively. While one would expect the cell parameter to decrease in size slightly as the smaller La^{3+} substitutes the larger Sr^{2+}, this is not the case for the oxygen excess series. This is most likely due to the oxygen excess intergrowths where the packing is not as compact as in the perovskite layers. On the other hand, the A-site deficient titanate does show a negative slope which is in fact quite steep.

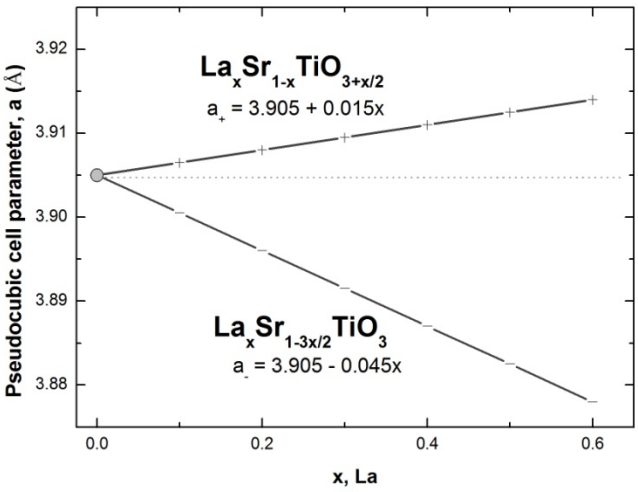

Figure 4-25 | Pseudo-cubic cell parameter as a function of defect concentration: substitution of Sr^{2+} by La^{3+} in the oxygen excess $La_xSr_{1-x}TiO_{3+x/2}$ (linear fit on data from ref [24]) and in the A-site deficient $La_xSr_{1-3x/2}TiO_3$ (linear fit on data from ref [25]).

Considering that La^{3+} is only slightly smaller than Sr^{2+}, it seems possible to admit that the A-ion vacancies are smaller, at most equal, but not larger than the dopant. If the size of the vacancy would be larger, then when their concentration becomes significant, one should observe a change in the slope pointing to the fact that the larger size of the vacancies are compensating the size of the dopant by increasing the size of the unit cell. Additional proof towards the assumption that $r_{V''_{Sr}} \leq r_{La^{\bullet}_{Sr}}$ comes from the fact that stronger tilting is observed in these systems as the number of vacancies increases,[25,12] which correlates to the presence of undersized species on the A-site (see Chapter 2).

Assuming Eq. 4-12 would apply for varying degrees of A-site deficiency, one could estimate the size of the A-site vacancy. The general formula $La_xSr_{1-3x/2}TiO_3$ could be written explicitly as $(V''_{Sr})_{y/3}La_{2y/3}Sr_{1-y}TiO_3$ and thus Eq. 4-12 would be written:

$$a_{(V''_{Sr})_{y/3}La_{2y/3}Sr_{1-y}TiO_3} \approx a_{SrTiO_3} + \zeta \cdot \left(\frac{1}{3} \cdot r_{V''_{Sr}} + \frac{2}{3} \cdot r_{La^{3+}} - r_{Sr^{2+}}\right) \cdot y \qquad \text{Eq. 4-18}$$

Or, with the known values included:

$$a_{(V''_{Sr})_{y/3}La_{2y/3}Sr_{1-y}TiO_3} \approx 3.905 + 0.3 \cdot \left(\frac{1}{3} \cdot r_{V''_{Sr}} + \frac{2}{3} \cdot 1.36 - 1.44\right) \cdot y \qquad \text{Eq. 4-19}$$

Thus, $0.3 \cdot \left(\frac{1}{3} \cdot r_{V''_{Sr}} + \frac{2}{3} \cdot 1.36 - 1.44\right)$ should equal the slope -0.045. This results in the size of the A-site vacancy being $r_{V''_{Sr}} \approx 1.15$ Å.

4.9 Summary and conclusions

The crystal structure and methodology used for deriving it from powder X-ray diffraction was discussed for various perovskites belonging to different defect chemistries. Most of the compositions were prepared for the first time during this study, based on considerations and rules also developed here.

In general, the pseudocubic cell parameter of perovskites seems to vary linearly with respect to the average size of the A and B site and corresponding doping levels, with the B-site contributing more considerably than the A-site ($\zeta < \beta$):

$$a_{p\,(A_{1-x}A'_xB_{1-y}B'_yO_{3\pm\gamma})} \approx a_{p\,(ABO_3)} + \zeta \cdot (r_{A'} - r_A) \cdot x + \beta \cdot (r_{B'} - r_B) \cdot y$$

Depending on the nonstoichiometry class of the perovskite and associated defect chemistry, unit cell size-composing cations size correlation can be anomalous.

References

1. P. Battle, J. E. Bennett, J. Sloan, R. J. D. Tilley, and J. F. Vente, *J. Solid State Chem.*, 2000, **149**, 360–369.
2. J. Canales-Vázquez, M. J. Smith, J. T. S. Irvine, and W. Zhou, *Adv. Funct. Mater.*, 2005, **15**, 1000–1008.
3. J. C. Ruiz-Morales, J. Canales-Vázquez, C. Savaniu, D. Marrero-López, W. Zhou, and J. T. S. Irvine, *Nature*, 2006, **439**, 568–571.
4. A. M. Glazer, *Acta Crystall. B-Stru.*, 1972, **28**, 3384–3392.
5. A. M. Glazer, *Acta Crystallogr. A*, 1975, **31**, 756–762.
6. P. M. Woodward, *Acta Crystall. B-Stru.*, 1997, **53**, 32–43.
7. P. M. Woodward, *Acta Crystall. B-Stru.*, 1997, **53**, 44–66.
8. C. J. Howard, B. J. Kennedy, and P. M. Woodward, *Acta Crystall. B-Stru.*, 2003, **59**, 463–471.
9. C. J. Howard and H. T. Stokes, *Acta Crystallogr. A*, 2004, **61**, 93–111.
10. C. J. Howard and H. T. Stokes, *Acta Crystall. B-Stru.*, 1998, **54**, 782–789.
11. Z. Zhang, G. R. Lumpkin, C. J. Howard, K. S. Knight, K. R. Whittle, and K. Osaka, *J. Solid State Chem.*, 2007, **180**, 1083–1092.
12. M. A. Carpenter, C. J. Howard, K. S. Knight, and Z. Zhang, *J. Phys.: Condens. Mat.*, 2006, **18**, 10725–10749.
13. C. J. Ball, B. D. Begg, D. J. Cookson, G. J. Thorogood, and E. R. Vance, *J. Solid State Chem.*, 1998, **139**, 238–247.
14. M. Avdeev, E. N. Caspi, and S. Yakovlev, *Acta Crystall. B-Stru.*, 2007, **63**, 363–372.
15. P. W. Barnes, PhD Thesis, The Ohio State University, 2003.
16. T. Ishihara, Ed., *Perovskite oxide for solid oxide fuel cells*, Springer, New York ;London, 2008.
17. M. Lufaso and P. Woodward, *Chemistry Faculty Publications*, 2001.
18. R. D. Shannon, *Acta Crystall. A-Crys.*, 1976, **32**, 751–767.
19. D.-J. Kim, *J. Am. Cer. Soc.*, 1989, **72**, 1415–1421.
20. J. Canales-Vázquez, J. C. Ruiz-Morales, J. T. S. Irvine, and W. Zhou, *J. Electrochem. Soc.*, 2005, **152**, A1458.
21. P. P. Hankare, M. R. Kadam, P. D. Kamble, S. D. Jadhav, U. B. Sankpal, R. P. Patil, V. B. Helavi, and N. S. Gajbhiye, *J. Alloy Compd.*, 2010, **489**, 233–236.
22. A. N. Ulyanov, Y. Kang, S.-I. Yoo, and S.-C. Yu, *J. Magn. Magn. Mater.*, 2006, **303**, e347–e350.
23. N. Trofimenko and H. Ullmann, *Solid State Ionics*, 1999, **118**, 215–227.
24. S. Hashimoto, L. Kindermann, F. Poulsen, and M. Mogensen, *J. Alloy Compd.*, 2005, **397**, 245–249.
25. C. Howard, G. Lumpkin, R. Smith, and Z. Zhang, *J. Solid State Chem.*, 2004, **177**, 2726–2732.

5 REDUCTION IN PEROVSKITES

5.1 Means of investigating reduction

As pointed out in Chapter 2, understanding how and to what extent perovskites can reduce is of great importance from both fundamental and application point of view.

During reduction, oxygen is stripped from the perovskite lattice by the reducing agent or upon heating due to thermal vibration/entropy. Each oxygen atom that is removed leaves behind an oxygen vacancy and two electrons:

$$O_O^x \rightarrow \frac{1}{2}O_2 + V_O^{\cdot\cdot} + 2e' \qquad \text{Eq. 5-1}$$

Because during reduction the sample loses mass (*i.e.* oxygen), this can be monitored thermo-gravimetrically, and the change in mass can be used to calculate the change in oxygen stoichiometry.

Considering the reduction of a perovskite ABO_3 to $ABO_{3-\delta}$, with the corresponding change of mass from m_{ABO_3} to $m_{ABO_{3-\delta}}$, since the number of moles of perovskite is conserved, the following equality can be written:

$$\frac{m_{ABO_3}}{\mu_{ABO_3}} = \frac{m_{ABO_{3-\delta}}}{\mu_{ABO_{3-\delta}}} \qquad \text{Eq. 5-2}$$

Where μ_{ABO_3} and $\mu_{ABO_{3-\delta}}$ represent the molar weights of the oxidised and reduced perovskite respectively. This can also be written as:

$$\frac{m_{ABO_3}}{\mu_{ABO_3}} = \frac{m_{ABO_{3-\delta}}}{\mu_{ABO_3} - \delta \cdot A_O} \qquad \text{Eq. 5-3}$$

Where A_O is the atomic weight of oxygen. Eq. 5-3 can be then rearranged:

$$\frac{m_{ABO_3}}{m_{ABO_{3-\delta}}} = \frac{\mu_{ABO_3}}{\mu_{ABO_3} - \delta \cdot A_O} \qquad \text{Eq. 5-4}$$

Or, equivalently (using fraction properties):

$$\frac{m_{ABO_3}}{m_{ABO_{3-\delta}} - m_{ABO_3}} = \frac{\mu_{ABO_3}}{-\delta \cdot A_O} \qquad \text{Eq. 5-5}$$

Thus, the extent of reduction is:

$$\delta = \frac{\mu_{ABO_3}}{A_O} \cdot \frac{m_{ABO_3} - m_{ABO_{3-\delta}}}{m_{ABO_3}} \quad \text{Eq. 5-6}$$

As implied by Eq. 5-6, δ is usually expressed in oxygen atoms per formula unit of perovskite (at/fu).

Also, because electrons are generated as reduction progresses, the conductivity of the sample should increase correspondingly, unless generated electrons are localised or trapped by other defects.

The conductivity is generally given by:

$$\sigma = n \cdot e \cdot \mu \quad \text{Eq. 5-7}$$

Where σ is the electronic conductivity, *n* is the concentration of (free) charge carriers (expressed as charge per volume), *e* is the elementary charge and μ is their mobility.

If all the electrons generated through reduction are free to conduct, in a reduced perovskite $ABO_{3-\delta}$ with a unit cell volume of V_{uc}, then by using Eq. 1-1, the following relation between *n* and δ may be written:

$$n = \frac{2 \cdot \delta}{V_{uc}} \quad \text{Eq. 5-8}$$

From section 4.7, V_{uc} may be approximated to be:

$$V_{uc} = a_p^3 = (a_0 + b \cdot x_{Ti^{3+}})^3 = (a_0 + 2 \cdot b \cdot \delta)^3 \quad \text{Eq. 5-9}$$

Combining Eq. 5-8 and Eq. 5-9, it follows that:

$$n = \frac{2 \cdot \delta}{(a_0 + 2 \cdot b \cdot \delta)^3} = \frac{2 \cdot \delta}{\left[a_0 \cdot \left(1 + \frac{2 \cdot b \cdot \delta}{a_0}\right)\right]^3} \quad \text{Eq. 5-10}$$

Generally for perovskites $a_0 \sim 3.9$ Å, while for most of the investigated systems $\delta < 0.1$, while $b \sim 0.07$ (see Figure 4.22). This means that in Eq. 5-10 the numerator $2 \cdot b \cdot \delta$ will be much smaller compared to the denominator a_0 and hence, $\frac{2 \cdot b \cdot \delta}{a_0} \to 0$, leading to:

$$n \approx \frac{2 \cdot \delta}{{a_0}^3} \qquad \text{Eq. 5-11}$$

This means n is in fact directly proportional to δ, $n \propto \delta$, which means σ is also directly proportional to δ,

$$\sigma \approx \frac{2 \cdot \delta}{{a_0}^3} \cdot e \cdot \mu \qquad \text{Eq. 5-12}$$

Thus, the extent of reduction may be monitored by measuring electronic conductivity.

5.2 Insights into the reduction of A-site deficient perovskites from a macroscopic perspective

As pointed out in earlier chapters, most of the compositions studied throughout this work stemmed from the composition $La_{0.4}Sr_{0.4}TiO_3$ which is the term $x = 0.4$ in the series $(V''_{Sr})_{x/2}La_xSr_{1-3x/2}TiO_3$. Among other reasons, the $x = 0.4$ member was brought forward because it exhibits the highest extent of reduction in the above mentioned series (see Figure 5-1). Thus, this subchapter will present some reduction characteristics of this specific composition.

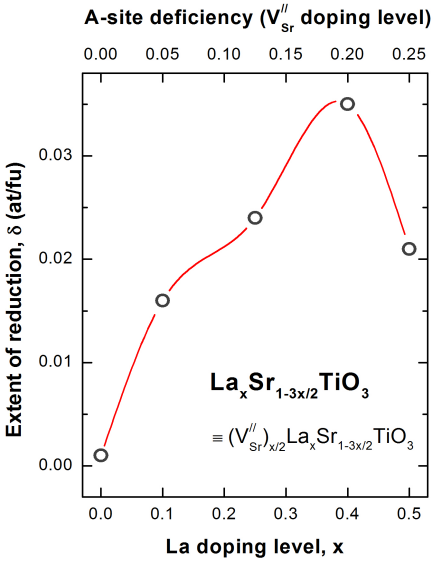

Figure 5-1 | The extent of reduction *vs.* dopant stoichiometry (La and/or A-site vacancies, V''_{Sr}) for the serie$(V''_{Sr})_{x/2}La_xSr_{1-3x/2}TiO_3$s. Reduction was carried out in 5%H_2/Ar, at 1000 °C, for 20 h. The errors are of the size of the points. The line interpolates experimental points.

Figure 5-2 presents a TGA experiment performed on two $La_{0.4}Sr_{0.4}TiO_3$ powders of different specific surface area: a coarse powder (0.035 m^2/g) and a fine powder (0.384 m^2/g). Both of them followed the same reduction program, with 4 h isothermal steps at 900, 1000, 1100, 1200 and 1300 °C, carried out in flowing 5%H_2/Ar. The plot in Figure 5-2 displays the change in sample weight on the left *y* axis and the corresponding change in oxygen deficiency (δ) on the right *y* axis, both as a function of reduction time. The experiment reveals that at 900 °C both powders reduce very slowly, but the extent of reduction increases considerably as temperature increases. The fine powder reduces faster and thus to higher extent compared to the coarse powder, the former reaching $\delta \sim 0.10$ at/fu and the latter $\delta \sim 0.08$ at/fu at the end of the experiment.

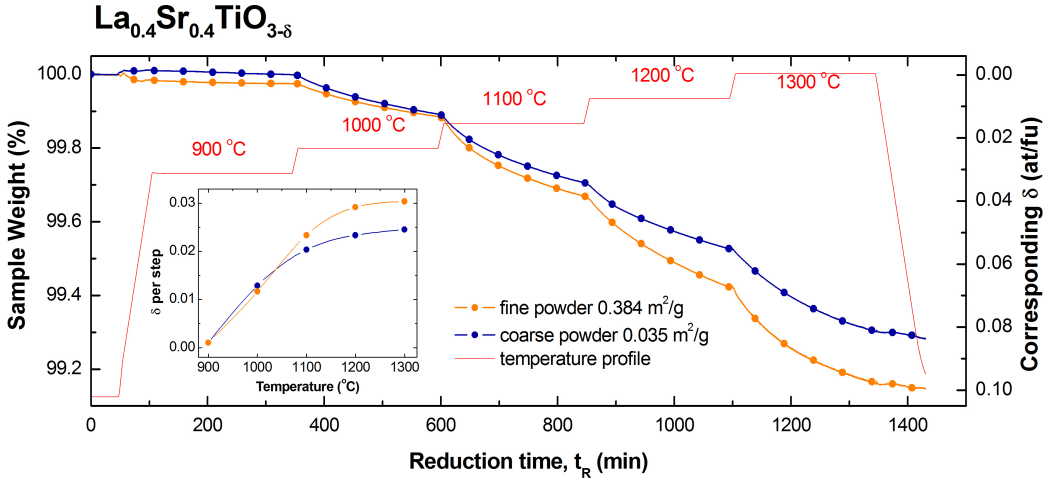

Figure 5-2 | TGA experiment performed on two$La_{0.4}Sr_{0.4}TiO_3$ powders with different specific surface area (0.035 and 0.384 m^2/g). The data was collected at 4 h isothermal steps at 900, 1000, 1100, 1200 and 1300 °C, under 5%H_2/Ar flow. The insets show a plot of δ per temperature step as a function of reduction temperature, as well as the XRD pattern of the fine powder after the experiment was finished.

The difference in reduction kinetics is most likely due to the much higher contact area between the gas phase and the material in the case of the fine powder. Also, it is important to highlight here the magnitude of the achieved oxygen deficiency, $\delta \sim 0.10$ at/fu, which is quite a substantial value considering the perovskite already had $\alpha = 0.2$ A-site deficiency. Since the amount of oxygen deficiency achieved during high temperature reduction appears to be preserved upon cooling to room temperature ("*frozen-in*" – see

Figure 5-2), both samples were analysed *via* XRD at room temperature. XRD may reveal if doping such a considerable amount of oxygen vacancies during the high temperature reduction altered the perovskite structure. As demonstrated by Figure 5-3 which shows the XRD pattern of the fine powder after the TGA experiment, the perovskite structure only became slightly more distorted but largely retained its quasi-cubic structure (slight rhombohedral distortion) implying that $\alpha = 0.2$ and $\delta = 0.1$ deficiency values may coexist in perovskites.

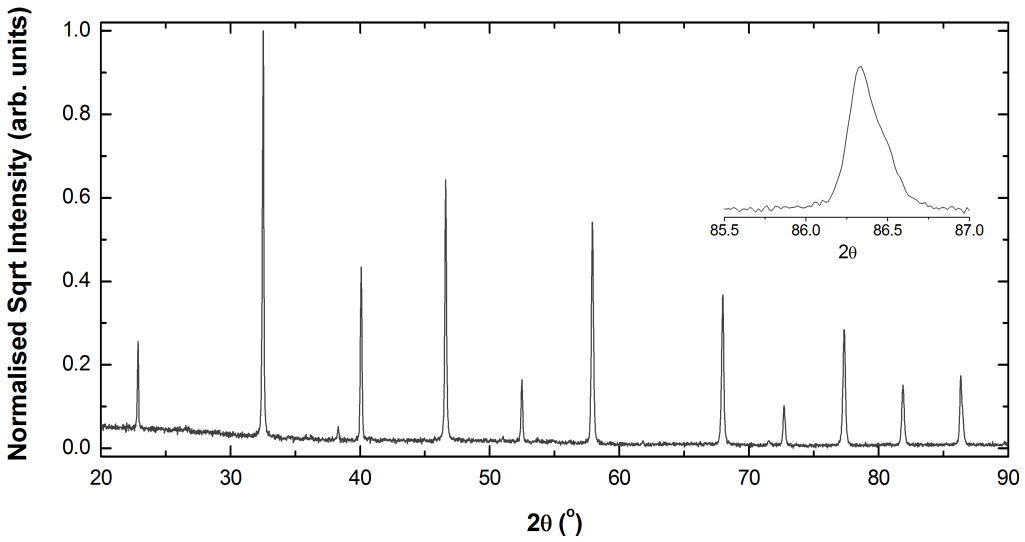

Figure 5-3 | XRD pattern of the fine $La_{0.4}Sr_{0.4}TiO_3$ powder used in the TGA experiment described in Figure 5-2.

However, a critical observation should be made here regarding the stability of this defect-rich perovskite. While XRD did not reveal any phase segregation from the A-site deficient perovskite phase, SEM analysis demonstrated that phase segregation does occur to a small extent locally, and on sufficiently small scale as to preclude identification by XRD. As illustrated in Figure 5-4, it was found that this A-site deficient perovskite ($La_{0.4}Sr_{0.4}TiO_3$) *exsolves* nanoparticles when reduced beyond a certain extent. Most likely this is due to the inability of the perovskite to accommodate a large number of defects on the A- and O-sites simultaneously, which *locally* may result in some of the B-site species precipitating:

$$A_{1-\alpha}BO_3 \xrightarrow{Reduction} A_{1-\alpha}BO_{3-\delta} \xrightarrow{Further\ Reduction} A_{1-\alpha}BO_{3-\delta_{lim}} \xrightarrow{Exsolution} (1-\alpha)ABO_{3-\delta'} + \alpha BO_{\xi} \quad \text{Eq. 5-13}$$

While this might appear as an undesirable phase segregation phenomenon, it will be shown in future chapters that it can be taken advantage of and employed in engineering perovskite surfaces decorated with uniformly dispersed nanoparticles of different composition.

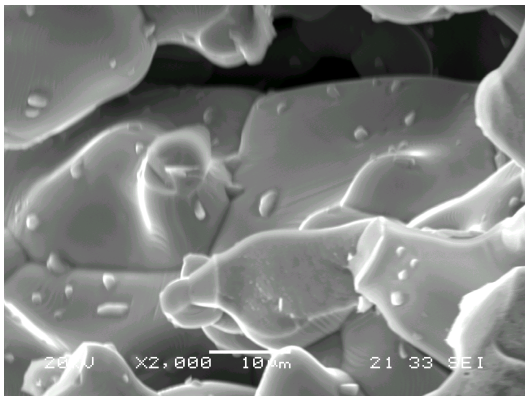

Figure 5-4 | $TiO_{2-\delta}$ nanoparticles exsolved from $La_{0.4}Sr_{0.4}TiO_3$ after reduction in 5%H_2/Ar, at 1100 °C.

Returning now to the TGA experiment, it should be noted that while the overall symmetry did not seem to change considerably, the cell parameter of reduced $La_{0.4}Sr_{0.4}TiO_3$ samples did, expanding as the extent of reduction increases. Figure 5-5 shows a plot of the pseudocubic cell parameter of $La_{0.4}Sr_{0.4}TiO_3$ as a function of the extent of reduction over the range $0 < \delta < 0.1$. On the upper x axis, the corresponding number of Ti^{3+} ions (at/fu) generated through reduction is also shown. As shown in Chapter 4, Ti^{3+} doping causes a linear increase in cell parameter for $La_{0.4}Sr_{0.4}TiO_3$, obeying Eq. 4-10 closely. Equations such as these could be used to determine the extent of reduction in samples by finding the cell parameter from XRD and calculating back the concentration of Ti^{3+} ions or oxygen deficiency. This method should be particularly useful were TGA measurements cannot be performed due to the size or geometry of the sample or, as a non-destructive post-test analysis on devices containing materials in reduced state.

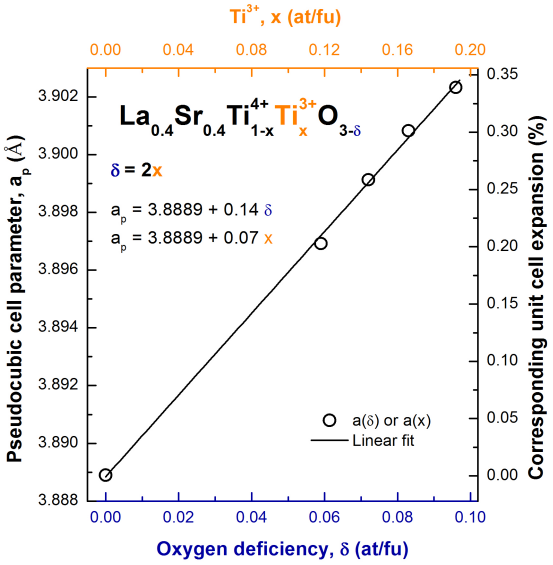

Figure 5-5 | Pseudocubic cell parameter a_p and corresponding unit cell expansion as a function of the extent of reduction δ for $La_{0.4}Sr_{0.4}TiO_3$. The number of Ti^{3+} doped corresponding to the extent of reduction shown on the bottom x axis is given at the top x axis. The errors are smaller than the points.

Another aspect that draws attention while examining Figure 5-2 is that for temperatures in excess of 1000 °C, in spite of having different reduction rates, both the fine and the coarse powders have very similarly shaped δ(t) curves, perhaps indicative of a kinetic behaviour characteristic to the material itself. Indeed, a kinetic model[1,2] composed of two exponentials was found to fit reasonably well all of the isothermal curves (temperatures > 900 °C):

$$m(t) = k_0 + k_{1a} \cdot e^{-k_{1b} \cdot t} + k_{2a} \cdot e^{-k_{2b} \cdot t} \qquad \text{Eq. 5-14}$$

This equation implies two diffusion processes are occurring: process 1 with associated constants k_{1a} and k_{1b}, and process 2 with constants k_{2a} and k_{2b}. The quality of the fits can be examined visually in Figure 5-6 for the case of the coarse sample, while the corresponding coefficients are listed in Table 5-1.

In absence of a wider range of data for each isothermal step, the following interpretations should be taken with some caution. The regression curves suggest that minimum time required for these samples to achieve equilibrium above 1100 °C is 10 h, although between the 4 h used in this

experiment and 10 h there is significantly less weight loss. The time constants in Table 5-1 suggest that process 1 is much faster than process 2 ($k_{1b} > k_{2b}$), but process 2 contributes more to the overall weight loss compared to process 1 ($k_{2a} > k_{1a}$).

Thus, this would imply that process 1 corresponds to surface reduction while process 2 corresponds to bulk reduction. In the light of the interpretation provided by the kinetic equation, surface reduction would indeed be expected to occur faster than the bulk reduction since surfaces are inherently more defective than the bulk, but contribute much less to the overall weight loss since the was majority of the mass of the sample is the bulk component.

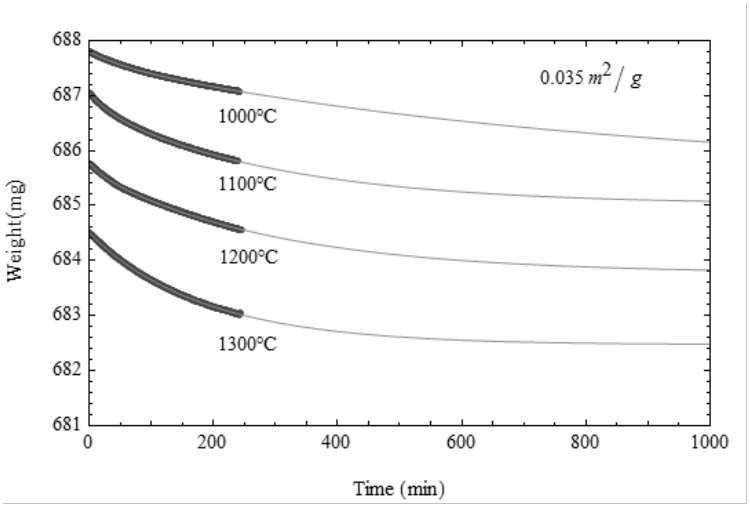

Figure 5-6 | Experimental data (points) and regression fit (continuous line) for the coarse $La_{0.4}Sr_{0.4}TiO_3$ powder TGA analysis shown in Figure 5-2.

Table 5-1 | Fitting parameters obtained for Eq. 5-14 and corresponding to the fitting curves presented in Figure 5-6.

Temperature (°C)	**k_0 (mg)**	**k_{1a} (mg)**	**k_{1b} (min^{-1})**	**k_{2a} (mg)**	**k_{2b} (min^{-1})**
1000	685.526	0.2090	0.0163	2.0663	0.0011
1100	685.018	0.2469	0.0311	1.7893	0.0034
1200	682.346	0.2939	0.0265	3.1373	0.0014
1300	682.466	0.0770	0.0189	1.9692	0.0052

More information about how reduction occurs in $La_{0.4}Sr_{0.4}TiO_3$ can be obtained from the conductivity experiment summarised in Figure 5-7. In this experiment an initially oxidised porous $La_{0.4}Sr_{0.4}TiO_3$ pellet (~ 60% dense) was subjected to reduction in 5%H_2/Ar at high temperature, while its conductivity was measured in a van der Pauw setup. It is important to note that for this composition the direct proportionality $\sigma \propto \delta$ has been validated (to be demonstrated in Chapter 6), and thus any change in (electronic) conductivity will directly reflect the extent of reduction in the material (*i.e.* amount of Ti^{3+} and $V_O^{\cdot\cdot}$ doped).

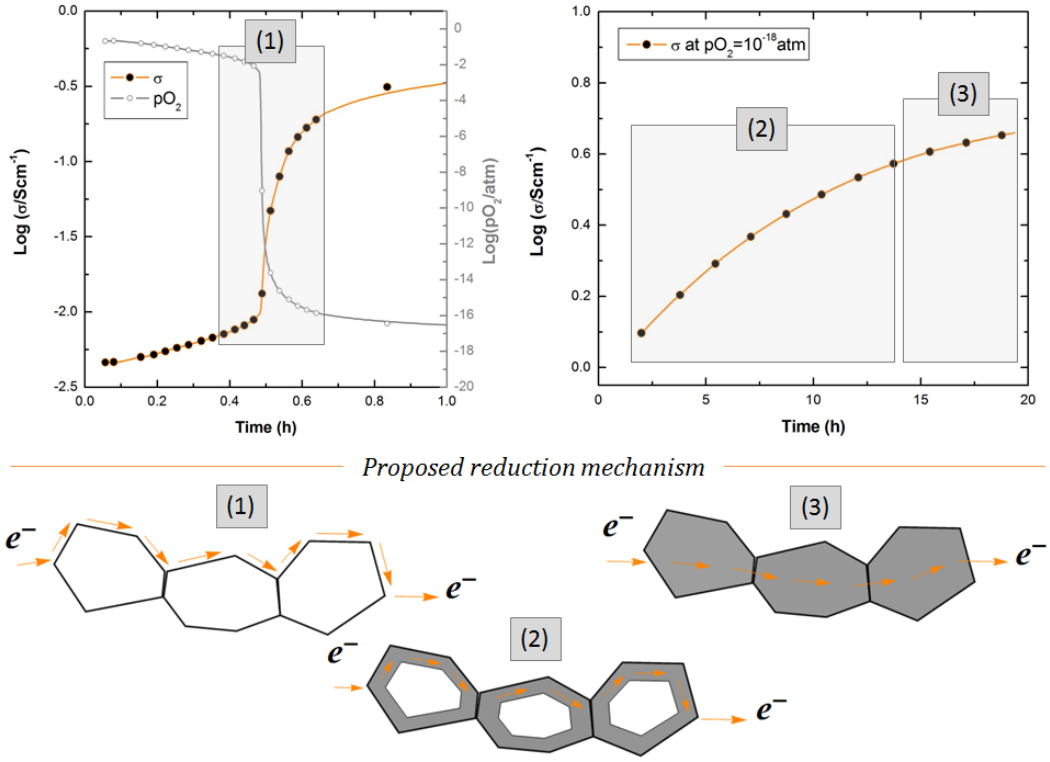

Figure 5-7 | The conductivity of a ~60% dense $La_{0.4}Sr_{0.4}TiO_3$ pellet measured on reduction in 5%H_2/Ar at 900 °C and the associated reduction mechanism proposed here. (1) Upon starting reduction (notice the lowering of the p_{O_2}) the conductivity shows a jump of 1-2 orders of magnitude within minutes, which implies that a thin layer of reduced material quickly covers the grains and acts as conductive path for the flow of electrons. (2) as the reduction proceeds towards the core of the grain, it becomes slower. (3) finally, all the bulk has been reduced and the conductivity does not increase further, reaching equilibrium.

Upon switching from air to reducing atmosphere the conductivity of the sample increases by more than one order of magnitude within 5 minutes and about 2 orders of magnitued within 1 h (left conductivity plot in Figure 5-7). This suggests the surface reaction between the gas phase and the grains is

very fast at this temperature (900 °C), and a thin film of reduced material will cover the surface of the grains rapidly as schematically shown in Figure 5-7 (1). This thin film of reduced and thus conductive material provides a path for the flow of electrons, accounting for the initial rapid increase of the conductivity. Moreover, this also implies that the grain boundaries are subject to the same fast reduction on atmosphere change, acting as conductive paths, rather than blocking features. As the reduction advances towards the core of the grain, the fraction of material that is reduced increases and consequently the conductivity increases as well, Figure 5-7 (2). However, the increase in conductivity is considerably slower at this stage. If in the first stage the conductivity increased by two orders of magnitude within minutes, the conductivity will hardly reach an additional order of magnitude by the end of the process, after a total of ~20 h, at equilibrium (Figure 5-7 (3)). A similar behaviour has been reported and interpreted in a similar manner for an A-site deficient yttrium doped strontium titanate[3] suggesting this behaviour might be general to A-site deficient titanates.

The conclusions reached from this experiment are very similar to the conclusion reached from the TGA experiment. The conductivity measurement presented above clearly distinguishes between a fast surface reduction and a very slow bulk reduction. Since reduction occurs with the removal of oxide ions from the perovskite crstal lattice, it seem that the observations coming from both the TGA and conductivity experiment converge towards the fact that the removal and transport of oxide ions in the bulk of titanates represents the rate determining step in the reduction process, limiting the rate and extent of the reduction. It is therefore worth identifying the key factors that influence it.

5.3 Factors involved in the reduction of perovskites from an atomic scale perspective

The experiments presented in the previous subchapter lead to a simple, easy to visualise model for the reduction in which the transport of oxide ions from the bulk to the surface of the grains was found to be the major controlling factor. The reducing atmosphere (*e.g.* H_2) that surrounds the grains strips oxide ions from the very surface of the perovskite grains, leaving behind oxygen vacancies and electrons. Since numerous oxygen vacancies exist now on the surface of the grains but few or 'none' in the layers beneath (in the bulk), a concentration gradient arises and oxide ions from within the bulk will naturally tend to *migrate* towards the surface to balance out the gradient.

From this perspective reduction should be related to *oxide ion conduction*, as oxide ions migrate across grains either due to difference in concentration or due to electric potential. Thus, the vast literature available on *oxide ion conduction in the perovskite lattice*[4–12] could offer some insight on how *reduction* occurs in the *perovskite lattice*. An overview of oxide ion conduction in perovskites has already been presented in Chapter 2. Here these aspects are briefly recalled in the light of the above mentioned comparison.

Oxide ion conduction (and diffusion) occurs where free oxygen sites are available (*i.e.* oxygen vacancies), by hopping of oxide ions. The diffusion pathway of the oxide ion through an undistorted perovskite is schematically depicted in Figure 5-8 and the factors controlling it can be synthetically expressed through the equation:[8]

$$D_{O^{2-}} \propto [V_O^{\cdot\cdot}] \cdot a^2 \cdot e^{-\frac{\Delta H_f + \Delta H_m + \Delta H_a}{R \cdot T}} \qquad \text{Eq. 5-15}$$

Eq. 5-15 describes oxygen diffusion as a thermally activated process which is proportional to the concentration of available and *mobile* oxygen vacancies, and the square of the cell parameter, a. Thus, higher oxygen mobility should be expected as the cell parameter increases. It should be noted that most of

the doping strategies used here resulted in larger unit cell, as shown in section 4.7, which should be beneficial towards enhanced oxide ion mobility.

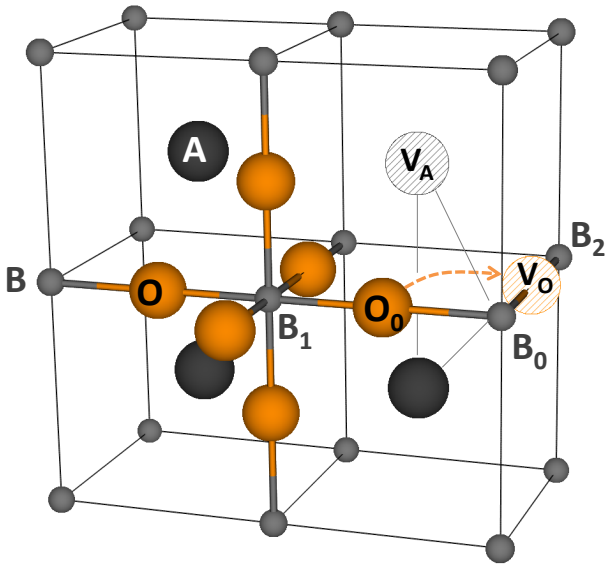

Figure 5-8 | Schematic diagram depicting the migration of the oxide ion in an ideal perovskite. V_A and V_O are used here to label vacant A-site and oxygen site, respectively.

With respect to the effect of temperature on the reduction process, the TGA experiment discussed in section 5.2 already showed that by increasing the reduction temperature the extent of reduction increases. This is demonstrated by the experiment presented in Figure 5-9 as well, in which $La_{0.4}Sr_{0.4}TiO_3$ pellets of varying porosity (~95% to ~55% dense) were reduced at different temperatures: 1100, 1200 and 1300 °C. Clearly, as the relative density of the samples increased, the achieved oxygen deficiency was far away from the equilibrium value. Thus, for minimizing the time required to reduce such samples porous microstructures (or fine powders) are desirable.

Diffusion also depends on three main processes and their associated thermal effects: *formation* (ΔH_f), *migration* (ΔH_m), and *association* (ΔH_a) of vacancies. The way these factors come into play can be better understood by examining Figure 5-8. Figure 5-8 depicts four adjacent ideal perovskite cells (B-site cations in corners, A-site cations in center of the 'cubes') in which most of the

oxide ions have been omitted for clarity. B-site cation labeled 'B_1', however, is shown with a full 6-fold coordination sphere.

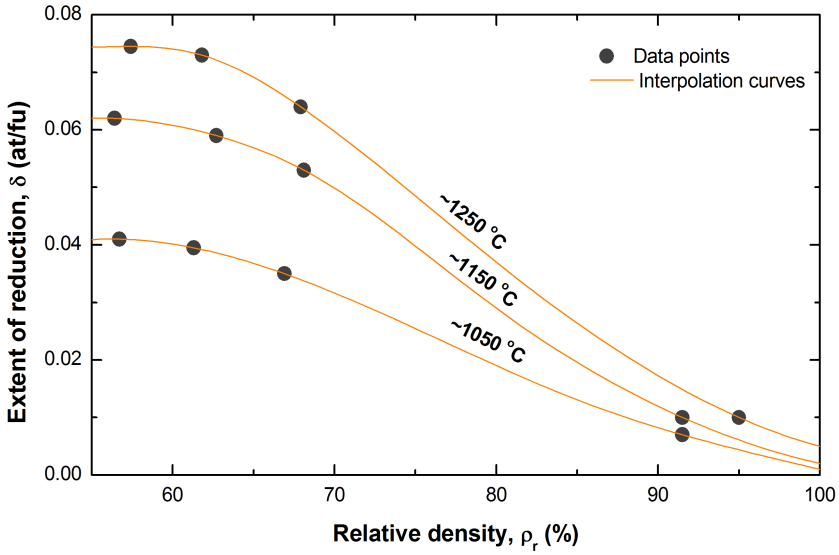

Figure 5-9 | Extent of reduction *vs.* the relative density of porous and dense $La_{0.4}Sr_{0.4}TiO_3$ pellets pre-reduced at different temperatures (1050, 1150 and 1250 °C) for 10 h, under continuous 5%H_2/Ar flow. The errors are of the size of the points. The curves represent interpolations derived from the data points.

Oxide ion diffusion can be visualized as follows. When the oxide ion labeled 'O_0' starts moving from its position towards the oxygen vacancy labeled 'V_0', it will have to break the bond shared with the adjacent B_1 cation. However, this step not only assumes that a strong B-O bond needs to be broken, but also that the coordination number of the B_1 cation is lowered from 6 to 5. Thus, the bond strength of B-O bonds and the ability to adopt coordination numbers lower than 6 (*e.g.* 5 or 4 depending on the surrounding defects) are among the first factors that emerge as potentially important for reduction. The latter aspect is also referred to as *cation coordination flexibility*. While bond strengths can be determined experimentally or calculated, coordination flexibility is not generally linked to a measurable parameter. An approach for the quantification of this term will be proposed in section 5.8. It should be added here that most of the cations that typically substitute on the B-site of perovskites tend to form strong bonds with oxygen and strongly prefer 6-fold coordination. As a result, the energy required for the formation of the vacancy is high. Ti^{4+} is a typical example of such a cation. Although the

stability of the Ti^{4+}–O bond is detrimental for achieving high extents of reduction or promoting oxide ion mobility, it also confers the remarkable stability of the titanates. On the contrary, other cations such as Mn, Co, Ga etc are known to be stable in coordination numbers lower than 6 as well,[13] and have been successfully employed in the design of materials with good oxide ion mobility.[14,15]

Once the B_1–O_0 bond has been broken, the oxide ion will have to *migrate* through the triangle described by the two A-site cations and the B-site cation (here one of the A-sites is vacant and hence labeled 'V_A'). Throughout this migration O_0 remains equidistant to B_0, describing a curved path towards V_O. In oxide ion conduction, this is one of the most energy intensive steps because of the considerably larger size of the oxide ion compared to the 'inner opening' of the A-B-A triangle.[5,8,10,11] As a consequence, factors such as the nature of the A-site cations (electronic structure, size etc) and the distortions of the lattice are expected to play an important role at this stage. Several studies suggest that the highest mobility for vacancy hopping should be expected in lattices exhibiting high symmetry where repulsing effects are minimal.[5,9,11] Thus, with respect to oxide ion migration, two factors should be considered to potentially impact reduction: the A-site cations with the A-B-A triangle and lattice distortion. From this perspective, A-site deficient perovskites offer from the start an interesting context since some of the A-site are vacant and thus some of the A-B-A triangles should be missing one vertex, potentially diminishing diffusion barriers. The impact of A-site vacancies on reduction will be discussed further in subchapter 5.6. In terms of lattice distortion it should be noted that all of the doped A-site deficient compositions prepared here show only slight distortion (except $La_{0.8}Ce_{0.1}Ni_{0.4}Ti_{0.6}O_3$) which is expected to diminish and eventually revert to cubic even before the typical reduction temperature is reached, 900 °C. This is because the A-O bonds expand much more than the B-O bonds with temperature; therefore symmetry also increases with temperature (see discussion in section 2.2.2 and references therein).

At low concentrations, the interaction between defects is negligible. However, when in sufficiently large numbers (see subchapter 5.5 also), defect-defect interactions can become a dominant factor in the energy requirements for ionic movement. These interactions usually manifest themselves as *associations* between defects of the same type and/or between defects of different nature. Associations can be local or extended over significant distances, in either cases potentially leading to an increase of the term ΔH_a and consequently the number of mobile vacancies becomes smaller than the stoichiometric one. Generally it is when defects are randomly distributed, not ordered, that oxide ion mobility is at a maximum. The effect of defect association on reduction is discussed in subchapter 5.6. Trapping can also occur due to size mismatch between host and dopant.[16] Where the size of the host and dopant are similar, for example when substituting Sr^{2+} (1.44 Å) for La^{3+} (1.36 Å) in lanthanum gallates, ΔH_a has been calculated to be zero.[16]

5.4 Enhancing the extent of reduction *via* dopants that promote oxide ion mobility

In the light of the arguments presented in the previous subchapter, various dopants were selected and doped in the $La_{0.4}Sr_{0.4}TiO_3$ perovskite in order to enhance its extent of reduction. This subchapter explains the thought process behind some of the choices in terms of dopants and doping strategies, and, of course, the results of doping. The following chapters aim to explain some of the trends observed in these results based on the parameters anticipated as important from the 'microscopic scale' perspective on reduction which was presented in subchapter 5.3.

Cations M^{m+} were doped on the B-site of the $La_{0.4}Sr_{0.4}TiO_3$ perovskite in two different ways: (**A**) mainly by compensating the charge difference between M^{m+} and the host cation (Ti^{4+}) by oxygen vacancies, $La_{0.4}Sr_{0.4}M_x^{m+}Ti_{1-x}^{4+}O_{3-\gamma}$, where $\gamma = \frac{4-m}{2} \cdot x$; and (**B**), for selected dopants, based on phase purity

considerations as explained in section 4.3, the charge difference between the dopant and the host was compensated by balancing the charge among the A-site cations, as exemplified in section 4.4, leading to the series $La_{0.4+x\cdot(4-m)}Sr_{0.4-x\cdot(4-m)}M_x^{m+}Ti_{1-x}^{4+}O_3$. The outcome of doping in both approaches is presented in Figure 5-10 (a) and (b), respectively, as extent of reduction as a function of dopant M^{m+} stoichiometry, x.

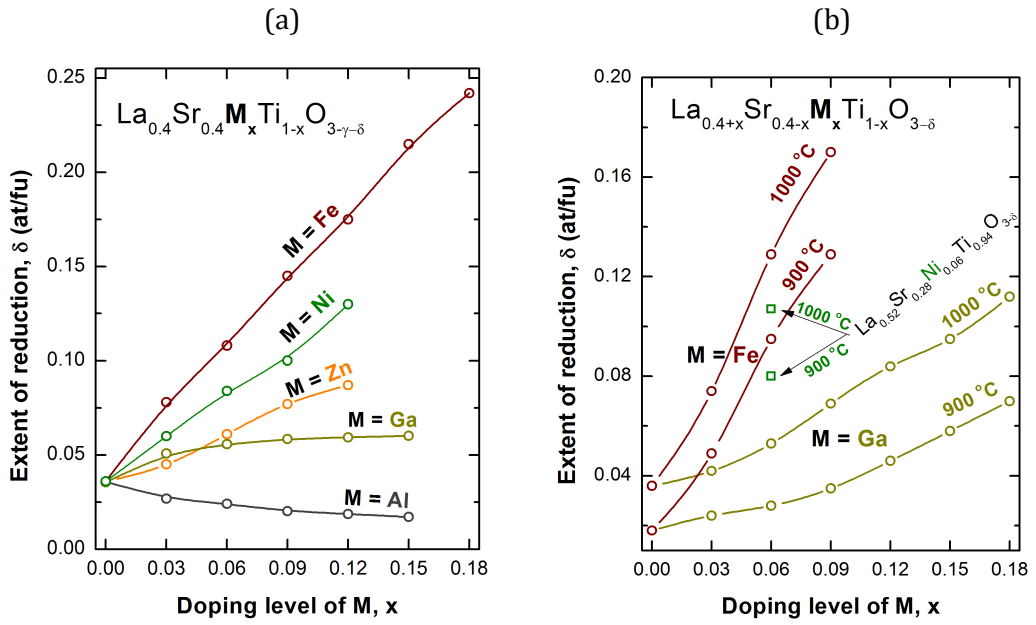

Figure 5-10 | The extent of reduction plotted against dopant stoichiometry for various M-doped $La_{0.4}Sr_{0.4}TiO_3$ systems. (a) M-doping was compensated by the creation of oxygen vacancies leading to the series $La_{0.4}Sr_{0.4}M_x^{m+}Ti_{1-x}O_{3-\gamma}$, where $\gamma = \frac{4-m}{2}\cdot x$ All the compositions were reduced in 5%H_2/Ar, at 1000 °C (20 h). (b) M-doping was compensated by balancing the stoichiometry of the A-site cations, leading to the series $La_{0.4+x\cdot(4-m)}Sr_{0.4-x\cdot(4-m)}M_x^{m+}Ti_{1-x}^{4+}O_3$, from which the members M^{m+} = Fe^{3+}, Ga^{3+} and Ni^{2+} were prepared and analysed here. The samples were reduced in 5%H_2/Ar, at the temperatures indicated on the curves for 20 h. In both cases the errors are of the size of the points and the curves represent interpolations derived from the data points.

The first strategy used was approach (A) and the first dopant chosen was Ga^{3+}. The main reason behind this choice was that Ga was the main component of the B-site of the well-known perovskites LSGM, $La_{1-x}Sr_xGa_{1-y}Mg_yO_{3-(x+y)/2}$ which is known to exhibit very high ionic conductivity around 900 °C,[4,17] the usual reduction temperature in this study. Thus, Ga^{3+} should favour to oxide ion mobility when substituted in the perovskite lattice. As expected, upon increasing Ga doping in $La_{0.4}Sr_{0.4}Ga_xTi_{1-x}O_{3-\gamma}$, the extent of reduction δ also increased (Figure 5-10

(a)). The increase reached a plateau, however, around $x = 0.09$. This aspect and other particularities related to Ga-doping will be extensively discussed in the dedicated subchapter 5.11.

The next dopant chosen was Zn^{2+} on the basis that Ga^{3+} and Zn^{2+} should be isoelectronic, and should thus exhibit similar properties, with the difference that Zn^{2+} should develop weaker bonds with oxygen because of the lower charge. Indeed, as Zn doping increases in $La_{0.4}Sr_{0.4}Zn_xTi_{1-x}O_{3-\gamma}$, up to $x = 0.06$ the δ values reached are close to the case of Ga-doping, but above that, the performance of the Zn-doped series clearly exceeds that of Ga-doped series (Figure 5-10 (a)).

For contrast, Al^{3+} doping was also considered. Al^{3+} has the same (fixed) charge as Ga^{3+} but much smaller ionic radius, $r(Al^{3+}_{CN=6}) = 0.535$ Å $< r(Ga^{3+}_{CN=6}) = 0.605$ Å. This should result in Al^{3+} exhibiting a stronger attraction field on the neighbouring oxygen ions compared to Ga^{3+} which should result in stronger Al-O bonds. Indeed, as Al doping increases in $La_{0.4}Sr_{0.4}Al_xTi_{1-x}O_{3-\gamma}$, the extent of the reduction gradually decreases, the overall trend $\delta(x_{Al})$ seeming a mirror image of the trend for the Ga doped series, $\delta(x_{Ga})$ (see Figure 5-10 (a)).

Transition metals were also investigated, and among them Fe-doping is shown as next example. Transition metal oxides (with partly filled *d*-shell) are well known for their predisposition towards oxygen nonstoichiometry, partly due to average M-O bond strengths and coordination number flexibility.[18,19] Fe doping lead to the highest extent of reduction observed in the family of compounds investigated here, with much better δ values compared to the dopants discussed so far (Figure 5-10 (a)). Remarkably, δ increase linearly with x in the case of Fe doping, $La_{0.4}Sr_{0.4}Fe_xTi_{1-x}O_{3-\gamma}$ for the entire range $0 < x < 0.18$. Similar trends were observed irrespective of reduction temperature or p_{O_2}. Figure 5-11 shows the extent of reduction for the $La_{0.4}Sr_{0.4}Fe_xTi_{1-x}O_{3-\gamma}$ series at different reduction temperatures, 900 and 1000 °C in either dry or humidified 5%H_2/Ar (3% H_2O). Since the driving

force for the reduction, the p_{O_2}, is orders of magnitude smaller in the case of the humidified gas ($p_{O_2} \sim 10^{-16}$ atm), compared to the dry gas ($p_{O_2} \sim 10^{-20}$ atm), the δ values are considerably smaller in the case of the reduction carried out in humidified gas.

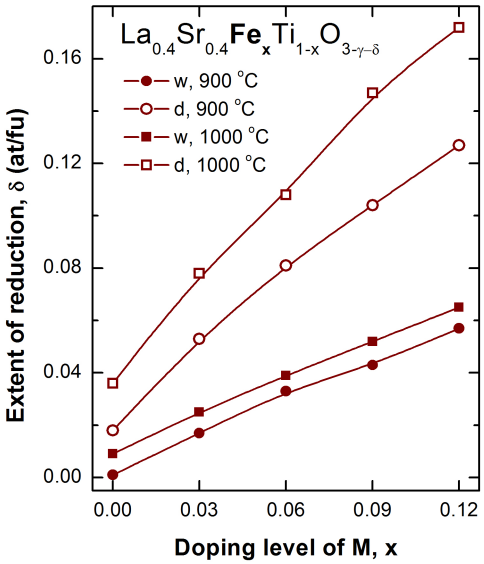

Figure 5-11 | The extent of reduction *vs.* the dopant stoichiometry for several members of the series $La_{0.4}Sr_{0.4}Fe_xTi_{1-x}O_{3-\gamma}$ reduced in various conditions. 'd' indicates samples were reduced in dry 5%H_2/Ar, while 'w' indicates that reduction was carried out in humidified 5%H_2/Ar (3% H_2O).

For doping approach (B), Ga^{3+}, Ni^{2+} and Fe^{3+} were selected as dopants. Their $\delta(x)$ variations are shown in Figure 5-10 (b), this time for both 900 and 1000 °C reduction temperatures. Figure 5-10 (b) shows that in the case of doping approach B the effectiveness of dopants in enhancing reduction increases from Ga to Ni and further to Fe. This trend is similar to the one found for doping approach A and discussed in the previous paragraphs. However, the same dopants, in the new stoichiometries show even higher δ values. It should be noted however that while the A-site deficiency values are the same, the ratio between La and Sr is required to change so that the dopant charge is compensated.

A comparison between Figure 5-10 (a) and Figure 5-10 (a) offers interesting insights into the dramatic effect on properties achieved through doping. Thus, for example, the undoped composition, $La_{0.4}Sr_{0.4}TiO_3$, achieves

$\delta = 0.036$ at/fu when reduced at 1000 °C. As little as 3% Fe doping, as in $La_{0.43}Sr_{0.37}Fe_{0.03}Ti_{0.97}O_3$, leads to much higher δ value, $\delta = 0.049$ at/fu, at the lower reduction temperature of 900 °C. Or, with as little as 6% Ni doping, as in $La_{0.52}Sr_{0.28}Ni_{0.06}Ti_{0.94}O_3$, the extent of reduction becomes more than double the magnitude, reaching $\delta = 0.08$ at/fu, again at the much lower reduction temperature of 900 °C as compared to the undoped titanate $La_{0.4}Sr_{0.4}TiO_3$.

Several other B-site dopants where then considered, based on 'chemical' similarity with previous choices or simply in an attempt to cover most of the first transition metal series and to investigate if certain trends emerged. The results of these experiments are summarised in Figure 5-12. In this figure δ is plotted as a function of metal dopant M, for various members belonging to the series $La_{0.4}Sr_{0.4}M_xTi_{1-x}O_{3-\gamma}$, having fixed doping ratio of $x = 0.06$. The dopants M are listed in the order of increasing atomic number. This is the same succession as in the periodic table and is used here in order to reveal trends that might correlate with *periodic* properties of the elements or corresponding cations.

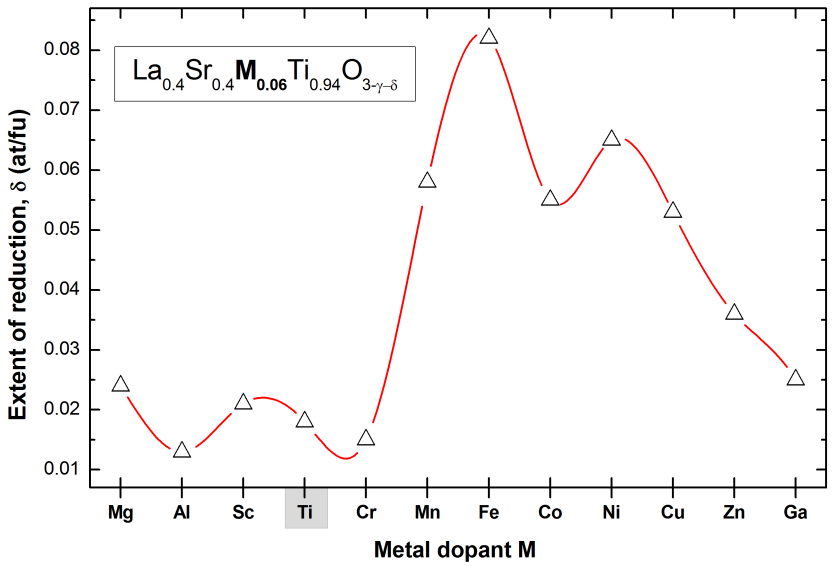

Figure 5-12 | The extent of reduction plotted against the dopant M (in the order of their atomic number) for the series $La_{0.4}Sr_{0.4}M_xTi_{1-x}O_{3-\gamma}$. Reduction was carried out in 5%H_2/Ar, at 900 °C, for 20 h. The errors are smaller than the points and the red curve represents an interpolation derived from the data points.

Examination of Figure 5-12 reveals that the selected dopants display a wide range of δ values at the reduction temperature of 900 °C, from just under 0.01 at/fu to slightly over 0.08 at/fu. Starting from lower atomic numbers, and compared to the host (Ti), Mg improves δ just slightly, but still more than Sc does. As discussed before, Al doping is severely detrimental for reduction and hence its position in the plot. Cr is the only true transition metal dopant (partly filled *d*-shell) to cause a decrease in δ compared to the host. This is perhaps not surprising considering the well-known stability of the chromates and lack of oxygen nonstoichiometry.[14,20] From Cr to Mn there is a significant increase in extent of reduction, which further increases going to Fe. Ni appears to be the second best dopant for enhancing δ, while the dopants following it in the periodic table gradually cause a decrease in δ.

Given the interesting variation of δ as a function of M displayed in Figure 5-12, it will be further analysed in the next subchapters seeking to uncover the main factors that govern this trend, which in turn would provide useful insight into the key factors that control the extent of reduction of perovskites.

5.5 The meaning of doping levels in perovskites – visualising doping in the crystal lattice

One of the first observations to arise after examining Figure 5-12 is that as little as 6% doping lead to a wide variation range for δ. So the question is *how much is as little as 6% B-site doping*?

The fact that 'as little as 6% doping' actually has a profound effect on the structure and properties of resulting materials can be better understood by looking at one of the cases in which doping had negative impact, namely Cr-doping. Thus, from Figure 5-12, the undoped composition $La_{0.4}Sr_{0.4}TiO_3$ exhibits δ = 0.018 at/fu. This means that $2 \cdot \delta = 0.036$ Ti^{3+}, or roughly 4% Ti^{3+} ions were introduced through reduction. When 6% Cr^{3+} is doped, δ = 0.015 at/fu, thus 3% Ti^{3+} were doped in this case upon reduction. So, in the undoped composition, initially 100 out of 100 B-sites are occupied by

Ti^{4+}, upon doping this comes to 4 Ti^{3+} ions and 96 Ti^{4+} ions. In the Cr-doped system, among the initially 100 B-sites 94 are Ti^{4+} and 6 are Cr^{3+}, which upon reduction changes to 91 Ti^{4+}, 3 Ti^{3+} and 6 Cr^{3+}. So the question arises: *among the initially 94 Ti^{4+}* ions in the Cr-doped system, can't we find *4 Ti^{4+}* that do not 'feel' the *negative influence of the 6 Cr^{3+}* ions such that they reduce to 4 Ti^{3+} ions, not just to 3 Ti^{3+} ions? How come chromium's influence is felt so strongly?

To gain a better understanding of the true meaning of doping in the perovskite structure, the following reasoning was used. The ideal perovskite crystal structure can be visualised as an array of cubes, each cube being one unit cell, containing one ABO_3 unit, having either the A-site cation in their centre or the B-site cation, as explained in Chapter 2. Since the B-site is important here, a perovskite unit cell with the B-site in its centre was used, as shown in Figure 5-13. Red was used to highlight the cells where the host was replaced by a dopant.

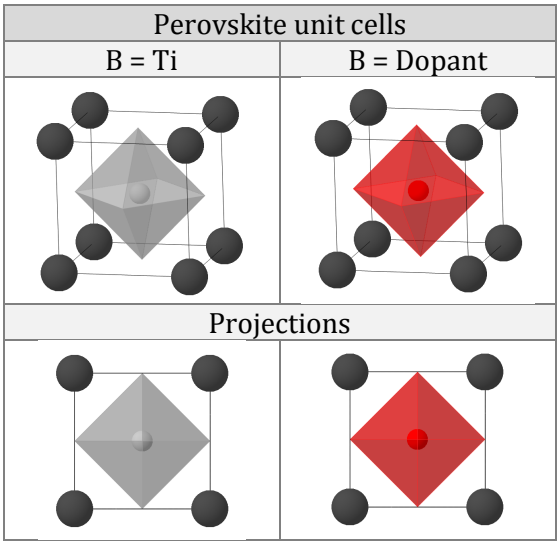

Figure 5-13 | Ideal perovskite unit cells drawn with the B-site in the centre of the cubic unit cell. The grey TiO_6 octahedra represent the host cations, Ti^{4+} and the red ones represent the ones in which the B-site is actually occupied by the dopant.

6% means 6 in 100 unit cells contain dopants, or roughly that among 17 unit cells 1 must contain the dopant. If the crystal lattice of perovskites developed in only one dimension, then 1 dopant in 17 cells would be visualised and represented as in Figure 5-14 (a). The B-site dopants would be very apart

from each other and they would each influence 2 neighbouring host cations. If the crystal lattice of perovskites was two-dimensional (2D - Figure 5-14 (b)), then 1 dopant should be found in each $\sqrt{17} \times \sqrt{17}$ array of cells, or roughly 1 dopant in each 4×4 array of cells. In this case the dopants are considerably closer to each other and have more surrounding host cations meaning that their influence extends over more of the host cations. However, in reality, the perovskite structure extends in all three orthogonal directions, hence, on average, 1 dopant should be found in each $\sqrt[3]{17} \times \sqrt[3]{17} \times \sqrt[3]{17}$ array of cells, which means 1 dopant in each $\sim 2.5 \times 2.5 \times 2.5$ cluster of cells.

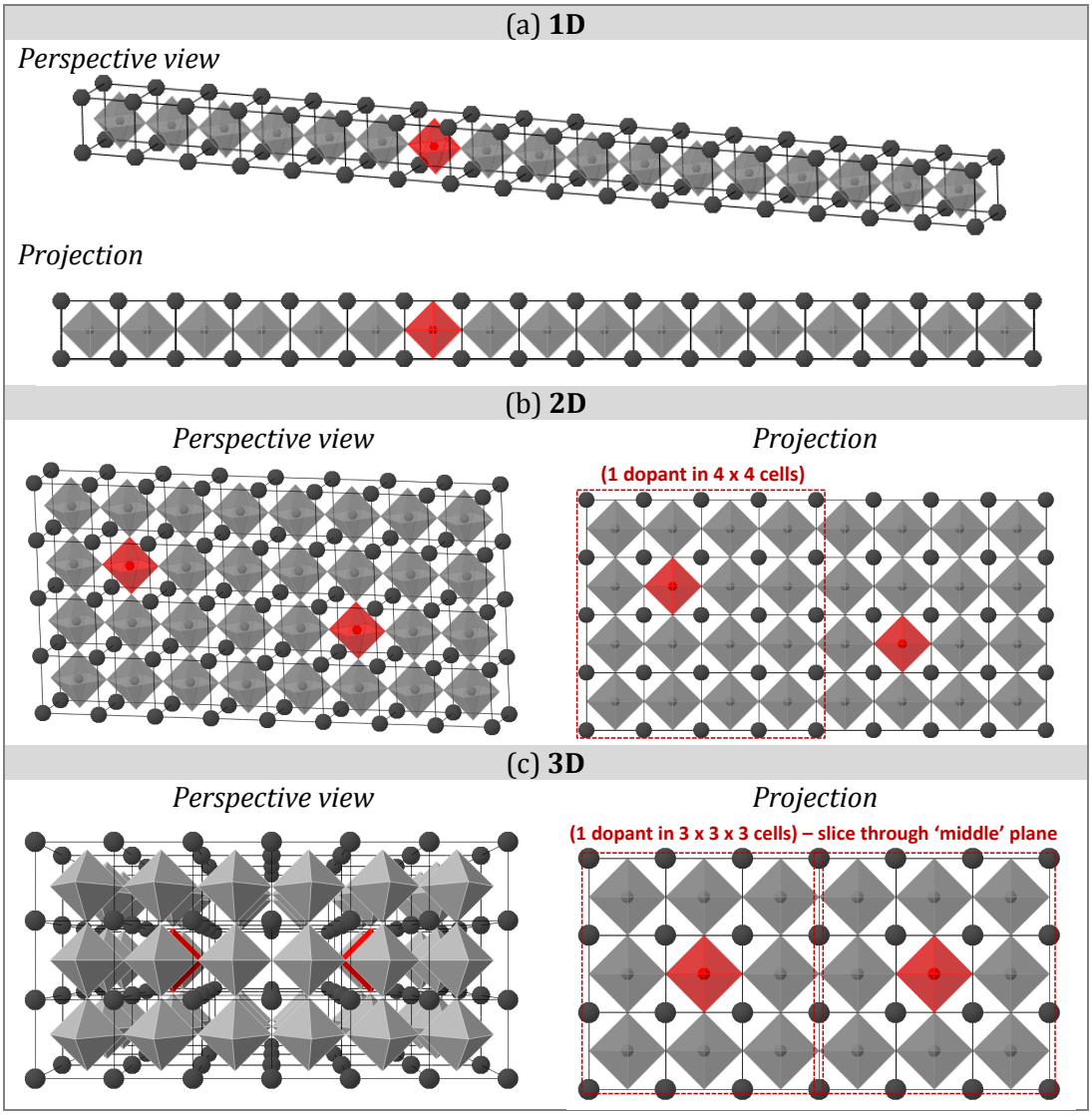

Figure 5-14 | Suggested ways to visualise 6% B-site doping in an ideal ABO_3 perovskite according to various scenarios: (a) the perovskite is a one-dimensional (1D) array of unit cells; (b) the perovskite is a two-dimensional (2D) array of unit cells; (c) the perovskite is a three-dimensional (3D) array of unit cells.

For simplicity, let us consider an integer number of cells for this case, for example 1 dopant in $3 \times 3 \times 3$ cells, which means that the dopant is now regarded as being more diluted than it is in reality. This scenario is presented in Figure 5-14 (c). From this figure it becomes clear that in a real perovskite 6% B-site doping means that roughly 1 dopant should be found in each $3 \times 3 \times 3$ cluster of unit cells, and if the dopant is *homogenously* and *regularly* distributed down to this scale, then each two dopants are separated by no more than two host cations, and effectively the vast majority of host cations cells are directly or in the direct proximity of doped cells. This perspective clearly explains why 'as little as 6% doping' can cause such a dramatic impact on properties.

Moreover, an important function can be derived from the reasoning presented above:

$$n(x) = \sqrt[3]{\frac{1}{x}} \qquad \text{Eq. 5-16}$$

Where x is the doping stoichiometry in a perovskite (*e.g.* $AM_xB_{1-x}O_3$) and the function $n(x)$ gives the 'edge-number' of a hypothetical cube array of perovskite unit cells that contain one dopant (in the assumptions discussed). For example, a doping stoichiometry of $x = 0.125$ (equivalently 12.5%) means that 1 dopant can be found (ideally, on average) in each distinct $2 \times 2 \times 2$ array of cells ($\sqrt[3]{\frac{1}{0.125}} = 2$). A plot of $n(x)$ is given in Figure 5-15, together with a visual representation of the $n(x) \times n(x) \times n(x)$ arrays.

Thus, the stoichiometry $x = 0.015$ (or 1.5%) corresponds to one dopant being contained by an array of $4 \times 4 \times 4$. This corresponds to very dilute doping where the dopant does not exert influence over a significant number of host cations. At $x = 0.037$ (or 3.7%), the number of unit cells in which 1 dopant can be found has decreased to $3 \times 3 \times 3$. Ideally, if the dopants were to be distributed *homogenously* and *periodically* like depicted in Figure 5-15, each two consecutive dopants should be separated by two host cation cells, in

each of the three orthogonal directions, meaning that the vast majority of host unit cells are in direct contact with a doped unit cell. $x = 0.125$ (12.5%) corresponds to another important point on the $n(x)$ curve where 1 dopant is contained in an array of $2 \times 2 \times 2$ cells. Again, if the dopants were to be distributed *homogenously* and *periodically* like depicted in Figure 5-15, then a doped cell would be alternating with an undoped cell in each orthogonal direction.

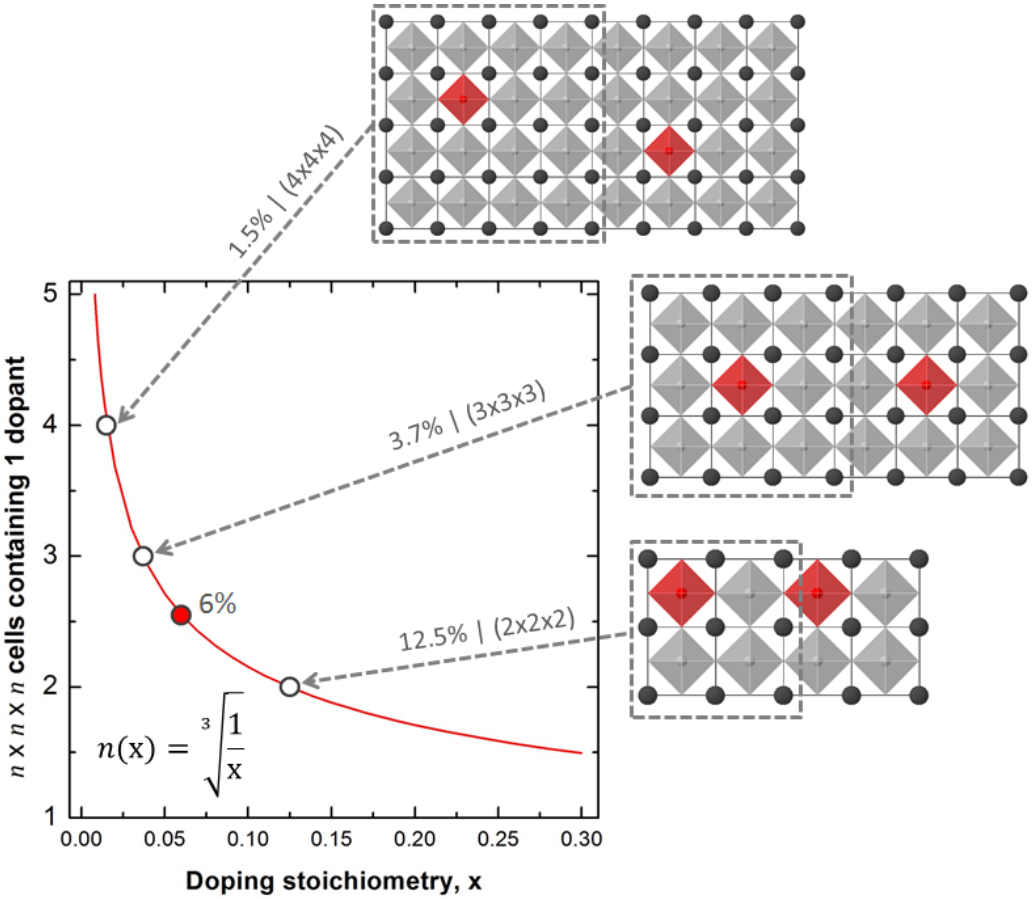

Figure 5-15 | The correlation between dopant stoichiometry (*e.g.* x in $AM_xB_{1-x}O_3$) and the number of primitive perovskite unit cells (containing an $AM_xB_{1-x}O_3$ unit) that make up the three-dimensional array of primitive perovskite unit cells which contain one dopant. Special cases are emphasized on the curve and illustrated with projections of the corresponding 3D structures (slice through selected planes based on the simplifications discussed in the text).

The approach presented here and exemplified through Figure 5-15 provides a simple, albeit it idealised manner to translate doping stoichiometry into a visual representation of dopant occurrence at an atomic level, in the perovskite crystal structure. It can be used for both A- or B-site doping since the perovskite unit cell can be regarded as having the A- or B-site cation,

respectively, in its centre. This includes A-site vacancies. Among other benefits, this approach should provide useful insight into the understanding of property – doping level relationships, the chances for cation or defect ordering, and provide an overall image on the extent of disruption certain doping levels can exert on the host cation sublattice.

5.6 The importance of *defect ordering* in reduction

As anticipated in subchapter 5.3, ordering of defects can have a profound impact on oxide ion mobility and hence on reduction. The best example of the effect of ordering on reduction was found in this study for the case of the $La_xSr_{1-3x/2}TiO_3$ series. The link between defect ordering and the extent of reduction is suggested in Figure 5-16 and explained below.

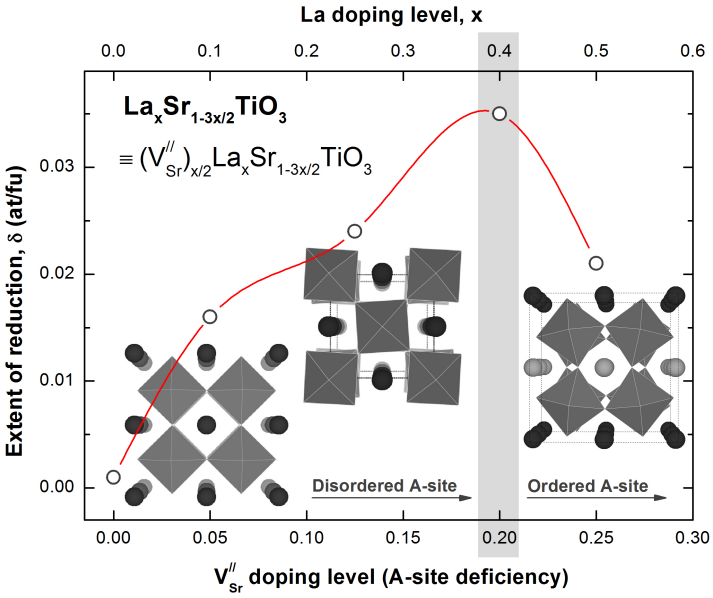

Figure 5-16 | The impact of defect ordering on reduction highlighted by plotting the extent of reduction against the A-site vacancy (V''_{Sr}) stoichiometry in the series $(V''_{Sr})_{x/2}La_xSr_{1-3x/2}TiO_3$. Reduction was carried out in 5%H_2/Ar, at 1000 °C (20 h). The insets depict generic crystal structures representative for different regions of the compositional range: cubic for $0 \leq x \leq 0.1$, tetragonal for $0.1 < x \leq 0.4$ and orthorhombic with A-site vacancy ordering for $x > 0.4$.The errors are of the size of the points. The red curve represents an interpolation derived from the data points.

Figure 5-16 shows that as the number of doped A-site vacancies increases in the series $(V''_{Sr})_{x/2}La_xSr_{1-3x/2}TiO_3$ (by substituting Sr with La), the extent of reduction increases as well, up to $x \sim 0.4$, or A-site deficiency $\alpha = \frac{x}{2} = 0.2$.

The beneficial effect of the A-site vacancies towards reduction up to a concentration of $\alpha \sim 0.2$ can be explained in two ways. It is likely that the large number of V''_{Sr} imposed through doping limits the number of intrinsic Schottky defects which in turn pushes Eq. 5-17 to the left and thus decreases the number of $V^{\cdot\cdot}_{O}$. For a given p_{O_2}, Eq. 5-18 right to oppose the change, facilitating the removal of lattice oxygen by the reducing gas.

$$Sr^{x}_{Sr} + O^{x}_{O} \rightleftharpoons SrO + V^{\cdot\cdot}_{O} + V''_{Sr} \qquad \text{Eq. 5-17}$$

$$O^{x}_{O} \rightleftharpoons 2e' + V^{\cdot\cdot}_{O} + \frac{1}{2}O_2 \qquad \text{Eq. 5-18}$$

Alternatively, from the perspective of the oxide ion diffusion mechanism detailed in subchapter 5.3, this might be explained as a lowering in the oxide ion migration barrier. Thus, when migrating, the oxide ion must pass through the triangle described by the two A-site ions and the B-site ion (Figure 5-8). However, in this case, a large number of A-sites are vacant and therefore the oxide ion might not be required to pass through a triangle shaped bottleneck, resulting in facilitated diffusion and enhanced reduction.

For α values above ~0.2 the extent of reduction falls dramatically. The position for the maximum in reducibility observed in this study coincides well with the borderline between a *disordered* A-site and an *extensive cation-vacancy ordering* on A-site in this series as revealed by various reports.[21–23] A detailed description of the structural changes that occur across the range of compositions $0.6 < x < 0.6$ was given in section 2.2.3 and will be briefly reviewed here. In the series $(V''_{Sr})_{x/2}La_xSr_{1-3x/2}TiO_3$, the symmetry changes from *cubic* (for $x = 0$) to *tetragonal* for $x \leq 0.4$ and finally to *orthorhombic* for $x > 0.4$. The tetragonal domain is characterised by slight octahedral tilting and randomly distributed A-site vacancies. The orthorhombic structure displays *ordered A-site vacancies* in alternate layers and significant tilting (see insets of Figure 5-16).

In the case of the oxygen excess series $La_xSr_{1-x}TiO_{3+x/2}$, a similar correlation was observed between reduction and ordering.[24] The transition point

between the extended ordering of the intergrowths and the structure where they are randomly distributed is marked by an increase of several orders of magnitude in conductivity, and hence in the extent of the reduction. The breaking of ordering was of significant importance for introducing functionality in this system, which with additional minor improvements could be successfully used as anode in a solid oxide fuel cell running on methane.[24]

5.7 The importance of *bond strength* in reduction

In subchapter 5.3 it was suggested that the bond strength between the B-site cation and oxygen should play an important role in the reduction of perovskites since reduction can only occur if some B-O bonds are broken. The scope of this chapter is to probe if such a connection exists between the extent of reduction of perovskites and the bond strength of the corresponding B-O bond. For this, the amount of oxygen that can be stripped upon reduction (*i.e.* δ) from differently B-site doped perovskites $La_{0.4}Sr_{0.4}M_xTi_{1-x}O_{3-\gamma}$, will be compared to corresponding bond strength of the dopant-oxygen bond (M-O).

An reasonable approximation of the strength of the M-O bond was considered to be given by the atomisation energy (E_{at}) of the corresponding oxide, M_aO_b:

$$E_{at} = \frac{\Delta H_{at}}{a} \qquad \text{Eq. 5-19}$$

Where ΔH_{at} is the atomisation enthalpy corresponding to the reaction:

$$\underbrace{M_aO_{b(s)}}_{M-O\ bonds} \rightarrow \underbrace{aM_{(g)} + bO_{(g)}}_{no\ bonds} \quad \Delta H_{at} \qquad \text{Eq. 5-20}$$

The value of ΔH_{at} can be calculated thermodynamically, from the reactions given below:

$O_{2(g)} \rightarrow 2O_{(g)}$	ΔH_d	Eq. 5-21
$M_{(s)} \rightarrow M_{(g)}$	ΔH_s	Eq. 5-22
$aM_{(s)} + \frac{b}{2} O_{2(g)} \rightarrow M_a O_{b(s)}$	ΔH_f	Eq. 5-23

Where ΔH_d is the enthalpy of dissociation of molecular oxygen into oxygen atoms, ΔH_s is the enthalpy of sublimation for the metal M, and ΔH_f is the enthalpy of formation of the metal oxide $M_a O_b$. By using Hess' Law on Eq. 5-20 to Eq. 5-23 it follows that:

$$\Delta H_{at} = -\Delta H_f + a \cdot \Delta H_s + \frac{b}{2} \cdot \Delta H_d \qquad \text{Eq. 5-24}$$

By combining Eq. 5-19 and Eq. 5-24, it follows that the atomisation energy can be calculated as:

$$E_{at} = -\frac{1}{a} \cdot \Delta H_f + \Delta H_s + \frac{b}{2a} \cdot \Delta H_d \qquad \text{Eq. 5-25}$$

By using Eq. 5-25 and thermochemical data from reference[25], the atomisation energy can be calculated for standard conditions $E_{at}^{25°C}$ (25 °C, 1 atm), or at the temperature at which the reduction was carried out (900 °C), $E_{at}^{900°C}$. The difference between the values $E_{at}^{25°C}$ and $E_{at}^{900°C}$ was found to be very small; the values $E_{at}^{900°C}$ will be used here since reductions were carried out at 900 °C.

Considering the B-O bond length should be roughly proportional to a_p, but inversely proportional to the bond strength, plot (b) and plot (d) in Figure 5-17 should show similar trends. From Figure 5-17 (b) it is apparent that the oxide atomisation energies trend shares some similarities to the trends of ionic radii and pseudocubic cell parameters, but differences can be identified as well. Differences may be partly attributed to the fact that in the oxides the coordination number of the cations with respect to oxygen (CN) was not considered. More reliable values for the bond energies might be given by $E_{at}^{900°C}$/CN. However, some of the considered oxides exhibit two CN values in the same oxide which makes it difficult to define an average CN.

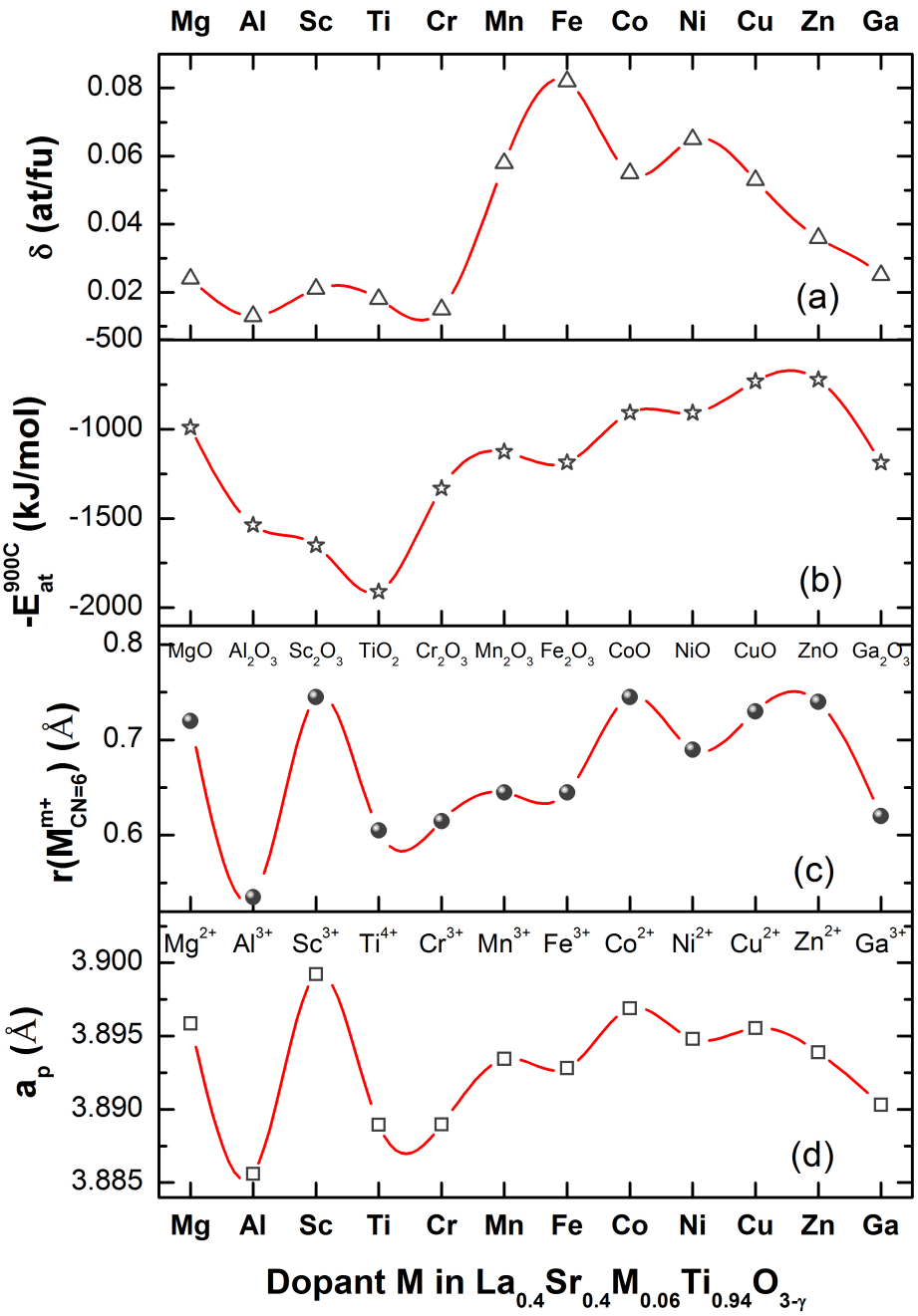

Figure 5-17 | Comparison between structural and reduction characteristics of the series $La_{0.4}Sr_{0.4}M_xTi_{1-x}O_{3-\gamma}$ (pseudocubic cell parameter a_p in (d), the extent of reduction δ, in (a)) and other relevant data of the doping cations (ionic radii of 6-fold coordinated cations $r(M^{m+}_{CN=6})$ in (c), and atomisation energy of the oxides E^{900C}_{at} corresponding to these cations in(b)), all plotted against the doping elements in the order in which they appear in the periodic table (the order of their atomic number). The δ values were obtained for reduction in 5%H_2/Ar, at 900 °C (20 h). The atomisation energy was calculated according to Eq. 5-25 for the temperature 900 °C. In all the plots the errors are smaller than the points and the red curves represent interpolation curves obtained from the data points.

Nevertheless, the atomisation energies confirm that the Ti-O bond is very strong compared to the other bonds and, generally, the energies seem to fall in three categories: high bond strength: Ti-O, average bond strength, Al-O and Sc-O, and lower bond strength, the remaining elements. Strangely, according to this estimation of bond strength Cr forms a rather weak bond with oxygen, of similar energy value as Zn forms with oxygen. Similarly, Al appears to form weaker bonds with oxygen compared to Ti, contrary to expectations. The weaker bonds that Mg, Sc or Zn (*non-transition* elements) form with O might explain why they exhibit higher extents of reduction compared to the undoped composition containing only Ti-O bonds, but it does not explain the trend in reduction of the true transition metals. Thus, in conclusion, within the premises of this approach, it can be said that with few exceptions, the B-O bond strength alone cannot account for the trend in reducibility observed for the doped A-site deficient perovskites.

5.8 The importance of the *coordination number* in reduction

As highlighted in subchapter 5.3, reduction occurs by removing oxide ions from the perovskite lattice. If the perovskite lattice is visualised as suggested in Chapter 2, as a three-dimensional corner-sharing BO_6 octahedra network, reduction can be regarded as a process in which oxide ions are removed from some of the BO_6 octahedra, leading to $BO_{6-\xi}$ polyhedrons. In perovskites ξ typically equals 1 or 2. By removing an oxide ion from a BO_6 octahedron ($\xi = 1$), the coordination number (CN) of the B-site ion is lowered to CN = 5 and the arrangement of oxide ions around it describes a square-pyramid (Figure 5-18). By removing an additional oxide ion ($\xi = 2$), the coordination number of the B-site cation further decreases to CN = 4 and the arrangement of the remaining oxide ions may describe either a square planar or tetrahedral geometry (Figure 5-18).

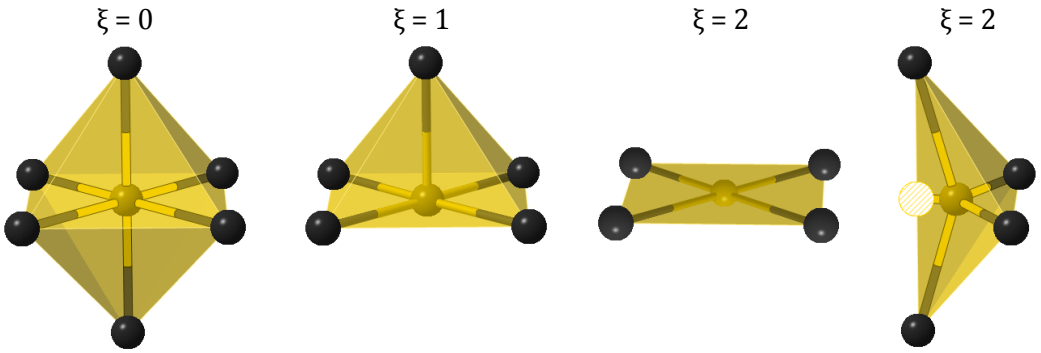

Figure 5-18 | Possible $BO_{6-\xi}$ geometries in perovskites.

However, a *change in the geometry* of the $BO_{6-\xi}$ polyhedrons, from $\xi = 0$ to $\xi = 2$ may also cause changes in the *electronic structure* of the B-site ion and subsequently to the *overall stability* of the $BO_{6-\xi}$ cluster. This is particularly important when the B-site cation is a transition metal cation since their *d* orbitals point towards the oxygen ions in an octahedral field configuration (see Figure 5-19). This was briefly addressed in section 2.3 from the perspective of covalent mixing in a BO_6 cluster and will be discussed next within the simplifying premises of Crystal Field Theory (CFT).[26–28]

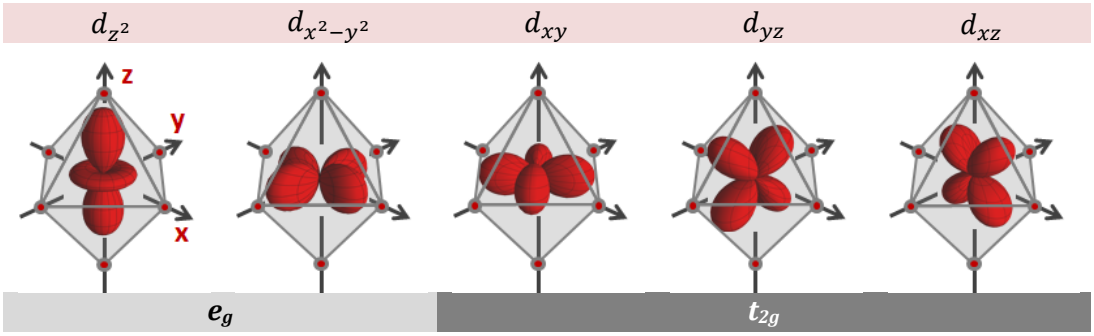

Figure 5-19 | *d* orbitals in the crystal field exerted by oxide ions (red circles) arranged in octahedral symmetry around the B-site ion.

CFT uses an electrostatic model of the BO_6 cluster in which the oxide ions are considered point charges and between the B-site cation and the oxide ion there are no covalent interactions. When the B-site transition metal cation is placed in the crystal field of the oxide ions, the *d* orbitals experience repulsion and rise in energy. If the crystal field of the oxide ions was spherical, the *d* orbitals would all increase their energy by the same amount (remaining *degenerate*), to an energy level known as the *barycentre*.

However, in an *octahedral* crystal field, different orbitals experience different repulsion depending how close they are located to the nearest (negatively charged) oxide ion, as shown in Figure 5-19. Thus, d_{z^2} and $d_{x^2-y^2}$ orbitals point directly towards oxide ions, are known as e_g orbitals, and their energy increases by $0.6 \cdot \Delta_O$ with respect to the barycentre. On the contrary, d_{xy}, d_{yz} and d_{xz} orbitals experience less repulsion, they are referred to as t_{2g} orbitals and their energy decreases by $0.4 \cdot \Delta_O$ with respect to the barycentre. The energy difference between the e_g and t_{2g} orbitals is known as the *octahedral field splitting*, Δ_O. Because of the uneven split of *d* energy levels, partly filled orbitals may result in an overall decrease in energy for the BO_6 cluster. Thus, the difference between the energy of the electrons occupying the orbitals *below* the barycentre (*e.g.* t_{2g}) and the energy of the electrons occupying the orbitals *above* the barycentre (*e.g.* e_g) is known as the *Crystal Field Stabilisation Energy* (CFSE). CFSE depends on the way the *d* orbitals are split, *i.e.* on the geometry of the $BO_{6-\xi}$ polyhedron, the magnitude of the split (Δ_O) and the way the resulting energy levels are filled with electrons. In real systems CFSE will be influenced by other factors as well, such as vacancy interactions,[29] but here the idealised form of CFSE will be used for estimation purposes. Nonetheless, the higher the CFSE in a certain $BO_{6-\xi}$ geometry, the more likely and easy will it be for the B-site cation to adopt that geometry. As such, CFSE may be used as a measure of *coordination flexibility*.

As discussed before, coordination flexibility is very important for reduction and for enabling fast ion conduction in general. Thus it is desirable for B-site cations to support as many coordination geometries as possible or at least 5-fold coordination. Square pyramid, and by similarity square planar geometry may play key roles on the surface as well. For example, it has been shown that if the cation supports both square pyramidal and octahedral oxygen coordination, this enables oxygen to be removed and attached with ease on the surface, which in turn creates sites in which other species may be adsorbed or desorbed.[30–33] By contrast, tetrahedral geometry is not suitable

for adsorption/desorption from the surface, but it is expected to play a more important role in oxide ion diffusion in the bulk since it maximises the unit cell free volume.[29,32] CFSE is routinely used in complex chemistry to predict the geometry of complexes.[26] In oxides it has been used in spinels to estimate if a certain cation can occupy the tetrahedral or octahedral site or, on the contrary, if it has no coordination preference whatsoever.[28,26]

As explained above, the splitting of the *d* orbitals changes if the arrangement of the oxide ion changes since the repulsion experienced by different *d* orbitals changes as well, as suggested by Figure 5-19. The relative energy of *d* orbitals for the geometries which $BO_{6-\xi}$ clusters may adopt in the perovskite environment (see Figure 5-18), is illustrated in Figure 5-20. The equations which allow the calculation of CFSE for each geometry are given below.[26,34]

$$\mathrm{CFSE}_{oct.} = \left(-0.4 \cdot n_{(d_{xy},d_{xz},d_{yz})} + 0.6 \cdot n_{(d_{z^2},d_{x^2-y^2})}\right) \cdot \Delta_O \qquad \text{Eq. 5-26}$$

$$\mathrm{CFSE}_{sq.pyr.} = \left(-0.45 \cdot n_{(d_{xz},d_{yz})} - 0.1 \cdot n_{(d_{xy})} + 0.1 \cdot n_{(d_{z^2})} + 0.9 \cdot n_{(d_{x^2-y^2})}\right) \cdot \Delta_O \qquad \text{Eq. 5-27}$$

$$\mathrm{CFSE}_{sq.pl.} = \left(-0.52 \cdot n_{(d_{xz},d_{yz})} - 0.4 \cdot n_{(d_{xy})} + 0.22 \cdot n_{(d_{z^2})} + 1.2 \cdot n_{(d_{x^2-y^2})}\right) \cdot \Delta_O \qquad \text{Eq. 5-28}$$

$$\mathrm{CFSE}_{td.} = \left(-0.6 \cdot n_{\left(d_{z^2},d_{x^2-y^2}\right)} + 0.4 \cdot n_{(d_{xy},d_{xz},d_{yz})}\right) \cdot \frac{4}{9} \cdot \Delta_O \qquad \text{Eq. 5-29}$$

Thus, by using Eq. 5-26 to Eq. 5-29, the CFSE of different cations can be calculated. For this, let us consider the cations encountered in the perovskite systems $La_{0.4}Sr_{0.4}M_xTi_{1-x}O_{3-\gamma}$. In *oxidised* (as-prepared) state these are (see section 4.7 for the estimation of oxidation state): Ti^{4+} (d^0), Cr^{3+} (d^3), Mn^{3+} (d^4), Mn^{2+} and Fe^{3+} (d^5), Fe^{2+} (d^6), Co^{2+} (d^7), Ni^{2+} (d^8), Cu^{2+} (d^9), Zn^{2+} (d^{10}); while in *reduced* state the following cations form additionally: Ti^{3+} (d^1) and the already mentioned Mn^{2+} and Fe^{2+}. Thus, these d^n values were used to fill up the energy levels illustrated in Figure 5-20 and then calculate the CFSE which corresponds to a certain crystal field splitting and electron configuration. In each case the orbitals were filled from the lowest energy

levels, while obeying Hund's rule (maximum spin). Two examples of the electronic configurations are given in Figure 5-21, while the CFSE for the considered range of electronic configurations and crystal field geometries are shown in Figure 5-22.

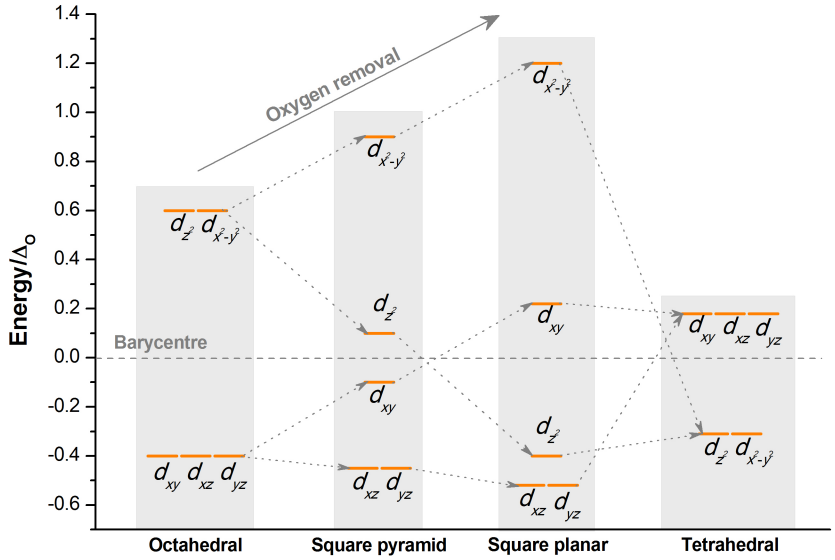

Figure 5-20 | Relative energy of *d* orbitals in the crystal field of various symmetries. Adapted after ref [26].

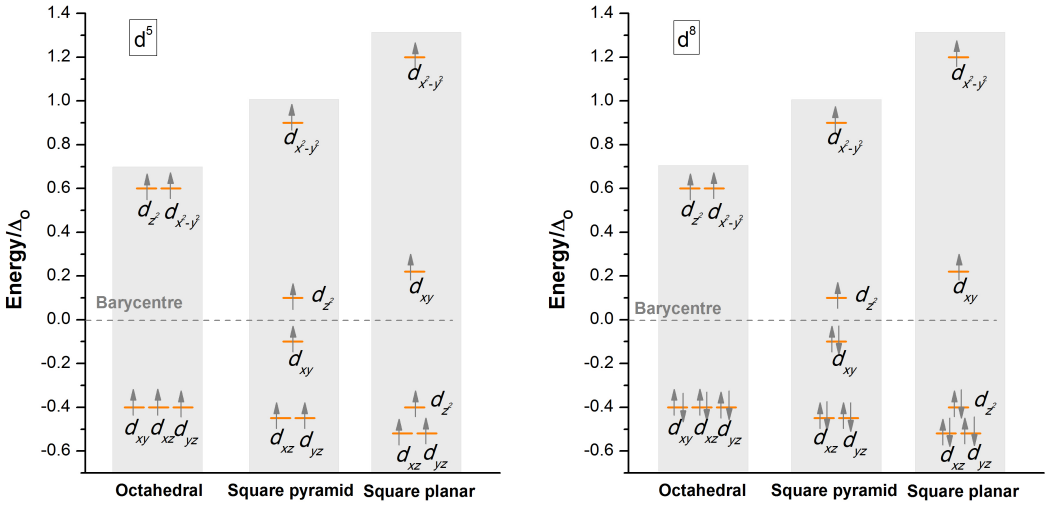

Figure 5-21 | Examples of electronic configurations used to calculate the diagram in Figure 5-22. These configurations obey Hund's rule.

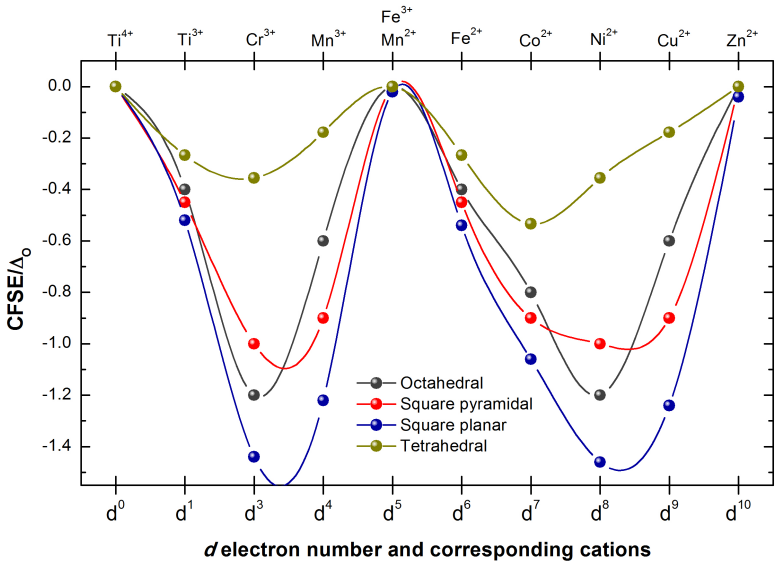

Figure 5-22 | Crystal field stabilisation energies (in Δ_O units) for various geometries and *d* electrons. The electronic configurations used in the calculations obey Hund's rule.

It is apparent from Figure 5-22 that most transtition metal cations with partly filled *d* shells show considerable gains in CFSE ranging from $-0.4 \cdot \Delta_O$ to $-1.4 \cdot \Delta_O$, for multiple geometries. To illustrate the potential impact of CFSE in facilitating the formation of various geometries, let us consider its magnitude. Δ_O usually takes values between 100 and 400 kJ/mol depending on the strength of the crystal field exerted by the negative charges (here, the oxygen ion), but other factors may affect it as well.[34] The oxide ion is considered a ligand with weak/average strength. Thus, in this case an average value of ~200 kJ/mol may be considered for Δ_O. Considering that the C-C bond energy is around 350 kJ/mol, the crystal field stabilisation energies found for most transition metal cations are significant.

Cations such as Ti^{4+}, Zn^{2+}, but also Mn^{2+} and Fe^{3+} do not benefit from CFSE. The lack of CFSE to 'catalyse' the lowering of coordination number and the very high bond energy betweent Ti^{4+} and O^{2-} (Figure 5-17 (b)) explains why Ti^{4+} is so difficult to reduce, being second only to Cr^{3+} among transition metal oxides (see Figure 5-12 or Figure 5-17 (a)). Cr^{3+} on the other hand has an average bond strength (Figure 5-17 (b)) but benefits from considerable CFSE in octahedral geometry and has a lower preference for square pyramidal geometry (Figure 5-22). Thus, the strong preference exhibited by Cr^{3+}

towards 6-fold coordination as pointed out by previous studies,[14,20] may be attributed to its high CFSE in this geometry.

Mn^{2+}, Fe^{3+} and Zn^{2+} appear not to benefit from CFSE either because of the symmetry of the d^5 and d^{10} configurations, respectively. However, they do have considerably lower bond energy with respect to oxygen, as compared to Ti^{4+} (Figure 5-17 (b)), which makes them easier to reduce. Strangely, Mn and Fe – based compositions in the series $La_{0.4}Sr_{0.4}M_xTi_{1-x}O_{3-\gamma}$ reduce to much higher extents compared to Zn-doped compositions, which by comparison to the Cr and Ti cases, was expected to be accounted for by the higher CFSE exhibited by these cations. Moreover, 5-fold square pyramid geometries are known for both $Fe^{2+/3+}$ and $Mn^{2+/3+}$ (see section 2.2.3 and references therein).

Another peculiar aspect arises by examining the proposed electronic configuration for d^8 (Ni^{2+}) square planar geometry (Figure 5-21). The proposed configuration which obeys Hund's rule of maximising spin yielded a paramagnetic d^8 configuration. However, it is widely known that at least in complex chemistry square planar Ni^{2+} is almost exclusively *diamagnetic*.[34,26] The oxide ion is generally considered too weak to cause a sufficiently strong splitting of energy levels as to lead to the formation of square planar diamagnetic Ni^{2+}. However, evidence was found that even in perovskite oxides, when in square planar geometry, Ni^{2+} exhibits almost null magnetic moment.[35] Thus, it appears that at least in the case of d^8 it is favourable to *pair* electrons into lower energy orbitals (*e.g.* in d_{z^2} – see Figure 5-23) rather than maximise the spin by placing the electron in the higher energy orbital $d_{x^2-y^2}$ which experiences significant repulsion from the oxide ions (see Figure 5-19). This would also result in a considerable increase in CFSE as shown Figure 5-24. In this figure, the electronic configurations d^5-d^8 were allowed to pair a single electron in a lower energy orbital instead of occupying the higher energy orbital $d_{x^2-y^2}$, following the example of square planar Ni^{2+}. A d^5 electron configuration of this kind is shown in Figure 5-23. However, these configurations for the calculation of CFSE were only

considered for square pyramidal and square planar geometries where $d_{x^2-y^2}$ stands at high energy, not for the octahedral or tetrahedral case where *d* orbital splitting is indeed not high enough (see Figure 5-20). Thus, in this scenario, a significant increase in CFSE was found for d^5-d^8 cations.

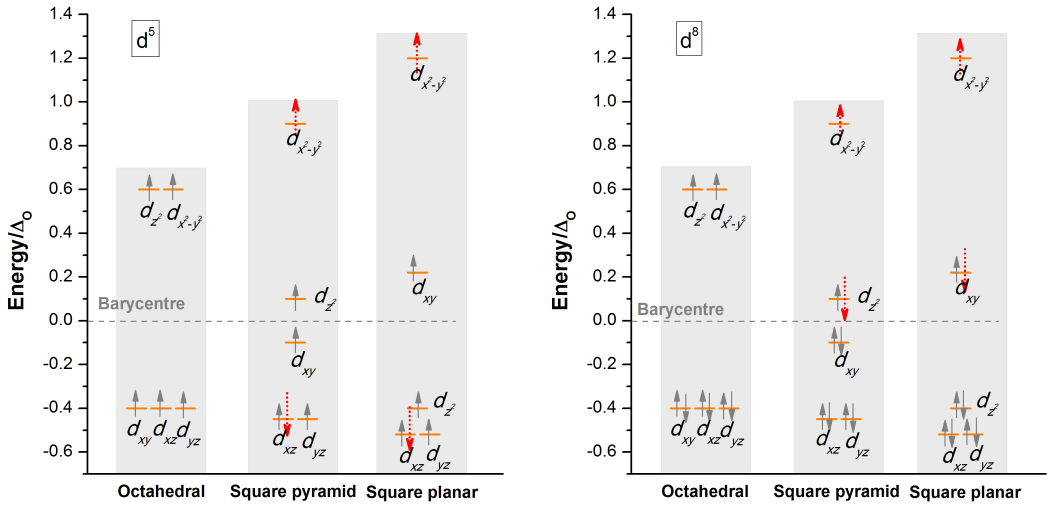

Figure 5-23 | Examples of electronic configurations used to calculate the diagram in Figure 5-24. These configurations do not obey Hund's rule (see text).

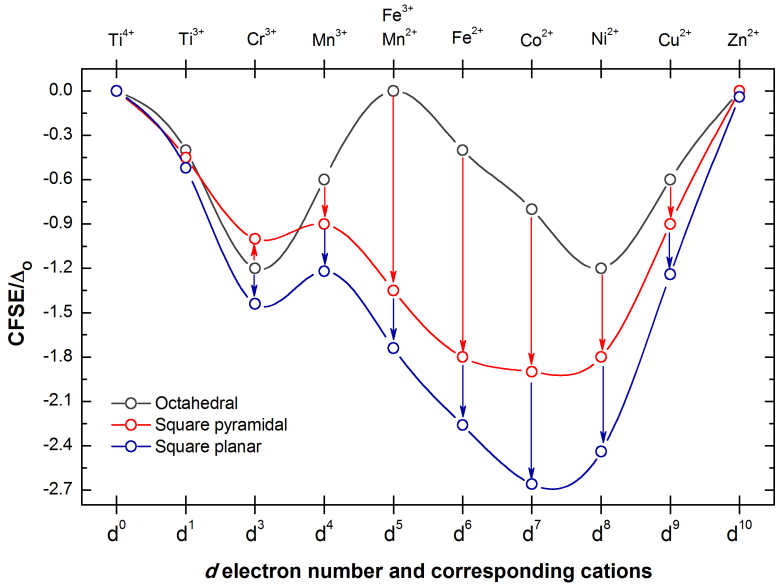

Figure 5-24 | Crystal field stabilisation energies (in Δ_O units) for octahedral, square pyramidal and square planar geometries for different *d* electrons. The electronic configurations used in these calculations do not obey Hund's rule (see text).

Let us consider now reduction in the series $La_{0.4}Sr_{0.4}M_xTi_{1-x}O_{3-\gamma}$. γ oxygen vacancies are present from the start (inherent) due to charge compensation of the dopant. Upon reduction, an additional δ oxygen vacancies per formula

unit are created. A plot of the number of vacancies per dopant, ξ, for the series $La_{0.4}Sr_{0.4}M_xTi_{1-x}O_{3-\gamma}$, with the δ values from Figure 5-12 (reduction in 5%H_2/Ar, 900 °C) is given in Figure 5-25.

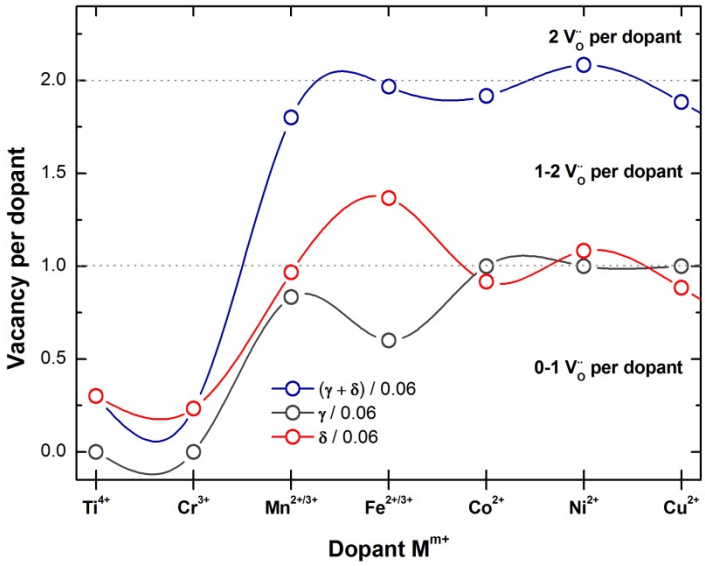

Figure 5-25 | Oxygen vacancy created through doping (γ), reduction (δ) and total (γ+δ) for each dopant in the reduced compositions $La_{0.4}Sr_{0.4}M_{0.06}Ti_{0.94}O_{3-\gamma-\delta}$. Reduction data from Figure 5-12. The curves interpolate the experimental data.

By examining the extent of reduction trend for the series $La_{0.4}Sr_{0.4}M_xTi_{1-x}O_{3-\gamma}$ (shown in Figure 5-12 or partly in Figure 5-25), and the estimated CFSE for the composing cations (Figure 5-24), it becomes clear there is a distinct relationship between δ and the *difference* in CFSE from the base, 6-fold coordination to lower coordination numbers.

Thus, from Figure 5-25, the extent of reduction in this series comprises of three main domains (red curve in Figure 5-25). First, the (left) branch where δ decreases from Ti^{3+} to Cr^{3+} and then increases to $Mn^{2+/3+}$ and further to $Fe^{2+/3+}$. By comparing this branch to the trend of CFSE in Figure 5-24 for the same domain, it can be said that the similarity between the two is striking. The CFSE trend implies that among this range only Cr^{3+} would show reluctance towards 5-fold coordination, and thus not promoting reduction, after which CFSE for square pyramidal coordination increases from Ti^{4+} to $Mn^{2+/3+}$ and further to $Fe^{2+/3+}$ just as δ increases as well. The second (middle) branch groups the dopants that exhibit the highest measured δ in the series:

$Fe^{2+/3+}$, Co^{2+} and Ni^{2+}. For all these cations CFSE is highest and reasonably similar, just like δ, although the Fe-doped composition does show higher δ value compared to the rest. The third (right) branch consists of Ni^{2+}, Cu^{2+} and Zn^{2+}. In this range, both δ and CFSE decrease consistently from Ni^{2+} to Zn^{2+}.

Thus, it appears that under the assumption of these calculations, it is in particular the coordination flexibility that enables achieving higher extents of reduction in titanates, although the influence of bond strength cannot be neglected in some cases.

5.9 The importance of perovskite *defect chemistry* in reduction

So far, the factors that come into play during reduction have been deduced, explored and exemplified based on A-site deficient perovskites. Whilst at first it might be difficult to conceive that the principles highlighted here for this particular perovskite class can be extended to other perovskite nonstoichiometry classes, it should be noted that all of these principles were in essence derived from structural considerations common to all perovskites. All perovskites are made of the corner sharing BO_6 building blocks to some extent, hence considerations based on bond strengths, coordination geometry, defect ordering etc, will still apply. On the other hand, each different perovskite nonstoichiometry class possesses its own, unique structural and defect context (*i.e.* defect chemistry) which can transfigure the same basic principles in its own unique way, giving rise to distinct behaviours and properties. Thus, this subchapter seeks to show how perovskites with similar composition but different defect chemistry can exhibit distinct reduction behaviour.

For this, the compositions belonging to different defect chemistries but that also mark the borderline between ordered and disordered structures have been considered for B-site doping. For the A-site deficient, oxygen stoichiometric series $La_xSr_{1-3x/2}TiO_3$ this is member $x = 0.4$, $La_{0.4}Sr_{0.4}TiO_3$,

and for the A-site stoichiometric, oxygen excess series $La_xSr_{1-x}TiO_{3+x/2}$ ($\equiv La_4Sr_{4-n}Ti_nO_{3n+2}$) this is the $x = 0.33$ (or $n = 12$) member, $La_{0.33}Sr_{0.67}TiO_{3.167}$ ($\equiv La_4Sr_8Ti_{12}O_{38}$). The A-site deficient, B-site doped series considered for comparison is the one discussed in previous subchapters, with 6% M^{m+} doping, $La_{0.4}Sr_{0.4}M^{m+}_{0.06}Ti_{0.94}O_{3-\gamma}$, where the decrease in oxygen stoichiometry upon doping is given by $\gamma = 0.06 \cdot \frac{4-m}{2}$. In the case of the oxygen excess perovskites, the reduction data was taken from the work of Miller *et. al.*[36] where the stoichiometry of the dopant was $x = \frac{1}{12}$ which is approximately $x \sim 0.08$, leading to the A-site stoichiometric, oxygen excess series $La_{0.33}Sr_{0.67}M^{m+}_{0.08}Ti_{0.92}O_{3.167-\Gamma}$, where the decrease in oxygen stoichiometry upon doping is given by $\Gamma = 0.08 \cdot \frac{4-m}{2}$. Since the compositions with M = Ni and M = Zn were not investigated in the cited study, the similar compositions $La_{0.3}Sr_{0.7}M_{0.06}Ti_{0.94}O_{3.167-\Gamma}$ (M = Ni, Zn) prepared in this study were used instead.

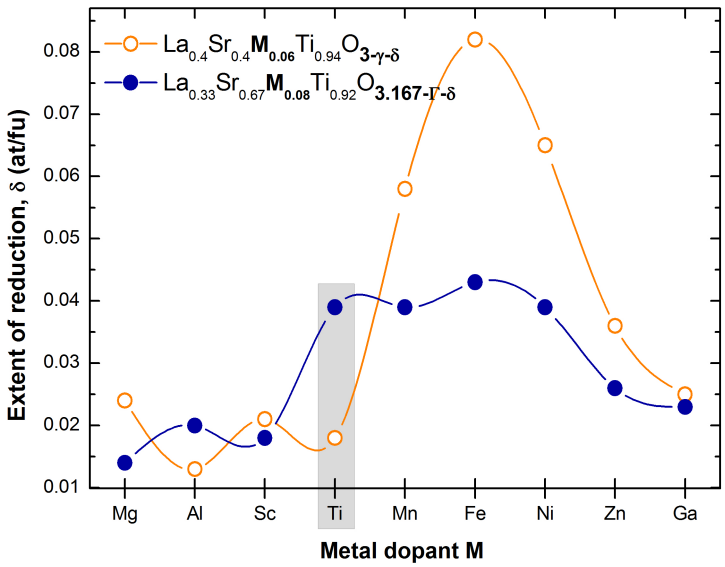

Figure 5-26 | The extent of reduction as a function of dopant for two different defect chemistries: the A-site deficient $La_{0.4}Sr_{0.4}M^{m+}_{0.06}Ti_{0.94}O_{3-\gamma}$ and the oxygen excess $La_{0.33}Sr_{0.67}M^{m+}_{0.08}Ti_{0.92}O_{3.167-\Gamma}$. Reduction was carried out at in 5%H_2/Ar, at 900 °C (20 h). The errors are smaller than the points and the curves represent interpolations derived from the data points.

Thus Figure 5-26 compares the extent of reduction of the A-site deficient series $La_{0.4}Sr_{0.4}M^{m+}_{0.06}Ti_{0.94}O_{3-\gamma}$ and of the oxygen excess series

$La_{0.33}Sr_{0.67}M^{m+}_{0.08}Ti_{0.92}O_{3.167-\Gamma}$, for M = Mg, Al, Sc, Ti, Mn, Fe, Ni, Zn and Ga. The variation of the extent of the reduction with different dopants is strikingly different for the two defect chemistries considered. The first aspect to notice is that the undoped oxygen excess sample reduces more at this temperature (900 °C) than the A-site deficient homologue. This was somewhat expected as the oxygen excess sample has an innate feature that allows for good mobility of oxide ions and overall locally weaker Ti-O bonds which reside in the oxygen excess intergrowths.

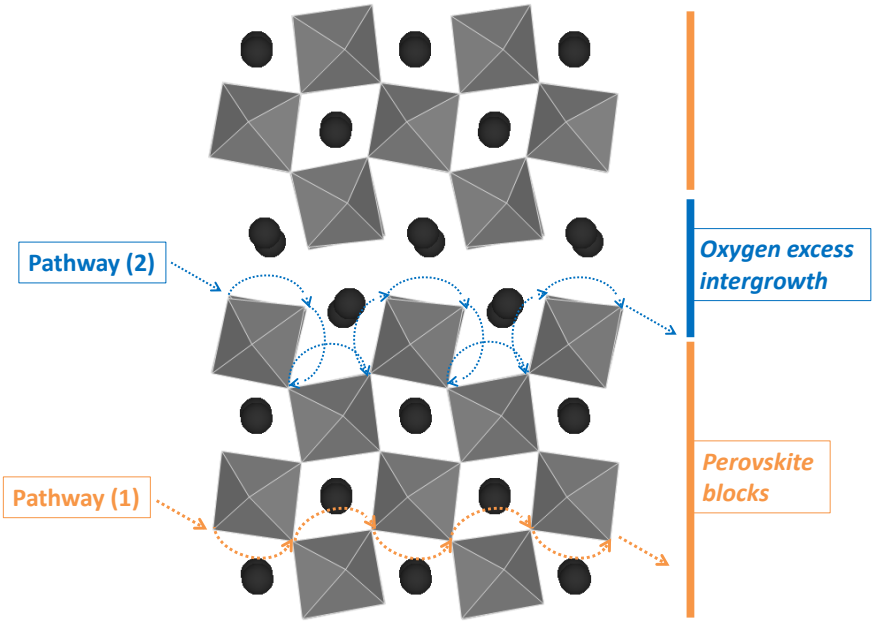

Figure 5-27 | Proposed diffusion pathways for the oxide ion (or oxide ion vacancy) in oxygen excess type perovskites.

Bearing in mind that oxide ions (or vacancies) can move only on the edges of the TiO_6 octahedra (see Figure 5-8), Figure 5-27 compares the path an oxide ion vacancy would take to travel from the bulk to the surface either in the perovskite-like slabs or near the intergrowth region. As pointed out in Chapter 2 describing the structure, at the oxygen excess intergrowths the TiO_6 octahedra are significantly stretched and the A-site ions are moved from their symmetry position towards the intergrowth. What is labelled as 'Pathway (1)' in Figure 5-27 would thus be representative to oxide ion/vacancy migration in the A-site deficient perovskite (with regular, continuously connected perovskite blocks), while what is labelled 'Pathway

(2)' would be representative of the oxygen excess compositions. It is apparent by comparing Pathway (1) to Pathway (2) that the oxide ion vacancy travelling near the intergrowth will migrate faster and easier mainly because of two reasons: the Ti–O bonds are stretched and therefore weaker, and the A-site cations are not hindering the movement of the oxide ions because they are situated further away from the diffusion pathway. Indeed, recent impedance measurements have pointed out that the oxygen excess structures are similar to yttrium-stabilized zirconium (a very good oxide ion conductor) in terms of oxide ion mobility, whereas the A-site deficient compositions are situated at the opposite pole, and resemble more the inflexible $SrTiO_3$ structure.[37]

A second aspect that arises from the examination of Figure 5-26 is the effect of the dopants in the two different defect chemistries. None of the dopants employed seemed to be able to effectively enhance the extent of the reduction of the oxygen excess composition, many of them having a rather negative impact. On the contrary, all the cations, apart from Al^{3+} increase the extent of the reduction of the A-site deficient titanate. This is most likely related to the way the dopant is compensated in the two different defect chemistries. In both cases the lower charge of the dopants (notice all dopants actually have lower charge than Ti^{4+}) will be compensated by oxygen vacancies. This means that in the A-site deficient titanate a number of available *hopping sites will be created* which will help bulk diffusion and thus the removal of oxide ions. On the other hand, in the oxygen excess stoichiometry, creating vacancies means *decreasing the number of the excess oxygen ions* which is in fact the species responsible for developing the intergrowths and hence for the good reducibility of this class. However, the effect of the dopants resides not only in the changes they impose on stoichiometry and the availability of charge carriers, but also in their ability to interfere with the diffusion process itself. Small ions with high charge and thus high attraction fields such as Al^{3+} will tend to pin oxide ions into strong bonds, impairing diffusion in both classes of titanates. Cations such as Mn^{3+},

Fe^{3+}, Ni^{2+} that are known to be able to adopt flexible coordination numbers and thus allow for an easier flow of oxide ions around them, greatly benefit reduction when doped in the A-site deficient titanate, and also help alleviate the effect of the decreased concentration of charge carriers in the oxygen excess composition, maintaining the extent of the reduction more or less at the same level as in the undoped sample. It should also be noted that Fe is the best dopant at promoting reduction in both defect chemistries (even if the increase in extent of reduction, δ, from $La_{0.4}Sr_{0.4}TiO_{3-\delta}$ to $La_{0.4}Sr_{0.4}Fe_{0.06}Ti_{0.94}O_{3-\gamma-\delta}$, is not as considerable as from $La_{0.33}Sr_{0.67}TiO_{3.167-\Gamma-\delta}$ to $La_{0.33}Sr_{0.67}Fe_{0.08}Ti_{0.92}O_{3.167-\Gamma-\delta}$), perhaps an indication of the particular effectiveness of Fe in this process, which emerges in spite of the constraints imposed by defect chemistry.

5.10 The extent of reduction as a measure of perovskite redox stability

Since the extent of reduction is directly related to the structural and compositional characteristics of the perovskite and therefore its integrity, δ could be used as an indicator for degradation, in particular on redox cycling.

Figure 5-28 summarises the extent of reduction of representative A-site deficient perovskites through several redox cycles, at 900 or 1000 °C. Although not shown here, the vast majority of the perovskites prepared in this study showed similarly good redox stability with respect to δ, demonstrating that they support oxygen being reversibly extracted and incorporated from and into their structure, thus demonstrating high redox tolerance.

Such studies may also reveal perovskites that for no immediately apparent reasons may not be entirely redox stable. An example of this kind is presented and analysed in detail in the next subchapter.

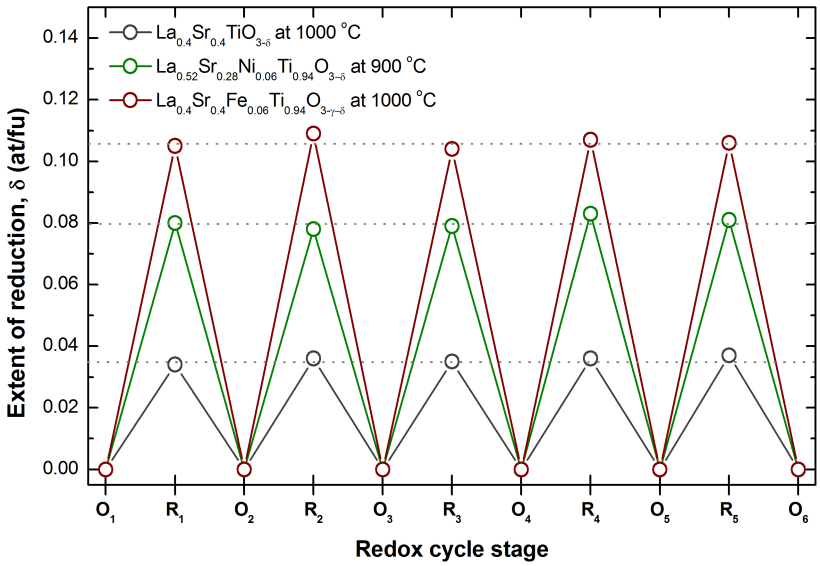

Figure 5-28 | The extent of reduction of various A-site deficient perovskites throughout several redox cycles (on the *x* axis O = oxidation, R = reduction). Compositions and reduction temperatures (in 5%H_2/Ar, 20 h) are indicated in the legend of the figure. Oxidation was always carried out in static air at 1000 °C, for 12 h.

5.11 Reduction in the special case of Ga-doped, A-site deficient perovskites

5.11.1 Ga volatilisation on reduction

The reasons for which reduction in the Ga-doped samples $La_{0.4}Sr_{0.4}Ga_xTi_{1-x}O_{3-\gamma}$ deserves special attention compared to the other compositions belonging to the same series can be understood by examining Figure 5-29 and Figure 5-30. The data in Figure 5-29 summarises some reduction experiments in which $La_{0.4}Sr_{0.4}Ga_xTi_{1-x}O_{3-\gamma}$ pellets (60-65% dense) were reduced in 5%H_2/Ar, at various temperatures (850 to 1000 °C). In Figure 5-29 the weight loss of the samples (on reduction) is presented as a function of Ga doping level, while on the right *y* axis the corresponding extent of reduction is given, in the assumption that all the lost weight would be lattice oxygen.

The 'δ values' observed in these experiments, even at reduction temperatures as low as 850 °C seemed unrealistically high. Moreover, redox studies carried out on these compositions revealed that during the first reduction a

considerable weight loss is observed, which is not regained in full upon oxidation (see Figure 5-30). This is contrary to the way other compositions behave for which the weight lost during reduction is of the same magnitude as the weight gain during oxidation, over several redox cycles.

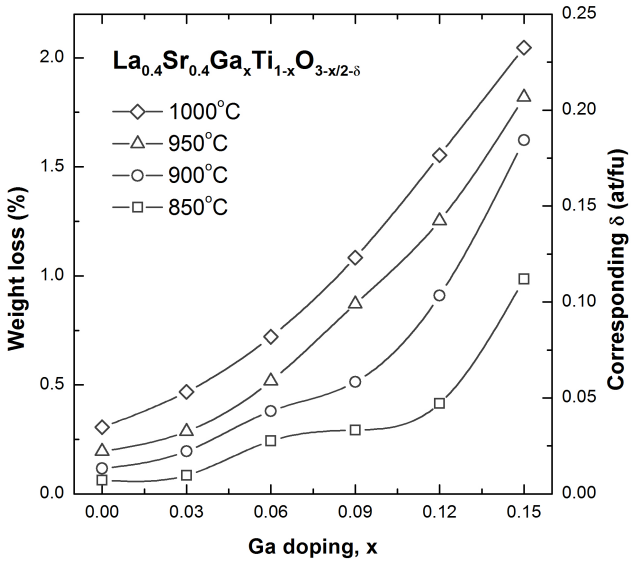

Figure 5-29 | Weight loss measured on 60-65% dense $La_{0.4}Sr_{0.4}Ga_xTi_{1-x}O_{3-\gamma}$ pellets during reduction at various temperatures for 20 h, in 5%H_2/Ar flow. The corresponding oxygen deficiency is plotted on the right y axis (under the assumption that all weight loss is oxygen loss). The errors are smaller than the points and the curves represent interpolations to the experimental data.

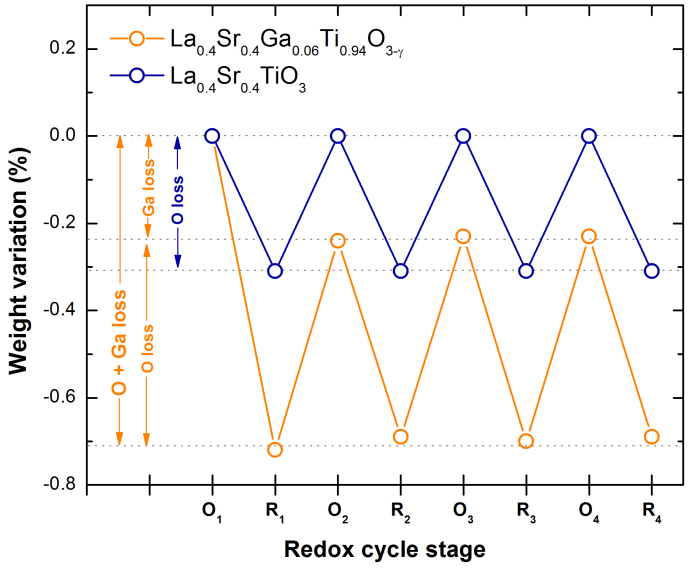

Figure 5-30 | Weight variation (+gain and -loss) at different stages of redox cycling (O-after a complete oxidation, R-after a complete reduction), carried out at 1000 °C, for undoped and Ga-doped $La_{0.4}Sr_{0.4}TiO_3$, 60-65% dense pellets. The errors are of the size of the points.

This suggests that there might be another process that occurs with weight loss when reducing the samples, besides oxygen loss. Because such behaviour was not observed in the undoped composition, this is probably an effect associated with the presence of Ga. Indeed, other Ga containing perovskites have been reported to lose Ga in reducing conditions, at higher temperatures.[38,39] Two different processes that account for Ga loss have been found:[40–42]

$$Ga_2O_{3(s)} + 2H_2 \rightarrow Ga_2O_{(g)} + 2H_2O_{(g)} \quad \text{Eq. 5-30}$$

$$Ga_2O_{3(s)} + 2H_2 \rightarrow 2GaOH_{(g)} + H_2O_{(g)} \quad \text{Eq. 5-31}$$

It has been suggested that the most abundant species during the volatilization of Ga based oxides is Ga_2O in dry reducing conditions,[40] and GaOH if water is present in the reducing gas.[41] However, these studies do not rely on direct observation of the species but are rather anticipated from indirect methods and thermodynamic calculations.

5.11.2 Quantification of Ga loss and extent of reduction

In order to find the true oxygen deficiency of the Ga doped samples in reducing conditions and the magnitude of the Ga loss, the materials were subjected to a redox cycle. The way this method allows to calculate Ga and oxygen loss during reduction is discussed with respect to Figure 5-31 which presents a schematic diagram of how the stoichiometry of a B-site doped perovskite, $AM_xB_{1-x}O_3$, changes upon reduction if M is volatile. During the first stage, the reducing atmosphere removes some of the oxygen and M cations from the perovskite lattice, leading to an average stoichiometry $AM_{x-\zeta}B_{1-x}O_{3-\delta}$. Thus, M loss upon reduction can be defined as ζ, which is an overall, *averaged* change in M stoichiometry over the perovskite mass. δ is used here with the same meaning as before, as the lattice oxygen that can be reversibly removed from the lattice during reduction. It should be noted here that the charge compensation required for the removal of ζ M cations was ignored since ζ values are expected to be low and thus the oxygen vacancies expected to form have negligible contribution to the molar weight μ_2

($\zeta \cdot A_O \ll \mu_2$). In the second stage of the cycle, when the materials are exposed to air, δ oxygen vacancies are being refilled with oxygen. m_i, μ_i $(i = 1, 2, 3)$ represent the sample weights and corresponding molar weights of the perovskite in each of the three steps of the cycle.

(1) As-prepared (oxidised)		(2) Reduction		(3) Oxidation
$AM_xB_{1-x}O_3$	→	$AM_{x-\zeta}B_{1-x}O_{3-\delta}$	→	$AM_{x-\zeta}B_{1-x}O_3$
m_1, μ_1		m_2, μ_2		m_3, μ_3

Figure 5-31 | Redox cycle showing the change in stoichiometry and characteristic parameters in each stage of the process.

Next, based on the conservation of moles of perovskite across the cycle, two *independent* equations can be written:

$$\frac{m_1}{\mu_1} = \frac{m_2}{\mu_2} \quad \text{Eq. 5-32}$$

$$\frac{m_2}{\mu_2} = \frac{m_3}{\mu_3} \quad \text{Eq. 5-33}$$

Or, equivalently, using proportions:

$$\frac{\mu_2 - \mu_1}{\mu_1} = \frac{m_2 - m_1}{m_1} \quad \text{Eq. 5-34}$$

$$\frac{\mu_3 - \mu_2}{\mu_3} = \frac{m_3 - m_2}{m_3} \quad \text{Eq. 5-35}$$

The terms in Eq. 5-34 and Eq. 5-35 can be expanded as follows (A_M and A_O represent the atomic weights of the element M and of oxygen, respectively):

$$\frac{-(\zeta \cdot A_M + \delta \cdot A_O)}{\mu_1} = \frac{m_2 - m_1}{m_1} \quad \text{Eq. 5-36}$$

$$\frac{\delta \cdot A_O}{\mu_1 - \zeta \cdot A_M} = \frac{m_3 - m_2}{m_3} \quad \text{Eq. 5-37}$$

Eq. 5-36 and Eq. 5-37 compose a system of equations with two unknowns, ζ and δ which can be solved to find:

$$\zeta = \frac{\mu_1}{A_M} \cdot \frac{m_1 - m_3}{m_1} \quad \text{Eq. 5-38}$$

$$\delta = \frac{\mu_1}{A_O} \cdot \frac{m_3 - m_2}{m_1} \quad \text{Eq. 5-39}$$

Using Eq. 5-38 and Eq. 5-39, the Ga lost and oxygen deficiency on reduction was determined for the series $La_{0.4}Sr_{0.4}Ga_xTi_{1-x}O_{3-\gamma}$ for three redox cycles, each carried out at different (reduction) temperatures 900, 950 and 1000 °C (oxidation always done at 1000 °C). The results are shown in Figure 5-32.

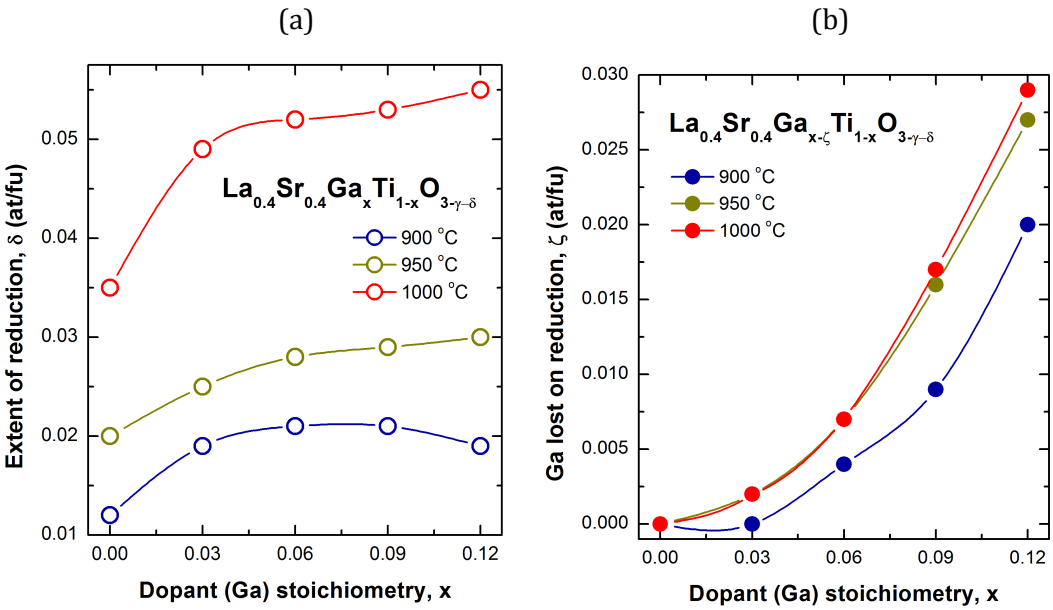

Figure 5-32 | Oxygen deficiency and Ga loss on reduction expressed as δ and ζ, respectively, in $La_{0.4}Sr_{0.4}Ga_{x-\zeta}Ti_{1-x}O_{3-\gamma-\delta}$ for the series with the initial stoichiometry $La_{0.4}Sr_{0.4}Ga_xTi_{1-x}O_{3-\gamma}$. δ and ζ are given at various temperatures and were calculated from the first redox cycle according to Eq. 5-38 and Eq. 5-39, on 60-65% dense pellets. A redox cycle consists of a reduction step (in flowing 5%H_2/Ar at the specified temperatures for 20 h) followed by an oxidation step (always performed at 1000 °C in static air for 12 h). Errors are smaller than the points and the curves are interpolations based on the experimental data points.

As expected, Ga-doping does enhance the extent of reduction at all temperatures, with the most considerable effectiveness for low doping levels ($x \leq 0.06$). However, as indicated by Figure 5-32, the magnitude of Ga loss on reduction also increases as the initial Ga content in the perovskite increases. Surprisingly, however, Ga loss does not increase significantly with temperature. In fact the same Ga loss was measured at 950 and 1000 °C (fresh, as-prepared samples were used in each of the three redox cycles). Moreover, it should be noted here that Ga loss on reduction only occurs during the first reduction, and any further reductions at temperatures lower than 1000 °C occur without Ga loss (see Figure 5-30 and Table 5-2). In order to have a better perspective over the magnitude of Ga loss, the data in Figure

5-32 is given in Table 5-2 as change in Ga stoichiometry, *i.e.* from Ga_x to $Ga_{x-\zeta}$. This table shows that while the changes of Ga stoichiometry on reduction are not dramatic, they do exist and they should be taken into consideration.

Table 5-2 | Change of Ga stoichiometry (x) due to Ga-loss (ζ) for 60-65% dense pellets belonging to the series $La_{0.4}Sr_{0.4}Ga_xTi_{1-x}O_{3-\gamma}$ after redox cycling at various temperatures. A redox cycle consists of a reduction step (in flowing 5%H_2/Ar at the specified temperatures for 20 h) followed by an oxidation step (always performed at 1000 °C in static air for 12 h).

Initial (*as-prepared*) x	**1st Redox** *at 900 °C* $x-\zeta_{900°C}$	**1st Redox** *at 950 °C* $x-\zeta_{950°C}$	**1st Redox** *at 1000 °C* $x-\zeta_{1000°C,1st}$	**2nd Redox at** *1000 °C* $x-\zeta_{1000°C,2nd}$
0.03	0.029	0.028	0.028	0.028
0.06	0.054	0.053	0.053	0.053
0.09	0.081	0.073	0.072	0.072
0.12	0.100	0.093	0.091	0.091

The more fundamental investigations performed here also solved a major problem encountered during the testing of these compositions. Thus, electrolysis cells having these materials as cathodes would suffer from poor current collection as soon as they were exposed to reducing atmosphere since the gold paste used as current collector was degrading significantly, most likely by forming an alloy with the evaporated Ga (see Figure 5-33 (a)).

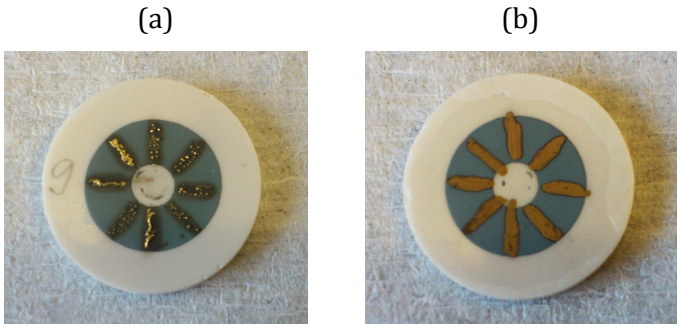

Figure 5-33 | The interaction between Au and $La_{0.4}Sr_{0.4}Ga_xTi_{1-x}O_{3-\gamma}$ on reduction at high temperatures. (a) When Au is applied on the $La_{0.4}Sr_{0.4}Ga_xTi_{1-x}O_{3-\gamma}$ screen printed electrode that did not undergo any reduction ('as-prepared') a severe interaction between the two phases is observed after high temperature reduction. (b) If Au is applied *after* the screen printed perovskite electrode was reduced once then no interaction is observed.

Since it was known that Ga would only leave the perovskite lattice during the first reduction, the samples were subjected to a redox cycle before testing, which resulted in no interaction between the gold current collector and the material (Figure 5-33 (b)).

5.11.3 Ga loss: possible reasons and proposed mechanisms

While the stability of Ga_2O_3 in reducing atmosphere is a known issue, the fact that the tendency of Ga^{3+} to form volatile species persists, even when part of the perovskite lattice, is rather unexpected. Thus, it seems likely that the defect chemistry of the A-site deficient perovskite itself might be involved in this process. Thus, Ga loss during reduction could be due to the incapacity of the perovskite lattice to accommodate such a high number of vacancies on both A-site and O-site at the same time. In oxidized (as-prepared) form the Ga doped systems already possess a number of oxygen vacancies, besides the large number of A-site vacancies, $La_{0.4}Sr_{0.4}Ga_xTi_{1-x}O_{3-x/2}$. When exposed to reducing conditions more oxygen vacancies are created: $La_{0.4}Sr_{0.4}Ga_xTi_{1-x}O_{3-x/2-\delta}$ ($0 < x < 0.12$, $0.035 < \delta < 0.06$ - Figure 5-32). By exsolving some B-site cations (as oxides or reduced oxides) from the perovskite lattice, the occupancy on the A-site and on the O-site would increase, thus making the system more stable. However, due to the fact that the Ga based species that form in reducing conditions are volatile (Eq. 5-30, Eq. 5-31), no exsolutions were observed on the grains (by means of SEM). The samples also retained their crystal symmetry after Ga loss and no secondary phase was observed by XRD. The proposed mechanism is in good agreement with the fact that Ga loss increases with Ga doping. The higher the initial Ga content, the higher the overall deficiency of the perovskite's lattice and therefore the less stable, making it more prone to exsolve B-site oxides. On the other hand it is not easy to explain why even slightly doped samples (3% Ga) and thus having less overall deficiency exhibit some Ga loss (Table 5-2). This might be due to the fact that Ga based oxides are inherently not stable enough as solids at low p_{O_2} and high temperature, regardless of the oxide system they are part of.[42,43]

In order to decide if Ga loss on reduction can be diminished by decreasing the A-site deficiency, samples with higher A-site occupancy were doped with Ga, as in $La_ySr_{1-3y/2}Ga_xTi_{1-x}O_{3-x/2}$, and analysed as previously explained in section 5.11.2 to find the corresponding changes in oxygen stoichiometry and Ga loss on reduction. Thus, it was found that as y decreased to 0.25 or 0.20 in $La_ySr_{1-3y/2}Ga_xTi_{1-x}O_{3-x/2}$, Ga loss remained essentially the same as previously measured for $y = 0.4$ (Table 5-2). It was only for $y = 0.1$ that a very slight improvement in Ga stability was observed, but at significant 'cost' in terms of achievable oxygen deficiency on reduction.

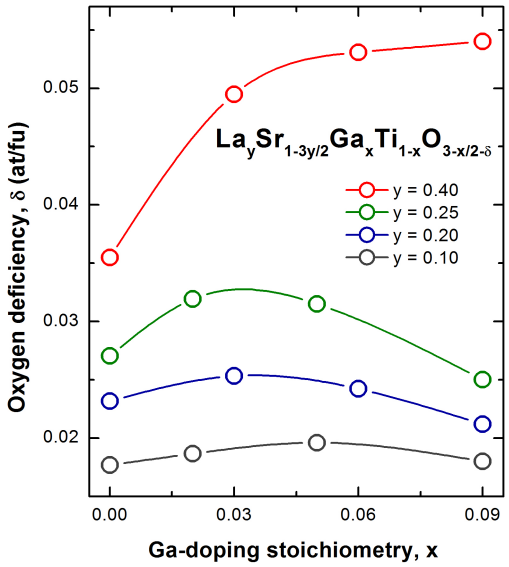

Figure 5-34 | The extent of reduction δ for various members of the series $La_ySr_{1-3y/2}Ga_xTi_{1-x}O_{3-x/2}$. Reduction was carried out in 5%H_2/Ar at 1000 °C, for 20 h. Errors are smaller than the points and the curves are interpolations based on the experimental data points.

As Figure 5-34 shows, by decreasing A-site deficiency (by decreasing y), a dramatic fall in the achievable extent of reduction is observed for the series $La_ySr_{1-3y/2}Ga_xTi_{1-x}O_{3-x/2}$, which increased Ga doping amounts cannot compensate. This is not surprising since it was shown earlier that in the series with $= 0$, the highest extent of reduction can only be achieved when $y = 0.4$. Thus, A-site deficiency seems to have no impact on Ga loss.

It appears that the magnitude of the loss scales in particular with the initial amount of Ga present in the perovskite perhaps suggesting that Ga is innately

unstable when exposed to reducing atmosphere and the higher its concentration in perovskites the more Ga will be lost from them. This perspective leads to another possible mechanism for Ga loss.

The above mentioned observation, coupled with the fact that only a fraction of the initial Ga content is lost on reduction, not all of it, and that even compositions with small initial Ga doping lose some Ga, point towards another way in which Ga loss occurs. It seems plausible that due to the inherent tendency of Ga to form volatile species in reducing conditions, the Ga ions from the outmost surface of the perovskite grains will be easily lost in contact with reducing conditions, at high temperatures. The thickness of the Ga-depleted perovskite layer would depend on various parameters such as the starting composition, the p_{O_2} or the temperature. However, this Ga-depleted layer could act as a barrier layer, effectively stopping the Ga ions in the bulk of the perovskite grains from reaching the surface and being reduced to volatile species. This perspective probably explains why Ga loss is only observed during the first reduction and not during subsequent reductions. It may also explain why even slightly doped compositions (3% Ga) lose some Ga, and perhaps also the fact that the amount of Ga lost changes so little when increasing the reduction temperature from 950 to 1000 °C, as shown by Figure 5-32.

In order to see if Ga loss is controlled by the Ga ions reaching the surface of the grains, some of the samples that lost Ga were annealed in air at 1300 °C for a long time (20 h). This annealing step should provide the system with sufficient energy to rearrange its structure and thus for the bulk Ga ions to re-populate the Ga-depleted surface layer covering the grains. If this happens, Ga loss should be detected again upon reduction. Therefore, after the annealing step the samples were reduced and oxidized again in order to calculate their oxygen deficiency and remaining Ga stoichiometry. The results of this experiment are given in Figure 5-35 (oxygen deficiency and Ga loss) and Table 5-3 (Ga loss as change in stoichiometry).

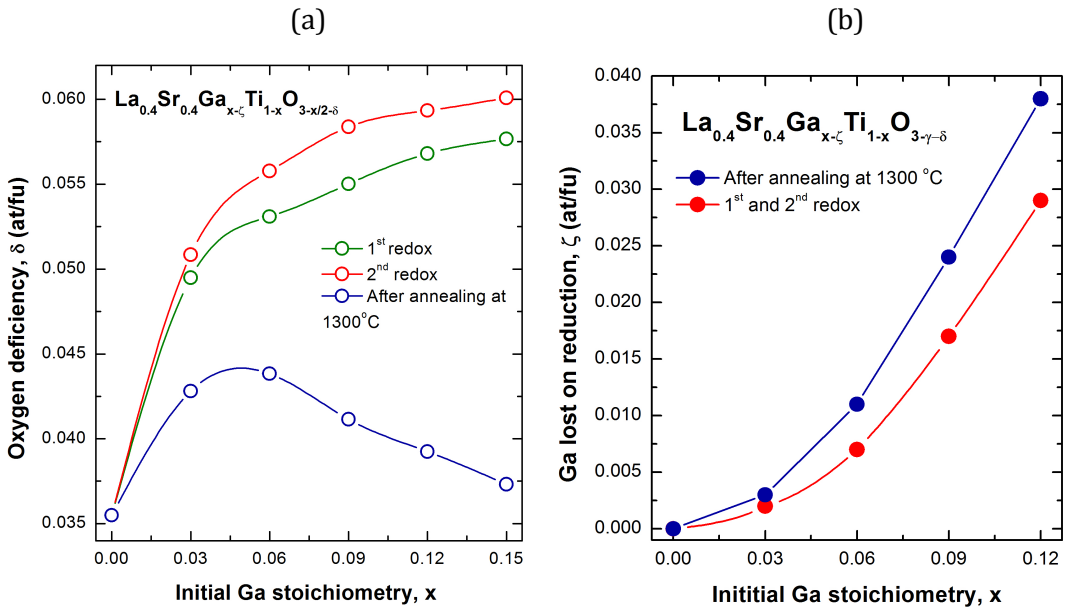

Figure 5-35 | Oxygen deficiency and Ga loss on reduction expressed as δ and ζ, respectively, in $La_{0.4}Sr_{0.4}Ga_{x-\zeta}Ti_{1-x}O_{3-\gamma-\delta}$ for the series with the initial stoichiometry $La_{0.4}Sr_{0.4}Ga_xTi_{1-x}O_{3-\gamma}$, determined on 60-65% dense pellets. δ and ζ were calculated according to Eq. 5-38 and Eq. 5-39 for the first, second and third redox cycle. Before the third redox cycle the samples were annealed at 1300 °C in static air for 20 h. A redox cycle consists of a reduction step (in flowing 5%H_2/Ar at 1000 °C for 20 h) followed by an oxidation step (at 1000 °C in static air for 12 h). Errors are smaller than the points and the curves are interpolations based on the experimental data points.

It is obvious from this data that the annealing step had a profound influence on the properties of the samples, triggering again Ga loss during reduction, decreasing the achievable oxygen deficiencies and thus suggesting that Ga loss is largely controlled by Ga diffusion to the surface of the grains.

Table 5-3 | Change of Ga stoichiometry (x) due to Ga-loss (ζ) for $La_{0.4}Sr_{0.4}Ga_xTi_{1-x}O_{3-\gamma}$ determined on porous pellets (60-65% dense), after redox cycling. A redox cycle consists of a reduction step (in flowing 5%H_2/Ar at the specified temperatures for 20 h) followed by an oxidation step (always performed at 1000 °C in static air for 12 h). Before the third redox cycle the samples were annealed at 1300 °C in static air for 20 h.

Initial (*as-prepared*)	**1st Redox** *at 1000 °C*	**2nd Redox** *at 1000 °C*	**3nd Redox at** *1000 °C, after annealing*
x	$x-\zeta_{1000°C,1st}$	$x-\zeta_{1000°C,2nd}$	$x-\zeta_{1000°C,3rd}$
0.03	0.028	0.028	0.026
0.06	0.053	0.053	0.049
0.09	0.072	0.072	0.065
0.12	0.091	0.091	0.082

In order to further test this premise, a TGA analysis was performed on a fine powder with 5% Ga (Figure 5-36). However, no clear evidence was found that an increased specific surface area would increase Ga loss, as the calculated change in stoichiometry for the powder was from $La_{0.4}Sr_{0.4}\mathbf{Ga_{0.05}}Ti_{0.95}O_{3-\gamma}$ to $La_{0.4}Sr_{0.4}\mathbf{Ga_{0.044}}Ti_{0.95}O_{3-\gamma\prime-\delta}$ corresponding to the powder, which was similar the one listed for porous pellets in Table 5-2. However, *direct* evidence that a Ga-depleted layer does form at the surface of particles during reduction was found *via* transmission electron microscopy as shown in the next subchapter. More *indirect* evidence towards the existence of this Ga-depleted layer will be presented in Chapter 6, when the conductivity of these samples will be discussed.

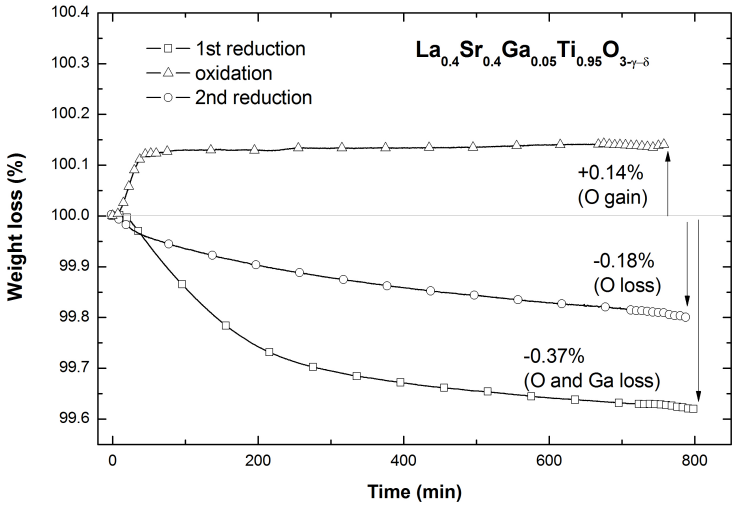

Figure 5-36 | TGA analysis showing the weight variation with time of a $La_{0.4}Sr_{0.4}Ga_{0.05}Ti_{0.95}O_{3-\gamma}$ fine powder during a redox cycle at 950 °C. Reduction was carried out in flowing 5%H2/Ar, while oxidation in flowing air.

5.11.4 TEM perspective of Ga loss

In order to find additional evidence for either of the two proposed mechanisms for Ga loss, Scanning Transmission Electron Microscopy (STEM) was used. The work presented in this subchapter was done at the *King Abdullah University of Science and Technology* (KAUST) in Saudi Arabia by Dr. Samir Boulfrad with the assistance of Dr. Dalaver Anjum and Dr. Dongkyu Cha. The STEM analysis was conducted on the composition $La_{0.4}Sr_{0.4}Ga_{0.06}Ti_{0.94}O_{3-\gamma}$. Figure 5-37 (a) shows the STEM image of this

sample after reduction, focusing on an area close to the surface (edge) of the grains. It is obvious from this image that the first ~10 nm close to the surface of the grains have a different appearance compared to the bulk. The region close to the surface seems homogenous while the bulk consists of a matrix which contains dark spots. Punctual EDS analysis given in Figure 5-37 (b) confirmed that the region close to the edge of the grains has lower Ga content compared to the bulk matrix, and the dark spots appear to be enriched with Ga. This confirms that reduction in these samples occurs with the removal of surface Ga. It should be noted, however, that not all of the examined grains displayed a Ga-depleted layer which suggests that occasionally the removal of Ga during reduction might not advance to such extent as to give rise to such distinct regions as exemplified in Figure 5-37 (a).

(a) (b)

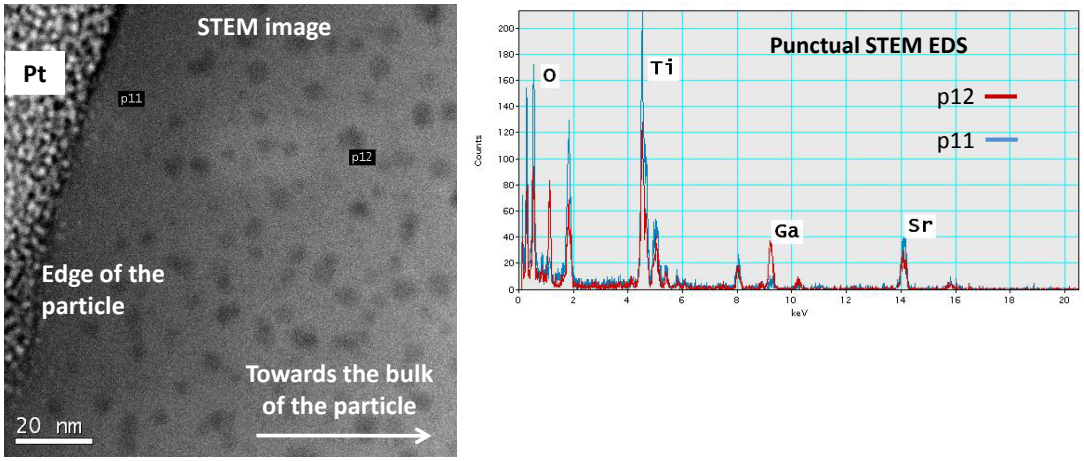

Figure 5-37 | (a) STEM image of a $La_{0.4}Sr_{0.4}Ga_{0.06}Ti_{0.94}O_{3-\gamma}$ sample reduced in 5%H_2/Ar, at 1000 °C, for 20 h. (b) EDS analysis of the points indicated in part (a) of this figure.

Upon oxidation the dark spots become white spots and appear to be slightly larger, less frequent, while still remaining Ga-rich, as shown in Figure 5-38 (a). This might suggests that during reduction Ga also precipitates into Ga-rich phases inside the bulk which upon oxidation is slowly reintegrated into the bulk. The fact that some Ga-rich regions can be found in the oxidised sample (Figure 5-38 (a)) seems to indicate that oxidation related processes were not complete. On the other hand, in the absence of STEM data on the as-

prepared sample (prior to reduction) it is impossible to tell if the Ga-rich spots were there to start with.

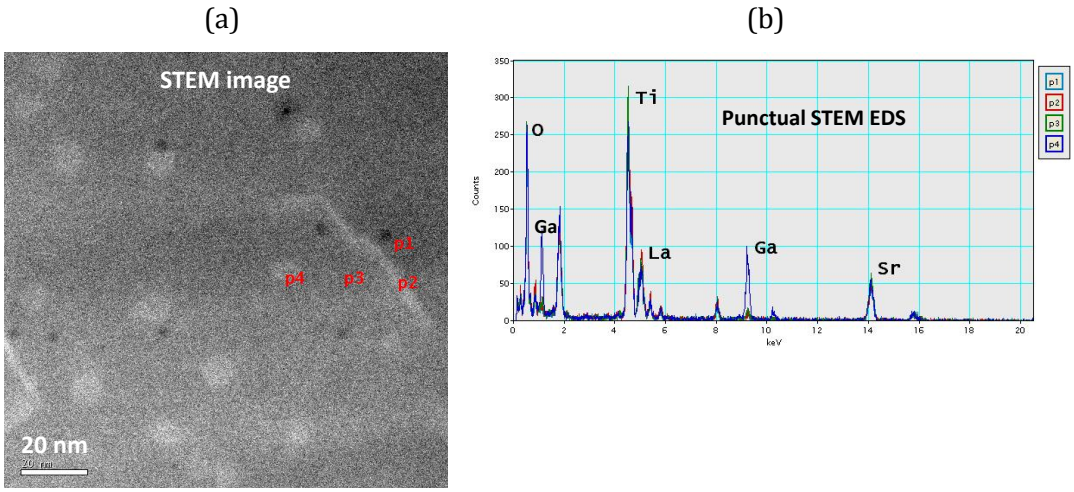

Figure 5-38 | (a) STEM image of a $La_{0.4}Sr_{0.4}Ga_{0.06}Ti_{0.94}O_{3-\gamma}$ sample reduced in 5%H_2/Ar, at 1000 °C, for 20 h and then oxidised in static air at 1000 °C, for 12 h. (b) EDS analysis of the points indicated in part (a) of this figure.

5.11.5 Designing Ga-containing perovskites that do not lose Ga on reduction

In the previous subchapter it was shown that A-site deficiency has little to no effect on the stability of Ga^{3+} on the B-site of the perovskite lattice. The other perovskite primitive site with deficiency in the series $La_{0.4}Sr_{0.4}Ga_xTi_{1-x}O_{3-\gamma}$ is the oxygen site. In order to investigate if oxygen stoichiometry has in impact on Ga loss, A-site stoichiometric, Ga-doped, oxygen stoichiometric or excess compositions such as $La_{1/3}Sr_{2/3}Ga_{1/3}Ti_{2/3}O_3$ and $La_{1/3}Sr_{2/3}Ga_{1/6}Ti_{5/6}O_{3.083}$, respectively, were prepared and investigated. It was found that both these perovskites were remarkable stable with respect to Ga loss. The corresponding Ga loss calculated after redox cycling was $\zeta < 0.003$ at/fu, much lower than the values listed in Table 5-2 for the oxygen deficient series $La_{0.4}Sr_{0.4}Ga_xTi_{1-x}O_{3-\gamma}$, and perhaps not even due to Ga loss, but most likely due to a very small amount of adsorbed water. Thus, it appeared that it was oxygen deficiency more than A-site deficiency that controlled Ga-loss. In consequence, a new series of A-site deficient, *oxygen stoichiometric*, Ga-doped titanates was designed as described in section 4.4,

with the general formula $La_{0.4+x}Sr_{0.4-x}Ga_xTi_{1-x}O_3$. All the members of this series prepared in this study up to $x = 0.18$ were found to be phase pure, as shown in section 4.4.

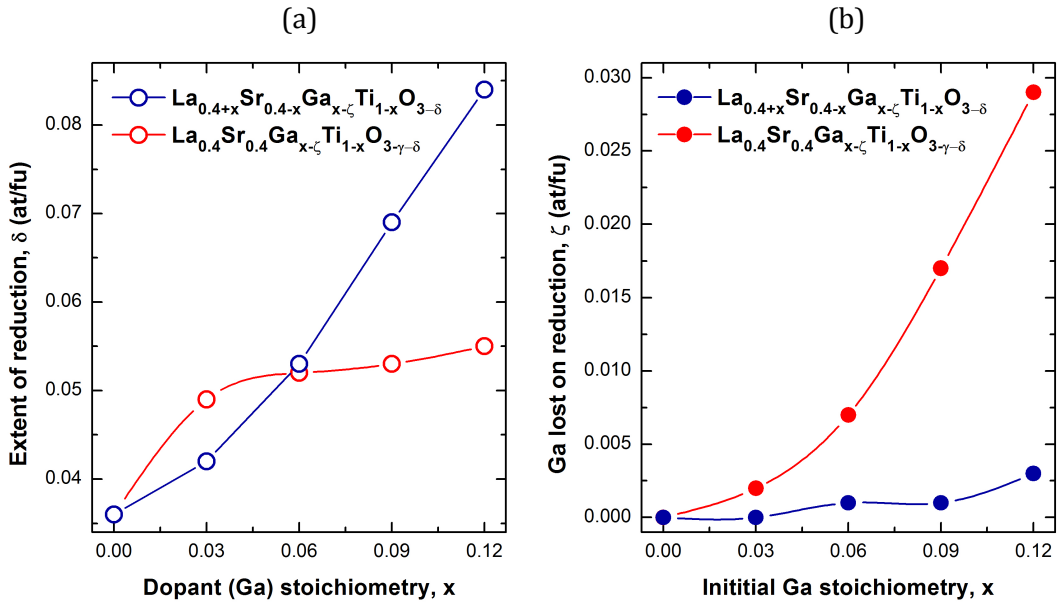

Figure 5-39 | Minimising Ga loss on reduction and enhancing the extent of reduction of Ga-doped, A-site deficient perovskites through control of defect chemistry. Oxygen deficiency and Ga loss on reduction expressed as δ and ζ, respectively, are plotted with respect to dopant stoichiometry (Ga) for two series with different defect charge compensation: (I) Ga^{3+} compensated by oxygen vacancies, $La_{0.4}Sr_{0.4}Ga_xTi_{1-x}O_{3-\gamma}$ and changing to $La_{0.4}Sr_{0.4}Ga_{x-\gamma}Ti_{1-x}O_{3-\gamma-\delta}$ after reduction; and (II) Ga^{3+} compensated by balancing the stoichiometry of the A-site cations, $La_{0.4+x}Sr_{0.4-x}Ga_xTi_{1-x}O_3$ and changing to $La_{0.4+x}Sr_{0.4-x}Ga_{x-\zeta}Ti_{1-x}O_{3-\delta}$ on reduction. δ and ζ were calculated according to Eq. 5-38 and Eq. 5-39 from a redox cycle performed on porous pellets. A redox cycle consists of a reduction step (in flowing 5%H_2/Ar at 1000 °C for 20 h) followed by an oxidation step (at 1000 °C in static air for 12 h). Errors are smaller than the points and the curves are interpolations based on the experimental data points.

Most importantly, when these compositions were subjected to the redox cycling tests to reveal any Ga loss, they were remarkably stable showing Ga losses close to none, $\zeta \leq 0.001$ at/fu for $x \leq 0.09$ and $\zeta \leq 0.004$ at/fu for $0.12 \leq x \leq 0.18$. These values are considerably smaller than the values seen for the family of compositions $La_{0.4+x}Sr_{0.4-x}Ga_xTi_{1-x}O_3$, with *e.g.* ζ as high as 0.029 at/fu for $x = 0.12$. The slight increase of ζ with Ga doping x in the series $La_{0.4+x}Sr_{0.4-x}Ga_xTi_{1-x}O_3$ could be again interpreted as a small uptake of adsorbed water rather than actual Ga loss, since as x increases the sinterability decreases in this series, resulting in more porous structures as shown in Figure 5-40.

(a) $x = 0.03$

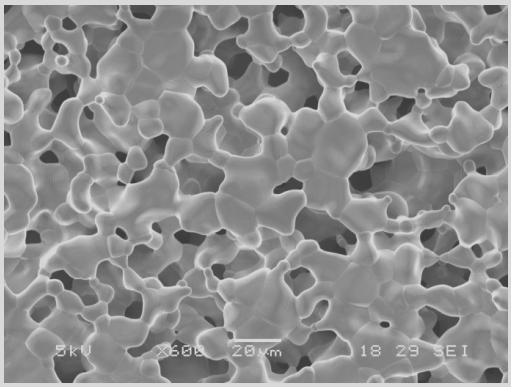

(b) $x = 0.06$

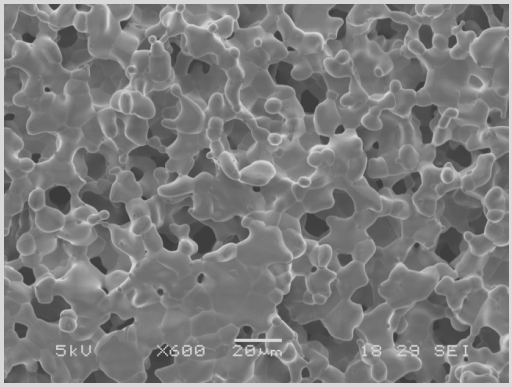

(c) $x = 0.09$

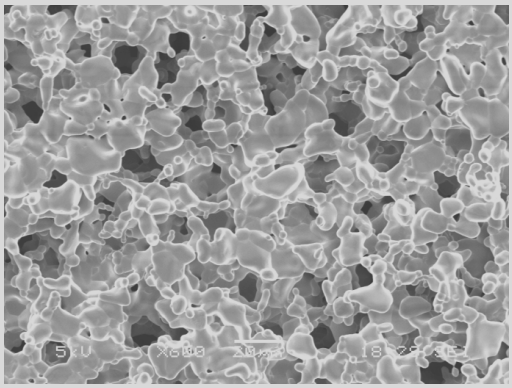

(d) $x = 0.12$

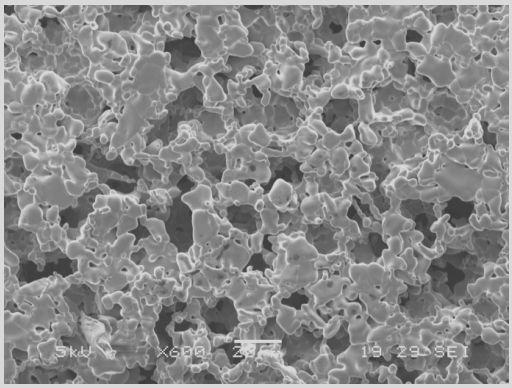

Figure 5-40 | Microstructure of the pellet samples corresponding to the members $x = 0.03$ (a), $x = 0.06$ (b), $x = 0.09$ (c), $x = 0.12$ (d) belonging to the series $La_{0.4+x}Sr_{0.4-x}Ga_xTi_{1-x}O_3$ and used in the thermo gravimetric analysis shown in Figure 5-40. These were obtained in the same conditions, by pressing mixtures of 17% glassy carbon and 83% sintered powder and firing them at 1400 °C for 7 h in air.

References

1. T. D. McColm and J. T. S. Irvine, *Solid State Ionics*, 2002, **152-153**, 615–623.
2. D. Neagu and J. T. S. Irvine, *Chem. Mater.*, 2010, **22**, 5042–5053.
3. S. Hui and A. Petric, *J. Eur. Ceram. Soc.*, 2002, **22**, 1673–1681.
4. T. Ishihara, H. Matsuda, M. Azmi bin Bustam, and Y. Takita, *Solid State Ionics*, 1996, **86-88**, 197–201.
5. T. Ishihara, in *Perovskite Oxide for Solid Oxide Fuel Cells*, ed. T. Ishihara, Springer, 2009.
6. H. Iwahara, in *Perovskite Oxide for Solid Oxide Fuel Cells*, ed. T. Ishihara, Springer, 2009.
7. V. V. Kharton, F. M. B. Marques, and A. Atkinson, *Solid State Ionics*, 2004, **174**, 135–149.
8. J. A. Kilner, A. Berenov, and J. Rossiny, in *Perovskite Oxide for Solid Oxide Fuel Cells*, ed. T. Ishihara, Springer, 2009.
9. M. Mogensen, D. Lybye, N. Bonanos, P. V. Hendriksen, and F. W. Poulsen, *Solid State Ionics*, 2004, **174**, 279–286.
10. P. R. Slater, J. T. S. Irvine, T. Ishihara, and Y. Takita, *J. Solid State Chem.*, 1998, **139**, 135–143.
11. M. Yashima, in *Perovskite Oxide for Solid Oxide Fuel Cells*, ed. T. Ishihara, Springer, 2009.
12. M. Yashima, *Solid State Ionics*, 2008, **179**, 797–803.
13. J. Irvine, in *Perovskite Oxide for Solid Oxide Fuel Cells*, ed. T. Ishihara, Springer, 2009.
14. S. Tao and J. T. S. Irvine, *Nature Mater.*, 2003, **2**, 320–323.
15. M. J. Escudero, J. T. S. Irvine, and L. Daza, *J. Power Sources*, 2009, **192**, 43–50.
16. M. S. Islam and R. A. Davies, *J. Mater. Chem.*, 2004, **14**, 86.
17. K. Huang, R. S. Tichy, and J. B. Goodenough, *J. Am. Cer. Soc.*, 1998, **81**, 2565–2575.
18. T. Ishihara, Ed., *Perovskite oxide for solid oxide fuel cells*, Springer, New York ;London, 2008.
19. N. Sakai, T. Horita, Y. P. Xiong, K. Yamaji, H. Kishimoto, M. E. Brito, H. Yokokawa, and T. Maruyama, *Solid State Ionics*, 2005, **176**, 681–686.
20. S. M. Plint, P. A. Connor, S. Tao, and J. T. S. Irvine, *Solid State Ionics*, 2006, **177**, 2005–2008.
21. C. Howard, G. Lumpkin, R. Smith, and Z. Zhang, *J. Solid State Chem.*, 2004, **177**, 2726–2732.
22. E. Kendrick, M. S. Islam, and P. R. Slater, *Solid State Ionics*, 2005, **176**, 2975–2978.
23. P. R. Slater and J. T. S. Irvine, *Solid State Ionics*, 1999, **124**, 61–72.
24. J. C. Ruiz-Morales, J. Canales-Vázquez, C. Savaniu, D. Marrero-López, W. Zhou, and J. T. S. Irvine, *Nature*, 2006, **439**, 568–571.
25. I. Barin, *Thermochemical data of pure substances*, VCH, 1995.
26. C. Housecroft and A. G. Sharpe, *Inorganic Chemistry*, Prentice Hall, 3rd edn., 2007.
27. K. F. Purcell and J. C. Kotz, *Inorganic Chemistry*, W B Saunders Co, 1977.
28. A. R. West, *Basic Solid State Chemistry*, Wiley, 2nd edn., 1999.

29. S. Stølen, E. Bakken, and C. E. Mohn, *Phys. Chem. Chem. Phys.*, 2005, **8**, 429–447.
30. J. B. Goodenough and Y.-H. Huang, *J. Power Sources*, 2007, **173**, 1–10.
31. J. Suntivich, K. J. May, H. A. Gasteiger, J. B. Goodenough, and Y. Shao-Horn, *Science*, 2011.
32. A. Demont, M. S. Dyer, R. Sayers, M. F. Thomas, M. Tsiamtsouri, H. N. Niu, G. R. Darling, A. Daoud-Aladine, J. B. Claridge, and M. J. Rosseinsky, *Chem. Mater.*, 2010, **22**, 6598–6615.
33. A. Reller, J. M. Thomas, D. A. Jefferson, and M. K. Uppal, *Proc. R. Soc. Lond. A*, 1984, **394**, 223–241.
34. M. Pilkington, *Principles of Inorganic Chemistry - Brock University Lectures (http://www.mpilkington.com/Teaching.html)*, 2011.
35. J. A. Alonso, M. J. Mart, and J. L. Garc, *J. Phys.: Condens. Mat.*, 1997, **9**, 6417–6426.
36. D. N. Miller and J. T. S. Irvine, *J. Power Sources*, 2011, **196**, 7323–7327.
37. G. Tsekouras and J. T. S. Irvine, *J. Mater. Chem.*, 2011.
38. K. Yamaji, T. Horita, M. Ishikawa, N. Sakai, and H. Yokokawa, *Solid State Ionics*, 1998, **108**, 415–421.
39. K. Yamaji, T. Horita, M. Ishikawa, N. Sakai, and H. Yokokawa, *Solid State Ionics*, 1999, **121**, 217–224.
40. D. P. Butt, Y. Park, and T. N. Taylor, *J. Nucl. Mater.*, 1999, **264**, 71–77.
41. M. Stanislowski, U. Seeling, D.-H. Peck, S.-K. Woo, L. Singheiser, and K. Hilpert, *Solid State Ionics*, 2005, **176**, 2523–2533.
42. J. W. Stevenson, T. R. Armstrong, L. R. Pederson, J. Li, C. A. Lewinsohn, and S. Baskaran, *Solid State Ionics*, 1998, **113-115**, 571–583.
43. K. Yamaji, Negishi, Horita, Sakai, and Yokokawa, *Solid State Ionics*, 2000, **135**, 389–396.

6 ENHANCING ELECTRONIC CONDUCTIVITY IN STRONTIUM TITANATES

6.1 The strategy

As indicated before, at a macroscopic scale, the electronic conductivity σ is proportional to the concentration of (free) charge carriers, *n* (as charge per volume), their charge Z, and their mobility μ:[1]

$$\sigma = n \cdot \mathrm{Z} \cdot e \cdot \mu \qquad \text{Eq. 6-1}$$

In strontium titanates the charge carriers are electrons that may be introduced by reduction:[2]

$$\mathrm{O_O^x} \rightarrow \frac{1}{2}\mathrm{O_2} + \mathrm{V_O^{\cdot\cdot}} + 2\mathrm{e'} \qquad \text{Eq. 6-2}$$

This may also be written as

$$2\mathrm{Ti_{Ti}^x} + \mathrm{O_O^x} \rightleftharpoons 2\mathrm{Ti'_{Ti}} + \mathrm{V_O^{\cdot\cdot}} + \frac{1}{2}\mathrm{O_2} \qquad \text{Eq. 6-3}$$

The Kröger–Vink notation $\mathrm{Ti'_{Ti}}$ does not necessarily mean that the generated electrons are bound to the Ti site.

Also, in section 5.1 it was shown that if the electrons generated through reduction are free to conduct then by combining Eq. 1-1 and Eq. 6-3 it follows that if there is no association of electrons, the *electronic conductivity is directly proportional to the extent of reduction*:

$$\sigma \approx \frac{2 \cdot e \cdot \mu}{{a_0}^3} \cdot \delta \qquad \text{Eq. 6-4}$$

Where *e* is the elementary charge and a_0 is the pseudocubic unit cell parameter of the perovskite in its oxidised form (see section 5.1 and Eq. 5.12).

Since $\sigma \propto \delta$, it follows that titanates which exhibit higher extent of reduction might also exhibit higher electronic conductivity. Thus, by designing materials that are able to reduce to higher extents, one might also improve their conductivity. On the other hand, a strategy for improving δ in titanates was already presented and exemplified in Chapter 5.

Thus, the strategy proposed here for enhancing the electronic conductivity in strontium titanates relies on improving their extent of reduction. This in turn was shown to be considerably augmented by various defects (vacancies and cation substitutions) that act to promote oxide ion mobility and maximise the overall ability of titanates to support higher concentrations of oxide ion vacancies.

This strategy will be exemplified and validated throughout this chapter by making use of selected compositions derived from the parent composition $La_{0.4}Sr_{0.4}TiO_3$. Thus, initially a summary of conductivity characteristics will be presented for the $La_{0.4}Sr_{0.4}TiO_3$ system, following with a close comparison between σ and δ for the series $La_{0.4}Sr_{0.4}Ga_xTi_{1-x}O_{3-\gamma}$ and eventually extending the range to transition metal cation doping, $La_{0.4}Sr_{0.4}M_xTi_{1-x}O_{3-\gamma}$ (M = Fe, Ni, Zn).

6.2 Factors that determine the conductivity of perovskite titanates

According to Eq. 6-4, multiple factors may influence the electronic conductivity of titanates and these should be kept in mind when analysing and comparing conductivity data. These factors are summarised in Figure 6-1 and discussed below and exemplified on the different perovskite systems throughout this chapter.

The electronic conductivity of titanates depends primarily on the concentration of electrons (*i.e.* Ti^{3+} ions) which in turn depends on the extent of reduction, δ. As such, it will be greatly influenced by the conditions in which the sample has been prepared and/or processed. There are several means of changing the Ti^{3+} content in a titanate, and all gravitate around the defect chemistry of the starting composition and the way this changes when exposed to different environments usually characterized by the oxygen partial pressure and temperature.

The first step in which the Ti^{3+} content can be controlled is the synthesis stage. When prepared in air, the vast majority of the Ti ions are at 4+, and dopants are usually compensated by oxygen defects (oxygen excess or deficiency). For example, when *synthesized in air*, the oxygen excess series discussed previously can be written as $La_x^{3+}Sr_{1-x}^{2+}Ti_{\varepsilon}^{3+}Ti_{1-\varepsilon}^{4+}O_{3+x/2-\varepsilon/2}^{2-}$. In this case, the number of Ti^{3+} ions, ε, will be very small since air cannot remove oxide ions. However, some Ti^{3+} may exist since these phases are prepared at high temperatures (1450-1650 °C) which may act as slightly reducing because of the significant increase in the entropic factor. Because of this effect oxide ions can be lost from the lattice and a very small number of electrons ε are subsequently generated. Consequently, most titanates prepared in air (thus in *oxidized form*) show dilute semiconducting electronic conductivity, with conductivities *e.g.* between $10^{-3} - 10^{-2}$ S·cm^{-1} when measured in air at 900 °C, owing to the very dilute electronic conductivity (ε very small).[3,4]

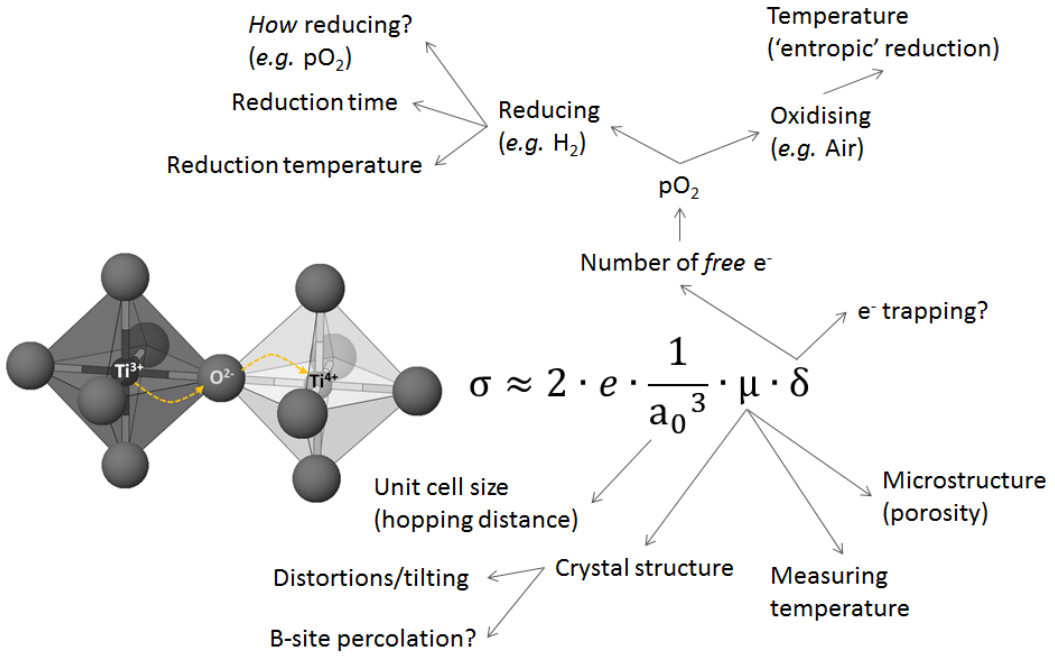

Figure 6-1 | Schematic diagram of the factor that may affect the electronic conductivity of titanates as derived from Eq. 6-4.

On the other hand when the phase is *synthesised in reducing conditions* (e.g. pure H_2, 5%H_2/Ar, etc), many more oxide ions can be removed and hence a much greater number of Ti^{3+} ions, ε can be generated. Typically the perovskite will tend to become oxygen stoichiometric, so ε will tend to become equal to x. If the reducing conditions are even stronger, the titanate could even step into the oxygen deficient domain for $\varepsilon > x$. Thus, after being sintered in highly reducing conditions, at 1650 °C, the above mentioned series shows metallic behaviour rather than semiconducting. Also, the conductivity (measured in reducing conditions as well to preserve the reduced Ti^{3+}) reaches 100 to 400 $S \cdot cm^{-1}$ at 1000 °C, when x increases from 0.1 to 0.4.[4] As it can be noticed, the difference in the conductivity values between the same composition when sintered in air or reducing conditions lies on the order of 5 orders of magnitude and directly reflects the distinct defect chemistry of the same series depending on the conditions employed during phase formation.

Nonetheless, the conductivity of the phases sintered in oxidizing condition can be increased by subsequently reducing them. There are several ways to conduct such reduction experiments and each of these can provide complementary information about the reduction process in titanates. The main parameters that can be varied and which may influence the 'instantaneous' and/or final extent of reduction and hence conductivity values are the p_{O_2} and temperature at which the reduction is carried out and the duration of the reduction (*i.e.* is the sample equilibrated in the given conditions or not?).

Other factors that may affect the measured conductivity values are related to the mobility of the charge carriers. At the microscopic level of the crystal lattice the mobility may be determined by a multitude of factors, including the *distance between B-sites* (shorter distances – *i.e.* smaller unit cells – makes electron hopping easier), *lattice symmetry* (higher symmetry – less collisions, small octahedral tilting – higher orbital overlap), *B-site percolation* (do all the B-site cation support conduction or just some of them create a

percolating, conductive network?), *thermal motion* (depending on temperature, electrons may interact differently with the lattice environment, hence the temperature at which a certain conductivity value was measured holds valuable information) etc. At a macroscopic level, the mobility of the charge carriers is inherently hindered by the polycrystalline nature of the samples used here, be it boundaries between crystallites or even grain boundaries. In fact it is important to highlight here that the samples used in the conductivity studies are deliberately very porous (30-40% porosity) in order to mimic the porosity of electrodes. However, as opposed to *e.g.* SOFC anodes where the size of the grains is usually well below 1 μm on average to maximise surface area, here grains of 10-20 μm were used in order to create mechanically robust samples for conductivity testing.

6.3 Conductivity characteristics of the undoped, A-site deficient titanate $La_{0.4}Sr_{0.4}TiO_3$

6.3.1 The effect of synthesis conditions (air *vs.* 5%H_2/Ar) on conductivity

Upon heating in air, as-prepared (oxidised), porous $La_{0.4}Sr_{0.4}TiO_3$ exhibits semiconducting behaviour, as shown in Figure 6-2 (a). At 900 °C, the porous sample with ~40% porosity reaches a conductivity of about $\sim 5 \cdot 10^{-2}$ S·cm^{-1} while the activation energy for the conduction is rather high, ~1.8 eV (Figure 6-2 (a)).

When synthesised and measured in 5%H_2/Ar the conductivity is more than 4 orders of magnitude higher as a result of much greater extent of reduction and higher Ti^{3+} content. Additionally, the sample now exhibits metallic behaviour and consequently displays a considerable drop in conductivity upon heating, with values from ~430 S·cm^{-1} at 100 °C to 100 S·cm^{-1} around 900 °C. However, since the concentration of Ti^{3+} in this sample does not correspond to the equilibrium value at this temperature the conductivity decreases very slowly over time, as shown in Figure 6-3 (a). Correspondingly,

upon cooling the conductivity shows hysteresis compared to heating since the decrease in temperature causes the metallic character to exacerbate conductivity differences especially at low temperatures (Figure 6-3 (b)).

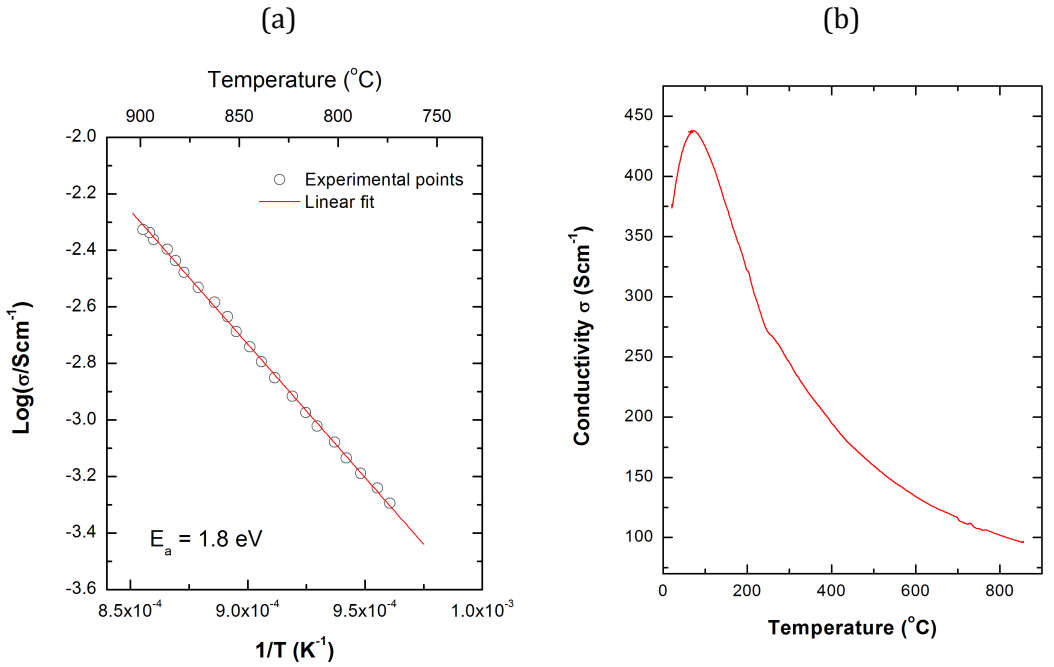

Figure 6-2 | Comparative conductivity plots for $La_{0.4}Sr_{0.4}TiO_3$ prepared at 1400 °C in air *vs.* 5%H_2/Ar. (a) Arrhenius plot of the air-synthesised sample with ~40% porosity, measured in air. (b) σ *vs.* T plot for the sample synthesised in 5%H_2/Ar having ~10% porosity, measured in 5%H_2/Ar.

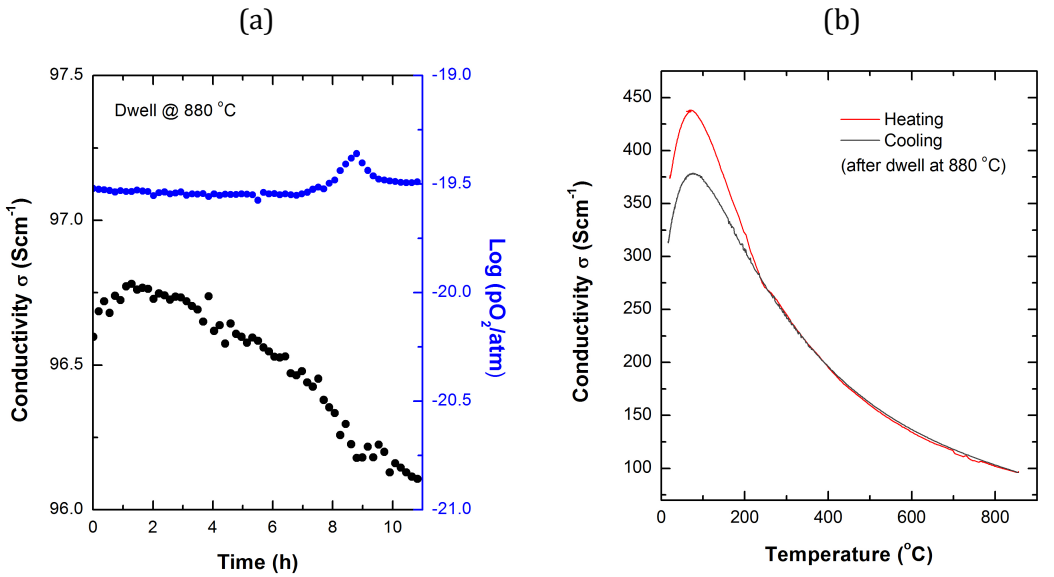

Figure 6-3 | (a) Slow progress of the sample sintered in 5%H_2/Ar (Figure 6-2 b) towards equilibrium at 880 °C, in 5%H_2/Ar. (b) After the 11 h dwell at 880 °C the same sample shows hysteresis upon cooling compared to the initial data collected on heating.

6.3.2 The σ – T and μ – T dependencies

The shape of the σ(T) dependency for the sample prepared in reducing conditions (Figure 6-2 (b)) deserves additional attention since it appears to be characteristic to titanates. Most of the compositions prepared in this study have this characteristic, but there are other examples in the literature as well.[5–7]

As shown in section 5.2, the concentration of Ti^{3+} formed at high temperatures through reduction tends to remain largely constant upon cooling down to room temperature, if the atmosphere is reducing enough. This should also be valid upon re-heating samples in reducing conditions for electrical measurements. Thus, in the case of the measurement presented in Figure 6-2 (b) it could be said that δ is constant upon heating (obviously, during the dwell at 880 °C, δ decreased slightly). Thus, if δ is approximately constant *during heating*, according to Eq. 6-4 the σ – T dependency presented in Figure 6-2 (b) should in fact reflect the variation of the mobility of charge carriers, μ, with temperature, μ(T).

Thus, the 'μ(T)' curve presented in Figure 6-2 may be regarded as being composed of two branches: a low temperature branch in which the material displays *semiconducting* behaviour, followed by a higher temperature branch where the sample exhibits *metallic* type conduction.

The temperature corresponding to the semiconductor to metallic transition seems to depend on defect chemistry and perhaps on the microstructure as well. This transition appears to consistently occur at higher temperatures (300-500 °C) in oxygen excess titanates compared to A-site deficient titanates, based on the data in this study and other reports.[5,7]

In the metallic temperature range, the μ(T) dependency is generally given by a *power law*, which is an indication of phonon scattering:[8,6]

$$\mu(T) = \frac{\mu_0}{T^m} \qquad \text{Eq. 6-5}$$

By taking the logarithm of the above equation it can be converted to linear form and slope of the resulting line equals *m*. It was found that the sample in discussion now (prepared in reducing conditions) follows this power law throughout the temperature range where it exhibits metallic character. This is outlined by re-plotting the data in Figure 6-2 (b) as Log(T/K) *vs.* $\mathrm{Log}(\sigma/(\mathrm{S}\cdot\mathrm{cm}^{-1}))$, as shown in Figure 6-4.

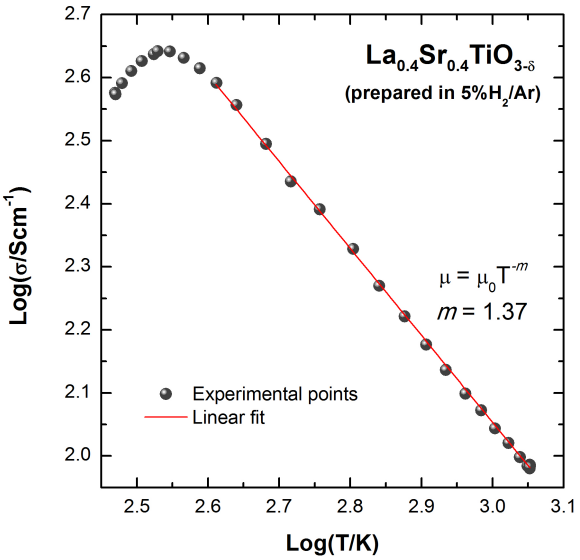

Figure 6-4 | The conductivity data of the sample prepared in 5%H_2/Ar (Figure 6-2 (b)) re-plotted as Log(T/K) *vs.* $\mathrm{Log}(\sigma/(\mathrm{S}\cdot\mathrm{cm}^{-1}))$, in order to outline the power law μ(T) dependency in the temperature range where the sample exhibits metallic character.

By examining Eq. 6-5 and Figure 6-4, it becomes clear that *m* is a measure of how 'abruptly' the conductivity falls upon heating due to phonon scattering. For this sample *m* was found to be *m* = 1.37. For comparison, the Nb-doped perovskite titanate $Sr_{0.94}Nb_{0.1}Ti_{0.9}O_3$ sintered in similar conditions (9%H_2/N_2, 1400 °C, 12 h) exhibited *m* = 1.95.[6] In terms of conductivity 'loss' on heating this is quite significant. For example, the conductivity of $La_{0.4}Sr_{0.4}TiO_3$ with *m* = 1.37 decreases from ~440 $\mathrm{S\cdot cm^{-1}}$ at room temperature to ~96 $\mathrm{S\cdot cm^{-1}}$ at 900 °C, while $Sr_{0.94}Nb_{0.1}Ti_{0.9}O_3$ with *m* = 1.95 exhibits a decrease in conductivity from ~710 $\mathrm{S\cdot cm^{-1}}$ to 120 $\mathrm{S\cdot cm^{-1}}$ within the same temperature range. Thus, ideally, a titanate with *m* value as low is possible is desirable.

6.3.3 The σ – δ dependency

As suggested in subchapter 6.2, the low conductivity showed by the titanates prepared in air may be improved through reduction. The means used to increase the extent of reduction without altering the (cation) composition was by increasing the reduction temperature (see section 5.3 for the effect of temperature on reduction).

To evaluate the increase in conductivity with the extent of reduction for $La_{0.4}Sr_{0.4}TiO_3$, the following experiment was carried out. Porous pellets (~60-65% dense) were reduced at increasingly higher temperatures and their extent of reduction measured, as explained before, by weighing them before and after the reduction. The conductivity of the samples was then measured in reducing conditions as a function of temperature and is given in Figure 6-5. The plot is given again, as $\mathrm{Log}(T/K)$ *vs.* $\mathrm{Log}(\sigma/(S \cdot cm^{-1}))$, in order to outline the power law dependency in the metallic temperature domain, but the corresponding temperature (in K) and conductivity are also displayed on the opposing axes. Figure 6-5 shows that the reduced samples exhibit higher conductivity as the reduction temperature increases. Additionally, they display the same type of σ(T) dependencies as the sample synthesised in reducing conditions (Figure 6-4).

Since the extent of the reduction is known for each sample, the electron mobility corresponding to each sample, across the studied temperature range μ(T) can be calculated by rearranging Eq. 6-4:

$$\mu(T) = \frac{{a_0}^3}{2 \cdot e} \cdot \frac{1}{\delta} \cdot \sigma(T) \qquad \text{Eq. 6-6}$$

By substituting the constants with their corresponding values ($e = 1.602 \cdot 10^{-19}$C, $a_0 = 3.8889 \cdot 10^{-8}$ cm), it follows that:

$$\mu(T) = 1.835 \cdot 10^4 \cdot \frac{1}{\delta} \cdot \sigma(T) \qquad \text{Eq. 6-7}$$

Thus, Eq. 6-7 can thus be used to calculate the electron mobility of the differently reduced samples, as a function of temperature. A plot of μ(T/°C) for the samples reduced at different temperature is presented in Figure 6-6.

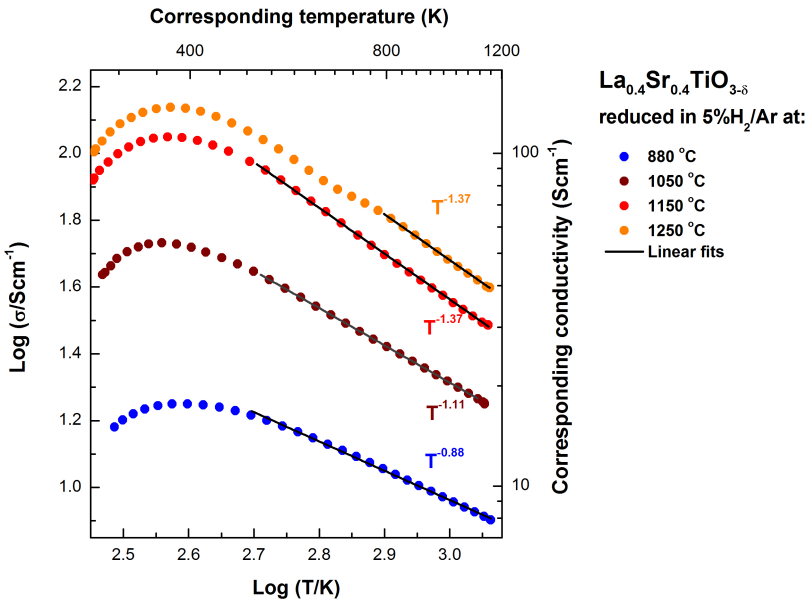

Figure 6-5 | Conductivity-temperature dependencies for $La_{0.4}Sr_{0.4}TiO_3$ pellets (60-60% dense) reduced in 5%H_2/Ar at different temperature prior to this measurement. The reduction temperatures are 880 °C (equilibrated in the conductivity jig), 1050, 1150 and 1250 °C (all equilibrated in the reduction furnace, 12 h).

The figure also contains the corresponding power law fits calculated by regression for Eq. 6-5, within the temperature range outlined in Figure 6-5. The power laws found by regression for each reduction temperature are given below. In the power laws the mobility is expressed in $cm^2V^{-1}s^{-1}$, the temperature in K and each reduction temperature is denoted by subscript *e.g.* 'μ_{H880}'.

$$\mu_{H880}(T) = \frac{42.4}{T^{0.88}} \quad \text{Eq. 6-8}$$

$$\mu_{H1050}(T) = \frac{220.7}{T^{1.11}} \quad \text{Eq. 6-9}$$

$$\mu_{H1150}(T) = \frac{1468.1}{T^{1.37}} \quad \text{Eq. 6-10}$$

$$\mu_{H1250}(T) = \frac{1578.6}{T^{1.37}} \quad \text{Eq. 6-11}$$

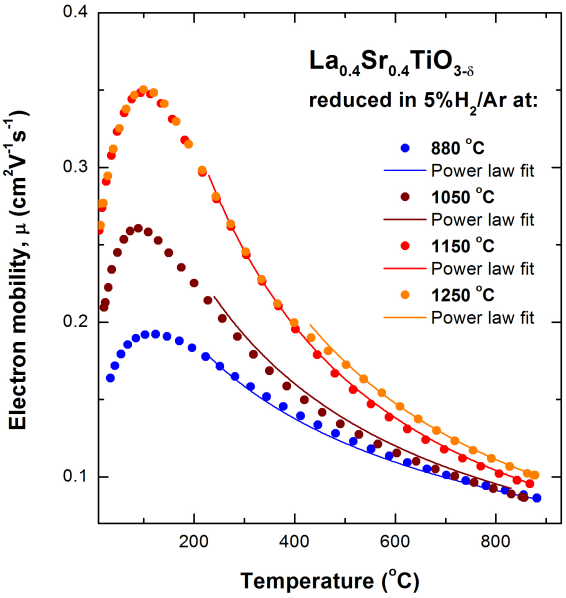

Figure 6-6 | Electron mobility-temperature dependencies for $La_{0.4}Sr_{0.4}TiO_3$ pellets (60-60% dense) reduced in 5%H_2/Ar at different temperature prior to the conductivity measurement. The mobility values are calculated by using Eq. 6-7. The reduction temperatures are 880 °C (equilibrated in the conductivity jig), 1050, 1150 and 1250 °C (all equilibrated in the reduction furnace, 12 h). The power law fits are also shown for the same temperature range as in Figure 6-5.

Several important aspects emerge by examining this figure and the outcome of the regression analysis. First, the shape of the μ(T) dependency is the same as the σ(T) dependency owing to the direct proportionality between μ and σ as expressed by Eq. 6-7. Secondly, the μ(T) curves tend to be situated at increasingly higher mobility values as the reduction temperature increases. Thus, the greater the extent of reduction, the higher the mobility. However, while this increase is continuous from the reduction temperature of 880 to 1050 and then to 1150 °C, the final increase in reduction temperature to 1250 °C does not result in further increase in mobility. In fact, the increase of mobility with the reduction temperature appears to arrive at a 'saturation limit' since the mobility of the sample reduced at 1150 °C *almost* overlaps with that of the sample reduced at 1250 °C across the entire temperature range. This can be also seen in the plot of the μ_0 coefficients (Eq. 6-8 to Eq. 6-11) against δ, shown in Figure 6-7 (a).

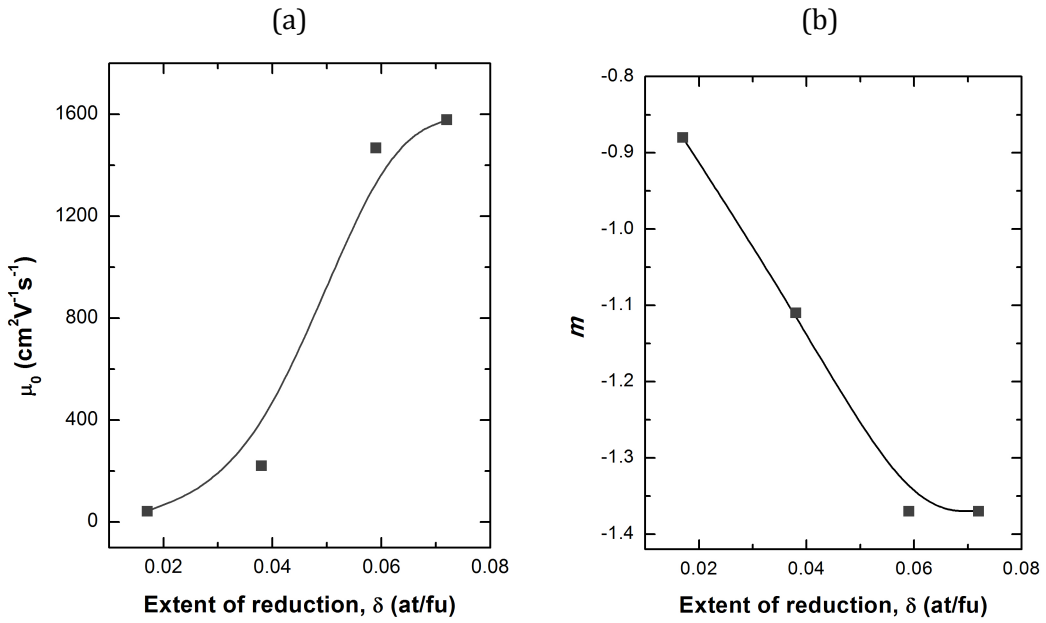

Figure 6-7 | (a) μ_0 and (b) m as a function of the extent of the reduction δ. μ_0 and m are the coefficients of the power law regressions shown in Figure 6-6 and given in Eq. 6-8 – Eq. 6-11. The line are guide for the eye.

A final observation regarding Figure 6-6 is concerned with the variation of mobility with (measuring) temperature. The mobility decreases quite abruptly on heating for a given sample and even more so with the increase in temperature at which the samples had been reduced. Equivalently, it can be said that for a given sample, the decrease in conductivity upon heating which is due to phonon scattering, increases with the extent of reduction in the sample. This is also reflected in the plot of the coefficient m against δ presented in Figure 6-7 (b). These coefficients increase almost linearly up to $m = 1.37$ which corresponds to a reduction temperature equal to 1150 °C. The value of m remains the same for the reduction at the next higher temperature, just as the value of μ_0 was seen to 'stagnate' at this temperature as well. Interestingly, the m value found here for the higher reduction temperatures, $m = 1.37$, equals exactly the value of this parameter for the sample that was prepared in reducing conditions (see Figure 6-4). Thus, it seems indeed that a plateau in the $m(\delta)$ variation is attained for extents of reduction or reduction temperatures in excess of 0.06 and 1250 °C, respectively.

An important consequence of the fact that samples with higher extents of reduction experience higher phonon scattering upon heating is that at a certain temperature the μ(T) dependencies of samples with different extent of reduction are bound to *converge* towards a common value. This is clearly seen in Figure 6-6 where the μ(T) dependencies become very close to each other for temperatures above ~800 °C. Above this temperature the mobility values of systems with different δ become almost equal. Hence, the *conductivity* becomes essentially *directly proportional* to the *extent of reduction*. This is shown in Figure 6-8.

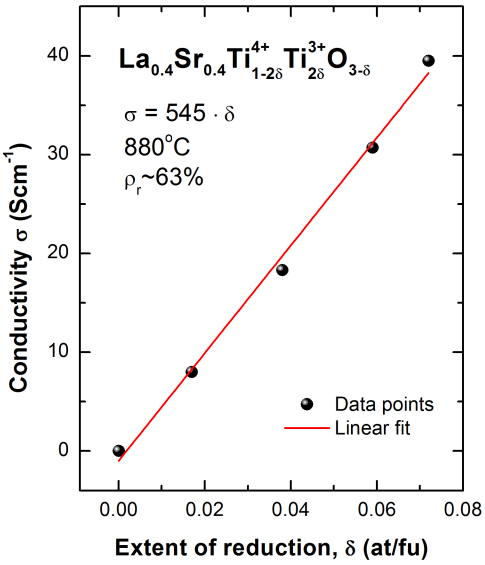

Figure 6-8 | The δ – σ dependency for $La_{0.4}Sr_{0.4}TiO_3$ at 880 °C. The data was obtained by reducing ~63% dense pellets at temperatures between 880 °C and ~1250 °C in 5%H_2/Ar and subsequently measuring their extent of reduction and conductivity. The conductivity was measured in 5%H_2/Ar and the plotted conductivity values correspond to the temperature 880 °C.

In conclusion it can be said that in $La_{0.4}Sr_{0.4}TiO_3$conductivity always increases with the extent of reduction, but conductivity is only directly proportional to the extent of reduction above ~800 °C measuring temperatures, where the electron mobility in this system becomes the same irrespective of the initial extent of reduction.

6.3.4 The conductivity dependence upon reduction temperature and sample porosity

In order to study the effect of porosity and reduction temperature on conductivity, $La_{0.4}Sr_{0.4}TiO_3$ pellets with relative densities of about 57, 63 and 68% with controlled microstructure were prepared by sintering in air and subsequently reduced at high temperatures and their conductivity measured at ~900 °C. A list of these conductivities is given in Table 6-1.

Table 6-1 | Conductivity of $La_{0.4}Sr_{0.4}TiO_3$ pellets of different relative densities previously reduced in 5%H_2/Ar at the specified temperatures. Conductivity was measured at 880 °C in 5%H_2/Ar.

Relative density	**Conductivity ($S \cdot cm^{-1}$) after reduction**			**Measurement technique**
	@ 1050 °C	@ 1150 °C	@ 1250 °C	
68%	22	28	44	4 points
63%	18	31	40	Van der Pauw
57%	16	20	32	4 points

As seen from Table 6-1 the conductivity was found to be strongly influenced by the porosity and reduction temperature. For a given porosity, the conductivity increases with the increase of the pre-reduction temperature, as expected. Conductivities of up to 44 $S \cdot cm^{-1}$ for samples having 68% relative density were measured at 880 °C, in 5%H_2/Ar. The effect of the porosity on the conductivity becomes more important as the material has a higher extent of the reduction. For example, for the pellets reduced at 1100 °C when increasing the relative density from 57% to 68%, the conductivity increases from 16 to 17 $S \cdot cm^{-1}$, respectively. However, when considering pellets pre-reduced at a higher temperature, for example 1200 °C, the increase is from 20 to 28 $S \cdot cm^{-1}$, for the same increase in relative density.

Of course, it is interesting to see whether these conductivities can be maintained for a long period of time. Surprisingly, the electrical properties do

not seem to degrade in time, but rather to improve slightly if the p_{O_2} is extremely low. Figure 6-9 shows that conductivity decreases slowly at 880 °C when the p_{O_2} is higher than about 10^{-19} atm. However, if the p_{O_2} is lower than $10^{-20} - 10^{-21}$ atm, the conductivity increases slightly at upon dwelling at 880 °C (Figure 6-10).

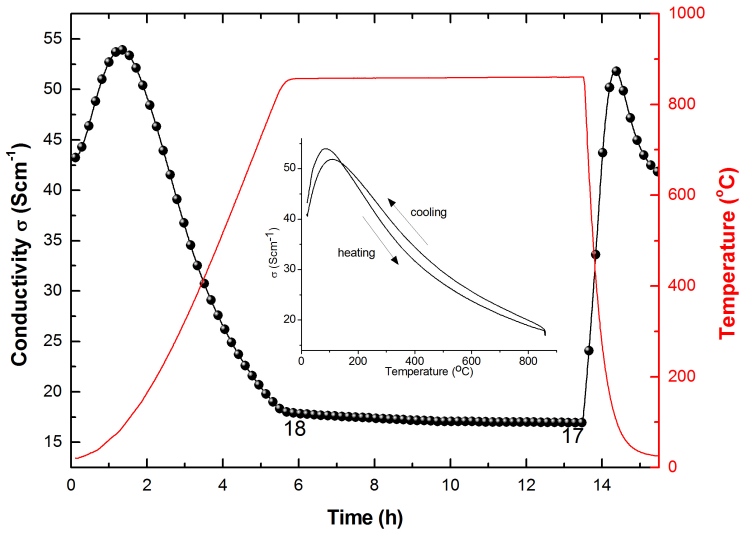

Figure 6-9 | Conductivity against time for a reduced porous pellet (5% H_2/Ar, 1050 °C, ~63% dense), showing the degradation of the electrical properties when the p_{O_2} is higher than 10^{-19} atm at 880 °C. The inset plot represents the temperature dependence of the thermal history shown on the main axes.

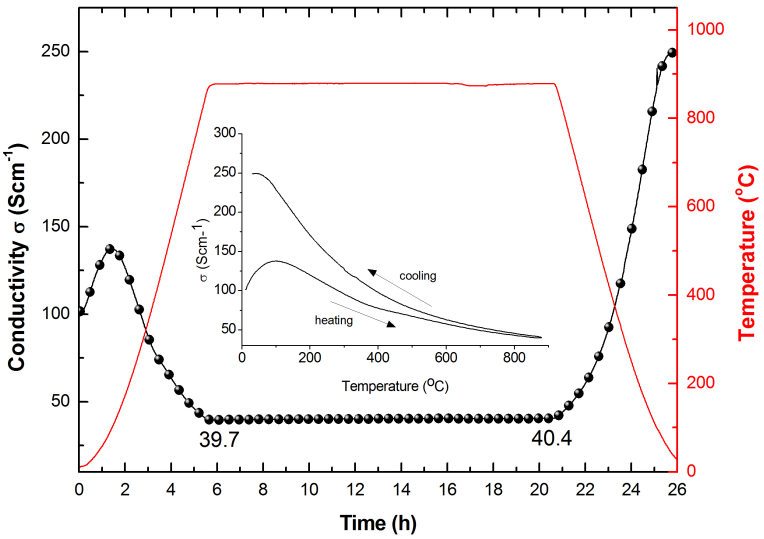

Figure 6-10 | Conductivity versus time and temperature profile for a reduced porous sample (5% H_2/Ar, 1250 °C, ~63% dense), showing the improvement of electrical properties when kept at 880 °C and p_{O_2} lower than $10^{-20.5}$ atm. The inset plot represents the temperature dependence of the thermal history shown on the main axes.

6.3.5 The effect of pO_2 variation on conductivity (redox cycling)

The change in conductivity of as-prepared (oxidised) $La_{0.4}Sr_{0.4}TiO_3$ samples upon exposure to reducing conditions has already been discussed in section 5.2. It was shown there that this composition displays fast initial reduction, followed by a long period of equilibration, even for highly porous samples. Here, the effect of switching the atmosphere back to air and then to $5\%H_2/Ar$ again will be discussed.

The redox behaviour was studied at two temperatures: 900 °C and 670 °C. The corresponding conductivity is plotted against time, on oxidation followed by reduction in Figure 6-11 and Figure 6-12, respectively. The pellets employed in this example have ~35% porosity and were previously reduced in $5\%H_2/Ar$ at 1050 °C for 12 h. The conductivity loss associated with the oxidation process strongly depends on the oxidation temperature. The sample exposed to air at 900 °C needed only 2 h to decrease its conductivity to about 10^{-2} S·cm^{-1}, which is roughly the conductivity of the oxidised $La_{0.4}Sr_{0.4}TiO_3$ in air (see Figure 6-2 (a)). The oxidation process is much slower at 670 °C, the sample needing 12 h to reach the same value.

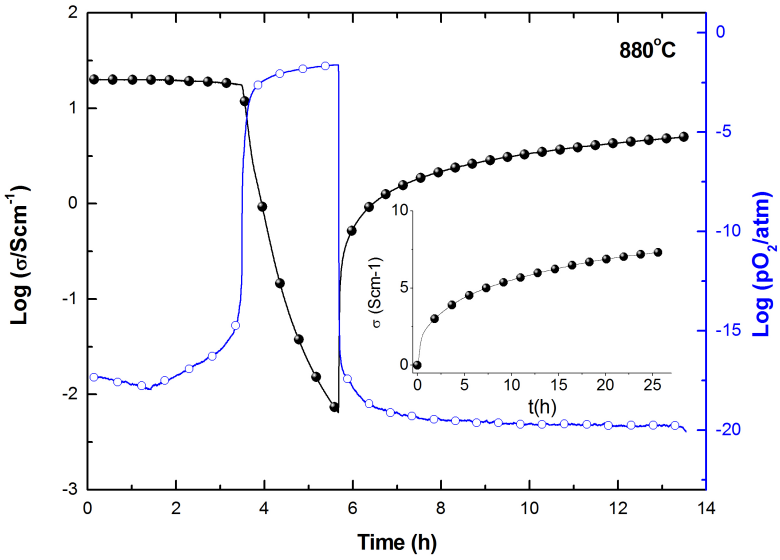

Figure 6-11 | Conductivity and p_{O_2} as a function of time during a redox cycle performed on ~65% dense $La_{0.4}Sr_{0.4}TiO_3$ pellets at 900 °C. The pellets were previously reduced in $5\%H_2/Ar$ at 1050 °C for 12 h.

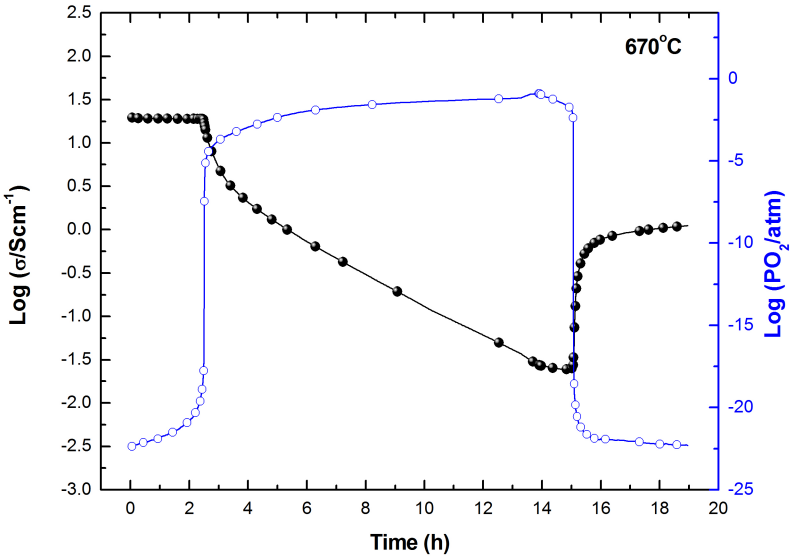

Figure 6-12 | Conductivity and p_{O_2} as a function of time during a redox cycle performed on ~65% dense $La_{0.4}Sr_{0.4}TiO_3$ pellets at 670 °C. The pellets were previously reduced in 5%H_2/Ar at 1050 °C for 12 h.

It can therefore be assumed that the oxidation process takes place in reverse compared to the reduction process. In the first stage the surface of the grains will be oxidized. Depending on the surface exchange coefficient and the bulk diffusion coefficient of the oxygen at the oxidation temperature, the oxidation will proceed at different rates. The oxygen ions will gradually re-occupy the vacant atomic position in the oxygen sub-lattice, causing the oxidation of Ti^{3+} ions and thus lowering the conductivity.

When the atmosphere was changed back to low p_{O_2}, the same fast initial response was noted for both temperatures (Figure 6-11 and Figure 6-12). It was, however, surprising to find that the material exhibited this type of behaviour at the lower temperature of 670 °C. This finding suggests surface reactivity and conductivity are still very good at this temperature. It is also interesting to note the conductivity of both samples is about 1 $S \cdot cm^{-1}$, just after the initial stage, suggesting that good conductivity may be achieved almost instantly upon exposure to reducing environment. As expected, equilibration of the samples is strongly hindered by the slow bulk reduction kinetics (see inset of Figure 6-11).

6.4 Conductivity in the Ga-doped series $La_{0.4}Sr_{0.4}Ga_xTi_{1-x}O_{3-\gamma}$

6.4.1 The σ – δ dependency

As discussed in section 5.11.2, Ga doping in $La_{0.4}Sr_{0.4}TiO_3$ leads to an increase in the extent of reduction. In order to study the correlation between conductivity and the extent of reduction in these compositions samples having 60-70% relative density were prepared in air, reduced at 1000 °C for 20 h in 5%H_2/Ar flow and heated to 880 °C in 5%H_2/Ar. All the samples showed high conductivity and a metallic type behaviour after a semiconductor to metallic transition around 100 °C, similar to the undoped composition. In Figure 6-13 the extent of the reduction and corresponding conductivity can be compared.

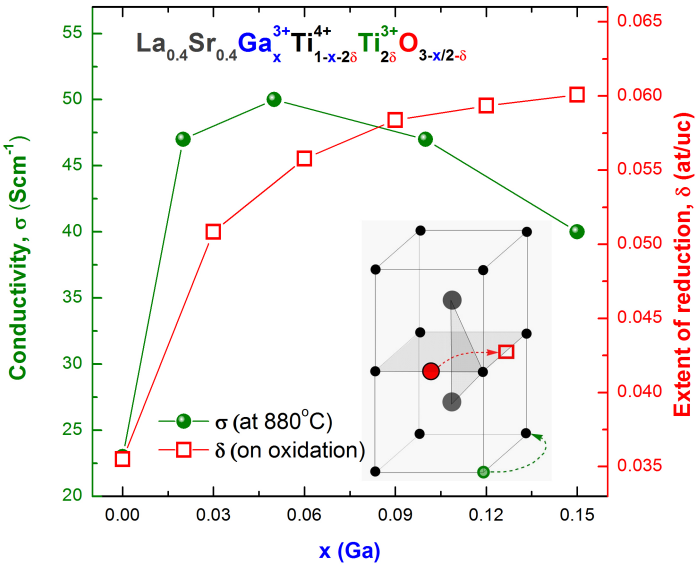

Figure 6-13 | The extent of reduction δ and conductivity σ (σ at 880 °C, 5%H_2/Ar) for 60-70% dense $La_{0.4}Sr_{0.4}Ga_xTi_{1-x}O_{3-\gamma}$ pellets previously reduced at 1000 °C for 20 h in 5%H_2/Ar. δ measured on oxidation, as explained in section 5.11.2.

The $\sigma(x)$ and $\delta(x)$ dependencies (x = Ga stoichiometry) shows the influence of doping on δ and σ is quite considerable and concerted towards enhancing electronic conductivity, as anticipated. In particular, the sharp rise upon doping 3% Ga is reflected exactly by both the $\sigma(x)$ and $\delta(x)$ variations. However, unlike the $\delta(x)$ trend which increases continuously, the $\sigma(x)$ trend

shows a maximum, after which a slow decrease in conductivity is observed. This is most likely due to the disruption that Ga doping cause in the B-site sublattice. Since Ga does not normally exhibit mixed oxidation states, and when it does the conductivity is very low in reducing conditions,[9,10] Ga^{3+}/Ga^{2+} reduction will not contribute positively to conductivity, essentially disrupting the Ti percolation which supports conductivity (see discussion in section 5.5 as well).

It is worth noting that not only does the conductivity increase with doping, but the increase in conductivity values is quite significant. For example in order to achieve a conductivity of about 45 $S{\cdot}cm^{-1}$ with the undoped sample, a reduction temperature of about 1250 °C was necessary, while with only 6% Ga B-site doping this conductivity can be achieved at the much lower temperature of 1000 °C, using the same gas as reducing agent ($5\%H_2/Ar$).

6.4.2 The effect of pO_2 variation on conductivity and the 'core-shell' effect

In order to see how the conductivity values change when equilibrated at 880 °C, a lower temperature compared to the reduction temperature used of 1000 °C, a redox cycle was performed. The results are plotted in Figure 6-14 as conductivity against composition, at different moments in time throughout the redox cycle. The stages highlighted are: after 2 h of oxidation (oxidation was carried out here for 2 h only), after 1 h of reduction and finally the equilibrium values, after 24 h of reduction.

It is interesting to note that while the undoped composition retained a conductivity of about 10^{-1} $S{\cdot}cm^{-1}$ after reoxidation, whereas the conductivity of the samples with $x > 0.10$ did not go below 2 $S{\cdot}cm^{-1}$. During the oxidation stage the conductivity is expected to drop by around 2 orders of magnitude due to the oxidation of Ti^{3+} to Ti^{4+}. Whilst this is clearly the case for the undoped composition, the drop is less and less significant as Ga doping level increases. This is better viewed when the conductivity on oxidation is plotted as Log(σ), as in Figure 6-15.

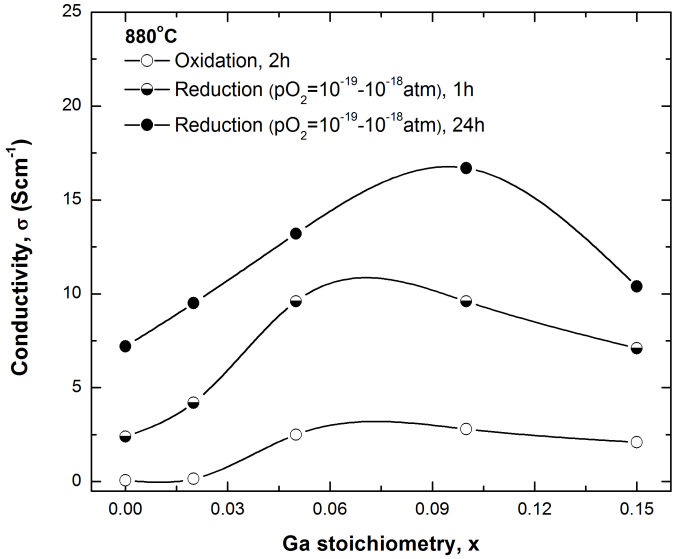

Figure 6-14 | Conductivity (σ) as a function of Ga stoichiometry composition (x) for $La_{0.4}Sr_{0.4}Ga_xTi_{1-x}O_{3-\gamma-\delta}$ samples with 60-70% relative density, at different times of a redox cycle at 880 °C. The initial conductivity is given in Figure 6-13. The stages highlighted are: after 2h of oxidation, after 1 h of reduction and finally the equilibrium values, after 24 h of reduction.

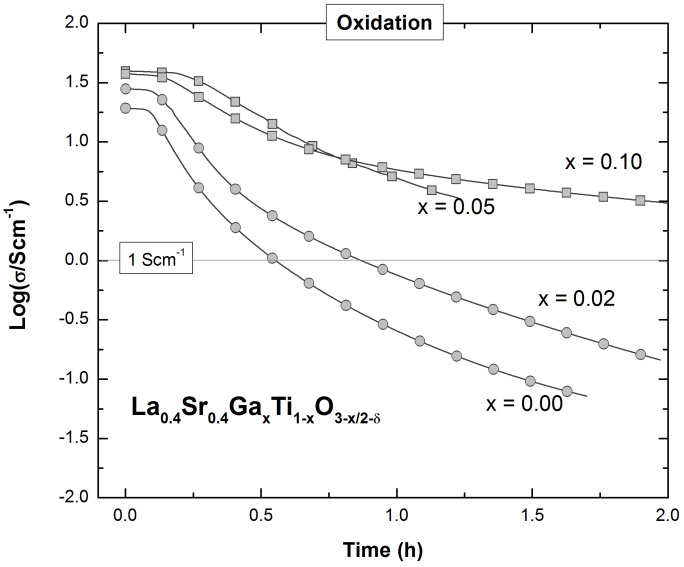

Figure 6-15 | Log($\sigma/(S \cdot cm^{-1})$) as a function of time for selected Ga-doped compositions, on oxidation (part of the experiment presented in Figure 6-14).

The fact that for 10% Ga doping the conductivity does not decrease below 2 $S \cdot cm^{-1}$ even after 2 h of oxidation is quite remarkable. This suggests that the Ga doped samples are more resistant to oxidation probably due to the effect that Ga has of stabilizing the formed oxygen vacancies. However, this effect might also be related to the way Ga loss takes place (see discussion in section 5.11.3). According to the proposed mechanism, a Ga-depleted layer

will cover the grains during the reduction of the samples at 1000 °C (see Figure 6-16).

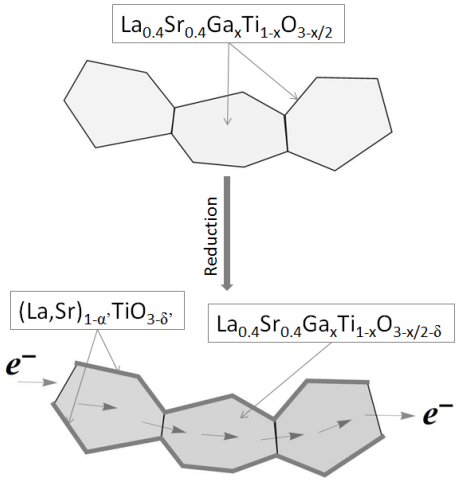

Figure 6-16 | Illustration of Ga loss on reduction (see discussion in section 5.11.3).

It seems likely that the Ga-depleted layer acts as a barrier that prevents the oxidation of the bulk, which in turn can still support electronic conduction. The fact that this effect is more pronounced as Ga doping increases can be explained by the oxygen exchange properties of the Ga-depleted layer. As explained earlier, the titanate composing this layer will have an A-site deficiency decreasing with initial Ga doping, x. On the other hand, Figure 5-1 shows that decreasing the A-site deficiency of a titanate significantly diminishes its oxygen exchange capability. This means that once the oxygen vacancies in this layer are filled, it will be more and more difficult for oxygen to migrate through it as x increases. Finally, when the samples are reduced again, the samples having higher Ga doping are able recover more than half of their equilibrium conductivity within minutes (see Figure 6-17), as most of the grain is still reduced. In this case however, the Ga-depleted layer does not seem to play an important role probably because the reduction of surface layers in A-site deficient perovskites occurs inherently fast, as shown section 5.2.

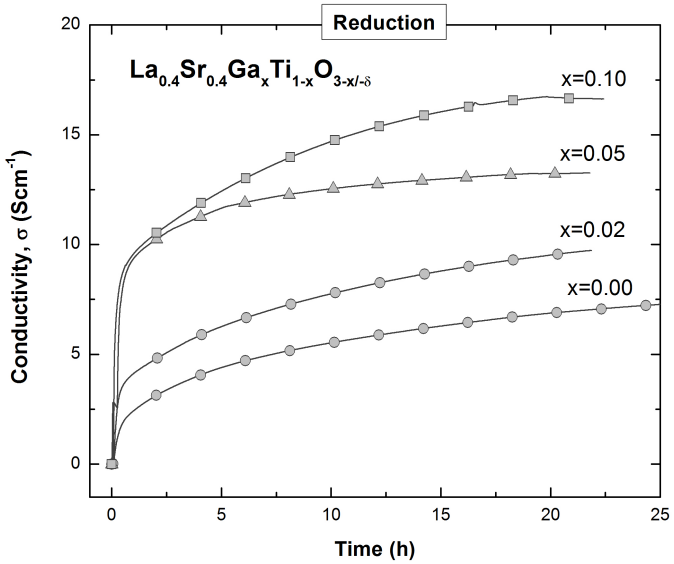

Figure 6-17 | Conductivity as a function of time on reduction of selected Ga-doped samples (part of the experiment presented in Figure 6-14).

6.5 Conductivity in the transition metal doped series $La_{0.4}Sr_{0.4}M_xTi_{1-x}O_{3-\gamma}$ (M = Fe, Ni, Zn, x = 0.06)

6.5.1 The σ – δ dependency

In order to evaluate the effect of δ on σ for the some of the transition metal doped compositions in the series $La_{0.4}Sr_{0.4}M_xTi_{1-x}O_{3-\gamma}$ ($x = 0.06$, M = Ti, Fe, Ni, Zn), porous samples were equilibrated at 880 °C in 5%H_2/Ar. The relative density of the samples for each corresponding dopant is Ti ~ 60%, Fe ~60%, Ni ~ 57%, Ga ~ 63%, Zn ~ 52%. The conductivity measured on cooling and the plot of conductivity at 880 °C *vs.* the corresponding extent of reduction these samples are given in Figure 6-18 and Figure 6-19, respectively.

From Figure 6-19 it appears that the overall proportionality between σ and δ is still maintained, with one exception. Thus, the Fe-doped composition shows the highest σ and the highest δ as well. As δ decreases for the Ni-doped composition the conductivity decreases as well. However, the Zn-doped composition shows remarkably high conductivity considering its δ, breaking the trend. This is especially significant since its relative density is lowest among the considered compositions (52% *vs.* an average of ~60%).

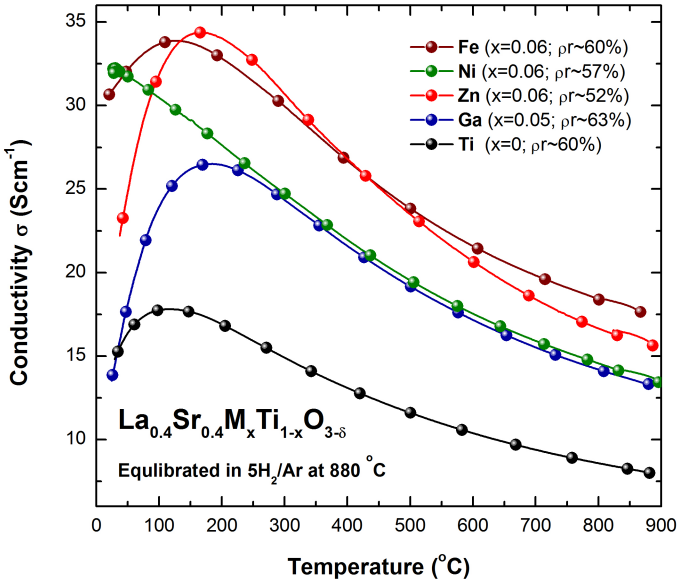

Figure 6-18 | Conductivity *vs.* temperature on cooling for $La_{0.4}Sr_{0.4}M_xTi_{1-x}O_{3-\gamma}$ $(x = 0.06)$ samples equilibrated at 880 °C in 5%H_2/Ar. The relative density of the samples is given in the plot. For all the samples, throughout reduction, p_{O_2} was in between $10^{-19.4} - 10^{-20.0}$ atm, being lowest while measuring the Zn-doped sample.

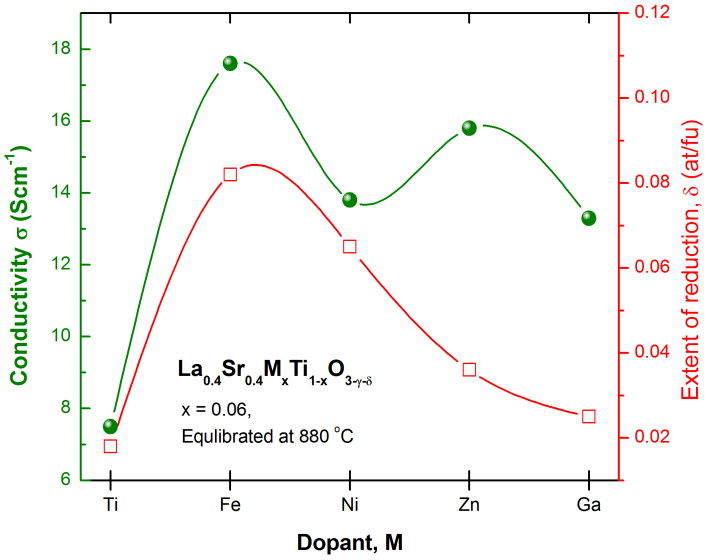

Figure 6-19 | The extent of reduction δ and conductivity σ after equilibration at 880 °C in 5%H_2/Ar for $La_{0.4}Sr_{0.4}M_xTi_{1-x}O_{3-\gamma}$ porous pellets. The relative density of the samples for each corresponding dopant is Ti ~ 60%, Fe ~60%, Ni ~ 57%, Ga ~ 63%, Zn ~ 52%. For all the samples, throughout reduction p_{O_2} was in between $10^{-19.4} - 10^{-20.0}$ atm, being lowest while measuring the Zn-doped sample.

The higher conductivity of the Zn-doped sample might due in part to the fact that during this particular measurement p_{O_2} was also lowest during reduction, albeit not by a considerable amount compared to the other samples (see caption of Figure 6-19). Thus, the higher conductivity of the Zn-

doped sample could be inherently high in this composition, perhaps due to better electron mobility. The Ni-doped sample has higher conductivity compared to the Ga-doped samples, as expected from the δ trend, but this is slightly masked by the difference in porosity – the Ni doped sample is more porous (~57% dense) compared to the Ga-doped sample (~63% dense).

6.5.2 The μ – T dependency

Since all the terms in Eq. 6-6 (*i.e.* a_0, δ, σ) are known for each of the doped compositions analysed above (Figure 6-18 and Figure 6-19), the mobility as a function of temperature μ(T) may be calculated for each composition. This is given in Figure 6-20 as $\text{Log}(\mu/(\text{cm}^2\text{V}^{-1}\text{s}^{-1}))$ *vs.* Log(T/K), again, in seeking to outline the power law dependency in the metallic temperature domain. Also, the power law (Eq. 6-5) fit parameters corresponding to each composition are given in Table 6-2.

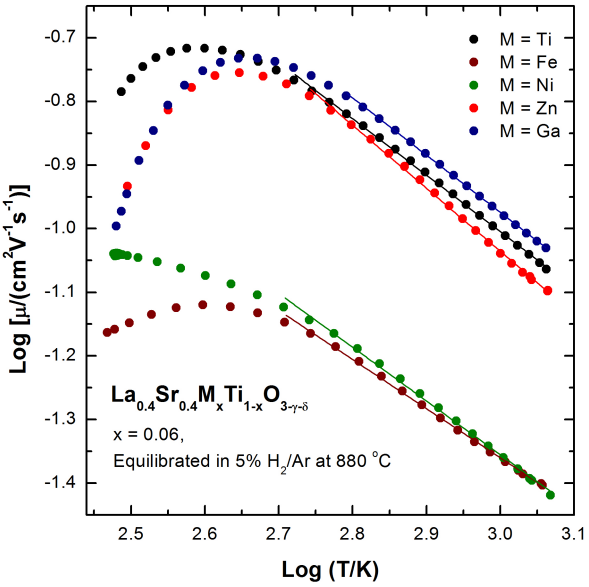

Figure 6-20 | Log(μ) *vs.* Log(T) plot derived by using Eq. 6-6 on the data presented in Figure 6-18 and Figure 6-19.

From Figure 6-20 it becomes clear that the selected dopants are grouped in two main categories with respect to their μ(T) dependencies. Transition metal cations such as Fe and Ni have lower 'base' mobility values (*i.e.* μ_0) across the whole temperature range. Thus, these dopants act to *disrupt* the base mobility of the titanate host.

Table 6-2 | Power law (Eq. 6-5) parameters corresponding to the linear fits shown in Figure 6-20.

$La_{0.4}Sr_{0.4}M_xTi_{1-x}O_{3-\gamma}$	μ_0 ($cm^2V^{-1}s^{-1}$)	m
M = Ti	45.1	0.88
M = Fe	9.1	0.77
M = Ni	15.1	0.84
M =Zn	86.3	0.99
M = Ga	52.5	0.90

However, overall they exhibit higher conductivity because of a combination of two key factors: 1) they are able to promote reduction better, hence they have higher δ values, and 2) their conductivity does not drop as fast upon heating due to phonon scattering, since they exhibiting the smallest *m* values in the studied dopant range (see Figure 6-21 or Table 6-2). The second group consists of the dopants Zn and Ga. Within experimental error and factoring in the porosity of the samples, these particular dopants do not appear to disrupt the base mobility of the titanate host $La_{0.4}Sr_{0.4}TiO_{3-\delta}$. The difference between the two groups of dopants as outlined by electron mobility data is that the former sums cations which are true transition metal oxides with partly filled *d*-shell, while the latter have their *d*-shell filled. It is possible that the interaction between the *d* orbitals of dopants such as Fe^{2+}/Fe^{3+} and Ni^{2+} disrupts the conduction of Ti^{3+}/Ti^{4+}.

Nonetheless, the higher extent of reduction generally prevails as key in enhancing the electronic conductivity of these titanate systems, as seen in the case of Fe or Ni doping. The decrease in base mobility upon doping these cations is simply not enough to supress the enhancement of σ due to higher δ. However, dopants such as Ga, or Zn in particular which appear to be non-disruptive to the Ti host sublattice are quite attractive for effectively enhancing electronic conductivity, even though they have moderate δ values. Of course, even these dopants will disrupt the Ti-sublattice if substituted in a larger number since the percolation between Ti sites would be severely

disrupted leading to decreased conductivity, as seen in the case of Ga doping (Figure 6-13).

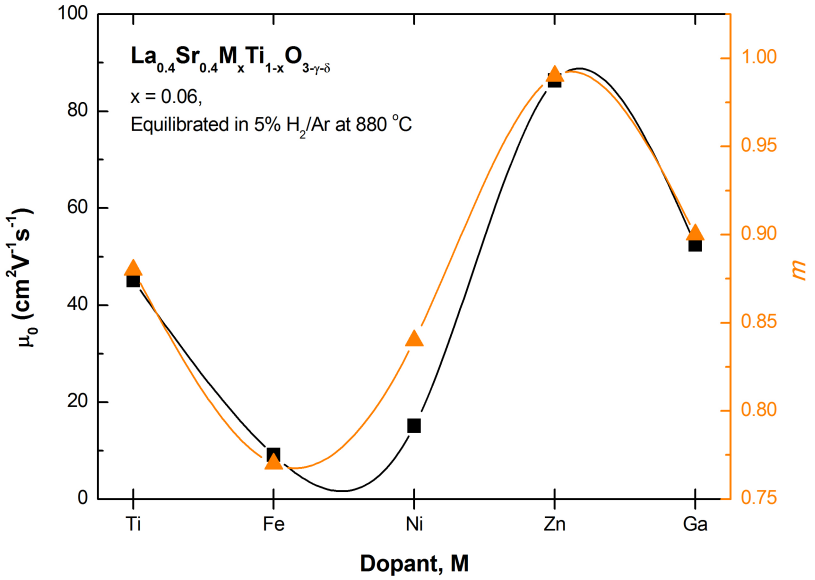

Figure 6-21 | Power law parameters μ_0 and m (Eq. 6-5) corresponding to the linear fits shown in Figure 6-20, plotted against the dopant in $La_{0.4}Sr_{0.4}M_xTi_{1-x}O_{3-\gamma}$.

References

1. A. R. West, *Basic Solid State Chemistry*, Wiley, 2nd edn., 1999.
2. P. R. Slater, D. P. Fagg, and J. T. S. Irvine, *J. Mater. Chem.*, 1997, **7**, 2495–2498.
3. D. N. Miller and J. T. S. Irvine, *J. Power Sources*, 2011, **196**, 7323–7327.
4. O. A. Marina, N. L. Canfield, and J. W. Stevenson, *Solid State Ionics*, 2002, **149**, 21–28.
5. J. Canales-Vazquez, S. Tao, and J. T. S. Irvine, *Solid State Ionics*, 2003, **159**, 159–165.
6. P. Blennow, A. Hagen, K. Hansen, L. Wallenberg, and M. Mogensen, *Solid State Ionics*, 2008, **179**, 2047–2058.
7. G. Tsekouras and J. T. S. Irvine, *J. Mater. Chem.*, 2011.
8. R. Moos and K. H. Hardtl, *J. Appl. Phys.*, 1996, **80**, 393–400.
9. T. Ishihara, in *Perovskite Oxide for Solid Oxide Fuel Cells*, ed. T. Ishihara, Springer, 2009.
10. H. Iwahara, in *Perovskite Oxide for Solid Oxide Fuel Cells*, ed. T. Ishihara, Springer, 2009.

7 PEROVSKITES DECORATED WITH *IN-SITU* EXSOLVED NANOPARTICLES THROUGH CONTROL OF DEFECT CHEMISTRY

7.1 B-site exsolution from A-site deficient titanates

In Chapter 5 the evolution of the extent of reduction with reduction temperature was studied for the system $La_{0.4}Sr_{0.4}TiO_3$. It was found that the extent of reduction δ increases with the increase in reduction temperature as shown below, in Figure 7-1:

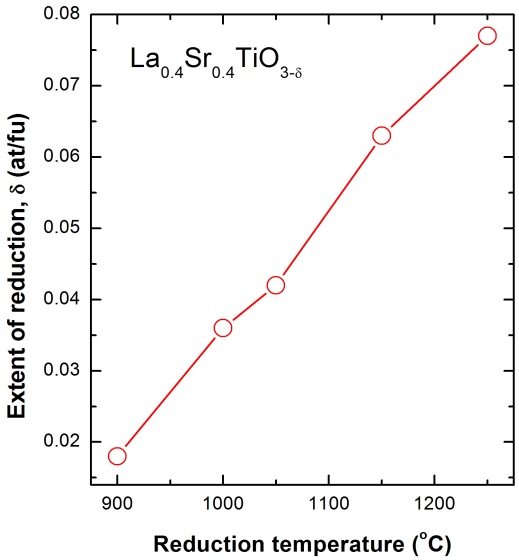

Figure 7-1 | Extent of reduction as a function of reduction temperature for $La_{0.4}Sr_{0.4}TiO_3$. Reduction was performed in 5%H_2/Ar for a minimum of 12 h at each temperature step.

While studying the δ-T behaviour in this system an important observation was made. When reduced above 950-1000 °C, the titanate perovskite grains occasionally developed submicron particles on their external surface. The lowest reduction temperature at which the number of these particles became significant (and thus readily apparent in SEM images) was found to be around 1100 °C. A representative SEM image of these nanoparticles as they grow out of the parent perovskite $La_{0.4}Sr_{0.4}TiO_3$ after reduction at 1100 °C is shown in Figure 7-2. This temperature corresponds to a δ value which will be henceforth referred to as δ_f. δ_f is thus chosen to refer to a certain extent of reduction that gives rise to a *frequently occurring* number of *precipitates* in the system $La_{0.4}Sr_{0.4}TiO_3$.

The exsolution of nanoparticles from the A-site deficient titanate appears to be a phase segregation process. However, some of its characteristics are quite

unusual. First, unlike other 'phase segregation' processes, the exsolutions from A-site deficient perovskites occur preferentially on the perovskite grains rather than at the grain boundaries suggesting it is a process innate to the perovskite and not driven by the defects or impurities that may be found at grain boundaries. Additionally, by fracturing the grains after the reduction was over, it was confirmed that the exsolution phenomenon only occurred on the *surface* of the grains and not in the bulk of the grains. Moreover, the exsolutions have fairly regular shape, are isolated, and have a rather *local* occurrence.

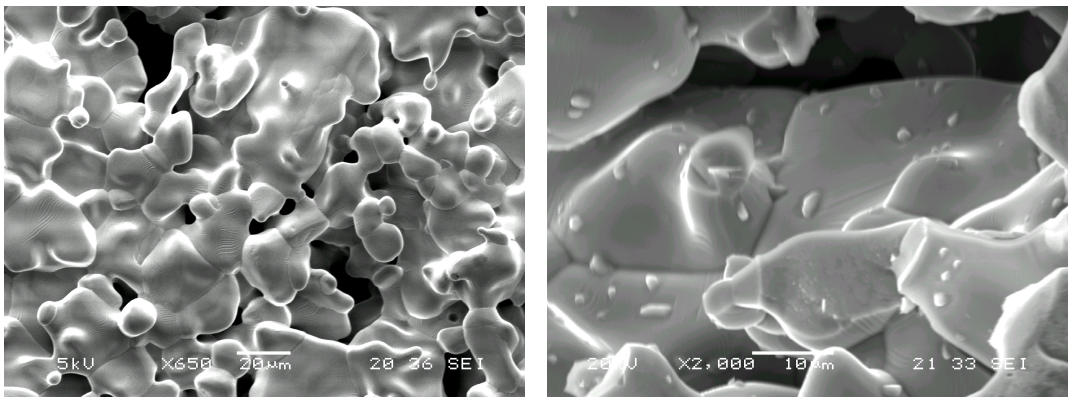

Figure 7-2 | Microstructure of $La_{0.4}Sr_{0.4}TiO_3$ porous pellets (Left) before reduction and (Right) after reduction at 1100 °C (5% H_2/Ar) and the formation of $TiO_{2-\delta}$ exsolutions.

The reason for the formation of the precipitates and their nature could be understood by considering the stoichiometry shift and therefore defect chemistry triggered by reduction, as summarised in the equations below.

Initially, $La_{0.4}Sr_{0.4}TiO_3$ is an A-site deficient, oxygen stoichiometric perovskite, $A_{1-\alpha}BO_3$ with *overall* $\alpha = 0.2$. Upon reduction this becomes an A-site deficient, oxygen *deficient* perovskite $A_{1-\alpha}BO_{3-\delta}$:

$$A_{1-\alpha}BO_3 \xrightarrow{Reduction} A_{1-\alpha}BO_{3-\delta} \qquad \text{Eq. 7-1}$$

The reduction of the titanate progresses until *locally* a limit is reached in the number of oxygen vacancies that can be accommodated in the given conditions, δ_{lim}:

$$A_{1-\alpha}BO_{3-\delta} \xrightarrow{Further\ Reduction} A_{1-\alpha}BO_{3-\delta_{lim}} \qquad \text{Eq. 7-2}$$

Although perovskites are known to be able to accommodate a large number of defects, the presence of a large number of "built-in" A-site vacancies, $\alpha = 0.2$, limits the number of oxygen vacancies that can be tolerated. It should also be noted that *locally*, the concentration of A-site vacancies could be higher than the average $\alpha = 0.2$ since for $La_{0.4}Sr_{0.4}TiO_3$ it is known that A-site vacancies occasionally associate in pairs over very short distances (see discussion in Chapter 2). Moreover, the δ value of the surface should be higher than the δ value of the bulk since the surface is in direct contact with the reducing atmosphere throughout the experiment. Overall it can be said that the surface will be much more defective than the bulk and the high A-site deficiency and oxygen deficiency experienced by the material as a whole will be particularly exacerbated on the surface. The local instability caused by such high values of *simultaneous* A- and O-site deficiency can be alleviated by expelling species from the only remaining 'non-defective' perovskite primitive site, the B-site:

$$A_{1-\alpha}BO_{3-\delta_{lim}} \xrightarrow{Exsolution} (1-\alpha)ABO_{3-\delta'} + \alpha BO_{\xi} \qquad \text{Eq. 7-3}$$

Alternatively, from a simplified, strictly stoichiometric point of view, reduced A-site deficient perovskites, $A_{1-\alpha}BO_{3-\delta_{lim}}$, may be regarded as B-site *excess* perovskites. Naturally, the perovskite will attempt to *locally* remove the B-site excess in order to re-establish the ABO_3 stoichiometry. Thus, considering for example the values $\alpha = 0.2$, $\delta_{lim} = 0.05$:

$$A_{0.8}BO_{2.95} \equiv A_{\frac{0.8}{0.8}}B_{\frac{1}{0.8}}O_{\frac{2.95}{0.8}} \equiv AB_{1.25}O_{3.68} \xrightarrow{Exsolution} ABO_{3-\delta'} + 0.25\ BO_{\xi} \qquad \text{Eq. 7-4}$$

Thus, based on the arguments presented above, the nanoparticles exsolved from $La_{0.4}Sr_{0.4}TiO_3$ consist of reduced titanium oxide, $TiO_{2-\delta}$. Experimental proofs that A-site deficient perovskites exsolve B-site containing nanoparticles will be presented in the following subchapters.

The fact that exsolutions preferentially occur on the outer surface of the grains, not inside them, or at the grain boundaries, is rather exceptional and thus it could be deemed as a potentially useful phenomenon rather than a

standard, undesirable, phase segregation process. Based on the observations above, the following strategy to exploit the phenomenon could be employed. Cations desired to be exsolved would be substituted on the B-site of the perovskite $La_{0.4}Sr_{0.4}TiO_3$, in *air*. The resulting materials, $(La,Sr)_{0.8}(M,Ti)O_3$ (stoichiometry would differ based on charge compensation, see section 5.5) would then be *reduced* to exsolve some of the B-site cations. It should be emphasized here that the vast majority of catalytically active cations substitute on the B-site in the perovskite structure. Hence the *in-situ exsolution* phenomenon holds great promise for designing perovskite-based systems that *deliberately exsolve certain catalytically active B-site dopants as nanoparticles*.

7.2 *In-situ* exsolution – literature context

Before passing to an account of the results obtained in this study by using the in-situ exsolution method, it is important to briefly review the current stage of knowledge and development in this area of research, in order to place the work carried out here in the appropriate context.

The concept of *in-situ* exsolution where the catalysts are initially incorporated as cations on the B-site of the perovskite lattice under oxidizing conditions, and subsequently undergo partial exsolution from the perovskite surface upon exposure to reducing conditions is not an entirely new approach. There have been a few reports in which this technique was used to decorate perovskite surfaces with catalytically active nanoparticles to be used in automotive emission control,[1–4] SOFC anodes,[5–10] and organic synthesis.[11]

Most of the work done on *in-situ* exsolutions stemmed from the work of Nishihata *et. al.*[1] and Tanaka *et. al.*[3] on the 'intelligent, self-regenerating catalyst' $LaFe_{0.57}Co_{0.38}Pd_{0.05}O_{3-\gamma}$ used in automotive emission control. It was shown that this perovskite is single phase in oxidising conditions but upon exposure to reducing conditions, metallic Pd nanoparticles precipitate. The

process was found to be reversible such that Pd can be reversibly precipitated as metallic nanoparticles and reintegrated as cation in the perovskite matrix upon exposure to reducing or oxidising atmosphere, respectively. The reversibility is key to retaining the high catalytic activity of this catalyst since Pd nanoparticles agglomeration and hence deactivation of catalysis may be avoided by re-oxidation. This concept has afterwards been extended to demonstrate Rh and Pt nanoparticle exsolution from calcium titanates, $CaTi_{0.95}Rh_{0.05}O_{3-\gamma}$and $CaTi_{0.95}Pt_{0.05}O_{3-\gamma}$, respectively.[3,4]

Two important characteristics of the exsolution process in the above mentioned systems should be pointed out. First, metallic nanoparticle exsolution in the case of $CaTi_{0.95}Rh_{0.05}O_{3-\gamma}$ and $CaTi_{0.95}Pt_{0.05}O_{3-\gamma}$ have been shown to form preferentially in the bulk rather than on the surface (particularly on re-oxidation).[12] Thus, the effectiveness of the exsolutions is expected to significantly decrease since most of them would be inaccessible for catalysis. This is in contrast to the exsolution process as observed in this study for $La_{0.4}Sr_{0.4}TiO_3$, where no precipitates were observed in the bulk. Secondly, in the case of $LaFe_{0.57}Co_{0.38}Pd_{0.05}O_{3-\gamma}$ exsolution occurs with essentially a large fraction of the perovskite (~20%) decomposing into the primary oxide (*e.g.* La_2O_3) and the exsolutes.[1] This is not surprising since perovskites may only accommodate a limited A-site excess, perhaps as Ruddlesden-Popper phases. The A-site species that cannot be accommodated in this way will simply precipitate:

$$ABO_{3-\delta} \xrightarrow{Exsolution} (1-\alpha)ABO_{3-\delta'} + \alpha AO + \alpha B \qquad \text{Eq. 7-5}$$

The formation of AO from A-site deficient perovskites on exsolution is unlikely to happen because there is already a lack of A-site species by stoichiometry. In this scenario, the exsolution simply acts to locally revert the perovskite stoichiometry towards a stable ABO_3 stoichiometry not to an A-site excess stoichiometry:

$$A_{1-\alpha}BO_{3-\delta} \xrightarrow{Exsolution} (1-\alpha)ABO_{3-\delta'} + \alpha B \qquad \text{Eq. 7-6}$$

Therefore A-site deficiency is the natural choice for designing systems that exsolve the B-site since in this case A-site cation containing species should not precipitate alongside the desired exsolutes. A-site-type cations generally known to be catalytically inactive, may additionally contribute towards sample degradation, and are thus undesirable.

The other systems in which deliberate exsolution was reported are based on lanthanum chromites $La_{1-x}Sr_xCrO_{3-x/2}$ B-site doped with Ru or Ni,[5] and $La_{0.75}Sr_{0.25}Cr_{0.5}Mn_{0.5}O_{3-\gamma}$ B-site doped with Ni. These were employed as SOFC anodes exhibiting promising performance. Incidental Ni metal exsolution from chromites has also been reported.[13] It is mainly from the work conducted on these chromite systems that the current understanding of the main driving factor for exsolving metal nanoparticles comes from.[5–7] It is generally accepted that the principle on which *in-situ* exsolution works relies on having a perovskite matrix that is sufficiently resilient to reduction, but on the contrary the dopants desired to exsolve must be very easy to reduce so that in reducing atmosphere they will readily convert to metal which will naturally tend to segregate from the ceramic matrix, yielding the nanoparticles.

From the context presented so far there are at least two key aspects that motivate exploring the possibility of exsolving B-site species from A-site deficient perovskites. First, all the studies so far have focused on A-site stoichiometric, oxygen deficient perovskites, $ABO_{3-\delta}$; no A-site deficient perovskite systems $A_{1-\alpha}BO_3$ have been explored. Second, according to the current understanding the single, main driving force for the formation of exsolutions on reduction is the reducibility of the dopant. Thus, so far, only easily reducible cations (Ni^{2+}, Ru^{2+}, Rh^{4+}, Pd^{4+} and Pt^{4+}) have been demonstrated to exsolve. On the other hand, as shown at the start of this chapter, cations which would otherwise serve as the reduction-resilient matrix, may exsolve as well from A-site deficient perovskites, *e.g.* as $TiO_{2-\delta}$ from $La_{0.4}Sr_{0.4}TiO_3$. Thus, this implies that *A-site deficiency* could serve as a

general driving force for triggering the *exsolution of B-site cations from perovskites.*

In order to put the reducibility of different cations into perspective, the Gibbs free energy of the reduction reaction of the corresponding oxides was calculated at 900 °C as shown in Eq. 7-7:

$$M_xO_y + \frac{y}{2}H_2 \xrightarrow{Reduction} xM^0 + yH_2O \quad | \Delta G_{red.}^{900C} \qquad \text{Eq. 7-7}$$

The $\Delta G_{red.}^{900C}$ values *per mole of metal* were plotted as a function of the oxide M_xO_y in Figure 7-3.

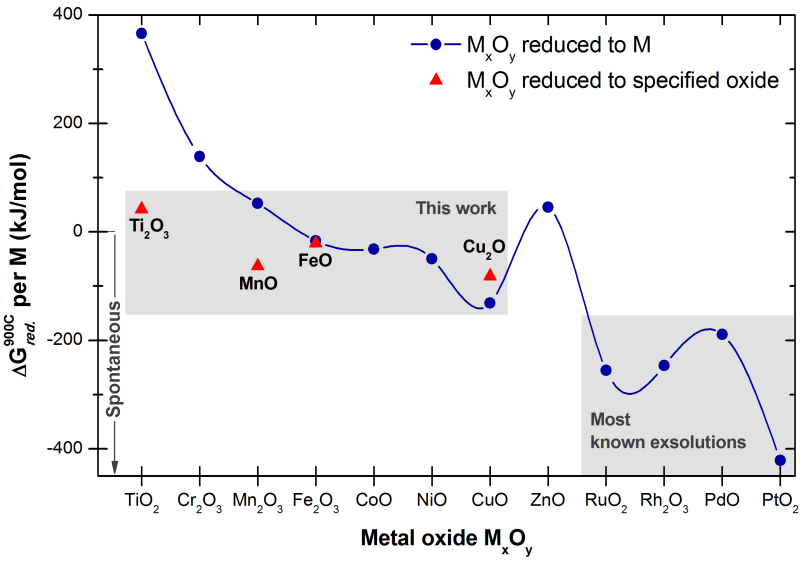

Figure 7-3 | Gibbs free energy of reduction of oxides to either metals or selected oxides, at 900 °C in H_2 (according to Eq. 7-7).

It is apparent from this plot that most of the cations known to exsolve are indeed the easiest to reduce within the selected cation range, with very negative reduction free enthalpy values, $\Delta G < -200$ kJ/mol. The only exception is Ni which shows a higher ΔG, around -50 kJ/mol, but still negative, meaning that NiO reduction to Ni at 900 °C is still spontaneous. TiO_2 however is situated at the opposite pole, with positive ΔG value ~42 kJ/mol for reduction to Ti_2O_3, and thus is not thermodynamically favourable. Not even at 1100 °C does the reduction of TiO_2 to Ti_2O_3 become spontaneous ($\Delta G_{red.TiO_2 \rightarrow Ti_2O_3}^{1100C} = +38$ kJ/mol). The fact the presence of A-site deficiency

does promote reduction and the formation of exsolution where the reduction of cation to metals or other species is not thermodynamically favourable, shows that A-site deficiency can act as a general driving force for the exsolution phenomenon, more general than the simple reducibility of the doping cation. *A-site deficiency can trigger the formation of exsolutions where cation reducibility cannot*. This will be demonstrated in subsection 7.4.

7.3 The microstructure of the perovskites used in exsolution studies

Before passing on to the results of this chapter it is important to briefly highlight the microstructural characteristics of the samples employed here for the in-situ growth of nanoparticles.

For these experiments, the substituted A-site deficient perovskites $(\mathrm{La,Sr})_{0.8}(\mathrm{M,Ti})\mathrm{O}_3$ (but also relevant members of other nonstoichiometry classes) were made into porous pellets. Generally, the microstructures consist of perovskite grains with 10-20 μm size and pores of similar size, with an overall porosity of 30-40%. An example is shown in Figure 7-4.

This type of microstructure was chosen for several reasons. First, the level of porosity is similar to those used in hydrogen electrodes for *e.g.* SOEC, albeit the size of the grains is smaller in the latter. Thus, it would be interesting to study how the nanoparticles develop in a porous framework that is reasonably similar to the microstructures used in real devices. Also, the high porosity allows for a high surface area of the perovskite to be exposed to the gas and also enables facile gas diffusion within the sample. Nonetheless, the samples are strong enough to be manipulated without the risk of altering the obtained microstructure as it would probably be in the case of a powder. Also, any additional changes in the overall microstructure, perovskite surface morphology or formation of secondary phases is much easier to observe and analyse in a porous pellet with well-defined initial microstructure as opposed to a powder.

(a) Surface

$La_{0.4}Sr_{0.4}Fe_{0.06}Ti_{0.94}O_{3-\gamma}$

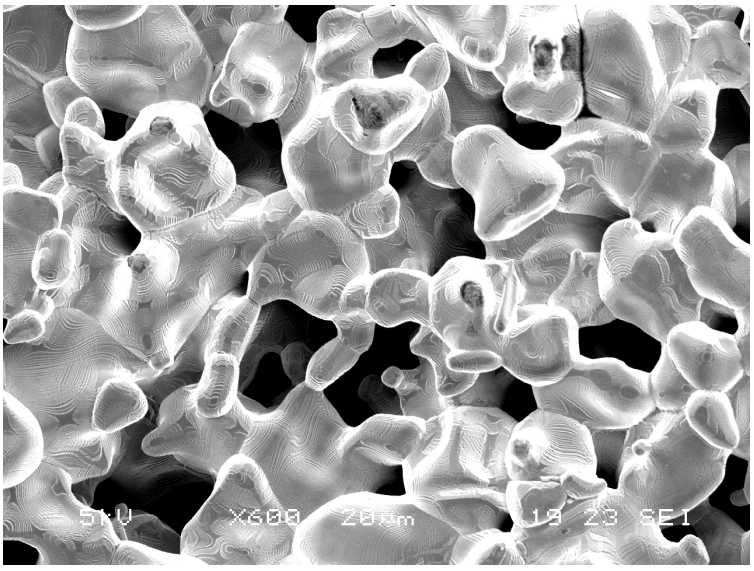

(b) Cross section

$La_{0.4}Sr_{0.4}Fe_{0.06}Ti_{0.94}O_{3-\gamma}$

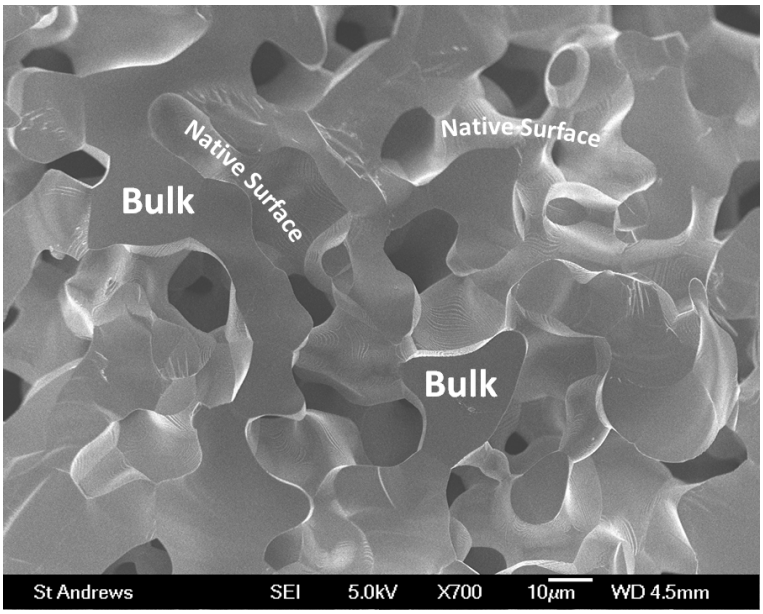

Figure 7-4 | Example of microstructure used in the *in-situ* exsolution studies. (a) Surface view. (b) Cross-section view after cleaving the pellet in half.

7.4 Defect chemistry-driven exsolutions

As explained before, reduction experiments are carried out on pellet-like porous samples since this sort of microstructure mimics best the microstructure of an electrode intended for *e.g.* SOEC.

A first important observation regarding the role of defect chemistry in the exsolution of B-site species emerges by comparing the effect of reduction on two compositions belonging to two different nonstoichiometry classes, $ABO_{3+\gamma}$ and $A_{1-\alpha}BO_3$. Furthermore, the compositions were chosen such that

the same fraction of Ni was present in both compositions, in which case the driving force related to reducibility would be comparable for both compositions. As the A-site stoichiometric, oxygen excess perovskite $La_{0.3}Sr_{0.7}Ni_{0.06}Ti_{0.94}O_{3+\gamma}$ was chosen, while for the A-site deficient, oxygen stoichiometric perovskite, $La_{0.52}Sr_{0.28}Ni_{0.06}Ti_{0.94}O_3$ was considered a suitable candidate. The SEM micrographs of the two samples after reduction at 930 °C (20 h) in 5%H_2/Ar is shown in Figure 7-5. It is obvious from this figure that the A-site deficient Ni-doped perovskite develops numerous metallic Ni nanoparticles (10-30 nm) which uniformly cover the surface of the parent perovskite (Figure 7-5 (b)). No sign of exsolutions was found in the A-site stoichiometric, Ni-doped sample, even though both samples possess the same amount of Ni on the B-site (6%).

This experiment clearly demonstrates that A-site deficient perovskites can trigger B-site exsolutions where traditional A-site stoichiometric formulations cannot. Moreover, the exsolutions produced by the A-site deficient perovskite are remarkably uniform in terms of size (10-30 nm) and surface distribution which makes *in-situ* exsolution a very attractive procedure for producing supported nanoparticles for various applications and perovskite surface functionalization.

The complete absence of exsolutions from the A-site stoichiometric, oxygen excess composition is somewhat surprising, considering that some easily reducible cations are still present on the B-site. Furthermore, it should be added that the A-site stoichiometric sample did not show any exsolutions even when the reduction temperature was increased from 930 °C to 1000 °C. According to the traditional understanding of the phenomenon this may be attributed to the small concentration of the easily reducible species (6% Ni). However, as it will be shown in an upcoming subchapter, this is not the main reason for the observed behaviour.

(a) $ABO_{3+\gamma}$

A-site stoichiometric, oxygen excess perovskite $La_{0.3}Sr_{0.7}Ni_{0.06}Ti_{0.94}O_{3+\gamma}$

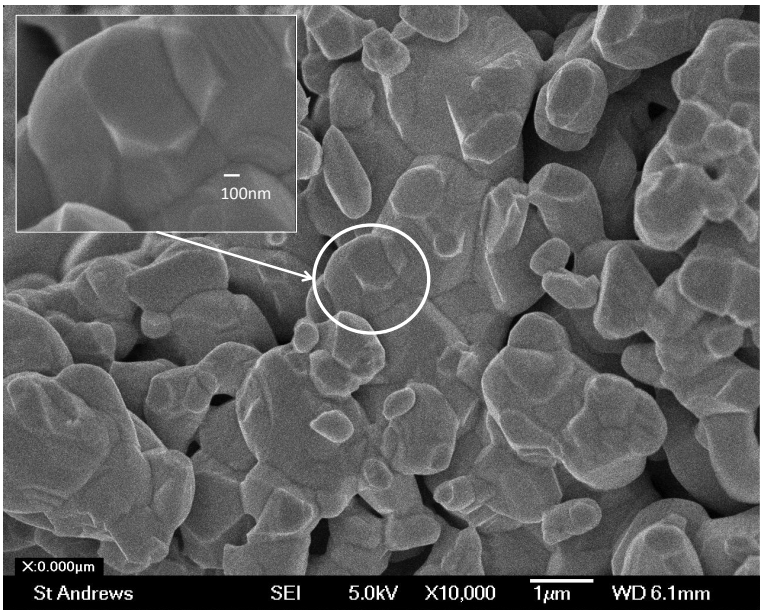

(b) $A_{1-\alpha}BO_3$

A-site deficient, oxygen stoichiometric perovskite $La_{0.52}Sr_{0.28}Ni_{0.06}Ti_{0.94}O_3$

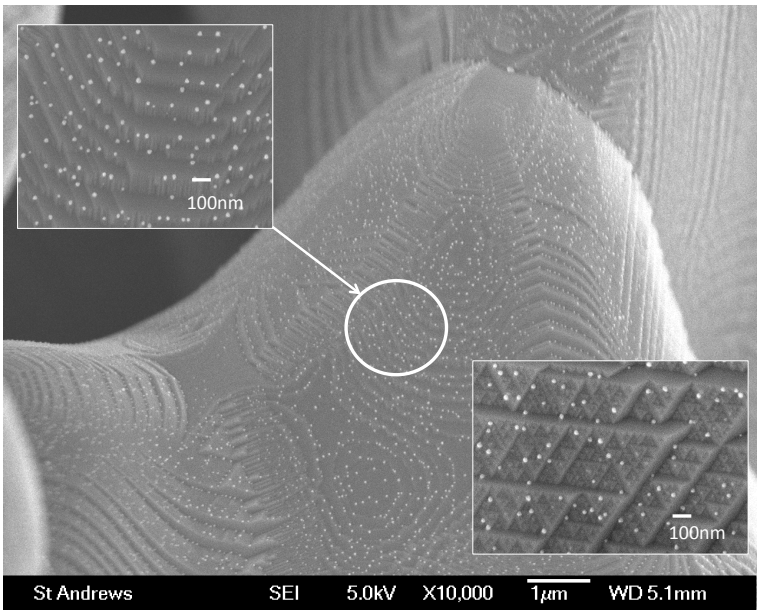

Figure 7-5 | The importance of defect chemistry in the formation of B-site exsolutions on reduction exemplified by reducing perovskites belonging to different nonstoichiometry class: (a) A-site stoichiometric perovskite and (b) A-site deficient perovskite. The images are SEM micrographs of the samples after reduction at 930 °C (20 h) in 5%H_2/Ar.

Fe exsolutions from A-site deficient, oxygen deficient titanates, *e.g.* $La_{0.4}Sr_{0.4}Fe_{0.06}Ti_{0.94}O_{3-\gamma}$, are rather inhomogenously distributed and of variable size (Figure 7-6 (a)). Both aspects improve significantly when A-site deficient, oxygen stoichiometric formulations are used instead, as in $La_{0.49}Sr_{0.31}Fe_{0.09}Ti_{0.91}O_3$ (Figure 7-6 (b)). It is worth nothing that A-site deficient, oxygen stoichiometric formulations consistently showed better homogeneity in terms of precipitate size and distribution, for both Fe and Ni

doping, irrespective of doping level (compare *e.g.* Figure 7-6 (a) to Figure 7-6 (b) and Figure 7-10 (a) to Figure 7-10 (b)). Possible reasons for this behavior will be examined throughout the next subchapter.

(a) $A_{1-\alpha}BO_{3-\gamma}$

A-site deficient, oxygen deficient perovskite $La_{0.4}Sr_{0.4}Fe_{0.06}Ti_{0.94}O_{3-\gamma}$

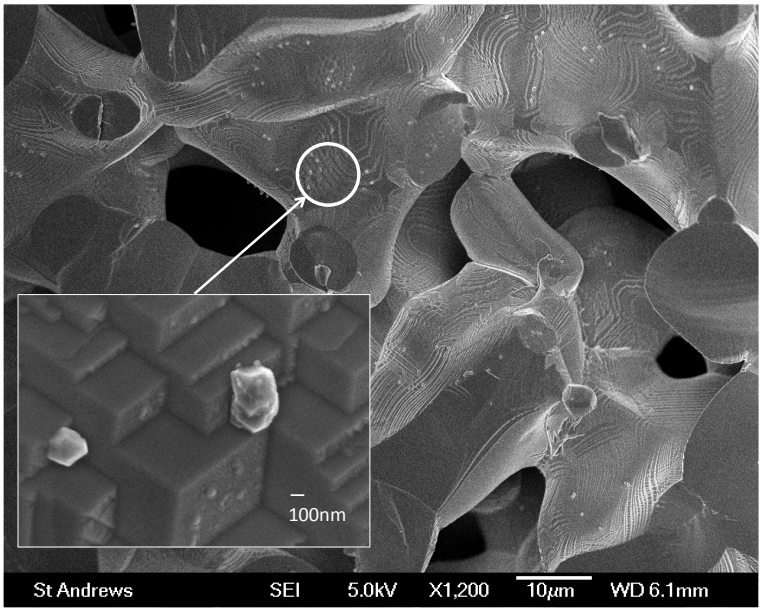

(b) $A_{1-\alpha}BO_3$

A-site deficient, oxygen deficient perovskite $La_{0.49}Sr_{0.31}Fe_{0.09}Ti_{0.91}O_3$

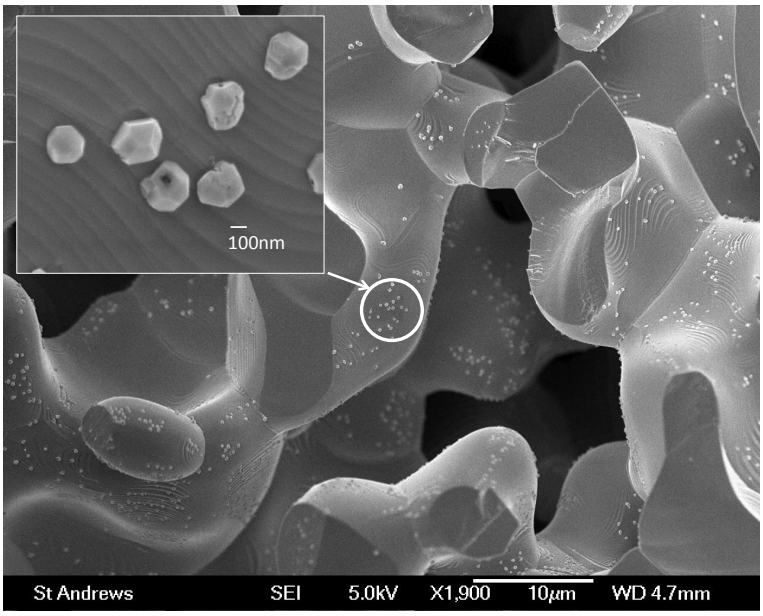

Figure 7-6 | SEM micrographs showing Fe exsolutions from different A-site deficient systems after reduction at 930 °C (20 h) in 5%H_2/Ar.

The precipitates arising from the Mn-doped sample are considerably larger than the ones in the Fe-doped systems (~1μm, see Figure 7-7) and are very similar to the ones observed for the undoped sample (Figure 7-2). The larger particle size is perhaps due to the higher reduction temperature used in these systems to trigger exsolutions (1000 °C) which may have increased the

grain growth of the exsolutes as well. This system is also the only one in which precipitates were observed at the grain boundaries too, and not only on the surface of the grains.

(a) $A_{1-\alpha}BO_{3-\gamma}$

A-site deficient, oxygen deficient perovskite $La_{0.4}Sr_{0.4}Mn_{0.06}Ti_{0.94}O_{3-\gamma}$

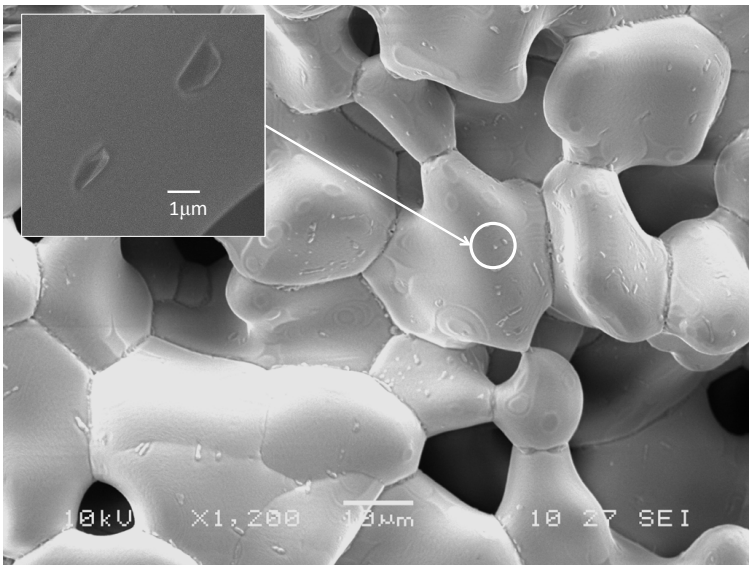

Figure 7-7 | SEM micrographs showing MnO_x exsolutions from $La_{0.4}Sr_{0.4}Mn_{0.06}Ti_{0.94}O_{3-\gamma}$, after reduction at 1000 °C (20 h) in 5%H_2/Ar.

Exsolutions in the Cu-doped system are not numerous and appear rather sporadically (see Figure 7-8 (a)). One important observation is that in the case of this system precipitates were occasionally observed inside the bulk as well. Figure 7-8 (b) shows the plate-like exsolutes observed when the sample was fractured after the reduction, to reveal the bulk. The platelets are perhaps as thin as 10 nm and not wider than 100 nm. Platelets appear to be positioned in 'sockets' into the parent perovskite matrix. Some of the sockets are empty perhaps because the fracture of the grain caused only part of them to remain attached to the part of the sample that was examined here.

The composition of the exsolutes in each system was anticipated based on the relative reducibility of the substituting cations (see Figure 7-3). This is easily verifiable in the case of Ni and Fe *e.g.* by XRD where (111) $Fm\bar{3}m$ Ni and Fe peaks, respectively, are visible (see Figure 7-9). However, this is not straightforward in the case of MnO_x or $TiO_{2-\delta}$ owing to the small dimensions of the nanoparticles and their lower number.

(a) $A_{1-\alpha}BO_{3-\gamma}$

A-site deficient, oxygen deficient perovskite $La_{0.4}Sr_{0.4}Cu_{0.06}Ti_{0.94}O_{3-\gamma}$

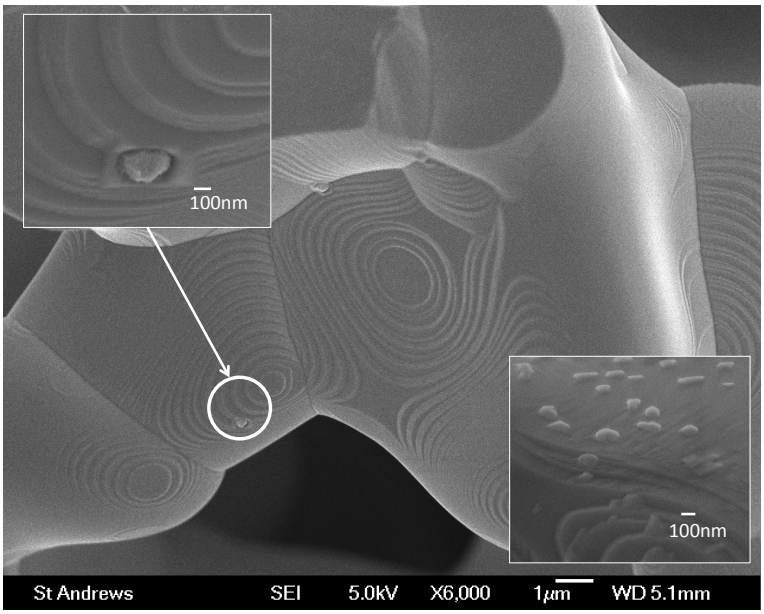

(b) Inside the bulk

A-site deficient, oxygen deficient perovskite $La_{0.4}Sr_{0.4}Cu_{0.06}Ti_{0.94}O_{3-\gamma}$

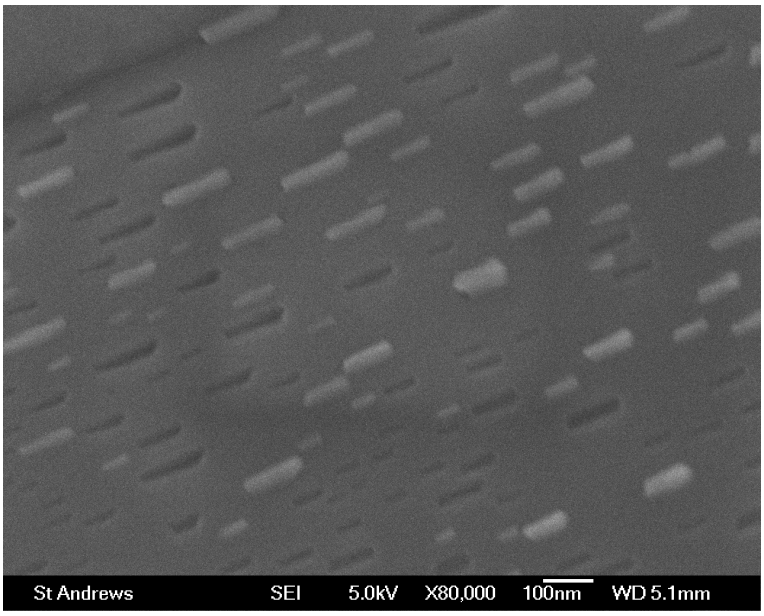

Figure 7-8 | SEM micrographs showing Cu exsolutions from $La_{0.4}Sr_{0.4}Cu_{0.06}Ti_{0.94}O_{3-\gamma}$. Exsolutions occur (a) on the surface of the grains (exterior); and occasionally (b) inside the bulk. Reduction was carried out at 1000 °C (20 h) in 5%H_2/Ar.

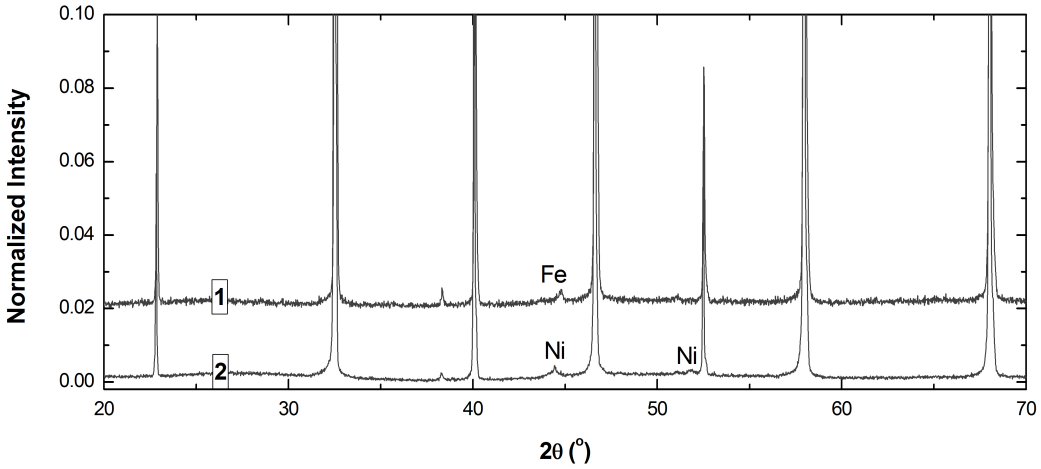

Figure 7-9 | XRD patterns of (1) $La_{0.46}Sr_{0.34}Fe_{0.06}Ti_{0.94}O_3$ and (2) $La_{0.52}Sr_{0.28}Ni_{0.06}Ti_{0.94}O_3$ reduced at 1000 °C in 5%H_2/Ar showing broad peaks of metallic Fe and Ni, respectively, indicative of very small particles.

7.5 Perovskite surface structuring and the exsolution phenomenon

7.5.1 Perovskite surface morphology

A close inspection of the micrographs presented so far reveals that deficient perovskites generally display distinctive, terrace-like surface structuring (see Figure 7-6 (a), Figure 7-8 (a) and Figure 7-10 (a)). Such features are almost absent in the case of A-site stoichiometric, oxygen excess stoichiometry (Figure 7-5 (a)). These terraces are outlined in Figure 7-10 (a) for the A-site deficient, O-deficient composition $La_{0.4}Sr_{0.4}Ni_{0.06}Ti_{0.94}O_{3-\gamma}$, for which the separation between terraces is significant.

These terraces may be characterized by two main structural features, henceforth referred to as: the terrace *edge* and the *sides* of the terrace, symbolised in Figure 7-10 a by 1 and 2, respectively. The sides of the terraces appear to be perpendicular to each other and have a smooth appearance and fairly uniform 'color', suggesting perhaps they are of similar composition (see the inset of Figure 7-10 (a)). On the contrary, the edges are darker, oblique, and seem to consist of additional, smaller edges with similar

appearance to the larger ones. This *self-similarity* at all scales reminds of *fractals* (Figure 7-10 (a) and (b)). From this point of view, the surface structuring may be regarded as an array of *parallelepipeds* of various sizes.

(a) $A_{1-\alpha}BO_{3-\gamma}$

A-site deficient, oxygen deficient perovskite $La_{0.4}Sr_{0.4}Ni_{0.03}Ti_{0.97}O_{3-\gamma}$

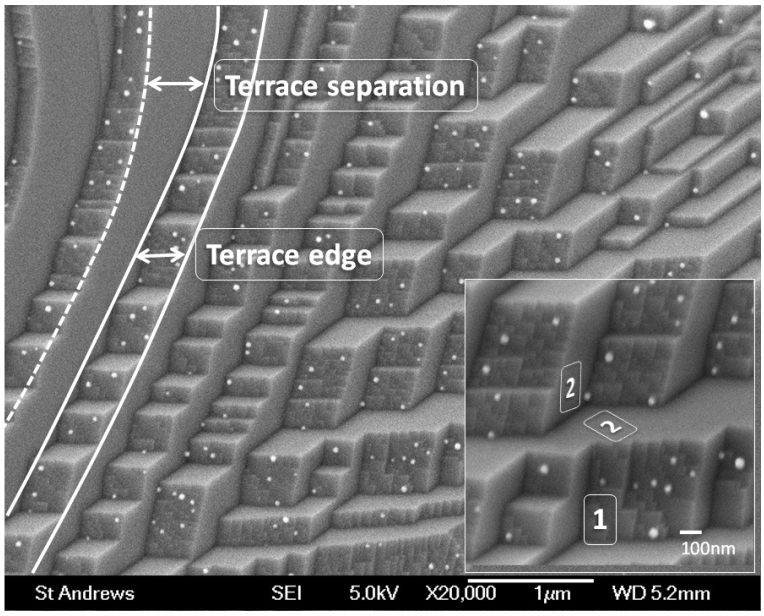

(b) $A_{1-\alpha}BO_3$

A-site deficient, oxygen stoichiometric perovskite $La_{0.52}Sr_{0.28}Ni_{0.06}Ti_{0.94}O_3$

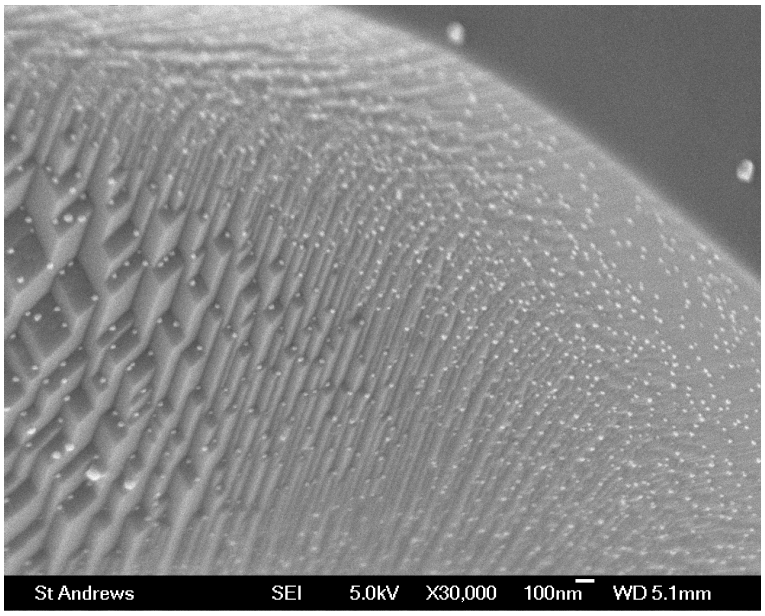

Figure 7-10 | Comparison between the surface morphology and exsolution growth of two perovskite classes: (a) A-site deficient, oxygen deficient, Ni-doped, perovskite $La_{0.4}Sr_{0.4}Ni_{0.03}Ti_{0.97}O_{3-\gamma}$ (after reduction in 5%H_2/Ar, at 930°C for 20 h then kept in humidified reducing gas, 3%H2O in 5%H_2/Ar at 900°C for 100 h). (b) A-site deficient, oxygen stoichiometric perovskite, Ni-doped, perovskite $La_{0.52}Sr_{0.28}Ni_{0.06}Ti_{0.94}O_3$(after reduction in 5%$H_2$/Ar, at 930 °C, for 20 h).

Interestingly, the exsolution phenomenon occurs preferentially along the edge of the terraces, and usually never on the sides of the terraces (*i.e.* in the

separation space between them), as illustrated in Figure 7-10 (a). Samples with similar A-site deficiency, but which are oxygen stoichiometric instead, display smaller separation between terraces (Figure 7-5 (b), Figure 7-6 (b) and Figure 7-10 (b)). This is perhaps one of the reasons why exsolutions in these latter compositions appear to be more numerous, overall leading to more uniformly distributed precipitates over the parent perovskite surface (see Figure 7-10 (b)).

Since the exsolution phenomenon tends to occur only from certain facets (*i.e.* terraces) it is likely that the surface of the studied A-site deficient perovksites ($A_{1-\alpha}BO_{3-\gamma}$ and $A_{1-\alpha}BO_3$) is structurally and/or compositionally inhomogeneous. Thus, the complete absence of B-site exsolutions on the sides of the terraces as exemplified in Figure 7-10, may indicate that this region of the perovskite surface does *not have exposed B-sites*. Thus, the *sides* of the terraces might correspond to an *A-site cation-terminated layer,* or, generally, to an *A-site cation-rich surface*. On the contrary, B-site exsolutions do form on the edges and thus some of the B-sites might be exposed in this region. Additionally, it is conceivable that A-sites are also present on the edges, and therefore A-site vacancies as well, which might have triggered the observed exsolutions. As such, the *edge* of the terraces might correspond to a termination layer or a surface containing both *A- and B-site species*.

In conclusion, the terraces may be regarded as being constructed from parallelepiped-like building blocks. The parallelepipeds appear to have A-site cation terminated/rich outer faces and AB(O)-terminated oblique faces. To understand if such a configuration of termination layers is possible in perovskites, the possible termination layers are examined next for $SrTiO_3$.

7.5.2 Possible termination layers for $SrTiO_3$ surfaces

The possible termination layers of $SrTiO_3$ have been widely studied either for fundamental or application-related motives.[14–19] Depending on the direction from which the ideal cubic perovskite crystal structure is viewed, it may be

regarded as being composed of sets of different atomic layers. This is illustrated in Figure 7-11.

Thus, for example, when viewing down the [100] direction, the viewer's eye looks perpendicular to the (100) (see Figure 7-11 (a)). From this point of view, the perovskite structure may be regarded as being composed of atomic planes of TiO_2 stoichiometry alternating with atomic planes of SrO stoichiometry (Figure 7-11 (a)). Consequently, the (100) *surface* atomic plane in $SrTiO_3$, *i.e.* the *termination layer*, may be either a TiO_2 layer or a SrO layer. In the (100) orientation each atomic layer is quasi-neutral, hence a (100) surface is a weakly polar surface.[15] Similarly, looking down the [110] direction at the (110) planes, the $SrTiO_3$ crystal is made up from a stack of alternating O_2^{4-} and $SrTiO^{4+}$ layers (see Figure 7-11 (b)). In this case the surface of the crystal with this particular orientation will be *polar* since both possible terminations, O_2^{4-} and $SrTiO^{4-}$ bear (formal) charge. By analogy, the (111) orientation is also polar since it consists of SrO_3^{4-} and Ti^{4+} alternating layers (see Figure 7-11 (c)).

Initial calculations revealed that for (100) planes in $SrTiO_3$, both terminations have similar probability of occurrence.[20] However, other theoretical studies outline that generally perovskites tend to be A-site terminated,[21] a fact which is supported by multiple experimental reports coming from titanates but other perovskites as well.[22–27]

Considering now the observations made at the end of the last section (7.5.1) and the possible terminations in the simplified case of $SrTiO_3$, the following correspondences may be made. It seems possible that the small parallelepiped units that compose the terraces (Figure 7-10 (a) or Figure 7-12 (b)) originate from a rectangular cuboid array of $SrTiO_3$ unit cells with (100) A-site terminated faces, as illustrated in Figure 7-12 (a).

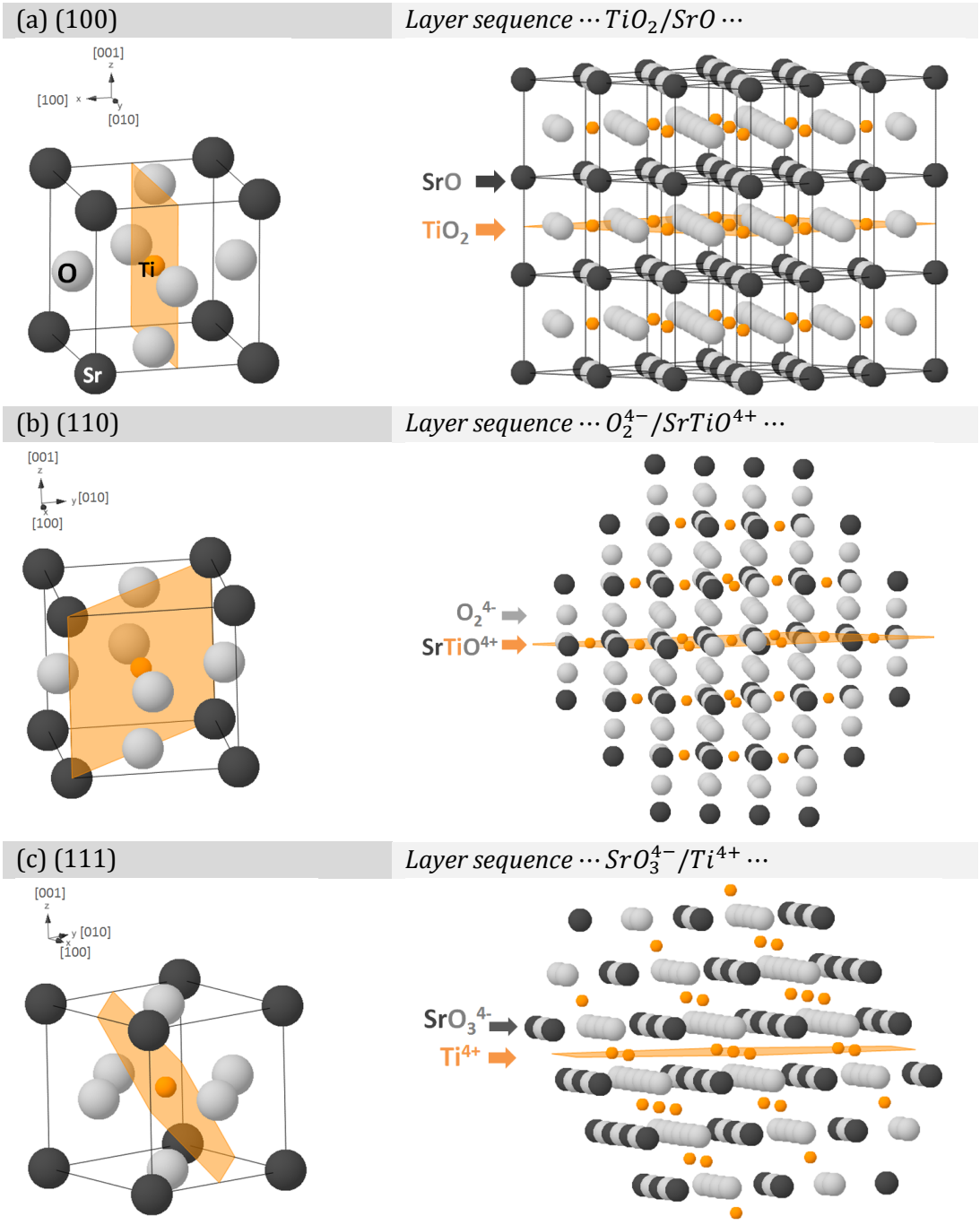

Figure 7-11 | The (100), (110), and (111) planes and termination surfaces of $SrTiO_3$.

By slicing through the (110) plane in this rectangular cuboid, an ABO-type surface would be exposed, *i.e.* one which would contain both A-site species (*e.g.* A-site vacancies and A-site cations) and B-site species (*e.g.* Ti and reducible cations) in the same atomic plane, and which consequently may give rise to B-site exsolutions. The similarity between the parallelepiped derived from the rectangular cuboid cluster of cells and the parallelepiped-

based fractal-like surface morphology of A-site deficient perovskites is quite striking (compare Figure 7-12 (b) to Figure 7-12 (c)).

While these conclusions were arrived at by articulating various experimental observations, it was not the purpose of this discussion to claim that the presence/absence of exsolutions is strictly associated with the above mentioned orientations. Instead, this idealised comparison may serve as a conceptual starting point for future investigations.

(a) (100) $SrTiO_3$

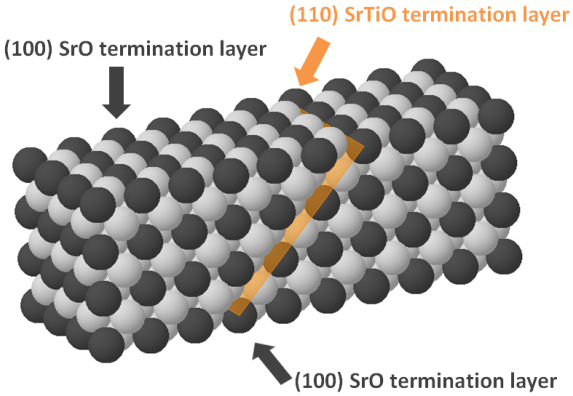

(b) Slice through (110)

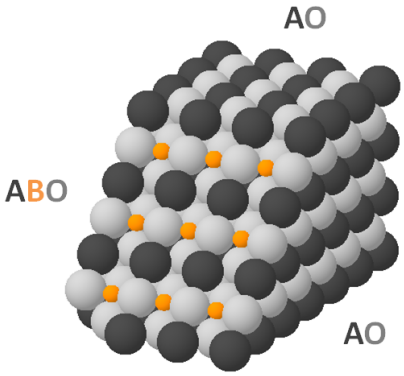

(c) Facets and exsolutions

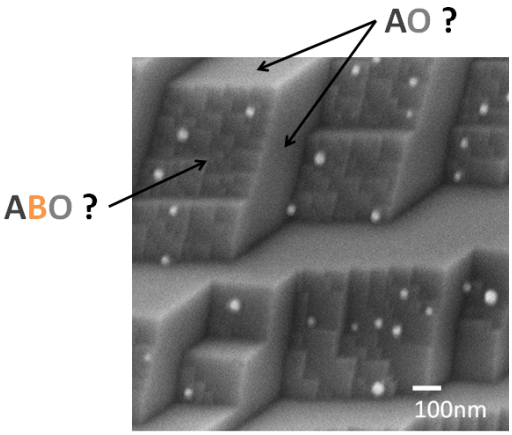

Figure 7-12 | Proposed (idealised) correspondence between the surface termination layers of a rectangular cuboid array of $SrTiO_3$ unit cells and the parallelepiped-based fractal-like surface morphology of A-site deficient perovskites in order to explain the preferential occurrence of exsolutions on certain facets. (a) A rectangular cuboid array of $SrTiO_3$ unit cells with (100) A-site terminated faces. (b) Slice through the rectangular cuboid to expose a (110) termination layer which contains both the A and B-site in the same atomic plane. (c) Typical example of terrace like microstructure of A-site deficient titanates in which the terraces may be regarded as consisting of very small parallelepipeds.

7.5.3 Exsolutions from native *vs.* 'randomly' terminated perovskite surfaces

In section 7.5.1 it was concluded that the exsolution phenomenon tends to occur preferentially on certain facets, hence it is likely that the surface of the studied perovskites is structurally and/or compositionally inhomogeneous.

To further assess the extent to which the *native surface structuring* (*i.e.* the inherently occurring surface terracing) affects the exsolution phenomenon, it is important to produce randomly terminated surfaces absent of native surface structuring. A simple way to produce surfaces that do not consist exclusively of the native surface is by simply cleaving the porous pellet-like samples in half. This is schematically represented in Figure 7-13.

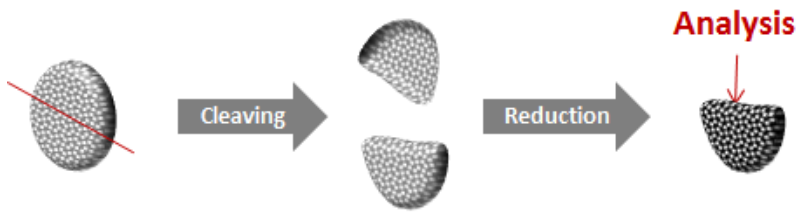

Figure 7-13 | Schematic representation of pellet cleaving used to expose the bulk of the perovskite grains and hence a differently terminated surface (more 'randomly terminated') compared to the native terraced surface.

Fortunately, all the pellets made in this study when cleaved the break occurs through the grains as well, not through the grain boundaries only. Thus, this method directly exposes *bulk termination layers*. An SEM image of the microstructure obtained by cleaving such a porous pellet is shown in Figure 7-4 (b). Naturally, the cleaved sample consists of two types of surfaces: native surfaces exhibiting terracing and bulk-like terminated surfaces.

Of course, if cleaving tends to occur preferentially along certain crystal orientations then the bulk surface generated in this way might not be locally randomly terminated either. On the other hand it is worth noting that generally when the pellets are broken, the fracture surface in the grains appear to be mostly planar (see, for example Figure 7-4 (b)). This, combined with the fact that crystallites in the grains should be randomly oriented implies that generally the fracture surface is not preferentially oriented and

in a reasonable approximation, the bulk surface exposed through cleaving may be considered *randomly terminated* and representative of the bulk stoichiometry and structure, definitely more so than the native structured surface.

Since cleaved samples consist of both native and bulk-like terminated surfaces, they offer an ideal framework to carry out *in-situ* comparative reduction studies for such distinctly terminated surfaces. Thus, representative samples were cleaved to expose a 'randomly terminated' bulk surface, and subsequently reduced to trigger the growth of exsolutions. The compositions selected for this experiment included $La_{0.3}Sr_{0.7}TiO_{3+\gamma}$, $La_{0.3}Sr_{0.7}Ni_{0.06}Ti_{0.94}O_{3+\gamma}$, $La_{0.4}Sr_{0.4}TiO_3$ and $La_{0.52}Sr_{0.28}Ni_{0.06}Ti_{0.94}O_3$ to allow comparison between different nonstoichiometry classes and B-site cation constitution.

The most striking result was obtained for the A-site deficient, Ni-containing composition in which all the grains that were cleaved were covered with fine and uniformly distributed nanoparticles (Figure 7-14 (b)). Although the regular surface produced a number of exolutions, they were not as abundant as on the cleaved area, implying the terrace structuring of the surface has a detrimental effect on the exolution process by restricting particle growth to certain parts of the terraces, as suggested in section 7.5.1. Additional SEM images of this sample, at different magnifications, are shown Figure 7-15.

The A-site stoichiometric, Ni containing compositions did exsolve Ni in this experiment, but only from what appears to be the cleaved grains (Figure 7-14 (a)), whereas the regular surface remained pristine, as seen in the previous experiment (Figure 7-5 (a)).

(a) $ABO_{3+\gamma}$

A-site stoichiometric, oxygen excess perovskite $La_{0.3}Sr_{0.7}Ni_{0.06}Ti_{0.94}O_{3+\gamma}$

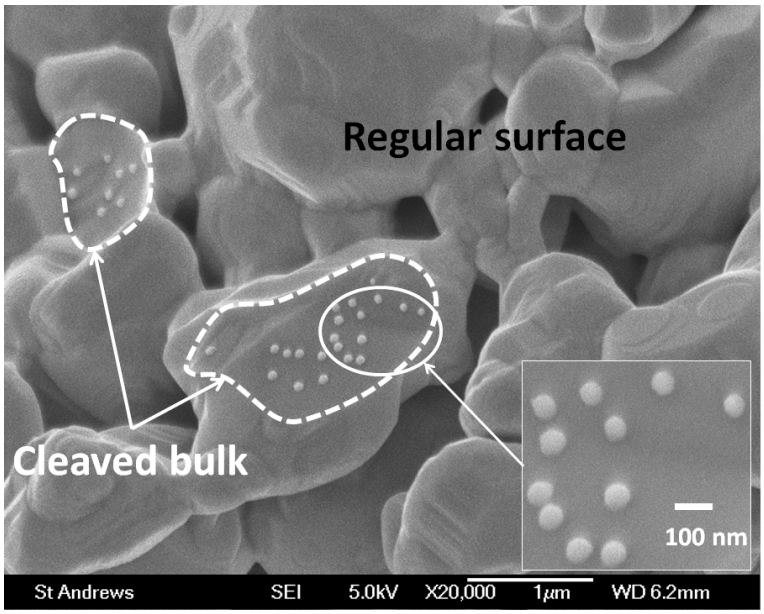

(b) $A_{1-\alpha}BO_3$

A-site deficient, oxygen stoichiometric perovskite $La_{0.52}Sr_{0.28}Ni_{0.06}Ti_{0.94}O_3$

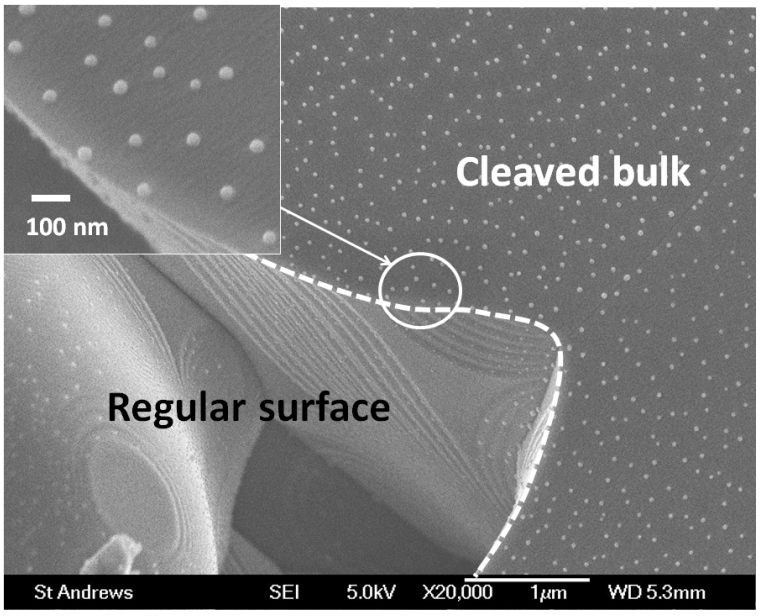

Figure 7-14 | The key role of the perovskite surface structuring in the formation of B-site exsolutions illustrated by reducing samples that were cleaved and thus possessed two differently terminated surfaces: regular (native) and bulk-like. This is exemplified through SEM images showing Ni exsolutions from (a) $La_{0.3}Sr_{0.7}Ni_{0.06}Ti_{0.94}O_{3+\gamma}$ and (b) $La_{0.52}Sr_{0.28}Ni_{0.06}Ti_{0.94}O_3$. Both samples were reduced in the same conditions reduced in $5\%H_2$/Ar, at 900 °C, for 15 h.

In the case in which the B-site is occupied solely by Ti, a similar contrast is observed between the A-site deficient and A-site stochiometric compositions on reduction at 1100 °C. The A-site deficient titanate forms numerous $TiO_{2-\delta}$ nanoparticles while the A-site stoichiometric, oxygen excess composition only exolved occasionally, as shown in Figure 7-16.

(a) $A_{1-\alpha}BO_3$

A-site deficient, oxygen stoichiometric perovskite $La_{0.52}Sr_{0.28}Ni_{0.06}Ti_{0.94}O_3$

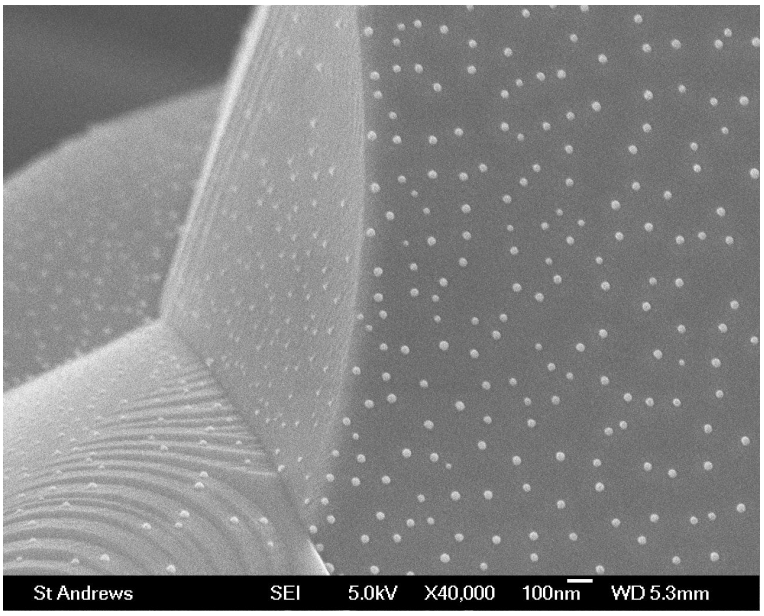

(b) $A_{1-\alpha}BO_3$

A-site deficient, oxygen stoichiometric perovskite $La_{0.52}Sr_{0.28}Ni_{0.06}Ti_{0.94}O_3$

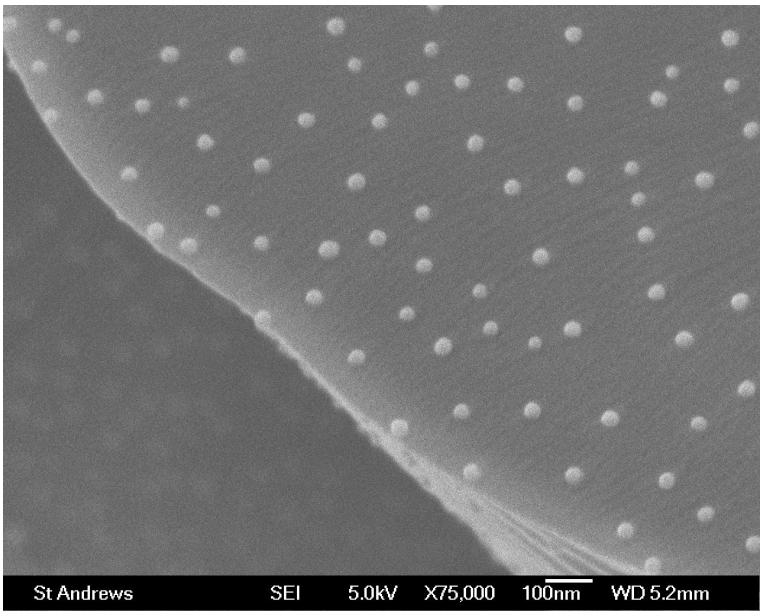

Figure 7-15 | Details of the sample presented in Figure 7-14 (b), at (a) average and (b) high magnification.

The fact that the A-site deficient systems display such a rich and evenly distributed growth of B-site exsolutions across the entire bulk-like terminated surface suggests that the defect chemistry of this class innately favors the *nucleation* of B-site containing phases virtually from everywhere on this surface.

On the contrary, the scarcely occurring and/or the bulky appearance of the B-site exsolutions arising in the case of the A-site stoichiometric, oxygen excess samples implies that the defect chemistry associated with this class is not

particularly suitable at promoting B-site exsolutions. Hence it is not the optimal or natural choice when attempting to create perovskite surfaces decorated with uniformly dispersed nanoparticles which would be desirable for well-defined and well-controlled microstructures leading to enhanced catalytic/electrochemical properties.

(a) $ABO_{3+\gamma}$

A-site stoichiometric, oxygen excess perovskite $La_{0.3}Sr_{0.7}TiO_{3+\gamma}$

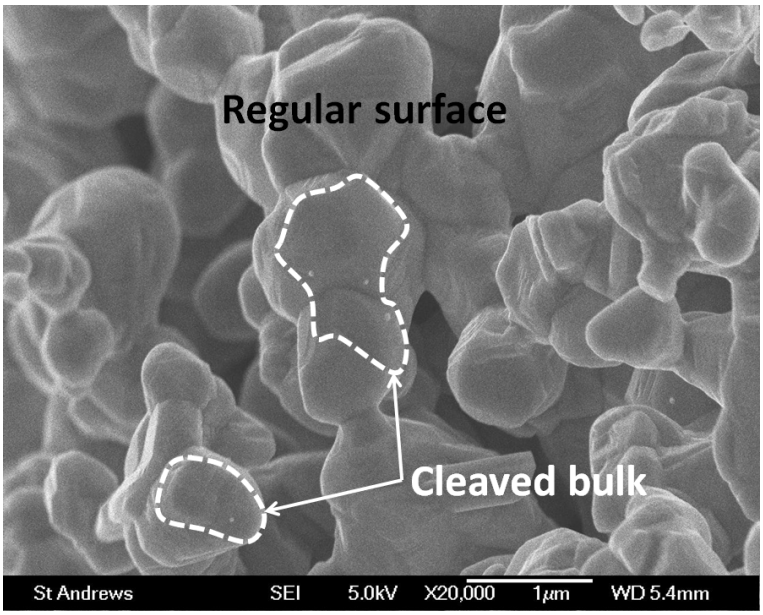

(b) $A_{1-\alpha}BO_3$

A-site deficient, oxygen stoichiometric perovskite $La_{0.4}Sr_{0.4}TiO_3$

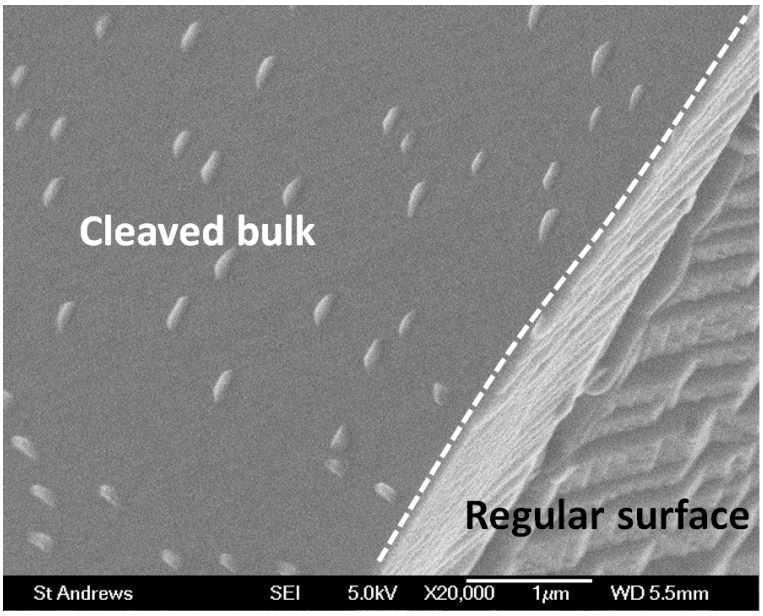

Figure 7-16 | The key role of the perovskite surface structuring in the formation of B-site exsolutions illustrated by reducing samples that were cleaved and thus possessed two differently terminated surfaces: regular (native) and bulk-like. This is exemplified through SEM images showing $TiO_{2-\delta}$ exsolutions from (a) $La_{0.3}Sr_{0.7}TiO_{3+\gamma}$ and (b) $La_{0.4}Sr_{0.4}TiO_3$. Both samples were reduced in the same conditions reduced in 5%H_2/Ar, at 1100 °C, for 15 h.

The scarcely occurring exsolutions restricted to the bulk termination layer of Ni-doped, oxygen excess stoichiometry (in Figure 7-14 (a)), can be explained within the traditional concept of exsolution which dictates that if easily reducible cations such as Ni^{2+} are present in the perovskite some of them will tend to reduce to metals and naturally segregate from the ceramic matrix (see discussion in section 7.2). Thus, the critical role of surface structuring on the exsolution of B-site species from perovskites demonstrated here for the first time places the traditional understanding of exsolution driving factors into a wider context.

The detrimental effect of surface structuring seems particularly strong in the case of the Co-doped A-site deficient composition $La_{0.4}Sr_{0.4}Co_{0.06}Ti_{0.94}O_{3-\gamma}$. In this system, exolutions originating from the native surface are very difficult to locate perhaps due to their very small size as well.

$A_{1-\alpha}BO_{3-\gamma}$

A-site deficient, oxygen deficient perovskite $La_{0.4}Sr_{0.4}Co_{0.06}Ti_{0.94}O_{3-\gamma}$

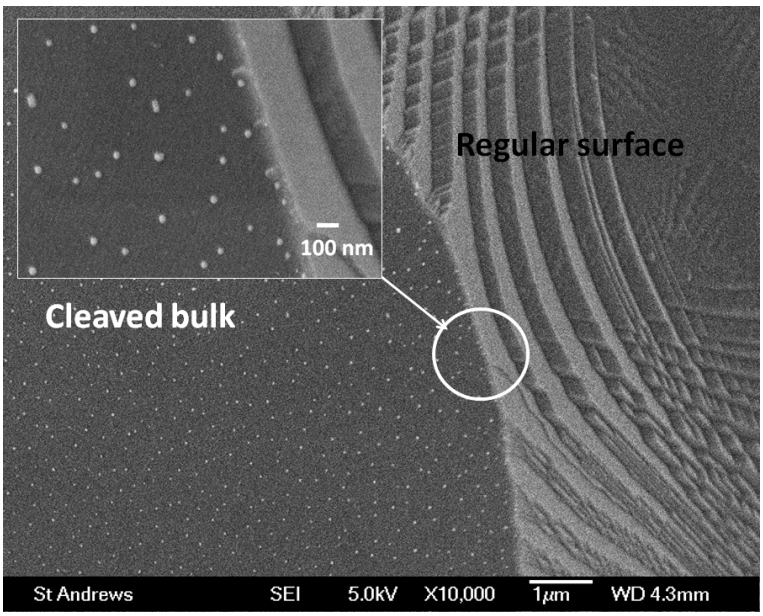

Figure 7-17 | The key role of the perovskite surface structuring in the formation of B-site exsolutions illustrated by reducing samples that were cleaved and thus possessed two differently terminated surfaces: regular (native) and bulk-like. This is exemplified through SEM images showing Co exsolutions from $La_{0.4}Sr_{0.4}Co_{0.06}Ti_{0.94}O_{3-\gamma}$ after reduction 5%H_2/Ar, at 930 °C, for 15 h.

However, when cleaved and reduced, the exposed bulk surface gives rise to numerous nanoparticles (Figure 7-17) very similar in appearance to the Ni exsolutions (Figure 7-14 (b)) but somewhat finer, especially considering the

reduction was carried out at 930 °C in the case of the Co-doped sample and at 900 °C in the case of the Ni-doped composition. This demonstrates that even though surface structuring may almost suppress exsolutions on the native surface in this composition, its bulk structure and composition naturally allows for it to happen as expected for this defect chemistry class.

7.5.4 Exsolutions from perovskites with different degrees of A-site occupancy

As demonstrated throughout this chapter so far, the presence of A-site vacancies is critical for driving the formation of exsolutions. In this section, the effect of varying the degree of A-site deficiency will be examined. For this purpose, undoped titanates were considered from the A-site deficient series $La_xSr_{1-3x/2}TiO_3$. The selected compositions included $x = 0.4$ (α = 0.2), $x = 0.2$ (α = 0.1), $x = 0.4$ (α = 0.05) and $x = 0$ (*i.e.* $SrTiO_3$, α = 0). The results obtained by reducing the bulk terminated surfaces of these compositions are shown in Figure 7-18.

As argued in section 7.5.3, by performing reduction on fractured bulk surfaces and thus without the interference from the native surface structuring, the inherent predisposition towards B-site exsolutions of samples may be revealed more clearly. Figure 7-18 shows that numerous and well delimited exsolutions form for α = 0.2.

By decreasing α to 0.1 the number of the exsolutions did not decrease significantly but their size did, which is a very desirable effect for maximising surface and hence catalytic/electrochemical performance. By further lowering α to 0.05 exsolutions become even smaller but very sporadic and disappear entirely in the case of A-site stoichiometric $SrTiO_3$.

(a) $A_{1-\alpha}BO_3$
α = 0.2

$La_xSr_{1-3x/2}TiO_3$

$x = 0.4$

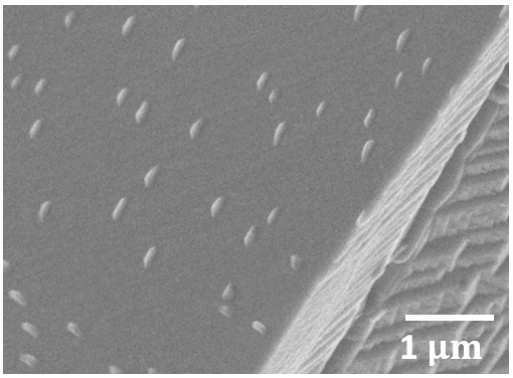

(b) $A_{1-\alpha}BO_3$
α = 0.1

$La_xSr_{1-3x/2}TiO_3$

$x = 0.2$

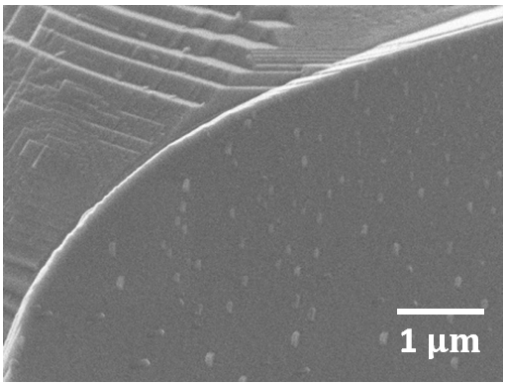

(c) $A_{1-\alpha}BO_3$
α = 0.05

$La_xSr_{1-3x/2}TiO_3$

$x = 0.1$

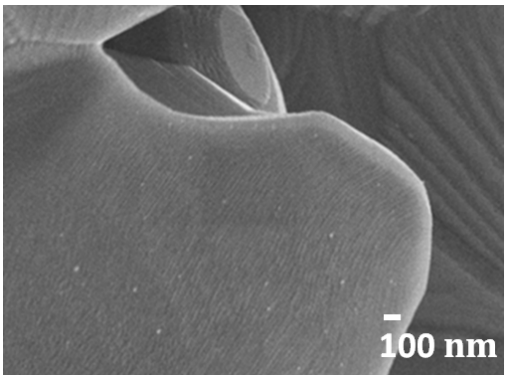

(d) ABO_3
α = 0

$La_xSr_{1-3x/2}TiO_3$

$x = 0$ ($\equiv SrTiO_3$)

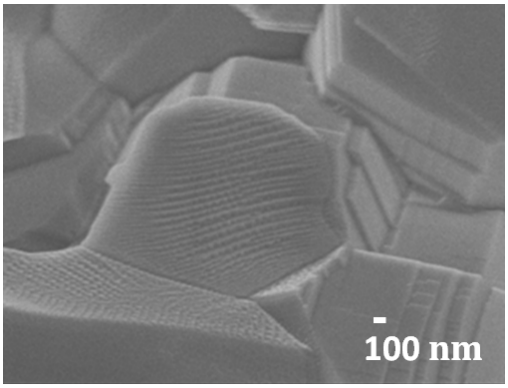

Figure 7-18 | Samples from the specified nonstoichiometry class and composition cleaved and reduced in 5%H_2/Ar at 1100 °C (20 h). α is the A-site deficiency, $\alpha = 1 - (x + 1 - 3x/2) = x/2$.

This comparison demonstrates that the *concentration of A-site vacancies* is potentially a key factor in controlling the *nucleation* (*i.e.* where the nanoparticles form and thus the overall distribution) and their *growth* (*i.e.* their final size). Thus, this additional parameter offers virtually unlimited possibilities for further tailoring the exsolution phenomenon for any particular functions and needs. This effect may be better understood and exploited in the context set by section 5.5 where the relation between the doping stoichiometry and the frequency of dopant occurrence in perovskites was discussed.

7.5.5 The stability of the exsolved nanoparticles on ageing

In order to test the stability of the obtained nanostructures on ageing, selected samples were kept at high temperatures in reducing conditions for long periods of time.

One example has already been shown in Figure 7-10 a which depicts the SEM microstructure of $La_{0.4}Sr_{0.4}Ni_{0.03}Ti_{0.97}O_{3-\gamma}$ sample initially reduced in 5%H_2/Ar, at 930˚C for 20 h and then then kept in humidified reducing gas, 3%H_2O in 5%H_2/Ar, at 900˚C for 100 h. As observed from this figure, the particles are still below 50 nm in size and well distributed, suggesting they are well anchored in the parent perovskite and thus unable to coalesce as the natural tendency of minimizing Ni surface energy would dictate. Indeed, designing systems in which Ni does not tend to agglomerate over time is particularly challenging (see discussion in section 7.8).

An even more interesting case was found after a sample of $La_{0.52}Sr_{0.28}Ni_{0.06}Ti_{0.94}O_3$ composition with initial microstructure shown in Figure 7-14 (b) was kept in humidified reducing gas, 3%H_2O in 5%H_2/Ar at 900 °C for 60 h. The microstructure of the sample after the ageing process is given in Figure 7-19. Compared to the previous example, more exsolutions appeared during this ageing stage but their size is remarkably similar, if not even slightly smaller than the size of the nanoparticles in the sample before ageing. Thus, after the ageing process the bulk terminated surface develops

an exceptional coverage with nanoparticles ~ 30 nm with no sign of particles clustering into larger particles. This may be attributed again to the 'unconventional' anchorage these particles may develop when exsolving from the parent perovskite phase.

(a) $A_{1-\alpha}BO_3$ (Ageing)

A-site deficient, oxygen stoichiometric perovskite $La_{0.52}Sr_{0.28}Ni_{0.06}Ti_{0.94}O_3$

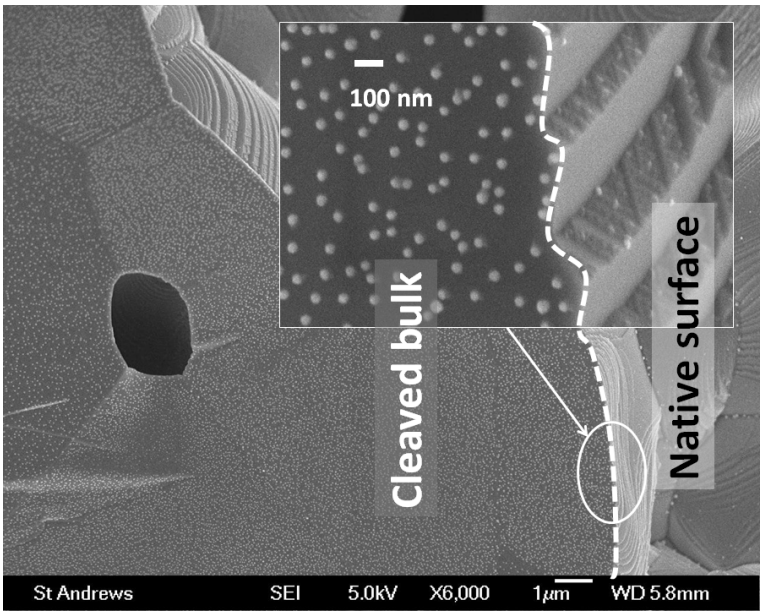

(b) $A_{1-\alpha}BO_3$ (Ageing)

A-site deficient, oxygen stoichiometric perovskite $La_{0.52}Sr_{0.28}Ni_{0.06}Ti_{0.94}O_3$

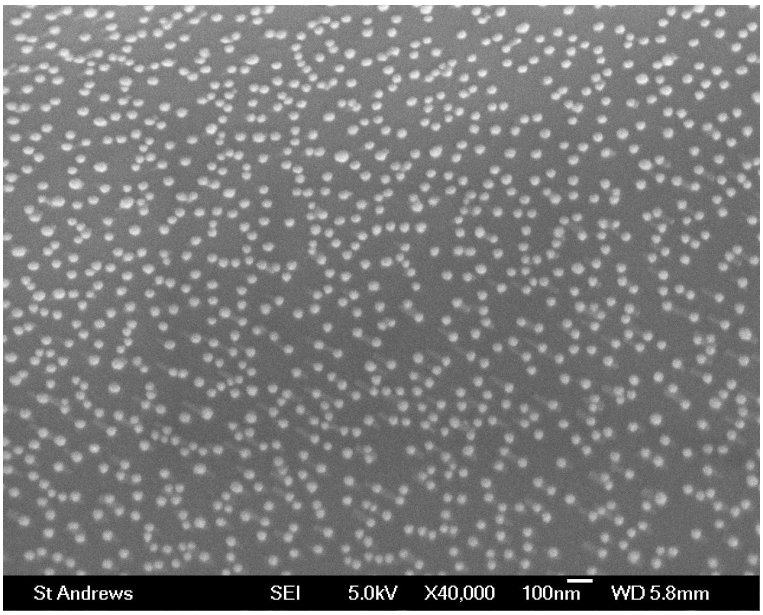

Figure 7-19 | Sample shown in Figure 7-14 (b) aged in humidified reducing gas, 3%H_2O in 5%H_2/Ar at 900 °C for 60 h. (a) Overview of native and bulk-terminated surfaces at smaller magnification. (b) Higher magnification detail of the bulk terminated surface.

7.5.6 The stoichiometry of A-site deficient perovskite surfaces

To understand if there is any compositional difference between the regular and fractured, bulk terminated surface of the deficient perovskites, X-ray Photoelectron Spectroscopy (XPS) analysis[xvii] was performed on a $La_{0.52}Sr_{0.28}Ni_{0.06}Ti_{0.94}O_3$ sample before and after cleaving and then after reduction. The experiment and its main findings are summarised in Figure 7-20 and discussed below.

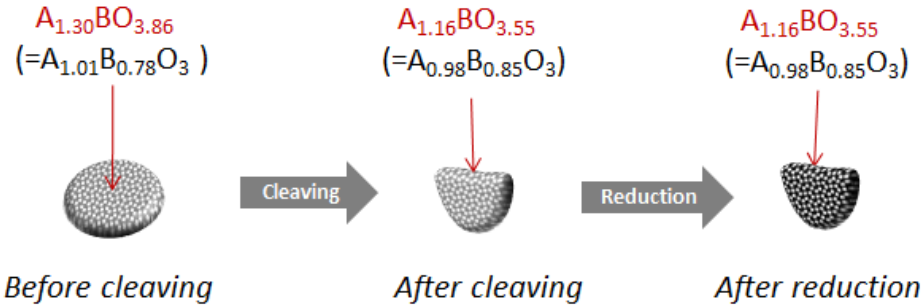

Figure 7-20 | Summary of the stoichiometry results obtained by XPS on a $La_{0.52}Sr_{0.28}Ni_{0.06}Ti_{0.94}O_3$sample (porous pellet – porosity denoted by the dotted texture of the pellet sketch).

Measurements revealed that instead of the expected $A_{0.8}BO_3$ stoichiometry, the regular surface displayed considerable A-site and oxygen excess: $A_{1.30}BO_{3.86}$. Upon cleaving the sample, the excess decreased to $A_{1.16}BO_{3.55}$, which was to be expected, because by cleaving some of the grains, additional surfaces closer to nominal $A_{0.8}BO_3$ stoichiometry are exposed (assuming random crystal orientations upon cleaving). It is worth noting that while there is significant difference in the A:B stoichiometry between the surface and the bulk, it was observed that the Sr/La ratios for the regular surface (0.52) and the cleaved surface (0.54) were almost identical to the nominal ratio (0.538), suggesting that both La^{3+} and Sr^{2+} contribute equally to the A-site enrichment, perhaps indicative of avoidance of B-site surface terminations.

[xvii] XPS was carried out at Sasol Technology (UK) in St. Andrews by Dr. Hervé Ménard. His involvement with data collection and interpretation is gratefully acknowledged.

The cleaved sample was then reduced *in-situ*, in the XPS, using 5%H_2/Ar, with 30 minutes isothermal steps at 600, 700, 800 and 900 °C, aiming to reveal any compositional changes that may occur in the fracture surface upon reduction. It was found that the surface stoichiometry of the cleaved, as-prepared (*i.e.* in oxidized state) surface did not change upon reduction, as indicated in Figure 7-20. Unfortunately, attempts to identify Ni metal on the surface *via* XPS were unsuccessful due to the low relative sensitivity factor (RSF) of Ni metal. Nonetheless, SEM analysis performed afterwards on the sample revealed that numerous exsolutions were in fact present (see Figure 7-21). It should be noted here that the total reduction time was 2 h at temperatures lower or at most equal to 900 °C, yet numerous nanoparticles exsolved, comparable to the case where the same sample was reduced at 900 °C for 15 h, as shown in Figure 7-14 (b). This suggests that the exsolution phenomenon occurs very fast, perhaps within minutes since reduction at temperatures below 800-900 °C is generally small in perovskites.

Nonetheless, the fact that the surface of this A-site deficient perovskite was found to be A-site rich within the 1-5 nm from the surface (this is the depth at which XPS provides reliable compositional information) is surprising, but in line with observations made in sections 7.5.1 and 7.5.2. In particular, the configuration of orientations (and the SEM image that supports it) proposed in Figure 7-12 implies that generally the areas on which exsolutions do not form (*i.e.* A-site rich) should dominate the ones having exposed B-sites, hence the superstoichiometric A/B ratio. However, the fact that XPS reveals information from the first 1-5 nm (*i.e.* several unit cell layers) it follows that it is unlikely that *only a single termination layer* may shift the A/B ratio from 0.8 in the bulk to 1.3 at the very surface. Thus, most likely, the surface A-site enrichment (1-5 nm) is due to a structural perovskite variant able to accommodate extra A-site cations. This would explain why surface structuring has such a strong effect on the exsolution phenomenon.

(a) $A_{1-\alpha}BO_3$ (Fracture surface)

A-site deficient, oxygen stoichiometric perovskite $La_{0.52}Sr_{0.28}Ni_{0.06}Ti_{0.94}O_3$

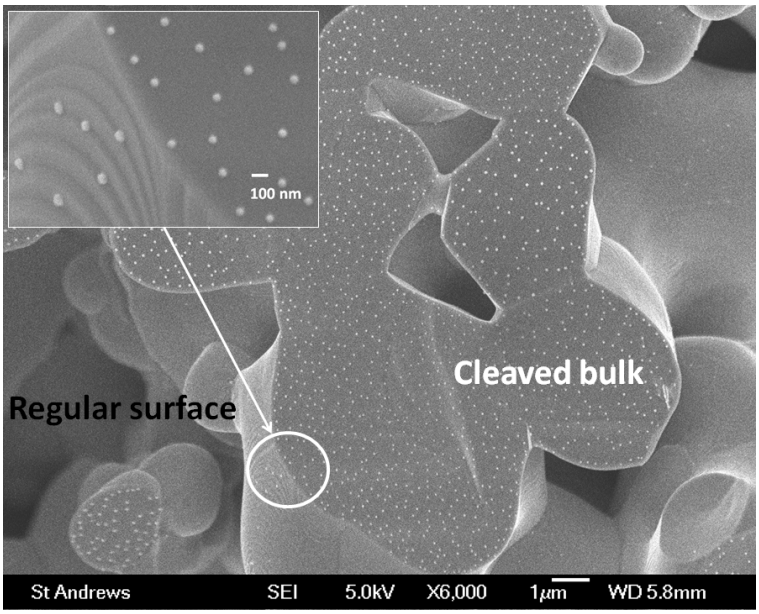

(b) $A_{1-\alpha}BO_3$ (Native surface)

A-site deficient, oxygen stoichiometric perovskite $La_{0.52}Sr_{0.28}Ni_{0.06}Ti_{0.94}O_3$

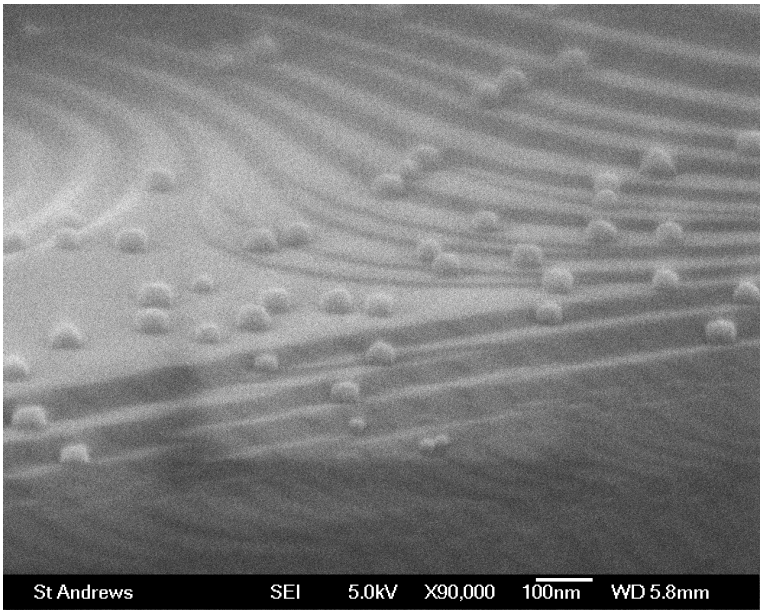

Figure 7-21 | SEM images of the sample used in the XPS study, after the in-situ reduction in the XPS specimen chamber.

The fact that perovskites generally tend to exhibit A-site enrichment at the surface has been reported on numerous occasions for various systems, [28,15,14,29,23,24,21,27] and even predicted by calculations.[21] Szot *et. al.* have shown that the A-site, oxygen rich surface layer is in fact, as the stoichiometry would imply, an A-site oxygen excess perovskite variant belonging to the Ruddlesden-Popper series $A_{n+1}B_nO_{3n+1}$, and, at least in the case of bulk-like terminated $SrTiO_3$ single crystals inherently forms during annealing in oxidizing conditions at high temperatures.[23,22] Therefore, an A-site rich layer

would be expected to develop during the synthesis of the perovskite phases which in this study, as in most others, is routinely performed in air at high temperatures. Thus, it is rather surprising that even A-site deficient perovskites exhibit surface A-site enrichment, but it is not surprising at all that this layer acts to locally suppress B-site exsolutions because it belongs to the excess perovskite nonstoichiometry class which it was showed that does not naturally promote B-site exsolutions. Alternatively, purely from a stoichiometry point of view, an A-site, oxygen excess compositions such as $A_{1.3}BO_{3.86}$ and $A_{1.16}BO_{3.55}$ can be regarded as B-site deficient, *i.e.* $A_{1.01}B_{0.78}O_3$ and $A_{0.98}B_{0.85}O_3$, respectively, which, again, would suggests poor predisposition towards B-site exsolution at the surface.

7.6 Demonstration of simultaneous *in-situ* exsolution of metallic and oxide nanoparticles

7.6.1 Stoichiometry design considerations for $La_{0.8}Ce_{0.1}Ni_{0.4}Ti_{0.6}O_3$

The studies presented so far on exsolutions led to a considerably more comprehensive understanding of the factors which allow the tailoring of the phenomenon as compared traditional approach based solely on cation reducibility. Most of the key observations made throughout this chapter went into the design of the stoichiometry of the all new perovskite $La_{0.8}Ce_{0.1}Ni_{0.4}Ti_{0.6}O_3$, as explained below.

The major aim with this composition was of course that it exsolves Ni metal. Additionally, it should be noted here that many attempts were made to substitute Ce on the B-site of the perovskite and trigger the exsolutions of $CeO_{2-\delta}$ nanoparticles since ceria is a well-known catalyst for many electrochemical reactions (see references [30–33] and references therein). However, Ce^{4+} proved to be too large to substitute on the B-site of the host used here, $La_{0.4}Sr_{0.4}TiO_3$ and seemed to fit better on the A-site (see Figure 2.4 and discussion in section 2.2.2).

One observation made during these studies was that smaller number of Sr^{2+} cations on the A-site seemed to be beneficial for yielding overall better microstructures in terms of exsolutions. For example, all members of the series $La_{0.4+x\cdot(4-m)}Sr_{0.4-x\cdot(4-m)}M_x^{m+}Ti_{1-x}O_3$ consistently display better exsolution uniformity compared to their oxygen deficient analogues $La_{0.4}Sr_{0.4}M_xTi_{1-x}O_{3-\gamma}$ which have higher Sr^{2+} content. Additionally, it was considered that perhaps Sr^{2+} might even favour the formation of Ruddlesden-Popper surface structures which are well known for containing Sr^{2+}, but not quite as much La^{3+}. Thus, it was desirable for the new perovskite to contain no Sr^{2+}.

In terms of stoichiometry, the new perovskite had to be oxygen stoichiometric, again since compositions starting as oxygen stoichiometric seemed to have smaller separation between terraces and thus yield more uniform coverage of nanoparticles. In terms of A-site deficiency, a value of $\alpha = 0.1$ was used based on the arguments presented in 7.5.4 according to which this particular value might favour nucleation instead of growth of nanoparticles, thus yielding more numerous, yet small nanoparticles.

With these compositional restrictions, the stoichiometry was formulated and the newly formulated composition was found to exhibit perovskite structure indeed as shown in section 4.6. The fact that perovskite can be designed to incorporate so many desired features demonstrates yet again their versatility.

7.6.2 The nature of the exsolutions in $La_{0.8}Ce_{0.1}Ni_{0.4}Ti_{0.6}O_3$

The exsolutions that formed from this A-site deficient perovskite after reduction in 5%H_2/Ar at 900 or 1000 °C are shown in Figure 7-22. The exsolutions formed in this system at 900 °C are by far the smallest (<10-20 nm) and most uniformly distributed among the compositions examined so far, in accord with the premises on which it was formulated. Even when the exsolutions form at 1000 °C they do not tend to agglomerate and are still within 50 nm size.

(a) $A_{1-\alpha}BO_3$ (Exolutions at 900 °C)

A-site deficient, oxygen stoichiometric perovskite $La_{0.8}Ce_{0.1}Ni_{0.4}Ti_{0.6}O_3$

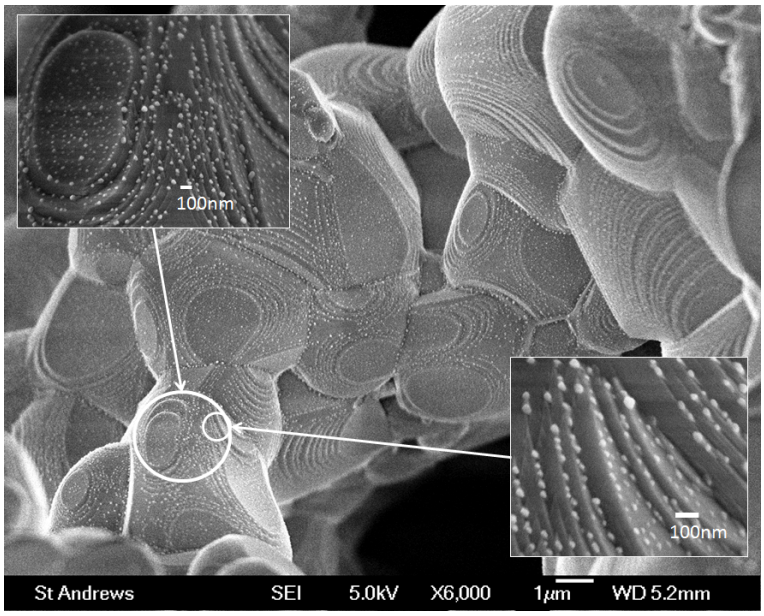

(b) $A_{1-\alpha}BO_3$ (Exolutions at 1000 °C)

A-site deficient, oxygen stoichiometric perovskite $La_{0.8}Ce_{0.1}Ni_{0.4}Ti_{0.6}O_3$

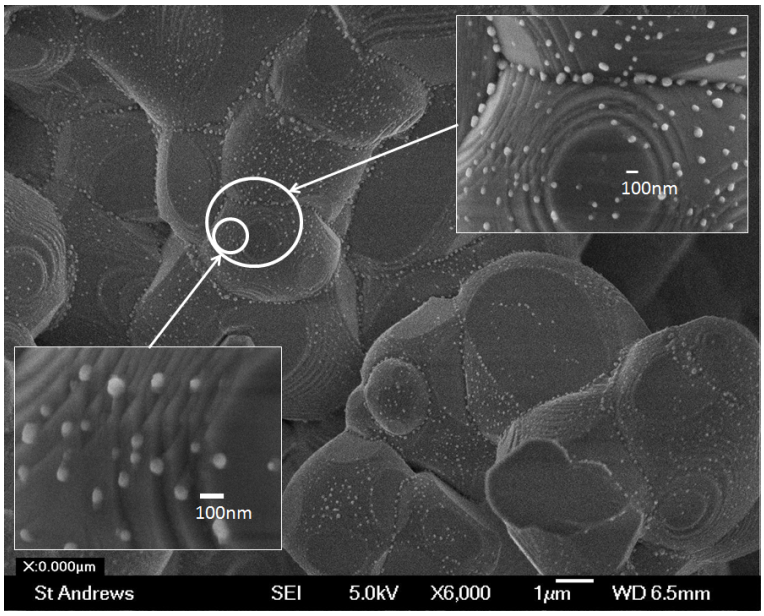

Figure 7-22 | SEM micrograph displaying the exsolutions formed from the A-site deficient $La_{0.8}Ce_{0.1}Ni_{0.4}Ti_{0.6}O_3$ system after reduction in 5%H_2/Ar, for 20 h, at (a) 900 °C or (b) 1000 °C.

Surprisingly, Ni is not the only nano-sized phase which richly decorates the surface of this composition upon reduction. The XRD pattern recorded from this sample reduced at 1000 °C showed that alongside the expected perovskite reflections and the broad peaks corresponding to metallic Ni nanoparticles several other broader peaks and shoulders are present (Figure 7-23).

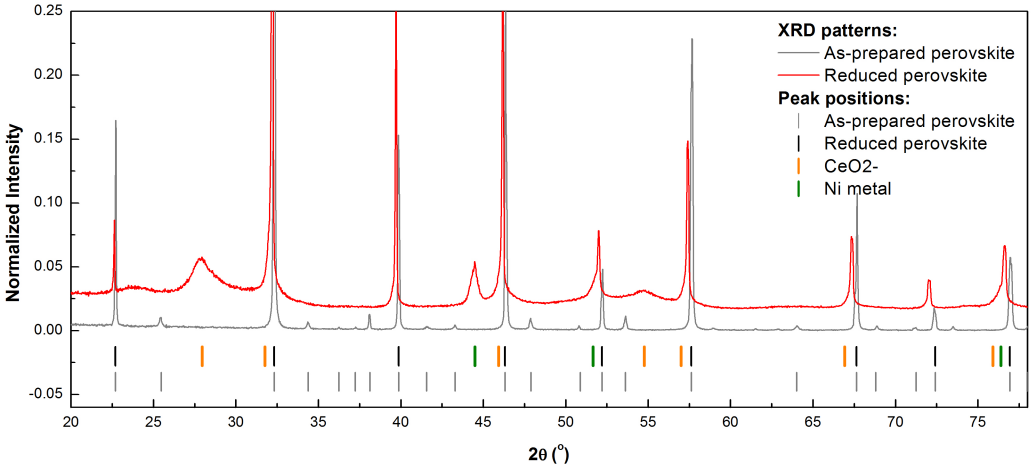

Figure 7-23 | XRD patterns of $La_{0.8}Ce_{0.1}Ni_{0.4}Ti_{0.6}O_3$ for the as-prepared (oxidized) phase and after reduction in dry 5%H_2/Ar, at 1000˚C for 20h.

This suggests that at least one more phase has exsolved from this sample, producing crystallites of even smaller size compared to Ni. The other species that will most likely tend to precipitate, besides Ni, would be $Ce^{4+/3+}$. Factors that would preferentially favor this scenario include the already high local depletion of the Ni on the B-site triggered by A-site deficiency, and the fact that the undersized $Ce^{3+/4+}$ causes significant distortion in the perovskite which might be alleviated upon its exsolution. Indeed, a fluorite type lattice ($Fm\bar{3}m$, CeO_2) having a unit cell parameter of ~5.56 Å accounts for the remaining broad reflections and peak broadening in the pattern (see peak positions in Figure 7-23). However, this unit cell is much larger than the value of ~5.45 Å measured for a pure CeO_2 sample reduced under the same conditions as the perovskite above. The expanded unit cell of the fluorite phase obtained by in situ exsolution could be attributed to the large number of defects (Ce^{3+}, $V_O^{\cdot\cdot}$) expected to arise through this unique formation mechanism, or possibly to a small number of La^{3+} ions doping it ($r(La^{3+})>r(Ce^{3+})$). A TEM analysis on this sample is given in Figure 7-24. Figure 7-24 a displays a TEM image showing details of the larger (~50 nm) Ni particles and the smaller (<10 nm) fluorite-type precipitates, in good agreement with the results from the XRD interpretation. Figure 7-24 (b) shows and EDS TEM elemental analysis confirming that the larger nanoparticles are composed of metallic Ni.

(a) $A_{1-\alpha}BO_3$
(Exolutions at 1000 °C)

A-site deficient, oxygen stoichiometric perovskite

$La_{0.8}Ce_{0.1}Ni_{0.4}Ti_{0.6}O_3$

Overview of Ni and fluorite-type exsolutions

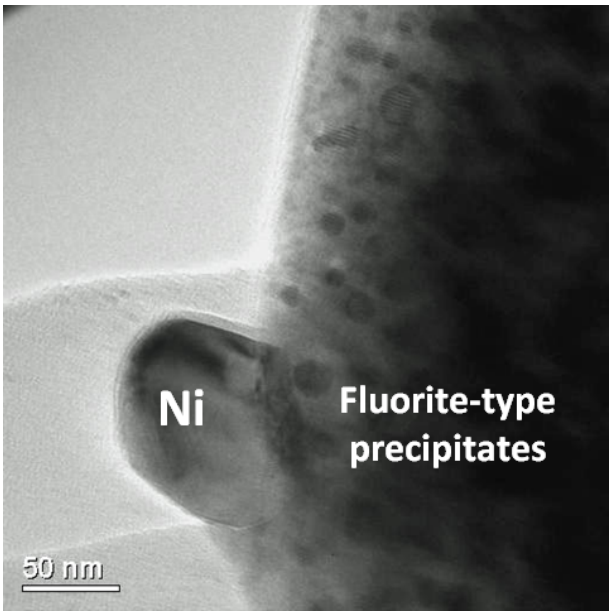

(b) $A_{1-\alpha}BO_3$
(Exolutions at 1000 °C)

A-site deficient, oxygen stoichiometric perovskite

$La_{0.8}Ce_{0.1}Ni_{0.4}Ti_{0.6}O_3$

Confirmation of the Ni nanoparticle composition

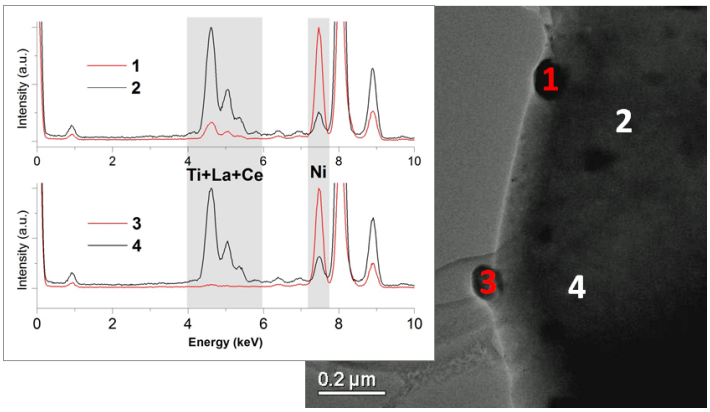

Figure 7-24 | TEM analysis[xviii] of the exsolutions formed in upon reduction 5%H_2/Ar, at 1000˚C for 20h. (a) TEM image showing details of the larger (~50 nm) Ni particles and the smaller (<10 nm) fluorite-type precipitates. (b) TEM elemental analysis confirming that the larger nanoparticles are composed of metallic Ni (see text).

However, an interesting point to note is the similarity between the unit cell of the fluorite, 5.56 Å, and the orthorhombic cell parameter of the perovskite matrix, which is ~5.55 Å in the *ab* plane. Thus, one could think that the expanded cell of the exsolved fluorite is due to the coherent growth from the perovskite. Interfaces such as these have been shown to exhibit remarkable properties.[34] Thus, for the first time, an oxide and a metal, both with remarkable catalytic potential have been simultaneously exsolved in the form of nanoparticles from a perovskite surface.

[xviii] TEM data shown here was collected by Dr. David Miller (St. Andrews). His involvement with data collection and interpretation is gratefully acknowledged.

7.7 Overview of the exsolution mechanism

The mechanism through which A-site deficiency promotes the exolution of B-site species was discussed in detail in section 7.1. Here, two perspectives of this mechanism will be presented in the light of the arguments presented after section 7.1.

From a defect chemistry perspective, the reason for which A-site deficiency naturally promotes B-site exsolutions upon reduction can be better understood by considering how different defects are expected to interact within the perovskite lattice. Thus, a perovskite that starts as A-site deficient, oxygen stoichiometric and loses oxygen ions through reduction becomes A-site deficient and oxygen deficient (Figure 7-25). The presence of vacancies on 2 of the 3 primitive sites destabilizes the perovskite lattice and locally may cause spontaneous exsolution of B-site species, in an attempt to re-establish stoichiometry across all the primitive sites.

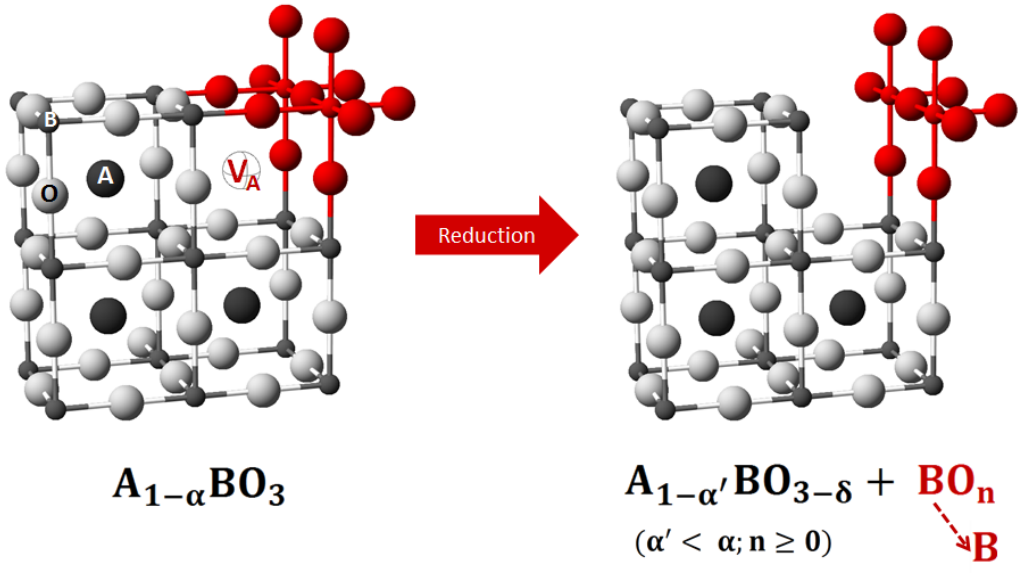

Figure 7-25 | Schematic representation the role of A-site deficiency and extent of reduction in the exsolution of B-site species from A-site deficient perovskites.

Thus, purely from a stoichiometry point of view, an A-site deficient, O-deficient perovskite can be regarded as B-excess which would again, explain the predisposition towards B-site exsolution. By contrast, in perovskites that are initially oxygen stoichiometric or excess, because of how defects are

incorporated, the B-site will rarely be 'under-coordinated' or 'exposed', either because of the extra oxygen shears or the rock-salt type intergrowths (*i.e.* in Ruddlesden-Popper phases).

Alternatively, exsolution from A-site deficient perovskites can be visualized on a rather local scale as depicted in Figure 7-25. Since the presence of A-site deficiency implies that some of the A-site positions are not occupied by cations, by removing some oxygens through reduction, the cell which possessed the vacant A-site no longer resembles a perovskite cell, as it only contains B-site species which are free to rearrange in new, more stable structures (*e.g.* oxides or metals). The perovskite cells with occupied A-site are left unaltered, overall appearing as the number of A-site deficient perovskite cells decreased, and the initial "B-site excess" was expelled leaving behind a fully stoichiometric perovskite.

Both perspectives of the phenomenon suggest that the extent of the reduction should play an important role in the occurrence of exsolutions, not only because it is a measure of the number of oxygen vacancies created, but because it also correlates to the number of reduced B-site ions (not necessarily to the metallic state):

$$2B_B^x + O_O^x \rightleftharpoons 2B_B' + V_O^{\cdot\cdot} + \frac{1}{2}O_2 \qquad \text{Eq. 7-8}$$

Indeed, it was found that for systems containing $\alpha = 0.2$ A-site deficiency exsolutions do not form at all or are sporadic when δ takes values below or around 0.05 (see Figure 7-26). This is the case of the samples which inherently do not reduce to high extents (*e.g.* $La_{0.4}Sr_{0.4}TiO_3$), or are exposed to insufficiently reducing conditions (*e.g.* $p_{O_2} > 10^{-16}$atm). On the other hand, because δ depends on p_{O_2} and temperature, these parameters can be adjusted to cause exsolution in virtually any A-site deficient system (*e.g.* the harder to reduce $La_{0.4}Sr_{0.4}TiO_3$ produces exsolutions when reduced at temperatures in excess of 1000-1100 °C – see Figure 7-2 (b)).

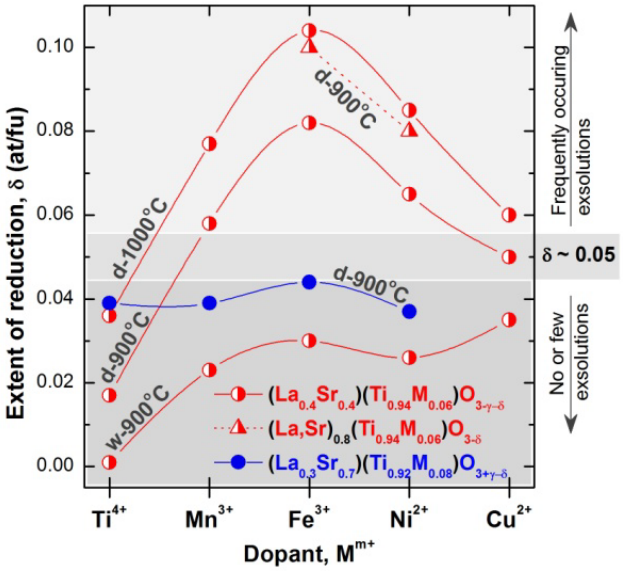

Figure 7-26 | The extent of reduction as a function of dopant for various systems and conditions, emphasizing the domains where the exsolution phenomenon was observed (from a regular surface). Reduction was performed in dry ("d") or humidified 3%H_2O ("w") reducing gas 5%H_2/Ar at different temperatures; $(La,Sr)_{0.8}(Ti_{0.94}M_{0.06})O_{3-\delta}$ stands for $La_{0.46}Sr_{0.34}Fe_{0.06}Ti_{0.94}O_{3-\delta}$ and $La_{0.52}Sr_{0.28}Ni_{0.06}Ti_{0.94}O_{3-\delta}$. Data points for the series $La_{0.3}Sr_{0.7}M_{0.08}Ti_{0.92}O_{3+\gamma}$ were taken from ref [35].

7.8 Summary, applications and implications of the exsolution phenomenon

This chapter demonstrated the use of defect chemistry as an entirely new concept that enables one to decorate perovskite surfaces with nanoparticles of diverse composition, nature and size, otherwise inaccessible *via* an exclusively 'change in composition' approach. The exsolution phenomenon was shown to be critically controlled by the innate surface restructuring displayed by perovskites, which is however subject to manipulation through defect chemistry as well.

The generality of the concept can be further refined by tuning the nucleation/growth balance *via* prudent adjustment of *driving forces* of '*intrinsic*' nature (defect concentration, cation composition) or '*extrinsic*' nature (p_{O_2}, temperature, atmosphere), and ultimately extended to other oxide classes in which defect chemistry might work in a similar manner.

The development of tailored functional materials consisting of catalytic nanoparticles dispersed over open surfaces or throughout the inner surface of porous frameworks such as the ones demonstrated in this study is of key importance in many fields including catalysis, photocatalysis and energy conversion and storage (*e.g.* fuel cells, electrolysis cells, batteries). Traditionally, these microstructures are produced *via* deposition techniques such as physical *vapor deposition*[36,37] or *chemical infiltration*.[38,39]

For example, in the chemical infiltration method the catalysts or the catalyst precursors are *attached* onto the surface during a thermal treatment. This method enables the realisation of microstructures with good electrochemical and catalytic performance, reasonable medium term stability and its flexibility allows for very broad applicability (catalysis, SOFC/SOEC electrodes etc).[31,33,38,40,41]

However, this method suffers from several drawbacks, one of the most important ones being that it may be difficult to control the size and distribution of the deposited species (see Figure 7-27 (b)) not only during preparation, but also during ageing, typically because of the poor anchoring of these species to the substrate surface. Moreover, these microstructures are produced in conditions (*e.g.* at medium temperatures in air) that are very different compared to the working conditions (*e.g.* medium-high temperatures in reducing conditions). Thus, these microstructure are most likely not thermodynamically stable in working conditions, hence they will start an irreversible chain of microstructural changes eventually leading to performance degradation. Additionally, infiltration may be very time consuming and costly since the procedure needs to be repeated multiple times for the catalyst particle load to reach reasonable number.

By contrast, *in-situ* growth of nanoparticles (Figure 7-27 (a)) offers elegant solutions to many of these problems, as demonstrated here. First, it offers superior control of nanoparticle size and distribution on the surface of the backbone parent phase. Since the catalytically active dopants are

incorporated as cations in the perovskite lattice initially, no precursors or multiple processing stages are required apart from a simple reduction. Thus, considerable time and cost savings may be made. Moreover, since the nanoparticles grow from the parent backbone rather than being attached to it, they will most likely exhibit very good surface anchorage preventing nanoparticle coalescence and hence performance degradation. Equally important is that the exsolution phenomenon occurs upon reduction, which means that the resulting microstructures are thermodynamically favoured and thus stable in these conditions. As such, *in-situ* exsolution is naturally suited for developing nanostructured materials for the hydrogen electrode of SOEC or SOFC.

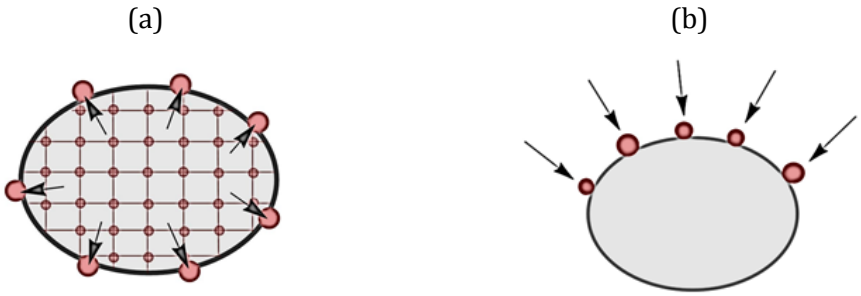

Figure 7-27 | Schematic comparison between the concept of (a) *in-situ* exsolution of catalysts and (b) the traditional deposition approach.

Finally, the results presented here on cleaved samples vividly illustrate that perovskite surfaces are preferentially A-site (rich) terminated to the detriment of the B-sites which are the sites generally occupied by catalytically active cations. As such, any assessment of perovskite surface properties based on an ideal bulk-like terminated surface can be anticipated to be fundamentally flawed and thus the true catalytic properties of many perovskites might have been underestimated.

References

1. Y. Nishihata, J. Mizuki, T. Akao, H. Tanaka, M. Uenishi, M. Kimura, T. Okamoto, and N. Hamada, *Nature*, 2002, **418**, 164–167.
2. Y. Nishihata, J. Mizuki, H. Tanaka, M. Uenishi, and M. Kimura, *J Phys. Chem. Solids*, 2005, **66**, 274–282.
3. H. Tanaka, M. Uenishi, M. Taniguchi, I. Tan, K. Narita, M. Kimura, K. Kaneko, Y. Nishihata, and J. Mizuki, *Catal. Today*, 2006, **117**, 321–328.
4. H. Tanaka, M. Taniguchi, M. Uenishi, N. Kajita, I. Tan, Y. Nishihata, J. Mizuki, K. Narita, M. Kimura, and K. Kaneko, *Angew. Chem. Int. Edit.*, 2006, **45**, 5998–6002.
5. B. D. Madsen, W. Kobsiriphat, Y. Wang, L. D. Marks, and S. Barnett, ECS Trans., 2007, vol. 7, pp. 1339–1348.
6. B. D. Madsen, W. Kobsiriphat, Y. Wang, L. D. Marks, and S. A. Barnett, *J. Power Sources*, 2007, **166**, 64–67.
7. W. Kobsiriphat, B. D. Madsen, Y. Wang, L. D. Marks, and S. A. Barnett, *Solid State Ionics*, 2009, **180**, 257–264.
8. W. Kobsiriphat, B. D. Madsen, Y. Wang, M. Shah, L. D. Marks, and S. A. Barnett, *J. Electrochem. Soc.*, 2010, **157**, B279–B284.
9. T. Jardiel, M. T. Caldes, F. Moser, J. Hamon, G. Gauthier, and O. Joubert, *Solid State Ionics*, 2010, **181**, 894–901.
10. D. M. Bierschenk, E. Potter-Nelson, C. Hoel, Y. Liao, L. Marks, K. R. Poeppelmeier, and S. A. Barnett, *J. Power Sources*, 2011, **196**, 3089–3094.
11. M. D. Smith, A. F. Stepan, C. Ramarao, P. E. Brennan, and S. V. Ley, *Chem. Commun.*, 2003, 2652–2653.
12. M. B. Katz, S. Zhang, Y. Duan, H. Wang, M. Fang, K. Zhang, B. Li, G. W. Graham, and X. Pan, *J. Catal.*
13. A. L. Sauvet and J. T. S. Irvine, *Solid State Ionics*, 2004, **167**, 1–8.
14. D. S. Deak, *Mater. Sci. Tech. Ser.*, 2007, **23**, 127–136.
15. C. Noguera, *J. Phys.: Condens. Mat.*, 2000, **12**, R367–R410.
16. J. Zegenhagen, T. Haage, and Q. D. Jiang, *Appl. Phys. A-Mater.*, 1998, **67**, 711–722.
17. A. Pojani, F. Finocchi, and C. Noguera, *Surf. Sci.*, 1999, **442**, 179–198.
18. Y. Mukunoki, N. Nakagawa, T. Susaki, and H. Y. Hwang, *Appl. Phys. Lett.*, 2005, **86**, 171908–171908–3.
19. J. Brunen and J. Zegenhagen, *Surf. Sci.*, 1997, **389**, 349–365.
20. B. Meyer, J. Padilla, and D. Vanderbilt, *Faraday Discuss.*, 1999, **114**, 395–405.
21. M. S. Islam, *Solid State Ionics*, 2002, **154-155**, 75–85.
22. K. Szot, M. Pawelczyk, J. Herion, C. Freiburg, J. Albers, R. Waser, J. Hulliger, J. Kwapulinski, and J. Dec, *Appl. Phys. A-Mater.*, 1996, **62**, 335–343.
23. K. Szot and W. Speier, *Phys. Rev. B*, 1999, **60**, 5909–5926.
24. K. Szot, W. Speier, R. Carius, U. Zastrow, and W. Beyer, *Phys. Rev. Lett.*, 2002, **88**, 075508.
25. Y. Chen, W. Jung, Z. Cai, J. J. Kim, H. L. Tuller, and B. Yildiz, *Energy Environ. Sci.*, 2012, **5**, 7979–7988.
26. W. Jung and H. L. Tuller, *Energy Environ. Sci.*, 2012, **5**, 5370–5378.

27. H. Jalili, J. W. Han, Y. Kuru, Z. Cai, and B. Yildiz, *J. Phys. Chem. Lett.*, 2011, **2**, 801–807.
28. G. Horvath, J. Gerblinger, H. Meixner, and J. Giber, *Sensor Actuat. B-Chem.*, 1996, **32**, 93–99.
29. D. A. Bonnell and J. Garra, *Rep. Prog. Phys.*, 2008, **71**, 044501.
30. J. B. Goodenough and Y.-H. Huang, *J. Power Sources*, 2007, **173**, 1–10.
31. S. Lee, G. Kim, J. M. Vohs, and R. J. Gorte, *J. Electrochem. Soc.*, 2008, **155**, B1179–B1183.
32. G. Kim, G. Corre, J. T. S. Irvine, J. M. Vohs, and R. J. Gorte, *Electrochem. Solid-State Lett.*, 2008, **11**, B16–B19.
33. J.-S. Kim, N. L. Wieder, A. J. Abraham, M. Cargnello, P. Fornasiero, R. J. Gorte, and J. M. Vohs, *J. Electrochem. Soc.*, 2011, **158**, B596.
34. E. Konysheva, R. Blackley, and J. T. S. Irvine, *Chem. Mater.*, 2010, **22**, 4700–4711.
35. D. N. Miller and J. T. S. Irvine, *J. Power Sources*, 2011, **196**, 7323–7327.
36. J. T. Yates and C. T. Campbell, *PNAS*, 2011, **108**, 911–916.
37. J. A. Farmer and C. T. Campbell, *Science*, 2010, **329**, 933–936.
38. R. J. Gorte and J. M. Vohs, *Curr. Opin. Colloid. In.*, 2009, **14**, 236–244.
39. S. P. Jiang, *Mat. Sci. Eng. A-Struct.*, 2006, **418**, 199–210.
40. T. Ikebe, H. Muroyama, T. Matsui, and K. Eguchi, *J. Electrochem. Soc.*, 2010, **157**, B970–B974.
41. G. Corre, G. Kim, M. Cassidy, J. M. Vohs, R. J. Gorte, and J. T. S. Irvine, *Chem. Mater.*, 2009, **21**, 1077–1084.

8 High temperature steam electrolysis with transition metal doped, A-site deficient titanate cathodes

8.1 The suitability of A-site deficient perovskites as HTSE cathodes

Previous chapters have shown that B-site doped, A-site deficient perovskites exhibit a range of properties that may act coherently to deliver good performance in applications such as hydrogen electrode materials for SOFC or SOEC. These properties are briefly reviewed below.

First, it was shown here that A-site deficient perovskite titanates accommodate an extensive range of B-site dopants which makes tailoring various properties very accessible. As such, oxide ion mobility, the extent of the reduction, the electronic conductivity or other properties of these phases can be considerably enhanced through modest amounts of B-site doping. This in turn may contribute positively towards the creation of sites for electrochemical reactions, improved electrocatalytic activity and overall quality of current collection. Notably, titanates are n-type conductors meaning that the stronger the reduction conditions the higher their oxygen deficiency and electronic conductivity becomes, hence they are a natural choice for hydrogen electrodes where extremely low p_{O_2} values may be reached during operation.

However, the key aspect demonstrated throughout this thesis was the critical importance of the unique defect chemistry context set by the presence of A-site vacancies. A-site vacancies act to enhance the extent of reduction of titanates which in turn increases conductivity and the number of potential sites for electrochemical reactions. Most importantly, however, A-site deficiency triggers the exsolution of B-site species into nanoparticles in reducing environment which enables one to decorate the parent perovskite surface with catalytically active nanoparticles.

8.2 HTSE experiment overview

Thus, selected B-site doped, A-site deficient titanates belonging to the series $La_{0.4}Sr_{0.4}M_{0.06}Ti_{0.94}O_{3-\gamma}$developed in this study were incorporated into button cell-type SOEC devices as described in section 3.1.3. The button cells were then mounted in the testing setup as described in section 3.3. It should be noted here that all the experimental work described in this chapter, including data processing, was carried out by Dr. George Tsekouras, formerly at the University of St. Andrews, presently at EMPA (Switzerland). His involvement with this work is gratefully acknowledged.

The HTSE performance of titanate cathodes was compared based on the *current density* observed in current – voltage (I–V) curves, which is directly proportional to the *quantity of hydrogen produced from the electrolysis of steam* (assuming 100% Faradaic efficiency).[1] I–V curves of electrolysis cells were measured in a 2-electrode, full-device arrangement, at 900 °C, in 47% H_2O/53% N_2, by performing linear sweep voltammetry from -1.7 V to -0.4 V, at a scan rate of 10 mVs^{-1}. Prior to the I-V measurement the cathodes were conditioned at -1.7 V applied potential.

8.3 The performance of selected A-site deficient titanates as HTSE cathodes

I–V curves obtained for SOECs based on $La_{0.4}Sr_{0.4}M_{0.06}Ti_{0.94}O_{3-\gamma}$(M = Ti, Fe, Co, Ni) cathodes operated in 47% H_2O/53% N_2 at 900 °C are shown in Figure 8-1. This figure demonstrates the dramatic increase in performance achieved by doping the selected transition metal cations compared to the undoped composition. Thus, for a given applied voltage, the achievable current density (*i.e.* hydrogen production) increases considerably from M = Ti, to Fe, Co, being highest upon introduction of Ni.

Apart from the current density, another critical parameter which relates to the performance of SOEC cathodes may be defined. This is referred to as the HTSE onset potential, E_{HTSE}, and is determined by extrapolating the ohmic

(linear) segment of I–V curves to zero current. Thus, E_{HTSE} reflects the activation barrier to steam electrolysis; a lower E_{HTSE} means that lower voltages need to be applied in order to start producing hydrogen.

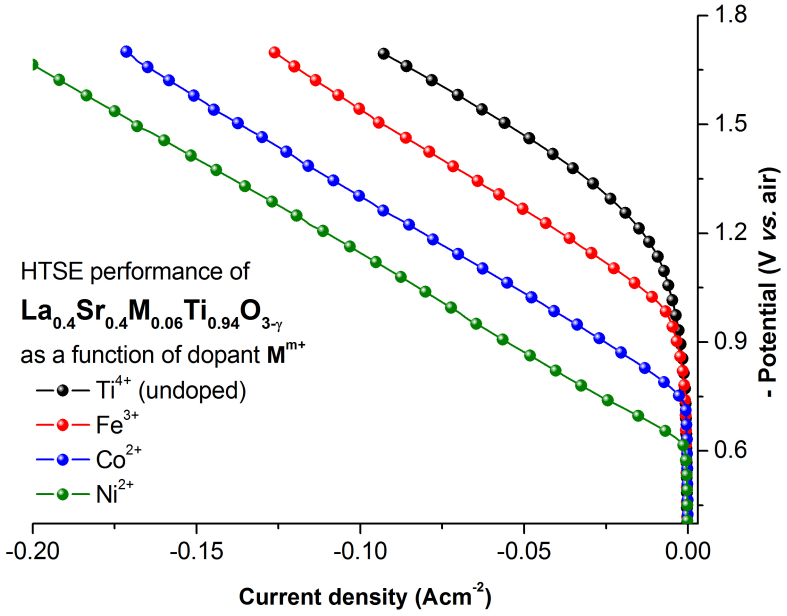

Figure 8-1 | I–V curves obtained for $La_{0.4}Sr_{0.4}M_{0.06}Ti_{0.94}O_{3-\gamma}$(M = Ti, Fe, Co, Ni) HTSE cathodes operated in 47% H_2O/53% N_2 at 900 °C.

Thus, by examining Figure 8-1, it is apparent that B-site doping of Fe, Co and Ni in $La_{0.4}Sr_{0.4}M_{0.06}Ti_{0.94}O_{3-\gamma}$ not only led to an increase in hydrogen production, but also significantly decreased the activation barrier for steam electrolysis. Thus, compared to the undoped composition which has $E_{HTSE} = -1.19$ V, the introduction of Fe decreased the onset potential to -0.98 V. Upon Co doping the onset potential decreased further to -0.76 V, while Ni doping resulted in the lowest decrease in onset potential found in this study, -0.63 V , almost half compared to the parent composition.

Interestingly, the E_{HTSE} value of -0.63 V found for the Ni-doped sample coincides with the E_{HTSE} of an in-house produced SOEC based on state-of-the-art Ni/YSZ.[2] This implies that in the case of the perovskite cathode $La_{0.4}Sr_{0.4}Ni_{0.06}Ti_{0.94}O_{3-\gamma}$ electrocatalytically active Ni metal nanoparticles exsolved during operation, as expected. This was confirmed by examining the sample by SEM after testing, as shown in Figure 8-2.

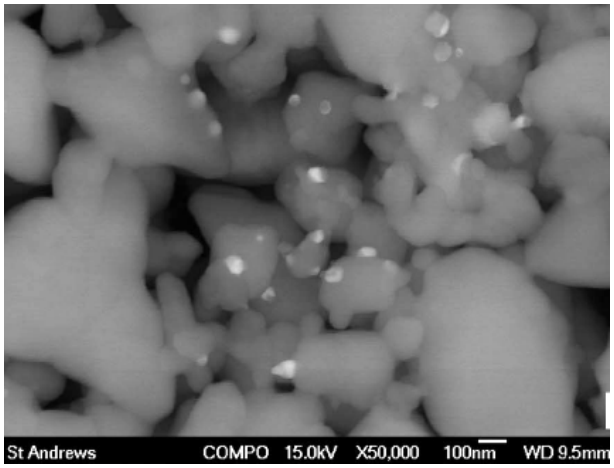

Figure 8-2 | SEM images of $La_{0.4}Sr_{0.4}Ni_{0.06}Ti_{0.94}O_{3-\gamma}$ electrolysis cell cathode after testing. The image was collected using a backscattered electron detector to ensure compositional contrast between the ceramic (perovskite) and the metal (Ni).

Post-test SEM analysis revealed that in fact exsolutions had occurred in the case of the other compositions as well, *i.e.* Fe from $La_{0.4}Sr_{0.4}Fe_{0.06}Ti_{0.94}O_{3-\gamma}$ and Co from $La_{0.4}Sr_{0.4}Co_{0.06}Ti_{0.94}O_{3-\gamma}$. By similarity to the case of Ni doping it may be implied that the dramatic enhancement HTSE performance, in terms of both current density and E_{HTSE}, occurred upon the exsolution of electrocatalytically active metallic nanoparticles from the corresponding perovskite cathodes, under operating conditions. Or, simply, the increase in performance correlates to the formation of exsolutions.

8.4 HTSE titanate-based cathode performance and defect chemistry

In order to verify the above mentioned statement, a greater range of substituted perovskites from the same series, $La_{0.4}Sr_{0.4}M_{0.06}Ti_{0.94}O_{3-\gamma}$, was considered. Additionally, compositions belonging to the A-site stoichiometric, oxygen excess defect chemistry, such as $La_{0.3}Sr_{0.7}M_{0.06}Ti_{0.94}O_{3+\gamma}$ (M = Ti, Ni) were also included. The results are plotted in Figure 8-3 in terms of E_{HTSE} against dopant M.

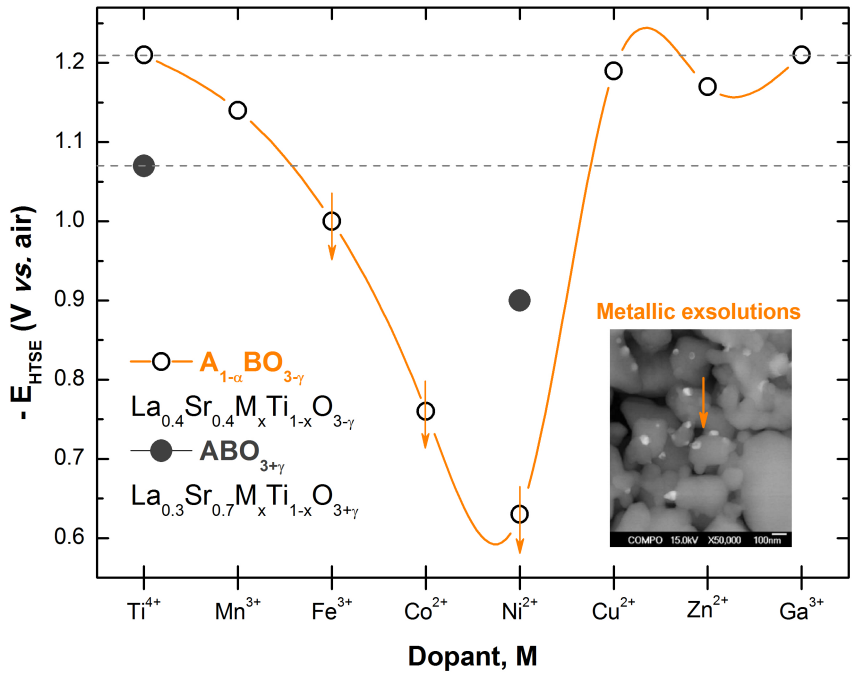

Figure 8-3 | HTSE onset potential as a function of dopant in different defect chemistries: A-site deficient $La_{0.4}Sr_{0.4}M_{0.06}Ti_{0.94}O_{3-\gamma}$ and A-site stoichiometric, oxygen excess . Dramatic decrease in steam electrolysis activation barrier coincides with the exsolution of electrocatalytically active metallic nanoparticles from A-site deficient perovskites. Compositions that exsolve such nanoparticles under SOEC operation are marked with an arrow pointing downwards.

Close examination of Figure 8-3 reveals several important aspects regarding the role of defect chemistry with respect to the steam electrolysis activation barrier, one of the major indicators of HTSE cathode performance. The baseline (absolute) onset potential in the case of the oxygen excess undoped composition, $La_{0.3}Sr_{0.7}TiO_{3+\gamma}$ lies below that of the A-site deficient analogue, $La_{0.4}Sr_{0.4}TiO_3$. This is not surprising considering the fact that the oxygen excess composition has an innate feature that allows for good of oxide ion mobility and electrocatalytic activity compared to the A-site deficient composition.[1] Consequently, upon Ni doping, the oxygen excess composition shows a considerable decrease in onset potential, possibly due to a synergistic effect between the oxygen excess intergrowth defects and the particular effectiveness of Ni^{2+} as electrocatalyst.[3,4] Even so, the onset potential of the Ni-doped, oxygen excess system is considerably higher compared to its A-site deficient analogue, owing to the Ni metal exsolutions occuring in the latter during operation. If the A-site stoichiometric Ni-doped

composition would be able to exsolve Ni metal as well, then its onset potential should equal -0.63 V as in the case of the Ni-doped A-site deficient composition. The fact that this is not observed is in good agreement with the conclusions reached in Chapter 7 according to which Ni doped, A-site stoichiometric perovskites are unlikely to exsolve metallic Ni nanoparticles even in strongly reducing environment.

Also, it should be noted that no exsolutions were observed after SOEC operation in the case of the HTSE cathodes based on $La_{0.4}Sr_{0.4}M_{0.06}Ti_{0.94}O_{3-\gamma}$ with M = Mn, Cu, Zn or Ga. Thus it seems reasonable to conclude that the dramatic lowering in activation barrier to steam electrolysis observed when M = Fe, Co or Ni were introduced in $La_{0.4}Sr_{0.4}M_{0.06}Ti_{0.94}O_{3-\gamma}$, coincides with the exolution of corresponding electrocataliticaly active metallic nanoparticles, driven by the defect chemistry of A-site deficient perovskites.

8.5 Conclusions and outlook

While the steam electrolysis performance of the $La_{0.4}Sr_{0.4}Ni_{0.06}Ti_{0.94}O_{3-\gamma}$ cathode was a significant step-change compared to other perovskites considered to date, electrochemical impedance spectroscopy analysis indicated that the overall performance of this material is still not as high as the Ni/YSZ cermet.[2] Nonetheless, as explained in sections 1.5 and 1.6 perovskite oxides offer numerous advantages over the cermet electrode which may compensate to some extent for the smaller performance, especially through significantly better redox tolerance and device lifetime. Moreover, the compositions and microstructures presented here are rather preliminary since they may be further optimised as explained in Chapter 7. Thus, the results shown here may be regarded as 'proof of concept' that the exolution phenomenon can be employed to achieve considerable increase in catalytic performances, as exemplified here for the particular case of high temperature steam electrolysis.

References

1. G. Tsekouras and J. T. S. Irvine, *J. Mater. Chem.*, 2011.
2. G. Tsekouras, D. Neagu, and J. T. S. Irvine, *Energy Environ. Sci.*, 2012, **6**, 256–266.
3. L. Yang, L. C. De Jonghe, C. P. Jacobsen, and S. J. Visco, *J. Electrochem. Soc.*, 2007, **154**, B949–B955.
4. J. Rossmeisl and W. G. Bessler, *Solid State Ionics*, 2008, **178**, 1694–1700.

DISCUSSION AND CONCLUSIONS

This study exemplified the use of defect chemistry as a powerful tool for tailoring the properties and general functionality of perovskites. The effectiveness of this approach was demonstrated by designing entirely new perovskite system which displayed unique properties leading to a step-change increase in performance, compared to other perovskites considered to date as hydrogen electrode materials in solid oxide electrolysis cells (SOECs).

This concept is essentially based on understanding and manipulating the exceptional ability of perovskites to accommodate a wide variety of defects. As pointed out before, it is useful to visualise the perovskite oxide ABO_3 structure as a 3D network of BO_6 corner-sharing octahedra, with the A-ions located in the resulting cuboctahedral cavities. Perovskite oxides can accommodate defects from three fundamental points of view: *size* of constituents through tilting or stretching of the octahedra; *deficiency* (A and/or O-site) by creation of vacancies, while preserving corner-sharing of the octahedra; and *excess* (A and/or O-site) through intergrowths, locally interrupting the corner-sharing octahedra chains. Additionally, since the BO_6 octahedra represent not only the 'building blocks' of the perovskite crystal structure but of the perovskite electronic structure as well, the above mentioned nonstoichiometry classes may be substituted on the B-sites with various dopants to allow further tailoring of the properties. Thus, multiple combinations of defects and structural features are possible, each creating a context with its own unique and potentially useful defect chemistry.

Here, primarily the A-site deficient titanate, $La_xSr_{1-3x/2}TiO_3$ ($x = 0.4$) defect chemistry was investigated, especially upon B-site doping. However, comparisons were made throughout the thesis with another relevant

nonstoichiometry class, the A-site stoichiometric, oxygen excess composition $La_xSr_{1-x}TiO_{3+x/2}(x = 0.3)$, also B-site doped.

The work carried out here revealed that each of these classes possesses a key feature that is distinctive and instrumental in dictating overall performance and behaviour. For the oxygen excess this is the oxygen excess intergrowths. These enable higher 'baseline' reducibility and electrochemical performance compared to the A-site deficient analogues, but since they locally disrupt octahedra connectivity, they also lead to slightly smaller electronic conductivity. For the A-site deficient perovskites this key feature is the A-site deficiency itself which acts to significantly enhance reducibility and subsequently the extent of reduction and electronic conductivity. But most importantly, A-site vacancies trigger the exsolution of B-site species as electrocatalytically active nanoparticles on the surface of the parent perovskite, upon reduction. Because of this, the functionalisation of A-site deficient perovskites offers so much more flexibility compared to A-site stoichiometric perovskites, opens possibilities and enables applications that previously were not easily accessible. For example, in the case of high temperature steam electrolysis exsolution of metallic nanoparticles coincided with a significant drop in the activation barrier for steam electrolysis, providing proof of concept that remarkable increase in electrocatalytic activity may be achieved through this phenomenon. This may be largely attributed to the inherent catalytic properties of the metallic nanoparticles (*e.g.* Ni, Co etc) but the possibility that the 'unconventional bond' shared between the nanoparticle and the parent phase may play a role as well should not be overlooked (*e.g*. coherent growth of $CeO_{2-\delta}$ nanoparticles was observed here from $La_{0.8}Ce_{0.1}Ni_{0.4}Ti_{0.6}O_3$).

Thus, while the work carried out through this thesis exemplified the use of defect chemistry in the particular case of hydrogen electrode materials for solid oxide electrolysis cells, the core concepts can be easily transferred to other fields including catalysis, electrocatalysis, electrochemical devices, growth of coherent nano-size phases etc.